



HAL
open science

Role of Liver X Receptor β in the development and myelination of the Peripheral Nervous System

Venkat Krishnan Sundaram

► **To cite this version:**

Venkat Krishnan Sundaram. Role of Liver X Receptor β in the development and myelination of the Peripheral Nervous System. Human health and pathology. Université Paris Cité, 2020. English. NNT : 2020UNIP5038 . tel-03879859

HAL Id: tel-03879859

<https://theses.hal.science/tel-03879859v1>

Submitted on 30 Nov 2022

HAL is a multi-disciplinary open access archive for the deposit and dissemination of scientific research documents, whether they are published or not. The documents may come from teaching and research institutions in France or abroad, or from public or private research centers.

L'archive ouverte pluridisciplinaire **HAL**, est destinée au dépôt et à la diffusion de documents scientifiques de niveau recherche, publiés ou non, émanant des établissements d'enseignement et de recherche français ou étrangers, des laboratoires publics ou privés.

Université de Paris

École doctorale [Médicament Toxicologie Chimie Imagerie ED563](#)

Laboratoire [INSERM UMRS 1124 – Equipe 3](#)

*Role of Liver X Receptor β in the development and
myelination of the Peripheral Nervous System*

[Rôle du Liver X Récepteur \$\beta\$ dans le développement et la myélinisation du
Système Nerveux Périphérique](#)

Par Venkat Krishnan SUNDARAM

Thèse de doctorat de [Neurosciences](#)

Dirigée par le Professeur Charbel MASSAAD

Présentée et soutenue publiquement le 27 Octobre 2020

Devant un jury composé de

Prof. Piotr TOPILKO, PUPH, Université Paris Est Créteil (Rapporteur)

Dr. Jocelyne CABOCHE, DR, Sorbonne Université (Rapporteur)

Dr. Thierry GALLI, DR, Université de Paris (Examinateur)

Dr. Ruth STASSART, Docteur en médecine, Leipzig University Hospital (Membre invité)

Dr. Julien GRENIER, MCU, Université de Paris (Membre Invité)

Dedicated to my parents, Mrs. Visalakshi SUNDARAM and Mr. Sundaram ATHUR VENKATAKRISHNAN

Your efforts and sacrifices have made me the person that I am today.

I am forever grateful and indebted for your unconditional love, support, guidance and for making this dream a reality.

ACKNOWLEDGEMENTS

At the outset, I would like to begin the acknowledgements by immensely thanking my parents who have played an important role in shaping my professional and personal pursuits. The emphasis laid on the fundamental principles of compassion, empathy, and patience by my mother and those of persistence, tenacity, curiosity, and scientific rigor by my father has stood me in great stead throughout my journey as a PhD student. I am fortunate to have been guided by these principles that reveal to be a cornerstone in having a fulfilling academic career. On the same note, I express my deepest gratitude towards my sister, Srividya SUNDARAM, for her support, appreciation and perspective over the years, which have played an integral part in my personal and professional achievements. Furthermore, I extend my profound gratitude to my partner, Pooja BALASUBRAMANIAN, who has been a great source of emotional and moral support throughout my PhD journey and beyond. I also take this opportunity to thank my aunt and uncle, Dr. Nagarajan and Dr. Malathi NAGARAJAN who were instrumental in providing me with their invaluable guidance and support towards my academic pursuits in France. I cherish and value the contributions of my family and needless to state, my dream of obtaining a doctoral degree would not have been possible without their help and support.

On the professional front, I express my deepest gratitude to Prof. Charbel MASSAAD for his meticulous efforts, patience, and mentorship. He has guided me immensely in honing my scientific skills and supported me, time and again, in pushing my boundaries and overcoming my apprehensions. I have learnt a great deal on project management, prioritizing and focusing on key questions and hypothesis by working with him on my PhD project. Furthermore, I would also go on to state that he has been a father figure to me in France and has extended his invaluable assistance towards my professional and personal aspirations.

I would also like to convey my special thanks to Dr. Julien GRENIER, my co-mentor, who has been there with me through the ups and downs of my PhD life, both at the bench and at the office. He has taught me that each observation needs to be looked at from different vantage points before getting down to formulating hypothesis and experiments. I have also learnt from him that effective scientific communication needs to be succinct, simple and should give due importance to the requirements of the scientific community at large. I look forward to incorporating these teachings as I take my first steps into my academic career.

On the same note, I thank Dr. Ruth STASSART and Dr. Robert FLEDRICH, our collaborators, and my future mentors, for their time and investment in bringing my PhD project to fruition. They have been a source of inspiration and I ardently look forward to working with them during my Post Doc.

I also thank my friend, colleague, and collaborator Dr. Nirmal Kumar SAMPATHKUMAR for his counsel and guidance at various instances during my PhD and also during the different projects that we have worked on together in the lab. I would like to mention that he played a profoundly significant role in introducing me to Prof. MASSAAD and the lab during my masters when I was scouting for internship opportunities. Hence, I am deeply grateful for his genuinity and his gesture that has indeed helped me realize my dream of pursuing a PhD.

Finally, I would like to thank my colleagues, Prof. Mehrnaz JAFARIAN-TEHRANI, Prof. Sophie BERNARD, Dr. Delphine MEFFRE, Dr. Mehdi HICHOR, Dr. Damien LE MENUET, Dr. Christel BECKER, Prof. Frédéric CHARBONNIER, Dr. Olivier BIONDI, Dr. Laure WEILL, Dr. Bruno Della GASPERA, Dr. Suzie LEFEVRE; fellow PhD students, Tatiana EL JALKH, Aida Padilla FERER, Rasha BARAKAT, Julia FATH, Alex CARRETE (now Dr. CARRETE); the technicians Julia MONTANARO, Fatima FAIS; the engineers, Dr. Anne SIMON, Celine BECKER, Dr. Françoise COURTIN; the collaborators, Prof. Piotr TOPILKO, Prof. Jean-Marc LOBACCARO, Dr. Amalia TROUSSON, Dr. Eric PASMANT and finally my student interns, Sylvain MATEU, Ines COLLARD, Manar HERRADI, Cecilia MFORO and Jenisha KUMARAKULASIGHAM for their help and assistance during my PhD.

Thus, as I prepare for my formal introduction into the academic world, I would like to conclude my acknowledgements with a few poetic phrases by an anonymous author that has deeply impacted my outlook and has inspired me to achieve greater heights.

I would rather be a 'could be' if I cannot be an 'are',

For a 'could be' is a 'may be' reaching for a star.

I would rather be a 'has been' than a 'might have been' by far,

Because a 'might have been' has never 'been' but 'has been' was once an 'are'.

- **Anonymous**

Résumé de these

Les LXR (Liver X Receptor) α et β sont des récepteurs nucléaires activés par la liaison à certains dérivés oxydés du cholestérol (oxystérols) comme le 25-hydroxy-cholestérol, entre autres. Les LXR sont connus pour intervenir dans de nombreux processus biologiques tels que le métabolisme des lipides, l'homéostasie du cholestérol ou l'inflammation. Ils exercent leurs influences dans tous les organes du corps, y compris le système nerveux, central et périphérique.

Mon laboratoire d'accueil étudie depuis des années l'implication de ces récepteurs dans la physiologie des cellules gliales et la myélinisation au moyen d'un mutant murin dénué de l'expression des deux isoformes du récepteur aux oxystérols (LXRdKO). L'équipe a ainsi montré un défaut de myélinisation du nerf sciatique en l'absence des LXR, suggérant leur importance dans ce processus.

Le développement et la mise en place de la gaine de myéline est un processus complexe qui repose sur un dialogue moléculaire étroit entre l'axone et la cellule de Schwann, cellule gliale myélinisante du système nerveux périphérique. Afin de mieux comprendre l'implication du LXR β , isoforme majoritaire dans le système nerveux, dans la physiologie de cette cellule, nous avons donc créé un mutant murin au sein duquel le LXR β est spécifiquement invalidé dans les précurseurs de cellules de Schwann (LXR β -SCP KO).

Ce mutant fut obtenu en croisant des animaux dont l'allèle du gène Nr1h2 codant pour le LXR β est floxé avec des souris exprimant l'enzyme de recombinaison génétique Cre sous la dépendance du promoteur de Dhh (Desert Hedgehog), spécifiquement exprimé par les précurseurs des cellules de Schwann pendant le développement embryonnaire à partir du stade E12,5 (jour embryonnaire 12,5).

De façon tout à fait intéressante, nous avons montré une absence quasi totale de cellules de Schwann dans les nerfs sciatiques des nouveau-nés mutants portant la délétion homozygote de LXR β . Cette absence est accompagnée d'un profond remaniement de l'architecture cellulaire du nerf qui apparaît translucide même à l'âge adulte. Dénué de cellules myélinisantes, le nerf en développement a laissé la place pendant aux cellules périneuriales qui colonisèrent l'espace endoneurial et créèrent des fascicules nerveux constitués d'agrégats d'axones aux diamètres considérablement augmentés.

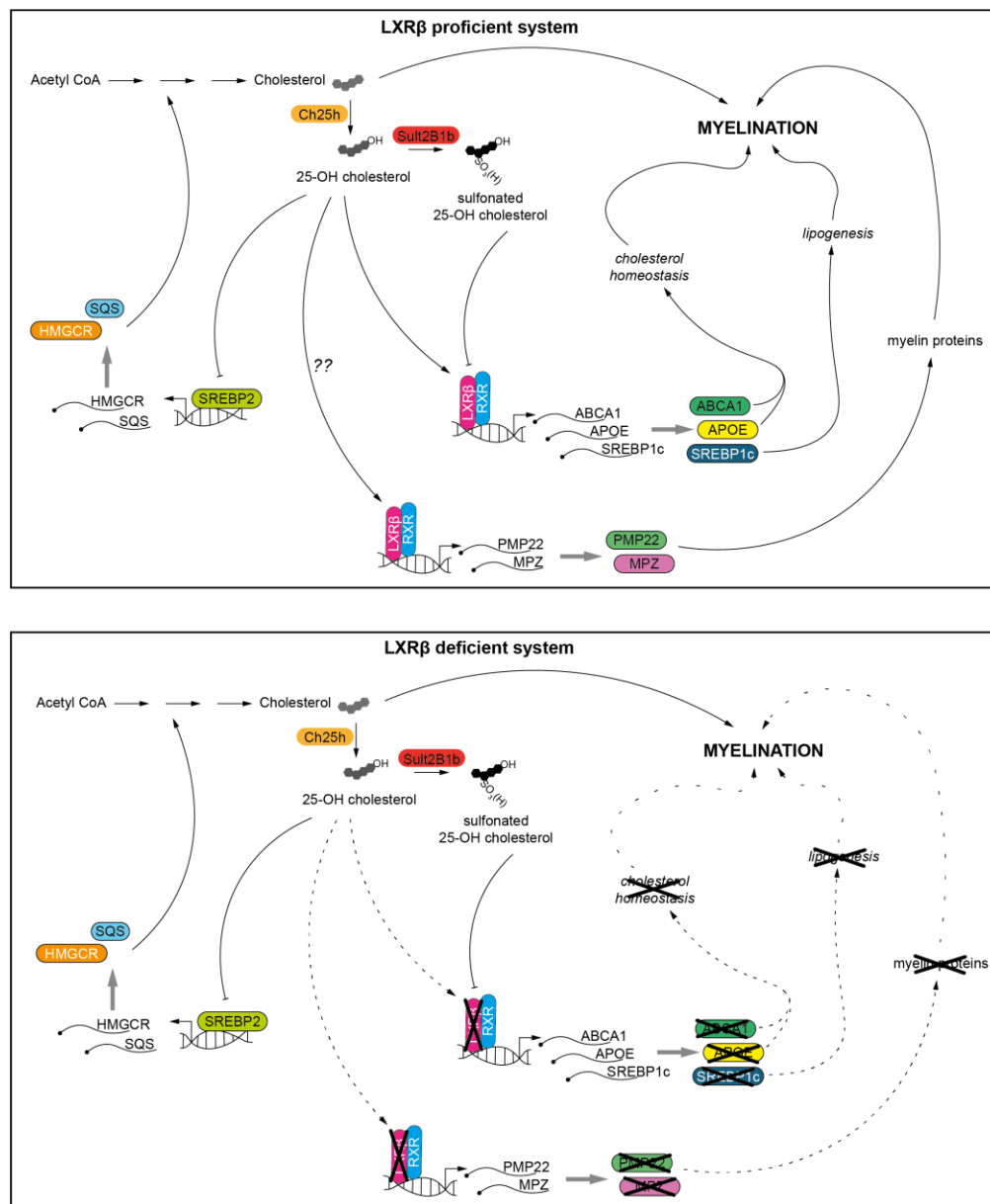
Afin d'étudier quand l'ablation du LXR β dans les précurseurs Schwannien menait à la disparition de la population dans les nerfs périphériques, nous avons mis au point au laboratoire la culture primaire d'explants de ganglions spinaux (DRG) qui récapitule la majorité des évènements embryonnaires nécessaires la myélinisation. Nous avons ainsi déterminé que les précurseurs Schwanniens mourraient entre 5 et 7 jours de culture *ex vivo*, correspondant à un stade développemental au cours duquel les précurseurs Schwanniens se différencient en cellules de Schwann immatures. L'analyse de données disponibles issues d'études transcriptomiques de la moelle épinière pendant l'embryogenèse nous a permis de constater l'importance de la régulation de l'homéostasie du cholestérol lors de la transition des cellules de Schwann du stade précurseur au stade immature.

En effet, alors que l'expression des gènes de la myéline est stimulée, toute comme le gène codant pour la 25-hydroxylase, impliqué dans la synthèse du 25-hydroxy-cholestérol, celui codant pour ABCA1, impliqué dans l'efflux de cholestérol, est lui, réprimé. On peut donc supposer que chez les animaux LXR β -SCP KO, les précurseurs Schwanniens ne peuvent maintenir une forte expression des gènes de la myéline et interrompent leur programme de différenciation vers le stade immature.

Dans un système exprimant LXR β , la synthèse du cholestérol donne naissance au 25-Hydroxycholestérol (25OH cholesterol) par l'enzyme Cholestérol 25 Hydroxylase (Ch25h). Cet oxystérol se lie au LXR β pour induire l'expression des gènes d'efflux du cholestérol ABCA1 et ApoE ainsi que le principal régulateur de la lipogenèse Srebp1c. Cependant, nos données suggèrent également que 25OH peut induire l'expression des gènes de la myéline sûrement par LXR β .

L'homéostasie du cholestérol, la lipogenèse et l'expression des protéines de la myéline contribuent à la différenciation des cellules de Schwann et à la myélinisation. En outre, un traitement prolongé des cellules de Schwann primaires avec du 25-Hydroxycholestérol entraîne une réduction des gènes cibles du LXR β , probablement médié par la forme sulfonée de l'oxystérol (sulfonated 25-OH cholesterol).

Dans un système déficient en LXR β , l'homéostasie du cholestérol, la lipogénèse et l'expression des protéines de la myéline pourraient être directement compromises en raison de l'absence du récepteur. De plus, les niveaux intracellulaires d'oxystérols et de cholestérol seraient dérégulés et pourraient conduire à un échec de la différenciation des cellules de Schwann et éventuellement ils meurent, incapables de contrôler la concentration en cholestérol nécessaire à la mise en place de la gaine de myéline. L'ensemble de ces résultats est présenté dans le schéma ci-dessous



Résumé graphique : Rôle de LXR β dans le développement des cellules de Schwann.

ABSTRACT:

Liver X Receptors (LXRs) are ligand-activated nuclear receptors that are expressed as two distinct isoforms: LXR α and LXR β encoded in mice by the genes Nr1h3 and Nr1h2, respectively. Although classified as orphan receptors upon discovery, oxidized cholesterol derivatives (oxysterols) such as 20(S), 22(R)-, 24(S)-, 25- and 27-hydroxy cholesterol (HC) and 24(S), 25-epoxycholesterols were later found to be their natural ligands. LXRs have been implicated in several physiological processes such as lipid metabolism, cholesterol homeostasis and inflammation in different systems including the Central and Peripheral Nervous Systems.

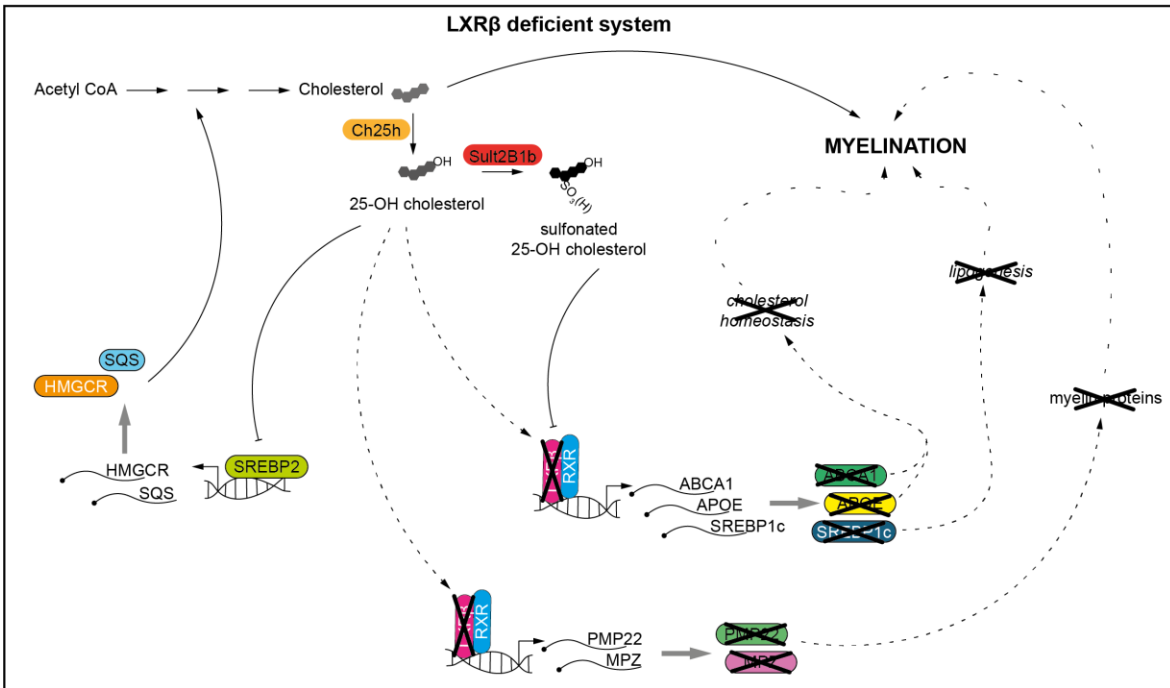
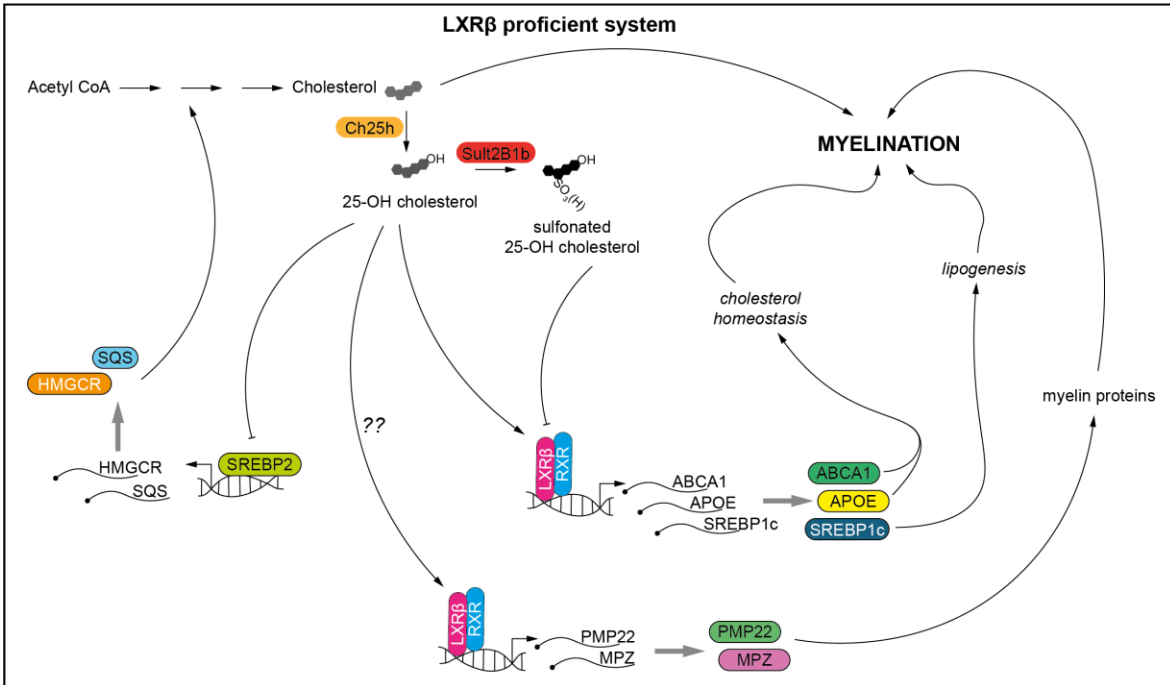
Previous studies conducted in my host laboratory have addressed the role of the nuclear receptors LXR α/β in peripheral myelination. LXR α/β ^{-/-} total mutants exhibited an upregulation of myelin genes (Mpz and Pmp22) at the RNA level but their protein levels were downregulated, and these animals displayed thinner myelin sheaths and electrophysiological deficits in adults. Thus, our first aim was to explain the discrepancies observed in Pmp22 and Mpz RNA and protein expression. To this end, we explored the redox homeostasis of the sciatic nerves in these animals based on a microarray analysis that revealed multiple hits pertaining to genes implicated in redox homeostasis mediated by Nuclear factor erythroid 2-related factor (Nfe2l2 also commonly known as Nrf2). Further investigation revealed that the absence of LXRs gives rise to oxidative stress in peripheral nerves, which in turn resulted in the aggregation of Pmp22 thus lowering its protein expression. Using cell culture and antioxidant rescue experiments *in vivo*, we demonstrated that LXRs play an active role in maintaining the redox homeostasis in Schwann cells of peripheral nerves.

Our second aim was to understand how myelin proteins and the myelin sheath were impacted by the ablation of the LXRs: is it due to the lack of LXR α or β in Schwann cells? To test this hypothesis, we generated a Schwann cell specific Knockouts of LXR α and LXR β by crossing floxed strains of the nuclear receptor with Desert Hedgehog:Cre (*DhhCre*) mice. This breeding assured the genetic ablation of the nuclear receptor from the Schwann cell precursor stage at around E12.5 in mutants.

Thus, we generated LXR α ^{f/f}:DhhCre and LXR β ^{f/f}:DhhCre mice wherein the former did not exhibit any phenotype, but the latter presented with a drastic phenotype. Although we found that both these isoforms are expressed in WildType Schwann cells, LXR β was found to be the functionally active isoform that governs lipogenesis and cholesterol homeostasis in Schwann cells. Therefore, it was not surprising to find that LXR β ^{f/f}:DhhCre mice exhibited a phenotype but LXR α ^{f/f}:DhhCre mice did not. LXR β ^{f/f}:DhhCre mice exhibited a drastic reduction in Schwann cell numbers at birth which was followed by a complete absence

of myelin sheath around axons at post-natal time points. This resulted in a dramatic alteration of the cellular anatomy of the peripheral nerves resulting in the invasion of perineurial cells into the endoneurial space that subsequently ensheathed naked axonal bundles. To understand the untimely disappearance of Schwann cells in $LXR\beta^{f/f}$ DhhCre mice, we retraced the embryonic development of Schwann cells using Dissociated DRG cultures established from E13.5 mutants and their respective controls. In mutant cultures, we observed that Schwann cells detach from axons and float in culture between DIV5 and DIV7, which corresponds to the Schwann cell precursor/Immature Schwann cell transition stage. To understand the role of $LXR\beta$ in this phenomenon, we analyzed previous transcriptomic studies conducted on embryonic spinal nerves. We found that Cholesterol 25 Hydroxylase is upregulated at the Precursor/immature transition, which is accompanied by a concomitant reduction in *Abca1* expression and an upregulation of myelin genes. To confirm our data, we treated WT primary Schwann cells with 25HC and observed a significant upregulation in myelin gene expression and a concomitant decrease in *Abca1* expression corroborating the *in vivo* data. We thus speculate that in an $LXR\beta$ deficient system, the Schwann cells are not able to increase myelin gene expression and regulate endogenous cholesterol levels during the precursor/immature transition and therefore they seemingly die embryonically due to an imbalance in cholesterol homeostasis and myelin gene expression. These results highlight the crucial role of $LXR\beta$ in the myelination process in the peripheral nerve.

Keywords: $LXR\beta$, Schwann cell development, oxysterols, myelination, cholesterol metabolism, lipid metabolism



Graphical Abstract: The role of LXR β in Schwann cell development. In an LXR β proficient system, the synthesis cholesterol gives rise to 25-Hydroxycholesterol (25OH) by the enzyme Cholesterol 25 Hydroxylase (Ch25h). This oxysterol binds LXR β to induce the expression of cholesterol efflux genes ABCA1 and ApoE as well as the master regulator of lipogenesis Srebp1c. However, our data also suggests that 25OH can induce myelin gene expression possibly through LXR β . Cholesterol homeostasis, lipogenesis and myelin protein expression together can positively Schwann cell differentiation and myelination. Furthermore, prolonged treatment of primary Schwann cells with 25OH results in a reduction in LXR β target genes, which is possibly mediated by the Sulfonated form of the oxysterol. In an LXR β deficient system, cholesterol homeostasis, lipogenesis and myelin protein expression might be directly compromised due to the absence of the receptor. Moreover, the intracellular oxysterol and cholesterol levels would be dysregulated and eventually lead to a failure in Schwann cell differentiation and possibly death.

LIST OF IMPORTANT ABBREVIATIONS

24(S)HC or 24(S)OH	24S-Hydroxycholesterol
25HC or 25OH	25-Hydroxycholesterol
27HC or 27OH	27-Hydroxycholesterol
ABCA1	ATP Binding Cassette Transporter A1
ANS	Autonomous Nervous System
APOE	Apolipoprotein E
Ch25h	Cholesterol 25 Hydroxylase
CNS	Central Nervous System
Cre	Transgenic Recombinase
DHH	Desert Hedgehog
DREZ	Dorsal Root Exit Zone
EGR2	Early Growth Response Protein 2 also known as KROX20
FASN	Fatty Acid Synthase
iSC	immature Schwann cell
LXRdKO	LXR double Knockout signifying the total ablation of both isoforms
LXR α	Liver X Receptor α
LXR α ^{f/f}	Liver X Receptor α homozygous flox strain
LXR α ScKO	Liver X Receptor α Schwann cell Knock Out
LXR β	Liver X Receptor β
LXR β ^{f/f}	Liver X Receptor β homozygous flox strain
LXR β ScKO	Liver X Receptor β Schwann cell Knock Out
MBP	Myelin Basic Protein
MEP	Motor Exit Point
MPZ	Myelin Protein Zero
mSC	Myelinating Schwann cell
nmSC/RSC	non-myelinating Schwann cell/Remak Schwann cell
PLP	Proteolipid Protein
PMP22	Peripheral Myelin Protein Zero
PNS	Peripheral Nervous System
SCP	Schwann cell Precursor

SNS	Sympathetic Nervous System
SOX10	SRY-Box Transcription Factor 10
SREBP1C	Sterol regulatory element-binding protein 1C
TrK	Tyrosine Kinase Receptor
ZO1	Zonula Occludens 1

Other acronyms and abbreviations are defined at first instance and subsequently repeated in each section.

Contents

Chapter 1: INTRODUCTION	1
1.1 The Peripheral Nervous System	1
1.1.1 The anatomy and functions of the PNS.....	2
1.1.2 The Sciatic Nerve	9
1.1.3 Ultra-structure and cellular composition of the sciatic nerve	10
1.1.4 Development of the PNS – An overview	13
1.1.5 Schwann cell development.....	23
1.1.6 Myelination in the PNS.....	40
1.1.7 Other cells in the PNS.....	48
1.2 Liver X Receptors (LXRs)	54
1.2.1 Description and Mechanism of Action	54
1.2.2 LXRs, Cholesterol Synthesis, Cholesterol Homeostasis and Lipogenesis	57
1.2.3 Role of LXRs in the Physiology of the PNS and Related Pathologies.....	63
1.3. Context of the Doctoral Thesis.....	77
Chapter 2: METHODS AND METHODOLOGICAL IMPROVEMENTS	79
2.1 Methods	79
2.2 Methodological improvements.....	86
2.2.1 Introduction.....	86
2.2.2 A novel qPCR data analysis workflow for reproducible and reliable results.....	88
2.2.3 Extracting sufficient amounts of RNA from mouse sciatic nerves across all ages	108
2.2.4 Establishing highly pure primary immature Schwann cell cultures from embryonic DRG cultures.....	137
Chapter 3: RESULTS	142
3.1 LIVER X RECEPTORS PROTECT SCHWANN CELLS FROM OXIDATIVE DAMAGES.....	142
3.2 LXR β IS INDISPENSABLE FOR THE SURVIVAL OF SCHWANN CELL PRECURSORS IN DEVELOPING SPINAL NERVES.....	158
3.2.1 Validation of the model:.....	158
3.2.2 Phenotypic description of LXR β ScKO animals:.....	160
3.2.3 Immunohistochemical analysis of younger mice reveals a drastic reduction in myelin content and Schwann cell numbers.....	162
3.2.4 The histochemical phenotype of LXR β ScKO nerves is not completely homogenous	166

3.2.5 Ultrastructure analysis reveals a paradigm shift in the cellular anatomy of the sciatic nerve	171
3.2.6 Perineurial cells invade into the Endoneurial space in the absence of Schwann cells	173
3.2.7 Schwann cells disappear embryonically in LXR β ScKO animals.....	175
3.2.8 Retracing Schwann cell developmental transitions in embryonic dissociated DRG cultures ..	177
3.2.9 Schwann cells in LXR β ScKO mice die between DIV5 and DIV8 in culture	198
Chapter 4: SUPPLEMENTARY RESULTS.....	200
4.1 LXR β is the functional isoform in Schwann cells	200
4.2 The putative role of 25HC in myelin gene regulation during Schwann cell development.....	203
Chapter 5: DISCUSSION.....	205
5.1 Embryonic disappearance of Schwann cells and changes in the cellular anatomy of the nerve....	205
5.2 Do Schwann cells die due to endogenous causes? Do they stop proliferating? Or do they detach from axons and thus die?	206
5.3 The plausible causes for Schwann cell death during the SCP/iSC transition or afterwards.....	207
5.4 The difference between total and specific LXR ablation.....	211
Chapter 6: PERSPECTIVES AND FUTURE DIRECTIONS.....	212
6.1 Question 1: Why is the phenotype in LXR β ScKO animals not completely homogenous?	212
6.2 Question 2: What are the complete set of transcriptomic modifications that arise as NCC transition into SCP and then iSC?	213
6.3 Question 3: What is the role of oxysterols (that are LXR ligands) in Schwann cell development and myelination?	214
6.4 Question 4: Why do LXRdKO mice not display such drastic phenotypes when compared to LXR β ScKO mice?	215
6.5 Benefit of this research in a clinical setting:.....	215
REFERENCES:.....	217

NB: The Figures and Tables are numbered for each chapter independently.

Chapter 1: INTRODUCTION

The mammalian nervous system, in general can be classified into two types – The central Nervous system (CNS) and the Peripheral Nervous System (PNS) (Kandel et al., 2000) . The CNS is primarily composed of the Brain, the cerebellum, the brain stem and the Spinal cord. The PNS, on the other hand, is composed of the nerves that emanate from the spinal cord all the way to the muscle, skin and other organs in different parts of the mammalian body.

This introductory section describes, in detail, the anatomy of the PNS, its development, its cellular composition and functioning in view of the different cellular subtypes, the process of myelination and other requisite information to understand the context of the research undertaken. This is followed by a general introduction to Liver X Receptors (LXRs), its implications in the physiology and pathology of the PNS and current research questions pertaining to the role of this nuclear receptor. Furthermore, I have also highlighted the presentation of the primary research objectives of my doctoral thesis along with the strategies that have been adopted to answer different scientific questions that ensued.

1.1 The Peripheral Nervous System

The mammalian peripheral nervous system is primarily composed of the different nerves that arise from the CNS along the rostro-caudal axis of the body (Catala and Kubis, 2013). These nerves consist of afferent sensory fibers from different peripheral locations of the body as well as efferent motor fibers that innervate target tissues. In addition to nerve fibers, the nerves also comprise of glial cells that help in the proper maintenance and functioning of these nerves (Rasband, 2016).

Based on the type of nerves, the PNS can be classified into cranial nerves and spinal nerves depending on where they originate along the rostro-caudal axis. Functionally, the PNS can be classified into two types – the Somatic Nervous System (SNS) and the Autonomous Nervous System (ANS) wherein SNS works under voluntary action and the ANS is involuntary by nature. The following sections shed more light into the anatomy and functioning of the PNS.

1.1.1 The anatomy and functions of the PNS

Cranial Nerves:

Based on the origin of the nerves, the peripheral nerves are classified into cranial nerves located inside the cranium and spinal nerves that originate along the spinal cord. There are 12 pairs of cranial nerves that arise from the cerebrum/brain stem and they are numbered from I to XII (Figure 1). It is to be noted that Cranial Nerves I (optical) and II (olfactory) are extensions of the CNS and are not populated by glial cells from the PNS. The rest of the cranial nerves fall under the ambit of the PNS. A detailed list of the Cranial Nerves and their target tissue is shown in Table 1.

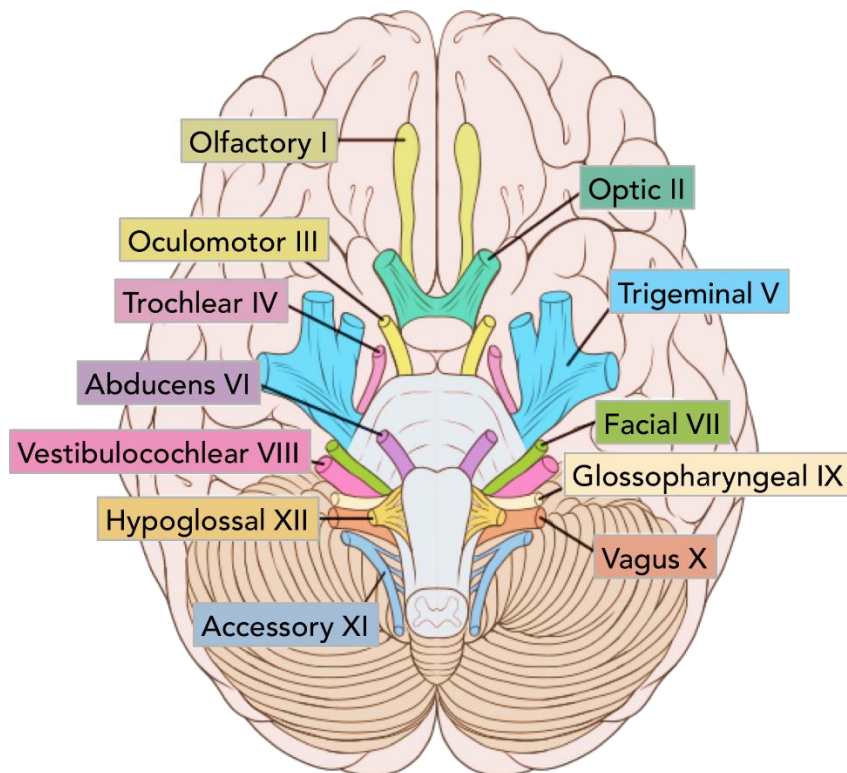


Figure 1: A transverse view of the brain stem and cerebellum. The origin of different cranial nerves is indicated along with their names and conventional numbers. [Source: Patrick J Lynch, Biomedical Illustrator, Yale School of Medicine, Yale University Press]

Number	Name	Target
1 (CNI) CNS	Olfactory	Nose for Smell
2 (CNII) CNS	Optic	Eyes for Vision
3 (CNIII)	Oculomotor	4 extrinsic eye muscles and levator palpebrae superioris.
		pupillary sphincter
4 (CNIV)	Trochlear	Superior oblique
5 (CNV)	Trigeminal:	
	<i>Ophthalmic</i>	Scalp, forehead and nose.
	<i>Maxillary</i>	Cheeks, lower eyelid, nasal mucosa, upper lip, upper teeth and palate.
	<i>Mandibular</i>	anterior tongue, skin over mandible and lower teeth.
		muscles of mastication.
6 (CNVI)	Abducens	Lateral rectus
7 (CNVII)	Facial	sensation to part of exterior ear.
		taste from anterior tongue, hard and soft palate.
		muscles of facial expression.
		lacrima, submandibular, sublingual glands and mucous glands of mouth and nose.
8 (CNVIII)	Vestibulocochlear	Ears for Hearing and balance
9 (CNIX)	Glossopharyngeal	posterior tongue, exterior ear, and middle ear cavity.
		carotid body and sinus.
		taste from post. 1/3 tongue.
		parotid gland.
		tylopharyngeus

10(CNX)	Vagus	ext. ear, larynx and pharynx.
		larynx, pharynx and, thoracic & abdominal viscera.
		taste from epiglottis region of tongue
		smooth muscles of pharynx, larynx and most of the Gastro intestinal tract
		most muscles of pharynx and larynx.
11 (CNXI)	Spinal accessory	trapezius and sternocleidomastoid.
		a few fibres run to viscera.
12 (CNXII)	Hypoglossal	Intrinsic and extrinsic tongue muscles (except the palatoglossus).

Table 1: Classification of different cranial nerves and their targets. Recapitulated from (Kandel et al., 2000)

Spinal Nerves:

The spinal nerves are mixed nerves that carry sensory, motor and autonomous signals between the spinal cord and different peripheral locations of the body. Humans contain 31 pairs of spinal nerves originating at different regions of the spinal cord. There are eight pairs of cervical nerves, twelve pairs of thoracic nerves, five pairs of lumbar nerves, five pairs of sacral nerves, and one pair of coccygeal nerves (Figure 2)

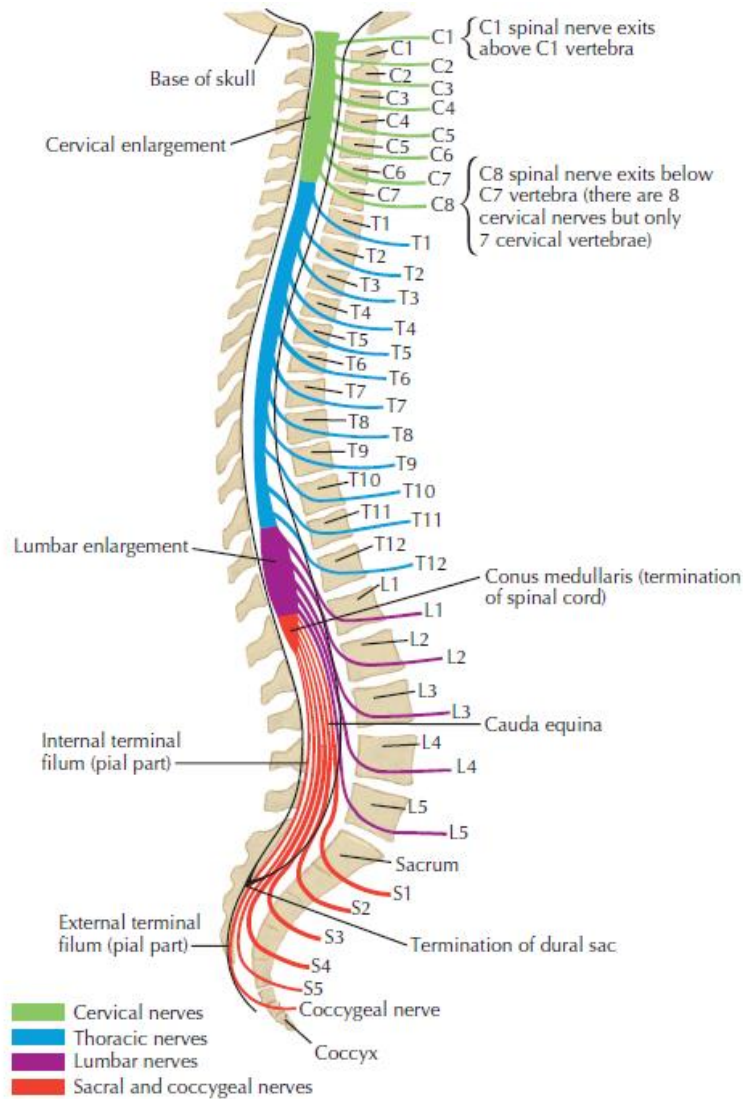


Figure 2: Spinal Vertebrates and Spinal Nerves. In humans, the spinal nerves are classified into 8 pairs of cervical nerves, 12 pairs of thoracic nerves, 5 pairs of lumbar nerves, 5 pairs of sacral nerves, and 1 pair of coccygeal nerves. [Source: (Felten and Shetty, 2014)]

The anatomy of the spinal nerves can be better understood by differentiating their function vis a vis somatic or autonomous. On the one hand, somatic fibers are completely mixed fibers and their functions are carried out by sensory neurons whose soma are located in the dorsal root ganglia and motor neurons that emanate from the ventral horn of the spinal cord. These nerve fibers innervate skeletal muscles and the skin.

On the other hand, the functioning of the autonomous nervous system is carried out but autonomous neurons that arise at the lateral horns of the spinal cord. These neurons innervate the ganglia of the autonomous nervous system that are situated outside the spinal cord. The sympathetic ganglia are located in close proximity to the spinal cord whereas the parasympathetic ganglia are positioned closer to organs innervated by the nerve fibers. This arrangement in turn gives rise to pre-ganglionic and post-ganglionic connections that are unique to the autonomous nervous system (Figure 3). The autonomous nervous system innervates smooth muscles, glands and different organs of the body. A detailed description of the target tissues of the ANS is given in Figure 4.

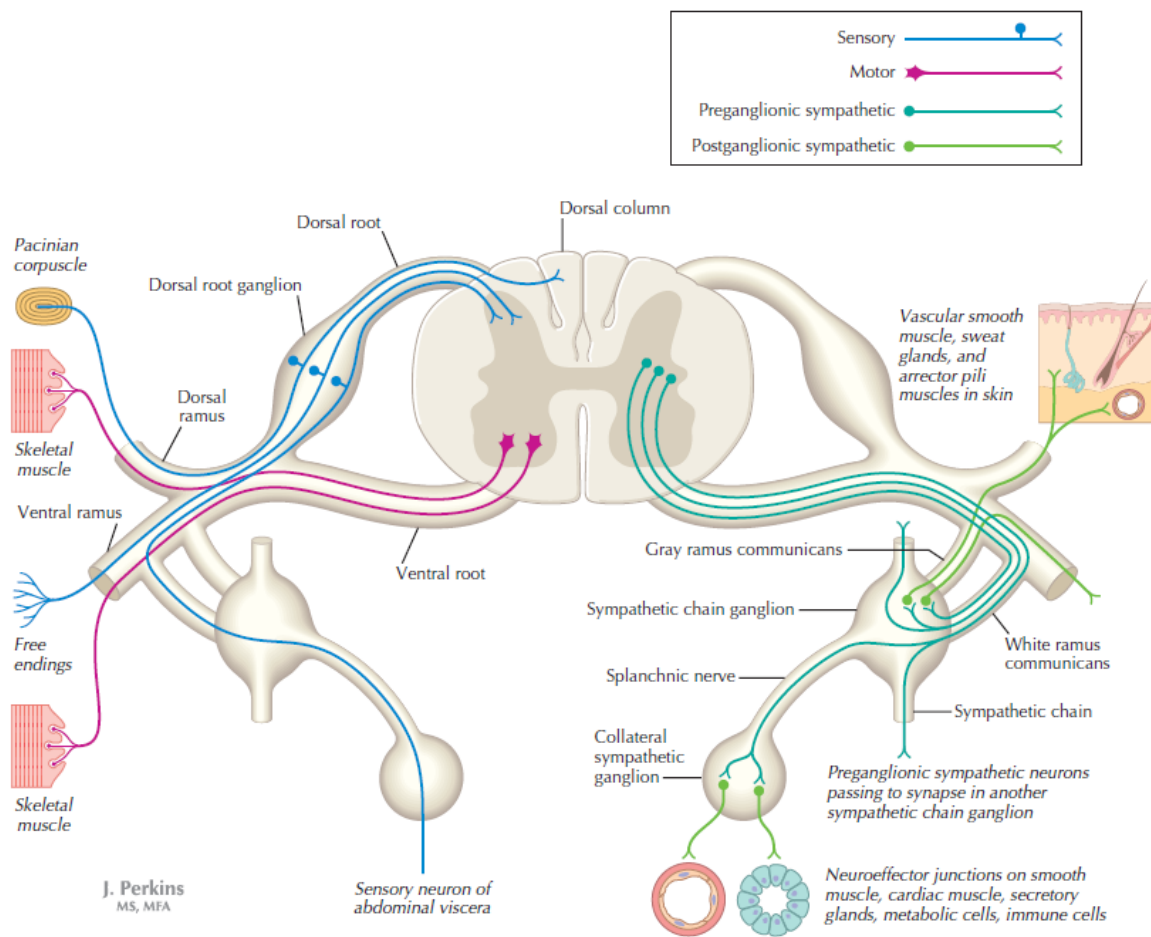


Figure 3: A transverse view of the human spinal cord. To the left is an example of the fiber arrangement in the somatic nervous system. To the right is an example of the autonomous nervous system. Only the sympathetic ganglia are shown in this figure. The parasympathetic ganglia are located closer to the organs innervated. [Source: (Felten and Shetty, 2014)]

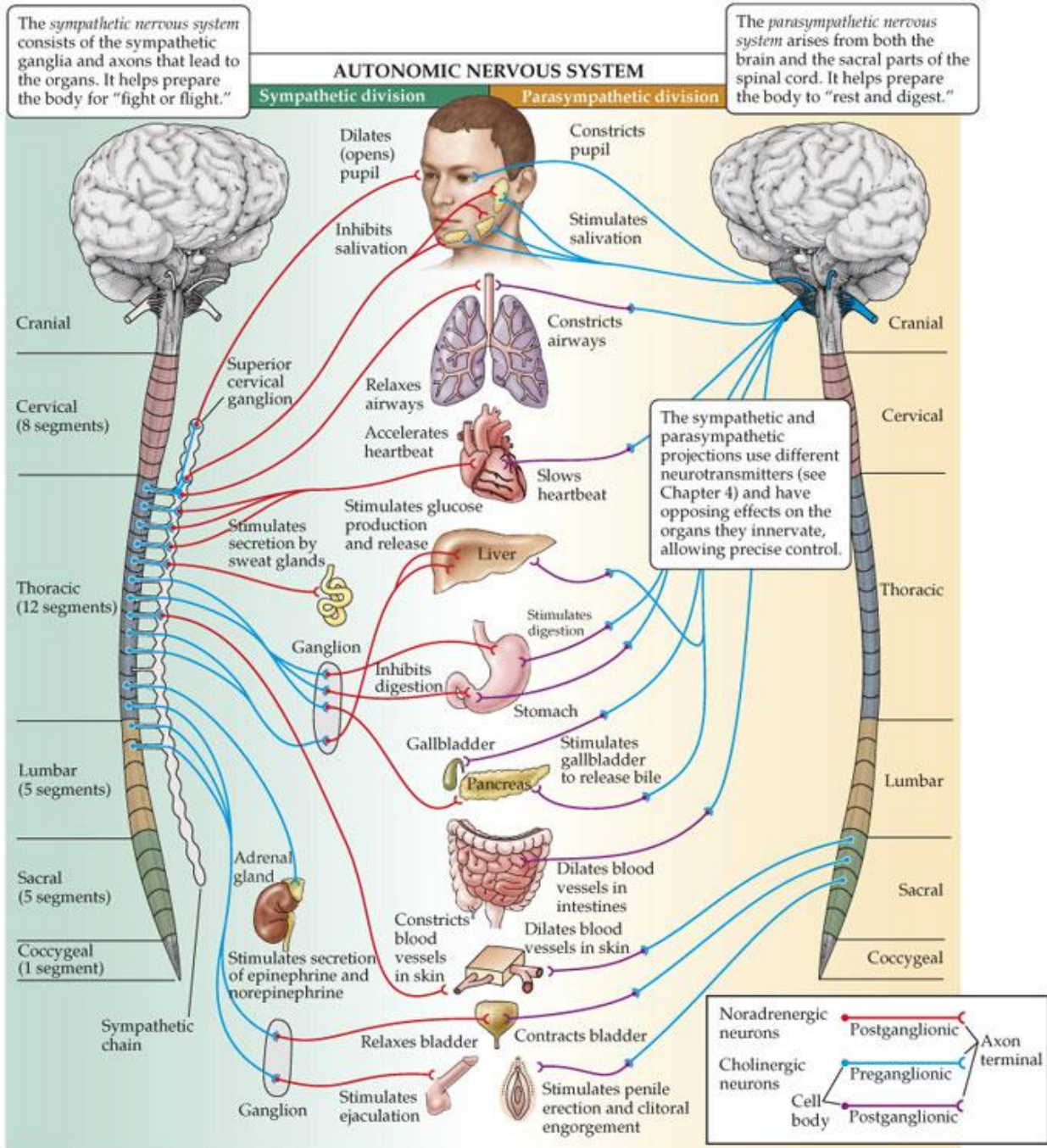


Figure 4: The target organs and functions of the ANS. Sympathetic division of the spinal nerves is described on the left and the parasympathetic division is described on the right along with the target organs that the nerves innervate. [Source : (Johnson and Weldon, 2016)]

1.1.2 The Sciatic Nerve

The sciatic nerve is one of the largest spinal nerves, and is extensively used for peripheral nerve research. Particularly, in mice and rats, the sciatic nerve has been used as a model to study nerve development, myelination, nerve regeneration post-injury and also the neuromuscular junction that the nerve innervates (Jessen and Mirsky, 2005; Liu et al., 2014). This is because of its size, the ease with which it can be dissected and the fact that sufficient amount of tissue can be used for both histological and biochemical studies (Bala et al., 2014).

The sciatic nerve in humans originates between L4 and S3 sections of the spinal cord. In rats, it is between L4 - L5 (Snyder et al., 2018). In mice it is around L3 – L4 (Figure 5). Nevertheless, certain minor variations have been observed across different strains of both rats and mice (Rigaud et al., 2008). The rodent sciatic nerve model has been majorly used to study the somatic aspects of the PNS. In line with this convention, in my doctoral thesis, I have used the mouse sciatic nerve as a model to study the role of Liver X Receptor β (LXR β) and its implications on Schwann cells' development and myelination of the PNS.

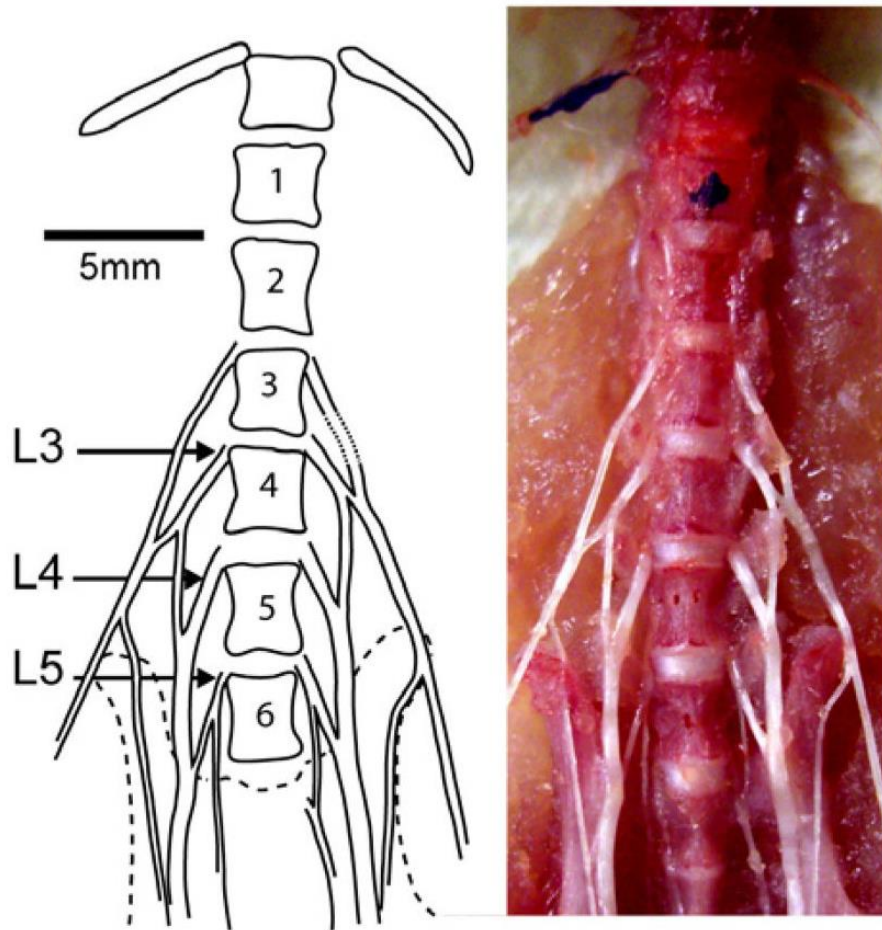


Figure 5 : A ventral view of the lumbar vertebral column of a C57BL6 mouse. Image on the right presents the actual view upon dissection. Image on the left highlights the vertebral segments and the origin of the sciatic nerve comprising of L3, L4 and L5 spinal nerves. [Source : (Rigaud et al., 2008)]

1.1.3 Ultra-structure and cellular composition of the sciatic nerve

To understand the development and provenance of the different cells of the PNS, a thorough understanding of the ultra-structure of the spinal nerves is required. The sciatic nerve, much like all peripheral nerves in the body is composed majorly of sensory and motor axons along, with specialized cells called glial cells that are situated all along the nerve. A gross transverse section of the nerve reveals a three-layer arrangement (Figure 6). The **epineurium** encapsulates the nerve in its entirety. Inside the

epineurium, the **perineurium** forms separate fascicle of nerves. Inside these fascicles is the **endoneurial space** that consists of nerve fibers with other glial cells. The perineurial space inside the epineurium also consists of blood vessels and adipose tissues.

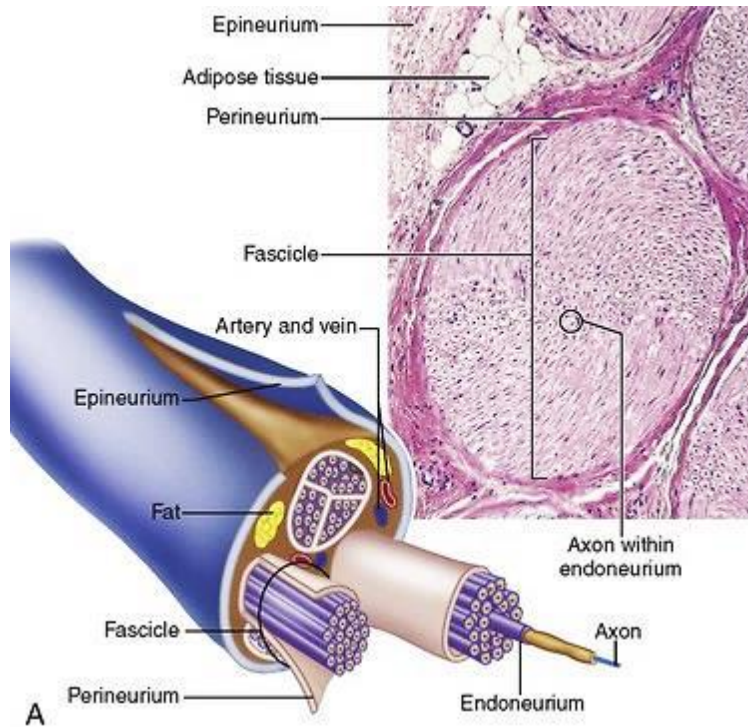


Figure 6: A macroscopic view of the transverse section of the sciatic nerve. The entire nerve is encapsulated by the epineurial connective tissue. Inside the epineurium, nerve segments are situated in compartments that are segregated by the perineurium. Fat deposits and blood vessels are found in-between the epineurium and the perineurial compartments. Axons are found inside the perineurium and are either myelinated by Schwann cells or are ensheathed by non-myelinating Schwann cells [Source : (Patton and Thibodeau, 2018)]

A more detailed view of the perineurial and endoneurial space can help us understand the cellular composition of the sciatic nerve (Figure 7). Sensory neurons emanating from the dorsal part of the spinal cord with their somata in dorsal root ganglia project their axons towards the spinal cord on the one hand and their peripheral endpoints on the other. Some of these sensory axons are myelinated by Schwann cells, and others are ensheathed by non-myelinating Schwann cells in specific structures called “Remak bundles”. Motor axons emanating from the ventral roots of the spinal cord are wrapped by myelinating Schwann cells. Perineurial cells surround multiple axons and Schwann cells to delineate fascicles. They

provide mechanical and structural integrity to these fascicles. Endoneurial cells are dispersed inside the fascicles. They provide major components of the extracellular matrix, perform immune-surveillance, and are implicated in remyelination. The vasculature is composed of endothelial cells surrounded by pericytes that provide the nerve-blood barrier.

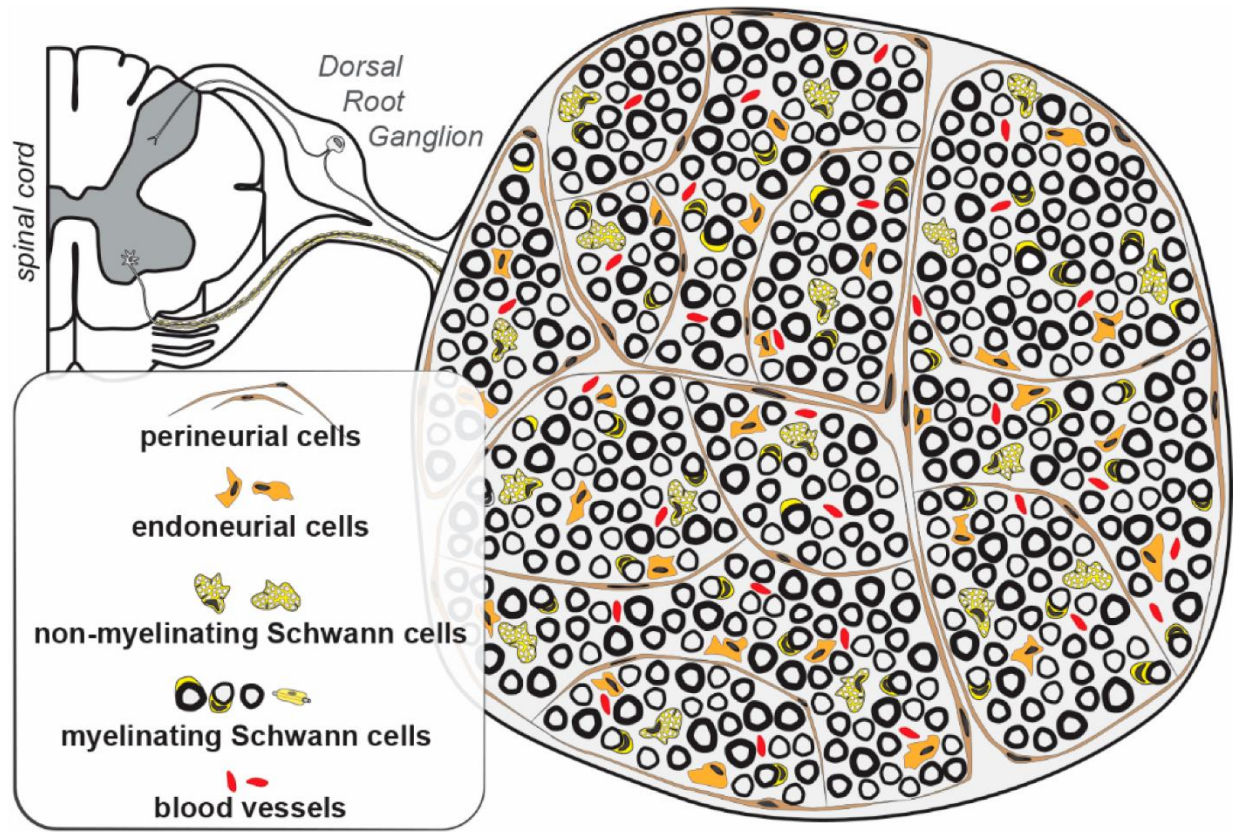


Figure 7: A detailed cross-sectional view of the mouse sciatic nerve. Different cells that constitute the nerve are highlighted in the legend to the left of the figure. [Source : (Sundaram et al., 2019a)]

1.1.4 Development of the PNS – An overview

Origin and migration of Neural Crest Cells (NCC):

Most of the glial cells and the sensory neurons in the DRGs are derived from migrating multipotent embryonic cells called as the neural crest cells (Prendergast and Raible, 2014). These cells give rise to a plethora of organs in the vertebrate body so much so that they can be considered as a fourth “germ layer” in addition to the other three layers – the ectoderm, the endoderm and the mesoderm (Le Douarin and Dupin, 2014).

Following gastrulation, the embryo is divided into the three classical germ layers mentioned above. This is followed by neurulation, which is characterized by the folding of the neural plate located in the ectoderm (neuroectoderm). On either side of the neuroectoderm is the non-neuronal ectoderm that gives rise to non-neuronal cells and organs. These two zones are separated by the Neural Plate Border (NPB). The inward folding of the neural plate gives rise to the meeting of the Neural Plate Borders from either side forming a crest like structure. This crest formed by the neural plates is called the neural crest and the cells that are situated therein are called as the Neural Crest Cells (Figure 8, left panel).

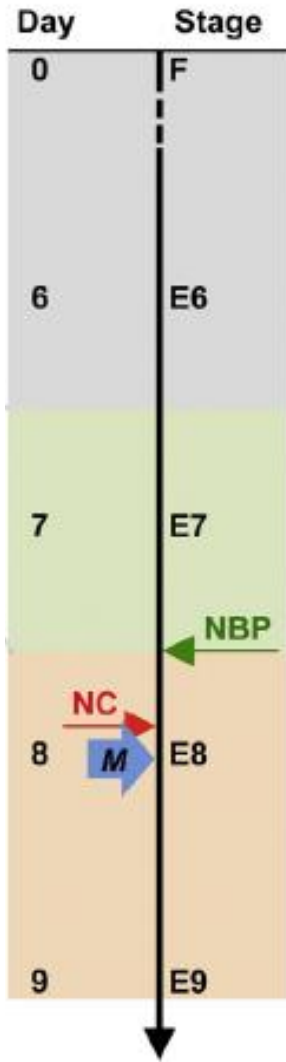
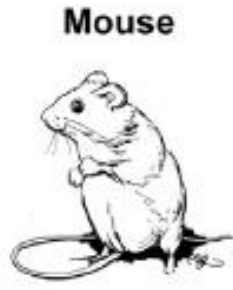
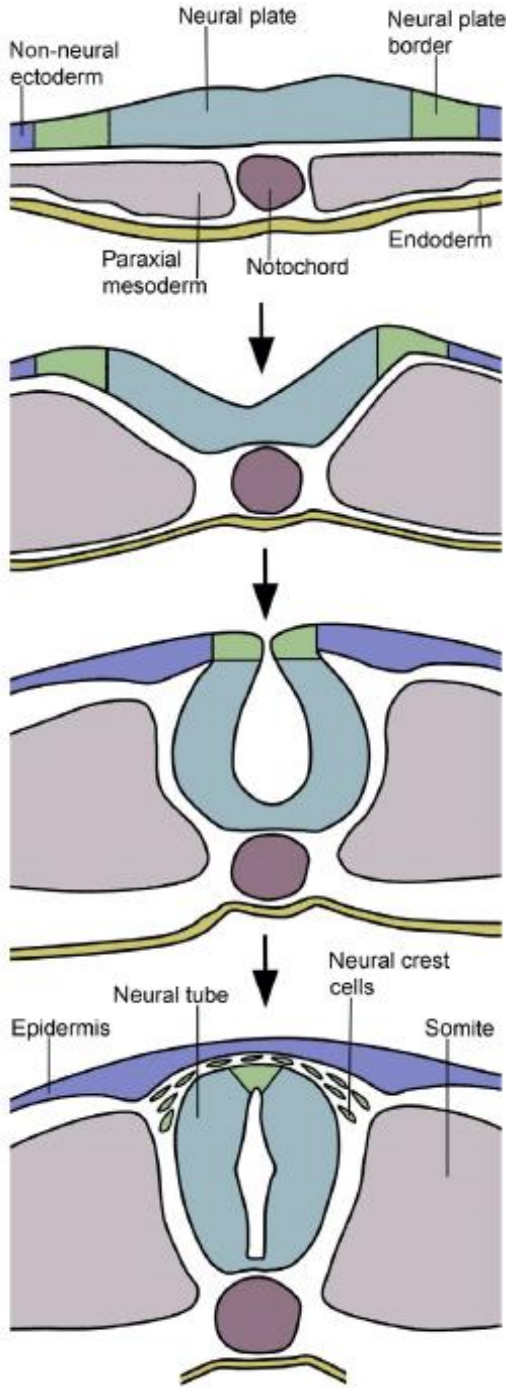


Figure 8: The formation of the Neural Crest cells (left panel) and its timing in mice (right panel). The neural plate is flanked by cells that form the neural plate border (NPB) during embryonic development at around E7.5 in mice. The plate then folds inwards such that the neural plates on either sides come into contact with one another. At the same time, the migratory Neural crest cells (NCC) detach from the plate and begin their migratory routes. Neural Crest Migration (M) begins at around E8 in mice.

The induction and formation of NCC at the NPB is tightly controlled by molecular cues from the surrounding tissue (Bae and Saint-Jeannet, 2014). The current understanding of this process is governed by the collective effect of 3 pathways. Firstly, a gradient of Bone Morphogenic Protein (BMP) ; inhibition is established by the secretion of BMP antagonists by the mesoderm. This gradient results in least BMP signaling at the neuroectoderm due to high concentration of antagonists such as Noggin. At the NBP, the antagonist concentration is slightly lower permitting the right amount of stimulation to induce the formation of the NBP specified cells. Secondly, the canonical Wnt/ β Catenin Signalling coupled with Fibroblast Growth Factor (FGF) stimulation (both ligands arising from the surrounding tissue) results in the expression of NBP specific protein such as Pax3 and Zic1. These proteins in turn result in the transcription of NCC markers such as Sox8, Foxd3, Sox9 and Sox10 in that order.

Once the folding of the neural plate is completed, the neural crest cells delaminate from the crest and start migration. Delamination and migration happen through a series of sequential steps that starts with the loss of intercellular adhesion proteins such as N-Cadherin followed by an acquisition of migratory capacity through Rho, Rac and Cdc42 proteins. The appropriate substrates for migration are provided by the surrounding tissues (Taneyhill and Padmanabhan, 2014). This process of delamination followed by migration is termed as the Epithelial to Mesenchyme Transition (EMT). The series of events are summarized in the figure below (Figure 9)

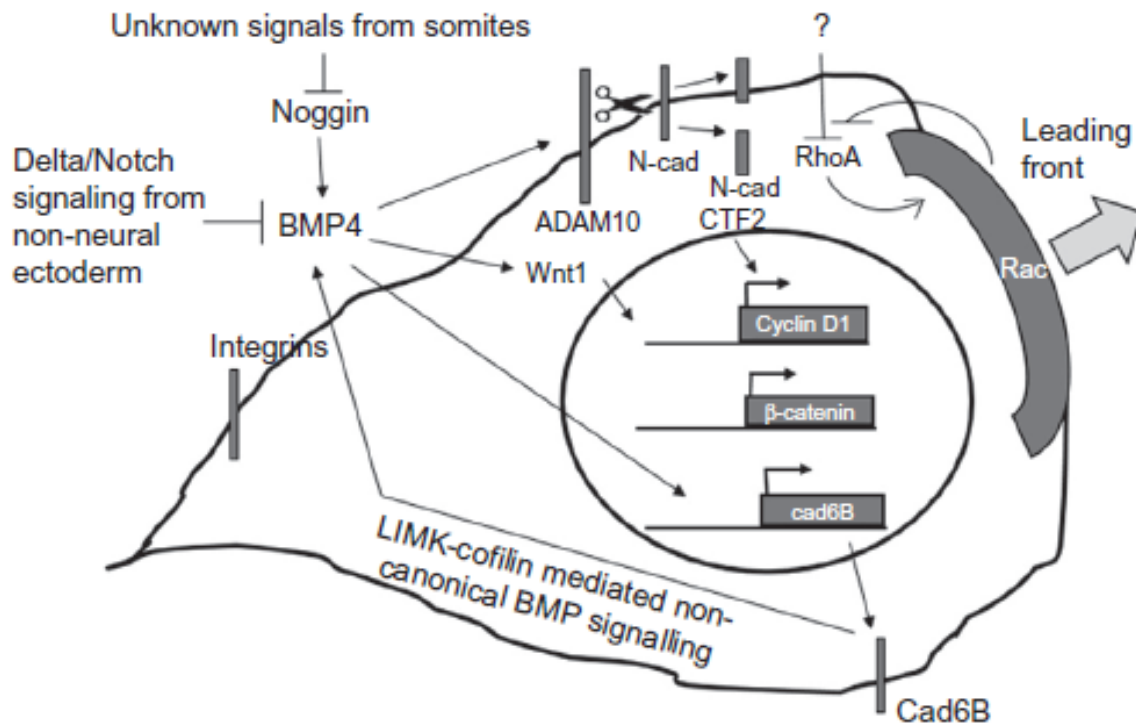


Figure 9: Delamination and Migration of NCC. The first step is the activation of BMP signalling either by a reduction of its antagonist noggin or by the removal of Delta/Notch Signaling from the non-neuronal ectoderm. The delamination is stimulated by BMP4, which activates ADAM10 that cleaves N-Cadherin. This permits the cells to detach from nearby cells. BMP4 also stimulates the transcription of Cadherin-6 (*Cad-6b* in chicks), which replaces N-Cadherin at the membranes. BMP signalling is also implicated in the spatiotemporal expression of Rac and Rho in the leading and trailing front of a migratory cell respectively. Additionally, BMP signaling also stimulates the Wnt/ β -Catenin Pathway that stimulates the production of CyclinD1 and permits the migratory cells to enter the S-Phase in their respective cell cycles. [Source: (Taneyhill and Padmanabhan, 2014)]

The migratory patterns of the neural crest cells depend largely on the location of the cells along the neural tube in the rostral-caudal axis. Consequently, the NCC and their progenitors are different at different locations along the neural tube. For instance, cranial NCC give rise to cells of the CNS along with odontoblasts, connective tissues in the facial region among others. Whereas, trunk neural crest cells give rise to melanocytes, sensory and autonomous ganglia, peripheral glia and sensory neurons (Bae and Saint-Jeannet, 2014). We will consider only the migratory patterns of trunk neural crest cells for pertinence to my doctoral studies.

The trunk neural crest cells display 3 predominant waves of migration (Figure 10). The 1st wave is called the dorsolateral wave (arrow 1, Figure 10; above the dorsal region of the somites and parallel to

the epidermis). This wave gives rise to melanocytes. The 2nd wave can in fact be classified into two – the ventrolateral (arrow 2, Figure 10) and the ventromedial wave (Arrow 3, Figure 10). The ventrolateral wave gives rise to the cells of the Dorsal Root Ganglia and other PNS glial cells whereas the ventromedial wave gives rise to autonomous ganglia and certain cells of the enteric nervous system (Mayor and Theveneau, 2012; Le Douarin and Dupin, 2014).

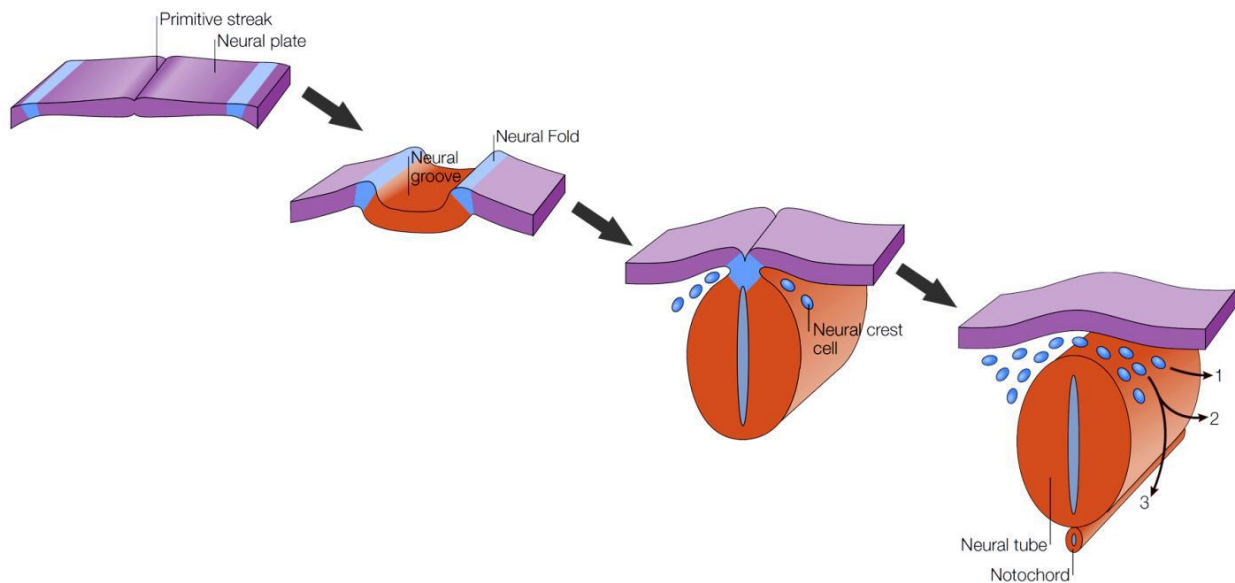


Figure 10 : Migratory paths of the NCC. Arrow 1 – Dorsolateral, Arrow 2 – Ventrolateral, Arrow 3 – Ventromedial. Each of these pathways give rise to different progenitors. Adapted from (Jessen and Mirsky, 2005)

Generation of Sensory Neurons in the DRG:

Migration of the NCC starts at around E8 in mice and by E10, the Dorsal Root Ganglia is populated by NCC that would eventually give rise to sensory neurons and other glial cells. Among the different derivatives of the NCC in the DRG, sensory neurons are the first to get specified (Ma et al., 1999). The sensory neurons of the DRG conduct multiple sensory signals from the periphery to the central nervous system. They can be classified into proprioception, mechanoreception, thermo-reception, and nociception. Each one of these sensations is conveyed by distinct neuronal subtypes (Marmigère and Ernfors, 2007). Therefore, the NCC differentiates to give rise to neurons specialized to each function. The identity of such neuronal subtypes is given by the type of Tyrosine Kinase Receptor (receptors for neurotrophins such as NT-3, NGF) that they express at their surface. The present consensus is that the DRG neuron specification occurs in two distinct but overlapping waves. In the first wave, large diameter TrkB+ and TrkC+ are born. In the second wave smaller diameter TrkA+ neurons are born. The former is mechano- and proprioceptive whereas the latter is nociceptive. The origin of first wave is from the migrating NCC and that of the second wave is probably from a small subset of NCC cells called as boundary cap cells which generate around 10% of the nociceptors. (Marol et al., 2004) (See *Generation of Peripheral Glial Cells*)

Nevertheless, irrespective of the timing of the waves, the commitment to the neuronal fate is mediated by two genes Neurogenin 1 and Neurogenin 2 (Ma et al., 1999; Prendergast and Raible, 2014). These two proteins help in the transcription of the specific Tyrosine Kinase Receptors in different neuronal populations. The molecular mechanisms that underlie the expression of Neurogenin 1 and Neurogenin 2 in migratory NCC is not well understood but hedgehog Signalling is likely to be involved, at least in zebrafish (Ungos et al., 2003).

The Neurogenins in turn activate two key transcription factors, Brn3a & Islet1 that retain and refine the neuronal differentiation of the NCC. These transcription factors regulate the expression of the Runx transcription factors. The Brn3a, Islet 1 and the Runx transcription factors result in the expression of different Trks in different neuronal subtypes (Dykes et al., 2011).

Generation of Peripheral Glial Cells:

The generation of peripheral glia from the neural crest involves molecular machinery that is very distinct and different from the ones explained above. This topic has been recently reviewed exhaustively (Jacob, 2015). Neural crest cells ultimately give rise to three kinds of glial cells namely **boundary cap cells**, **satellite glia** and **Schwann cell precursors**. Gliogenesis in the PNS can also be classified into two waves. Firstly, migrating NCC cells at the Dorsal Root Exit Zone (DREZ) and the Motor Exit Points (MEP) give rise to the Boundary Cap Cells at around E10 at these two junctures (Katarzyna and Topilko, 2017). These Boundary cap cells are multipotent, and they migrate into the DRGs to give rise to a small population of satellite glial cells (E12) as well as sensory Neurons. They also give rise to Schwann cell precursors at the DREZ and MEP at around E11.25 (Figure 11)

Besides, at E11 in mice, the neural crest cells also directly give rise to Schwann Cell Precursors and Satellite glial cells (Figure 11).

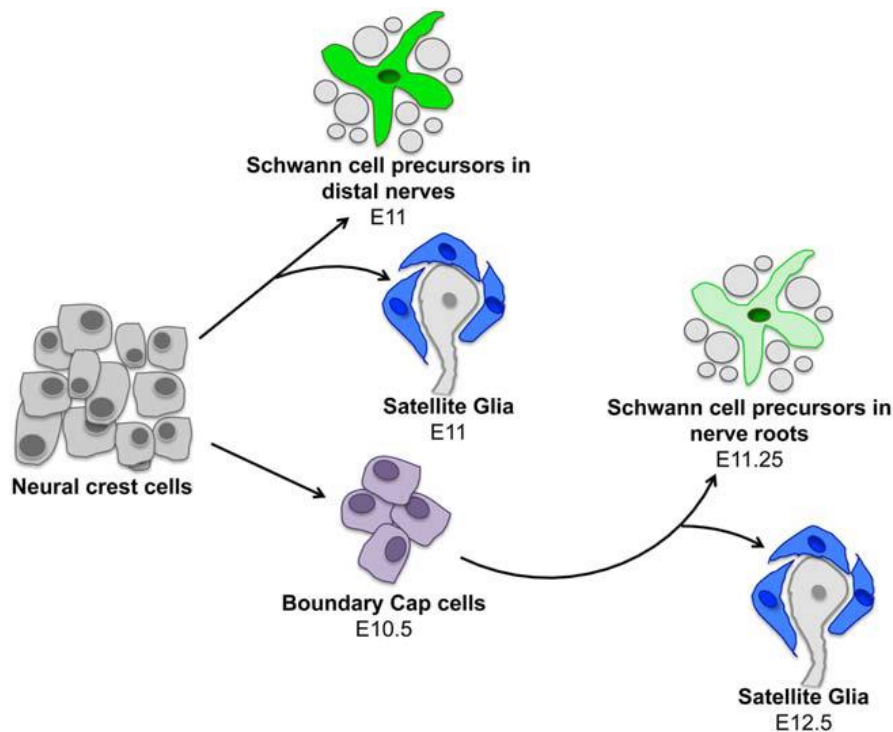


Figure 11: Generation of different peripheral glial cells in two distinct waves with their respective timings. Migratory neural crest cells give rise to two populations – Boundary Cap cells at the Dorsal and Ventral exit points of the spinal cord at E10.5 as well as Schwann cell precursors that migrate and populate the developing nerves. A subpopulation of the neural crest cells that migrate

into the DRG also give rise to satellite glia. Alternatively, Boundary cap can also give rise to satellite glial cells as well as Schwann cell precursors Source: (Jacob, 2015)

The migratory pathways of these two waves are quite different. For instance, Neural crest cells that directly give rise to SCPs and satellite glia migrate and accumulate into future DRGs. Once inside, these cells obtain different cell fates. The satellite cells remain attached to the soma of sensory neurons and SCPs migrate out of the DRGs along growing peripheral nerves. However, once the DRGs are formed some SCPs can migrate around the DRGs without entering them and then migrate to peripheral nerves that stem out of the DRGs. These different migratory routes are recapitulated in Figure 12.

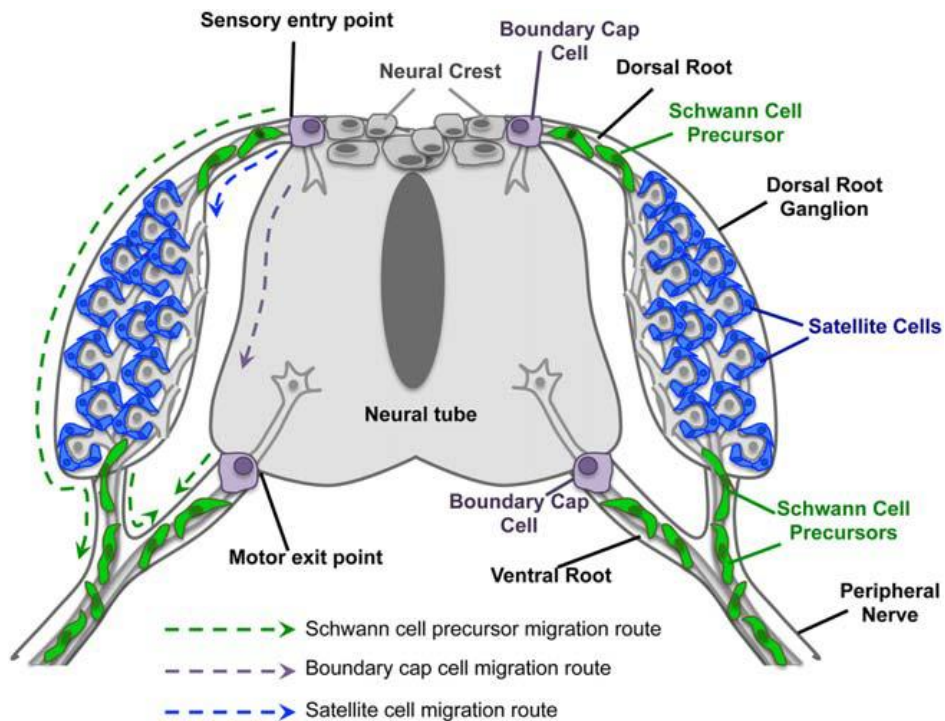


Figure 12: The different migratory routes adopted by SCPs, satellite cells and Boundary cap cells. Source: (Jacob, 2015)

The determination of NCC cell fate to glial cells depends on lot of molecular cues. Among others, Sox10 signaling seems to be crucial. Sox10 first stimulates the expression of Neuregulin1 receptor Erbb3 in migrating neural crest cells. Furthermore, activation of Erbb3 through Neuregulin1 further specifies the cells to the glial lineage (Mei and Nave, 2014; Fledrich et al., 2019). A secondary pathway involves HDAC1 and HDAC2, which increase the expression of Pax3 gene. Pax3 synergizes with Sox10 and binds to MSCS4 SOX10 enhancer to further increase the levels of Sox10. This ultimately results in the expression of glial Sox10 target genes such as Fabp7 (Fatty Acid Binding Protein 7) and P0 (Jacob et al., 2014).

Notch signaling also seems to be important for gliogenesis (Morrison et al., 2000). Morrison and colleagues show that exogenous expression of Notch ligands by developing neuroblasts seems to prevent neurogenesis in culture and accelerate gliogenesis in the immediate surrounding. Moreover, BMP signaling, which is involved in neurogenesis through neurogenin-2 (discussed earlier) needs to be downregulated for gliogenesis from NCC. This is achieved by the concerted action of FGF2 signaling which antagonizes the expression of neurogenin-2 and in turn helps in the activation of Notch signaling (Jacob, 2015). For the cells committed to the glial fate, including the subset of boundary cap cells, FoxD3 seems to play a role in promoting gliogenesis (Jacob, 2015). Briefly, increase in the expression of FoxD3 and the inhibition of neurogenin-1 facilitates the commitment to a glial fate.

A brief recapitulation of the cellular signaling pathways that govern the formation of Schwann cell Precursors and Neurons is provided in the figure below. (Figure 13)

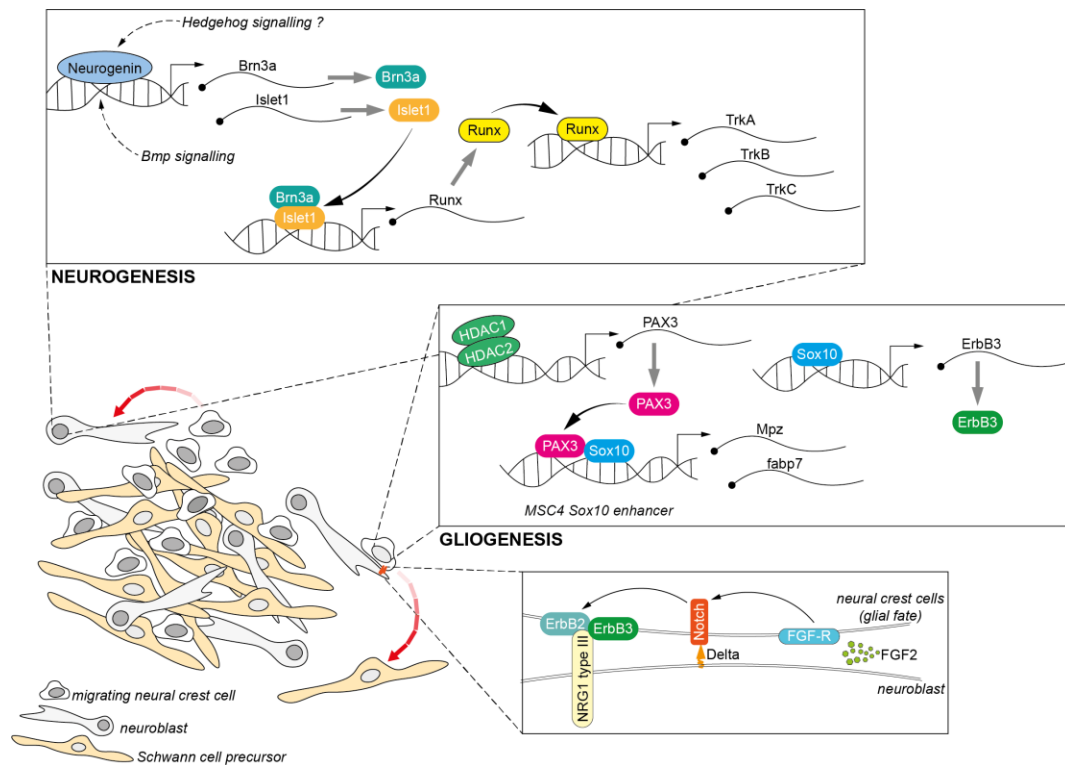


Figure 13: Formation of Schwann cell precursors and neurons from migrating Neural Crest Cells in the developing PNS. NCC first give rise to neuroblasts (future sensory neurons) in the DRG through a process called as neurogenesis. Briefly, BMP signaling and possibly Hedgehog signaling result in the activation of Neurogenins. Neurogenins, in turn, upregulate the expression of Brn3a and Islet1. These transcription factors together help in the expression of Runx. Runx activation finally results in the expression of different Tyrosine Kinase Receptors in neuroblasts as well as Notch ligands such as Delta and Jagged. Once neuroblasts are formed,

they interact with other Neural Crest Cells destined to a glial fate through the Notch pathway. Indeed, FGF2 signaling is crucial for this interaction as FGF2 binds to its receptor on NCC and suppresses BMP signaling (that promotes neurogenesis). On the other hand, it concomitantly activates the expression of Notch receptors on NCC thus promoting a glial fate. Once the Notch-Delta interaction is established, downstream signaling of Notch Intracellular Domain in NCC promotes the expression of ErbB2. Additionally, epigenetic modification in the NCC assured by HDAC1 and HDAC2 promotes Pax3 expression. Pax3 and Sox10 then synergize at the MSC4 SOX10 enhancer site to promote expression of glial genes such as Mpz and Fap7. Sox10 also increases the levels of ErbB3. The ErbB proteins then localize to the cell surface and interact with Neuregulin 1 Type III expressed by the neuroblasts. This interaction further restricts the NCC to a glial fate and results in the formation of Schwann cell Precursors. Brn3a: Brain Specific POU Domain Protein 3a; Islet 1: Insulin Gene Enhancer Transcription Factor 1; Runx: Runt-related transcription factor; HDAC: Histone Deacetylase; Pax3: Paired Box 3; Sox10 : SRY Box Transcription Factor; ErbB2/3: Receptor ErbB2/3 Tyrosine Kinase, FGF-R: Fibroblast Growth Factor Receptor.

1.1.5 Schwann cell development

At the outset, Schwann cell development is a continuous process that involves the transition of Schwann cell precursors to an intermediary population of immature Schwann cells (ISC) that further differentiate into myelinating and non-myelinating Schwann cells perinatally (Jessen and Mirsky, 2005; Monk et al., 2015). In the following sections, a brief outline of these different cell types including their molecular/cellular profiles and their functions are elucidated.

Schwann cell precursors (SCP):

As explained in the previous section, SCP are the first derivatives in the Schwann cell lineage from the neural crest. These cells originate at around E11 and populate the nerve roots as well as developing spinal nerves. SCP are multipotent precursor cells that give rise to a plethora of cell types besides the cells in the Schwann cell lineage (Furlan and Adameyko, 2018; Jessen and Mirsky, 2019a). These include melanocytes, chromaffin cells, enteric and parasympathetic neurons, endoneurial fibroblasts, dental mesenchymal stem cells and bone marrow mesenchymal stem cells. For the sake of pertinence to my PhD thesis, only the PNS derivatives of SCP will be detailed in the following sections.

SCP that eventually resolve to the Schwann cell-fate in the PNS first start clustering around the areas in the DRG where the sensory axons sprout and exit. Once the axons leave the DRG, SCP start migrating on these nascent axons all the way to their peripheral end points. Electron microscopy images of SCP show that these cells are situated around bundles of axons (Figure 14).

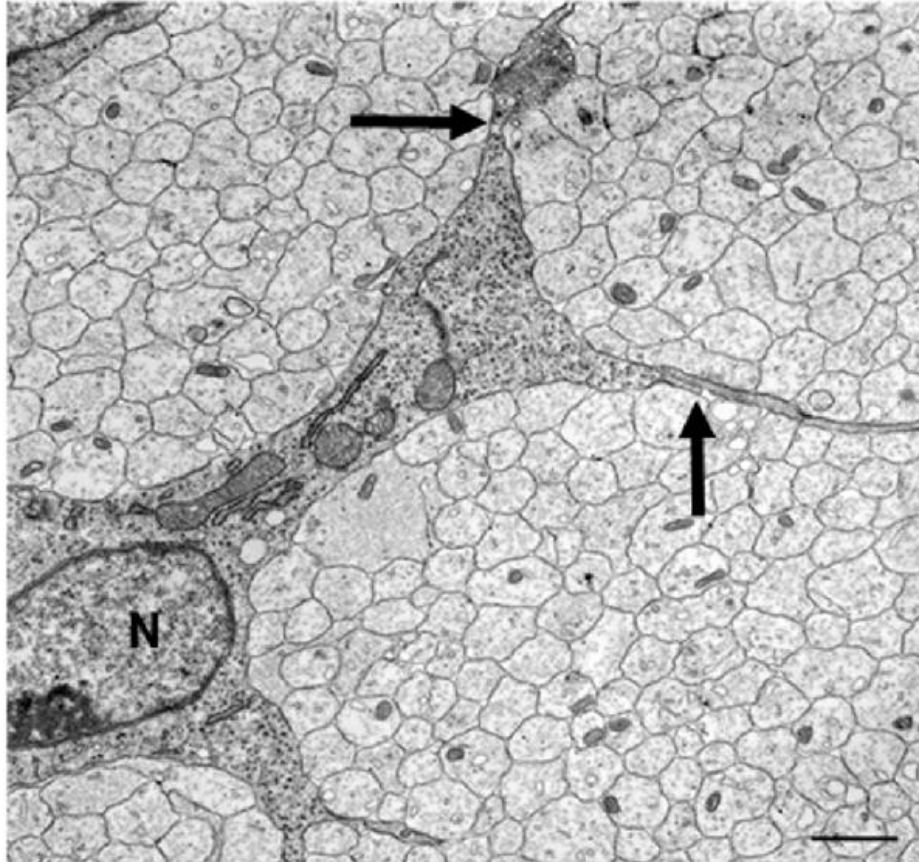


Figure 14: Electron-microscopy transverse section image of a rat sciatic nerve at E14 (corresponds to E12 in mice) Schwann cell precursors are shown using the arrow heads which indicate cytoplasmic extensions around groups of axons. N denotes the nucleus of a precursor cell. Source : (Jessen and Mirsky, 2005)

The transcriptional landscape of the transition between migrating neural crest cells (E9.5) and migratory SCP (E12) has been well documented in mice (Buchstaller et al., 2004). Hundreds of genes are implicated in this process and it is worthy to note that the number of genes upregulated are 2 to 3 folds more than the ones downregulated (Buchstaller et al., 2004; Jessen and Mirsky, 2019a). The former category includes genes that are involved in cell cycle, cytoskeleton formation, cell growth and certain transcription factors that are implicated in the expression of various myelin associated genes such as Peripheral Myelin Protein 22 (Pmp22), Myelin Basic Protein (Mbp), Myelin Protein Zero (Mpz or P0), Proteolipid Protein (Plp) (Buchstaller et al., 2004; D'Antonio et al., 2006b).

The survival of SCP have been studied extensively in the past to identify key actors that mediate and sustain SCP survival throughout its migration along peripheral nerves (Jessen et al., 1994; Dong et al., 1995). It was observed that SCP in culture would undergo apoptotic death in under 24 hours. However,

this could be prevented if the cells are co-cultured with neurons. Subsequently, Neuregulin1 (NRG1) was found out to be the factor that mediates survival in SCP and supplementing the cell culture media with NRG1 could prevent apoptotic death in cultured SCP (Dong et al., 1995). NRG1 is expressed as three different isoforms that are localized to the axolemma. They are named NRG1 Type I, NRG1 Type II and NRG1 type III. All three isoforms are characterized by an EGF domain. However, only Type I and Type II contain an IgG domain with the N terminal situated outside the axolemma. Type III is uniquely characterized by a cysteine rich transmembrane domain with the N-terminal situated in the cytosol of axons (Fledrich et al., 2019). All three isoforms are subjected to proteolytic cleavage by BACE and TACE (also termed as ADAM 17) secretases located in proximity to these proteins on the axonal surface. The action of these secretases on Type I and Type II isoforms results in the release of these proteins as soluble factors in the Schwann cell precursor/axon interface. However, NRG1 Type III remains anchored to the axolemma upon cleavage and interacts with the Schwann Cell Precursors and its derivatives of the Schwann cell lineage in a juxtacrine manner. Schwann cell precursors, on the other hand, express ErbB2 and ErbB3 which heterodimerize at the plasma membrane and act as cognate receptors to NRG1 Type III throughout development. In effect, the NRG1 Type III and ErbB2/3 interaction governs multiple tyrosine kinase receptor signaling cascades in Schwann cells all through their development and differentiation (Fledrich et al., 2019).

The importance of this interaction was further elucidated by the fact that NRG1 mutants display almost a complete absence of Schwann cell precursors although other PNS derivatives of the neural crest such as satellite glia and sensory neurons are still present (Birchmeier and Nave, 2008; Brinkmann et al., 2008; Fledrich et al., 2019). Similarly, mutations in ErbB2 or ErbB3 also result in similar phenotypes (Newbern and Birchmeier, 2010; Torii et al., 2014). In addition to survival, it is also quite probable the NRG1 also plays a role in SCP migration. To this effect, cell culture experiments have categorically shown that addition of NRG1 in cell culture enhances SCP migratory activity (Jessen and Mirsky, 2019a).

Furthermore, Notch signaling is also important for the survival of SCP, albeit indirectly (Woodhoo et al., 2009). Notch ligands such as Delta and Jagged are normally present on neurons and Notch is expressed in Schwann cells. Woodhoo and colleagues collectively showed that Notch is required for the expression of NRG1 receptor ErbB2/3 in Schwann cells. Inactivation of Notch signaling thus leads to lower levels of ErbB2/3 in Schwann cell precursors. Moreover, such inactivation also retards the appearance of immature Schwann cells *in vivo*. Complementarily, overexpression of Notch leads to the premature

appearance of iSC *in vivo*. Thus, NRG1 and Notch signaling are two key pathways that are crucial from the survival and transition of SCP to iSC in the PNS.

Functions of SCP:

The functions of SCP are myriad. Apart from acting as a developmental multipotent pool of cells, they have certain functions specifically in the PNS. SCP are implicated in the process of nerve fasciculation and the formation of neuromuscular junctions. In growing nerves, SCP are found at the nerve front where they form scaffolds around axonal growth cones (Wanner et al., 2006). They help in guiding the nerve fronts to their peripheral targets in the growing limb. The relevance of SCP in embryonic nerve development is seen in mutant models of SOX10 and NRG1 signaling (Woldeyesus et al., 1999; Wolpowitz et al., 2000; Britsch et al., 2001). In these models, SCP are not produced on time or are very few. Although, nerve development from the DRG and ventral roots occurs normally, nerve branching is affected, and the nerves are poorly fasciculated and disorganized near the target tissues. Furthermore, in these models, neurogenesis from neuroblasts in the DRG does not seem to be affected and the axons sprout on time. However, during late embryonic development, these axons start denervating from target tissues and eventually die. This shows that early glial populations may not be necessary for neurogenesis, but they are indispensable for axonal survival during late embryogenesis. It is indeed intriguing to note the interdependence of SCP and neurons for their survival during embryonic development of the PNS (Jessen and Mirsky, 2019a).

Immature Schwann cells (iSC):

The next cell type to arise out of SCP in the Schwann cell lineage are immature Schwann cells. These cells are quite distinct both in their molecular/cellular profile and function when compared to SCP. Some of the salient features of difference are as follows:

- iSC can survive independently from axons both *in vivo* and *in vitro* (Dong et al., 1995)
- iSC possess autocrine survival mechanisms (Jessen et al., 1994; Jessen and Mirsky, 2005)
- iSC segregate larger bundles of axons into smaller ones (Figure 15).
- In culture, iSC have a typical spindle shaped morphology in culture whereas SCP are more flattened and aggregated (Woodhoo et al., 2009)
- Molecular markers of iSC are significantly different from SCP (Buchstaller et al., 2004; D'Antonio et al., 2006b) (Figure 16)

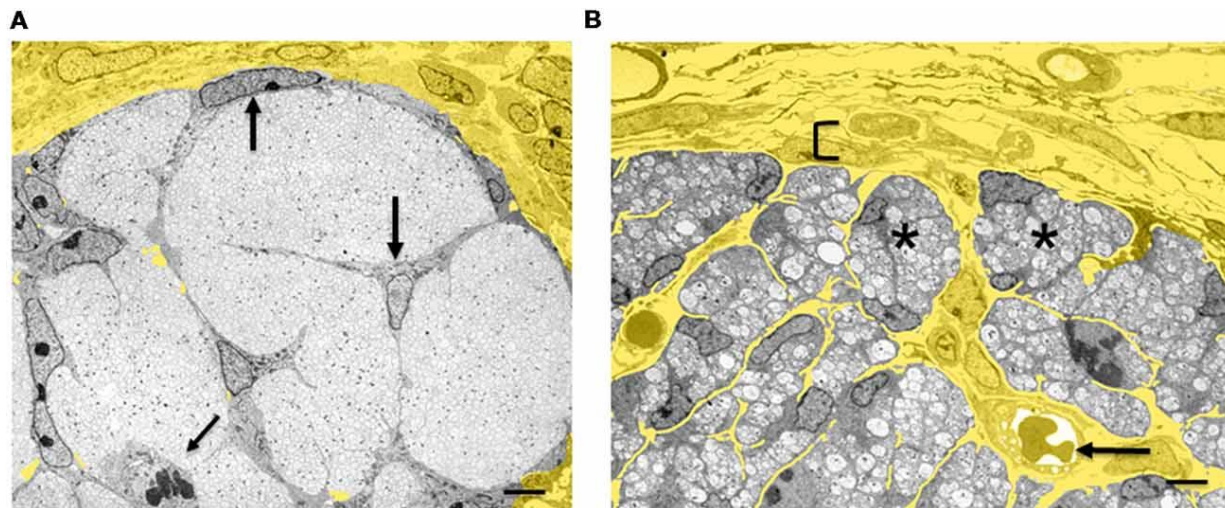


Figure 15: Differences in the morphology of SCP and iSC in rat sciatic nerve at E14 (A) and E18 (B) respectively. At E14 (A) SCP, denoted by arrow heads, are seen associated with large bundles of unsegregated axons. The connective tissue, colored in yellow, is located at the periphery of these clusters of SCP and axons. However, at E18 (B), the connective tissue invades into the endoneurial space and iSC can be seen associated with smaller unsegregated bundles of axons (denoted by asterisk). Source: (Jessen and Mirsky, 2019a)



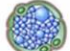
		
Neural crest	SCP	iSch
ECM - associated	Axon-associated Survival is axon-dependent	Axon-associated Survival is axon-independent Autocrine survival Basal lamina
	BFABP Connexin 29 Dhh Astrotactin GAP43 Serpin2 PMP22 NFIB PrPC Cad19	BFABP Connexin 29 Dhh Astrotactin GAP43 Serpin2 PMP22 NFIB PrPC
		GFAP Galectin S100 Desmoyokin Oct6 Reelin O4 Decorin MAL
α 4integrin AP2 Ncad	α 4integrin AP2 Ncad	

Figure 16: Some well-known molecular markers that are expressed at different stages of Schwann cell development. Source: (Jessen and Mirsky, 2019a)

The molecular factors that are implicated in this transition have been well documented. As stated earlier, NRG1 and Notch signaling are crucial for the survival and propagation of SCP into iSC. Sox10 also plays a key role in this transition. This pan-neural crest marker in fact intervenes in multiple stages of Schwann cell development (Jessen and Mirsky, 2005; Monk et al., 2015). During the transition of SCP to iSC, dimeric Sox10 is recruited at the Schwann Cell Enhancer (SCE) of Oct6 gene and promotes the latter's expression (Jagalur et al., 2011). Following that, Oct6, together with Brn2 and Sox10 are recruited at the Myelin Schwann Cell Enhancer (MSCE) of Krox20, the major pro-myelination transcription factor (Ghislain and Charnay, 2006; Reiprich et al., 2010).

The timing of SCP/iSC is of prime importance in Schwann cell development. Among other factors, it is controlled by Endothelins (Brennan et al., 2000). Ablation of Endothelin Receptor B (ET-B) in Schwann cells leads to an early appearance of iSC. Similarly, addition of endothelin in SCP cultures causes a delay in the appearance of iSC although it strongly promotes SCP survival (Brennan et al., 2000). These results taken together suggest that Endothelins also promote the Survival of SCP until they are ready to differentiate into iSC. This tightly controlled timing is also controlled by the expression (or the lack of it)

of the transcription factor Tfp2 α in SCP. (Stewart et al., 2001)Tfp2 α is strongly downregulated as SC progress from the SCP stage to iSC. Forced expression of this transcription factor in culture retards the transition of SCP into iSC.

Radial Sorting by immature Schwann Cells:

One of the most important functions of iSC in Schwann cell development is radial sorting of axons. As shown in Figure 14B, immature Schwann cells cluster around smaller groups of axons first. This is followed by radial sorting, which is the process of segregating axons based on their caliber (apparent diameter/size). Radial sorting is a crucial step in Schwann cell development as it determines the fate of both the axons and the Schwann cell associated with it. In other words, sorting basically segregates large caliber axons that form a 1:1 relationship with Schwann cells and smaller caliber axons that are aggregated into clusters called as Remak bundles. Indeed, the large caliber axons eventually become myelinated and the Remak bundles remain unmyelinated. From the viewpoint of Schwann cells, the cells in the Remak bundles develop into non-myelinating Schwann cells and the ones associated with larger axons (also called pro-myelinating SC) develop into myelinating Schwann cells. This process is recapitulated in the Figure 17.

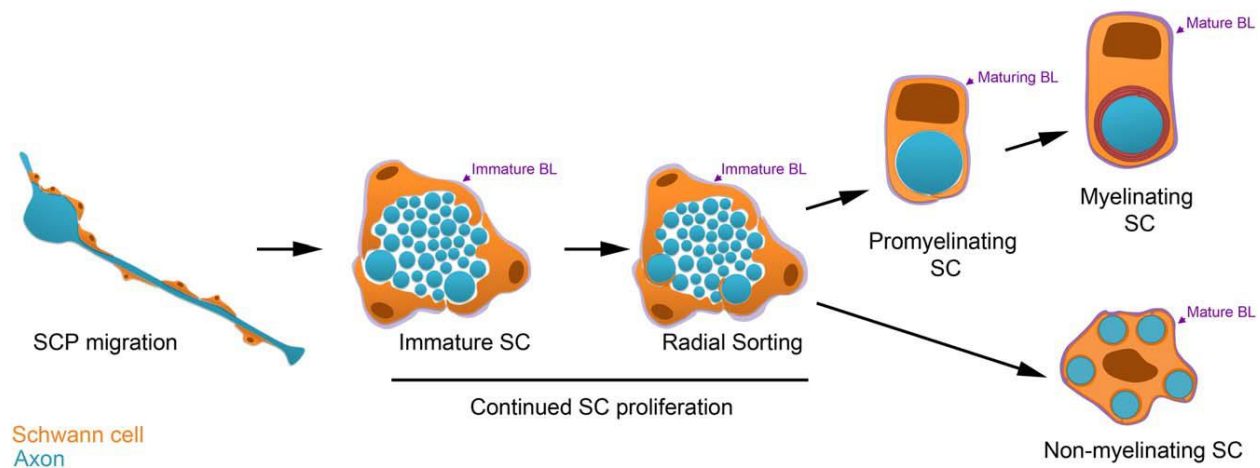


Figure 17: Schwann cell development from SCP. SCP migrate on developing nerves and differentiate into iSC at around E15.5 in mice (Jessen and Mirsky, 2005). iSC segregate the axons into smaller bundles first and then radially sort individual axons or a group of axons depending on their respective calibers. Thus, larger axons form a one on one relationship with Schwann cells and smaller axons are segregated into Remak bundles. This results in two different kinds of Schwann cells – myelinating and non-myelinating Schwann cells in the murine PNS. The formation of Basal Lamina (BL) also occurs at the iSC stage. Source: (Monk et al., 2015)

In fact, axonal sorting can be divided into 5 distinct stages that start around E15.5 in mice and continue until post-natal day 10 (P10) (Feltri et al., 2016). Stage 1 involves the segregation of large axonal bundles into smaller ones and the establishment of a basal lamina around iSC. Stage 2 begins with the

insertion of Schwann cell processes (like lamellipodia) into axonal bundles. Stage 3 involves the recognition of large caliber axons. Once the large caliber axons are identified, they are pushed radially towards the periphery of the bundle (hence the name radial sorting) which is identified as stage 4. Stage 5 begins by matching the number of Schwann cells to the number of axons i.e. an active phase of proliferation. This is followed by establishing a one to one relationship with large axons. The smaller axons that are left behind then resolve into future Remak bundles. In effect, radial sorting preferentially excludes larger axons and the Remak bundles are thus formed by simple exclusion. Different SC specific mutations have impacted radial sorting and the pathological eventualities that arise therein can also be linked to the developmental stage that was impacted by the mutation. The different developmental stages and pathological observations are recapitulated in Figure 18.

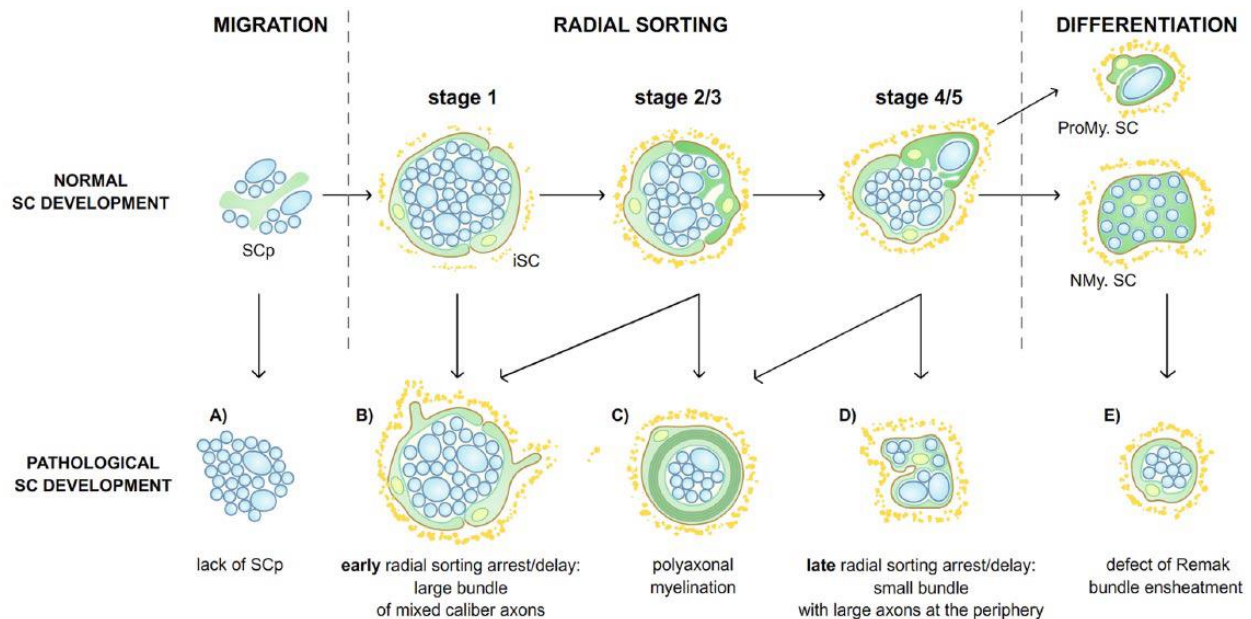


Figure 18: Progression of axonal sorting in murine PNS. The different stages of axonal sorting are depicted along with pathological conditions that arise when different mutations result in arresting radial sorting at multiple stages. These developmental stages and pathological outcomes help in identifying the effects of different genetic ablations that affect radial sorting. Source: (Feltri et al., 2016).

There are two key aspects that are important for efficient radial sorting. Firstly, radial sorting of cells is a complex multi-stage process that is orchestrated by a lot of molecular cues that are both Schwann cell intrinsic and extrinsic in nature (Monk et al., 2015; Feltri et al., 2016). Secondly, towards the beginning of stage 5, the number of iSC need to match the total number of neurons present in the environment

implying that Schwann cells would have to multiply. These two requirements are taken into consideration while deciphering the role of different genes in Schwann cell development and more importantly radial sorting.

The molecular cues that govern radial sorting are excerpted from a seminal review are detailed below (Feltri et al., 2016):

Extra-Cellular Matrix (ECM) and intra-cellular signaling pertaining to Actin polymerization:

ECM deposition of Laminin211, Laminin411, Collagen XV and their receptors on iSC such as Integrin $\alpha6\beta1$, Integrin $\alpha7\beta1$, Dystroglycan and its intracellular glycosylation enzyme Fukutin are all implicated in radial sorting. It is suspected that they aid in polarizing the Schwann cell membrane to extend its processes into axonal bundles and assure communication between the developing basal lamina and the Schwann cell (Feltri et al., 2016).

Additionally, proteins implicated in Actin polymerization such as ILK, FAK, Rho GTPase such Rac1& Cdc42, Profilin, Merlin/Nf2 and N-Wasp are equally crucial for the extension of Schwann cell processes and the establishment of apical and basal polarity in iSC (Jin et al., 2011; Novak et al., 2011; Guo et al., 2012, 2013; Grove and Brophy, 2014).

Axonal signaling in radial sorting:

NRG1/ErbB axis has been extensively studied to understand axo-glial interdependence during the different stages of SC development (Fledrich et al., 2019). However, NRG1 signaling could not be directly studied during radial sorting because NRG1 total mutants are not viable (Wolpowitz et al., 2000). However, using haplo-insufficient mutants, it was established that NRG1 is crucial for determining the ensheathment of large caliber axons (Taveggia et al., 2005). In other words, NRG1 signaling helps iSC to identify large caliber axons. Indeed, NRG1 Type III isoform is expressed more in larger axons than in smaller ones. This would mean that NRG1/ErbB signaling axis intervenes in Stage 5 of radial sorting. Similarly, inhibiting ErbB downstream signaling in iSC results in abnormalities in radial sorting in zebrafish (Monk et al., 2015), thus promoting the idea that NRG1 signaling axis could also be involved in radial sorting apart from SCP proliferation and sustenance. Furthermore, Schwann cell specific mutation of Gab1

(Grb2 Associated Binder 1), which is a downstream integrator of the Akt/Erk axis of NRG1 signaling also results in sorting abnormalities (Shin et al., 2014).

Wnt/ β Catenin signaling is another candidate pathway that has been recently studied with regard to axonal sorting (Grigoryan et al., 2013). Axons are known to secrete Wnt ligands and interact with Lgr and Lrp/Frizzled receptors present on Schwann cells in a paracrine manner. Conditional ablation of β Catenin in Schwann cells leads to mild radial sorting defects. Complementarily, constitutive activation of β Catenin speeds up the process of radial sorting and results in Remak bundles with smaller sized axons.

The third signaling pathway that has shed more light on axon/iSC interaction during radial sorting is Lgi4/Adam22 (Bermingham et al., 2006; Özkaynak et al., 2010). Under normal conditions SC secrete Lgi4, which binds to neuronal Adam22. Lgi4 Schwann cell mutants show delayed axonal sorting. Additionally, Adam22 mutants display an arrest in the pro-myelinating stage (i.e. right after Stage 5 of radial sorting).

Other signals implicated in radial sorting:

Recently, it was also demonstrated that lipids such as plasmalogens also regulate radial sorting (Da Silva et al., 2014). This is mediated through the Akt/GSK3 β axis as plasmalogen insufficiency resulted in elevated GSK3 β levels. However, treatment with GSK3 β inhibitors such as Lithium abrogated the pathological phenotype. Interestingly, miRNA have also been implicated in radial sorting (Pereira et al., 2010). Schwann cell *Dicer* mutants display a delay in radial sorting indicating that miRNA also have a role to play in Schwann cell development. This has been a growing field of interest in the last decade and various miRNA that regulate Schwann cell development at different stage have been discovered. (Gokey et al., 2012; Lin et al., 2018; Ji et al., 2019)

Factors that control iSC proliferation during radial sorting:

As mentioned earlier, mitogenic activity and SCP/iSC transition is assured by the coordinated effect of NRG1 and Notch signaling. These two pathways are also crucial to maintain and increase the number of iSC during radial sorting (Monk et al., 2015; Feltri et al., 2016). These results are also corroborated by the fact the addition of NRG1 and Notch ligands increase proliferation of iSC in culture (Woodhoo et al., 2009). ECM components are also required to increase Schwann cell numbers during radial sorting. For instance, ablation of Schwann cell laminin results in a drop in iSC proliferation rate (Yu et al. 2005). Other ECM/basal lamina related genes that are equally important in iSC proliferation are Rho

GTPase, Cdc42 and Focal Adhesion Kinase (FAK) (Laura Feltri et al., 2008; Grove and Brophy, 2014; Feltri et al., 2016). Laminin211 signaling is assured by Jun activation domain – binding protein 1 (Jab1). Inactivation of Jab1 also results in reduced proliferation of iSC (Porrello et al., 2014).

TGF β signaling is also implicated in iSC proliferation (D'Antonio et al., 2006a). Selective deletion of TGF β II receptor in Schwann cells results in reduced DNA synthesis resulting in reduced proliferation of iSC. On the other hand, normal Schwann cell apoptotic death was also reduced. Therefore, the role of TGF β signaling was not conclusive. However, in cell culture experiments, it was observed that addition of TGF β alone induced apoptosis in iSC. However, addition of TGF β in media containing NRG1 promoted proliferation (D'Antonio et al., 2006a). Therefore, the consensus is that TGF β promotes the proliferation of cells that are in contact with axons (through NRG1) and induces apoptosis in cells that are devoid of any axonal contact. Yap and Taz, regulators of the Hippo pathway are also important for iSC proliferation during radial sorting. Specific ablation of each of these genes in Schwann cells does not result in a drastic phenotype but simultaneous deletion results in a loss of Schwann cell numbers that further impact the myelination process (Grove et al., 2017).

Moderate activation of the cAMP pathway is important for sustained proliferation of iSC. Indeed, genetic ablation of R1A regulatory subunit of Protein Kinase A (PKA), the downstream effector of cAMP pathway results in a drastic reduction of immature Schwann cell proliferation (Guo et al., 2012, 2013). Additionally G-protein coupled Receptor 126 is also associated to the cAMP pathway and mediates its proliferative effect on Schwann cells *in vivo* (Mogha et al., 2013; Monk et al., 2015). The ligand for Gpr126 was previously thought to be axonal, but recent data demonstrate that ECM elements such as collagen and Laminin act through Gpr126 during radial sorting (Paavola et al., 2014; Petersen et al., 2015). The net effect of Gpr126 signaling is an increase in cellular cAMP levels by the activation of transmembrane Adenylate Cyclase (tAC) that promote iSC proliferation through the cAMP/Protein Kinase A (PKA) axis during radial sorting.

Negative regulation of the cAMP pathway that inhibit iSC proliferation has also been studied. This was performed using a Schwann cell specific deletion of gamma-aminobutyric acid type B1 receptor (GABBR1) (Procacci et al., 2013; Faroni et al., 2014). Binding of GABA (presumably secreted by peripheral axons) to GABBR1 in Schwann cells inhibits tAC thereby reducing intracellular cAMP levels and thus exerts a negative effect on iSC proliferation. The resulting phenotype is characterized by an increase in small diameter axons along with an increase in the number of Remak bundles. This was also corroborated by a

decrease in the number of large diameter axons. However, myelin protein levels were slightly increased as well as the myelin thickness. Intriguingly, Nrg1 expression in the peripheral nerves was decreased in these mice possibly because of neuronal loss as the mice age.

The different extracellular cues and intracellular pathways that are in play during radial sorting are recapitulated in the following figure (Figure 19).

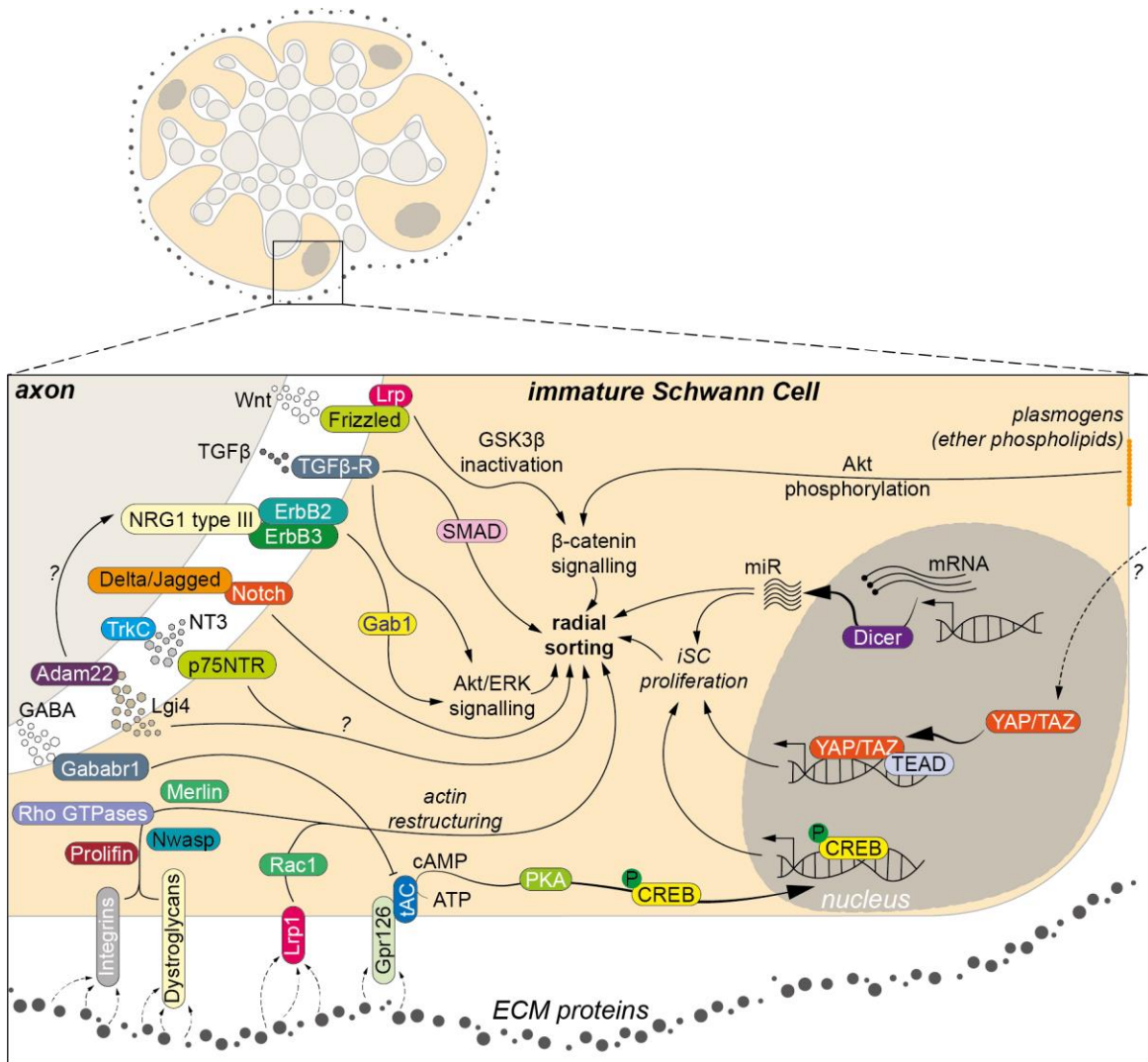


Figure 19: Extracellular cues and intracellular pathways that contribute towards radial sorting. Actin Restructuring to extend lamellipodia and iSC proliferation to match axon-SC numbers are the corner stones of radial sorting and almost all intra cellular pathways promote these outcomes. Most of these signaling cascades are activated by ligand-receptor interactions at the axon-glia interface. For instance, NRG1/ErbB signaling promotes radial sorting by acting through Akt/Erk cascade. Similarly, activation of the β catenin signaling by Wnt ligands that is further reinforced by membrane bound plasmogens results in iSC proliferation downstream as well as actin restructuring. TGF β signaling also integrates into the Akt/Erk axis either directly or indirectly. Delta/Notch signaling also promotes radial sorting through the Notch Intracellular domain (NICD). Furthermore, actin restructuring is directly controlled by ECM matrix proteins that bind to their receptors such as integrins and dystroglycans that exert their effect through various intra-cellular proteins that regulate actin polymerization and restructuring. Additionally, the proliferation of iSC is controlled by the canonical cAMP pathway that is activated by the binding of ECM proteins to Gpr126. cAMP is also controlled by the binding of GABA-b to Gabbr1 that in turn blocks the activity of tAC and reduces proliferation. These observations suggest that the cAMP is tightly controlled to achieve optimal proliferation at a required time. Other pathways have also been described but their downstream effectors remain poorly understood. For instance, Lgi4 ligand secreted by Schwann cells binds to axonal Adam22 but the resultant positive effect on radial sorting can be either axonal or neuronal. Similarly, NT3 can bind either to neuronal TrkC or to p75NTR in iSC to exert its positive effects on radial sorting. Actors of the Hippo pathways such as Yap and Taz also positively regulate radial sorting however their upstream and temporal regulators are poorly defined. They also promote iSC proliferation and increase the expression of ECM receptors in iSC (not shown in figure). Finally, recent studies also elucidate the role of some microRNA that can regulate iSC proliferation and radial sorting either directly or indirectly by inhibiting the expression of a plethora of genes.

Non-myelinating Schwann cells/Remak Schwann cells (RSC):

Two kinds of Schwann cells arise out of iSC during Schwann cell maturation – promyelinating SC and non-myelinating Schwann cell also called as Remak Schwann Cells (RSC) (Figure 17). This section describes the molecular mechanisms that are implicated in the generation and further maturation of RSC in the developing spinal nerves. These molecular mechanisms have been elaborated in a recent review (Harty and Monk, 2017).

Nrg1 Signaling:

The implications of Neuregulin signaling in RSC development was assessed by specifically deleting Nrg1 in sensory neurons using Sodium Channel Nav1.8-Cre (Fricker et al., 2009, 2013). This mutation would however impact both myelinated sensory fibers as well as Remak fibers in the PNS. Consequently, the authors observed larger Remak bundles along with poly-axonal pockets in Remak bundles . Larger axons that established a one to one relationship but are presumably sensory fibers also presented with thinner or no myelin at all. The authors thus concluded that Nrg1 signaling is rather important for the correct formation of Remak bundles.

Neuropathy Target Esterase (Nte):

Recently, McFerrin and colleagues observed an increased in the expression of Nte during immature Schwann cell maturation into Remak Cells (McFerrin et al., 2017). The expression of this enzyme was mostly localized to non-myelinating Schwann cells. The authors specifically deleted this protein using a Gfap-Cre system wherein Gfap is exclusively expressed in iSC and then in RSC but not in myelinating Schwann cells. They observed an incomplete ensheathment of Remak bundles but myelinating Schwann cells were seemingly unaffected. These results suggest that Nte is required for maturation of RSC but is not essential for the pro-myelinating SC.

LDL Receptor-related Protein 1 (Lrp1):

Schwann cell specific ablation of Lrp1 resulted in hypo-myelinating phenotype coupled with aberrant formation of Remak bundles (Orita et al., 2013). Lrp1 is known to bind Matrix Metalloprotease 9 (MMP9) and Tissue-Plasminogen Activator (t-PA) and regulates Schwann cell motility by activating Rac1. Therefore, it is quite probable that Lrp1 is important for lamellipodia extension mediated by the subtle

balance between Rho (focal adhesion)/Rac (motility) during radial sorting. Lrp1 ablation in Schwann cells resulted in a neuropathic phenotype where the mice experiences mechanical allodynia even in the absence of any nerve injury. However, following nerve injury, the phenotype was more aggravated with a dramatic loss of Schwann cell numbers due to apoptosis. These results show that Lrp1 is crucial for the proper formation of Remak fibers both during myelination and remyelination of peripheral nerves.

mTOR pathway:

The Akt/mTORC axis is classically known to be indispensable and a hallmark pathway required for myelination in the PNS (Monk et al., 2015; Salzer, 2015). However, recent evidence suggests that this signaling axis is also required for the proper formation of Remak bundles (Norrmén et al., 2014). In this mutant model, the researchers observed an increase in the number of axons inside the Remak bundles as well as the presence of naked axons. By contrast, activation of the mTORC pathway resulted in lesser number of axons in the Remak bundles and abnormal ensheathment of larger axons inside Remak bundles (Domènech-Estévez et al., 2016). These results taken together suggest that a fine balance in the Akt/mTORC axis is required for proper RSC maturation as much as it is required for myelination.

SC mitochondrial pathways:

Research over the last two decades have shown substantial evidence to support the notion that Schwann cells indeed provide trophic support to the axons that they are in contact with (Nave, 2010; Fledrich et al., 2019). In view of the same, recent work has sought to elucidate the role of SC mitochondrial metabolism in the maintenance of axonal integrity. The deletion of Mitochondrial Transcription Factor A (Tfam) in Schwann cells results in a preferential loss of non-myelinated fibers followed by myelinated fibers suggesting that SC mitochondrial metabolism is important for the maintenance of non-myelinated fibers (Viader et al., 2011). Secondly, numerous groups have elucidated the role of Liver Kinase B1 (Lkb1) in SC metabolism (Beirowski et al., 2014; Pooya et al., 2014; Shen et al., 2014). Of note, Pooya and colleagues demonstrate that the deletion of Lkb1 in SC results in hypomyelinated axons and impaired formation of Remak bundles. The authors postulate that SC undergo a metabolic transition from glycolysis to oxidative phosphorylation (OXPHOS) during differentiation due to a high demand for ATP for lipogenesis. Secondly, OXPHOS results in the production of Citrate (through Citrate Synthase), which is a precursor for lipogenesis. The authors further demonstrate that Citrate Synthase is regulated by Lkb1 in

Schwann cells. These results taken together suggest that SC intrinsic mitochondrial metabolism is indeed required for the maintenance of sensory fibers in Remak bundles.

The signaling pathways that contribute towards remak bundle formation and maturation are briefly described below (Figure 20).

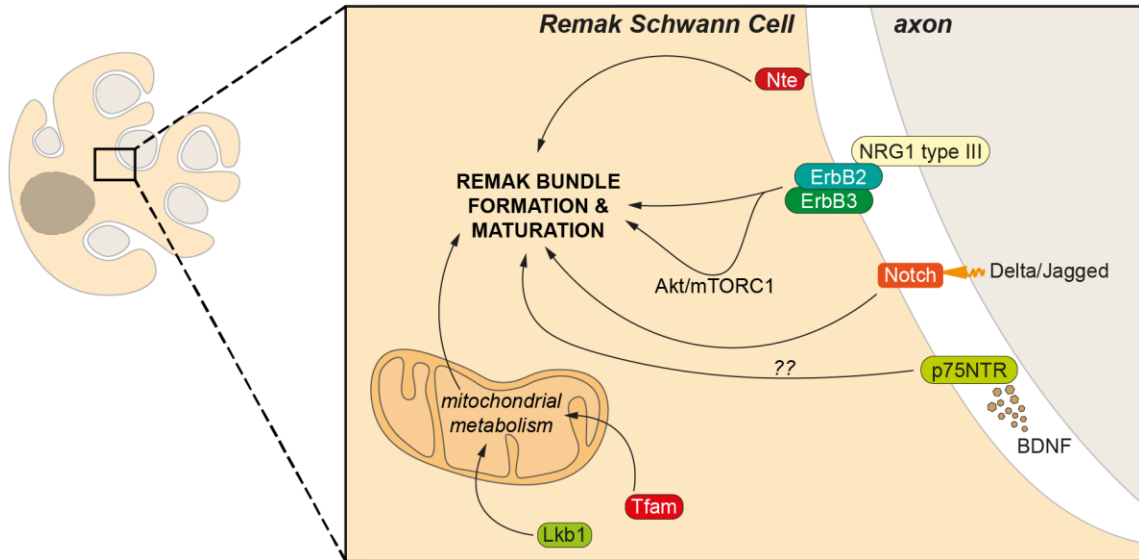


Figure 20: Formation and maturation of Remak Bundles. Genetic ablation/mutation of many genes implicated in radial sorting often result in poorly organized or disorganized remak bundles. These include, *NRG1* signaling through the *Akt/mTORC1* axis and *Delta/Notch* signaling. Additionally, *BDNF* binding through *p75NTR* also promotes Remak formation although the downstream actors remain unknown. Similarly, genes implicated in mitochondrial metabolism and ATP homeostasis such as *Lkb1* and *Tfam* also regulate Remak bundle maturation. Nevertheless, SC specific mutants of these genes also result in myelination deficits as explained in the following section. *Neuropathy Target Esterase (Nte)* is one of the genes known to specifically localize in Remak bundles to promote its maturation although the molecular effectors of the pathways are poorly defined.

1.1.6 Myelination in the PNS

Once radial sorting is completed, Schwann cells adopt two different fates depending on the axons that they are associated with as explained earlier. The cells that form a 1:1 association with axons and differentiate into pro-myelinating Schwann cells, which further develop into myelinating Schwann cells (mSC).

The myelination program in the Schwann cell has three important signalling axes. These include expression of SC intrinsic transcription factors coupled with epigenetic regulation, extracellular signals and intracellular signalling cascades that holistically drive myelination in SCs. Although these cellular events can be categorised into three different axes, these events need to be visualised as a continuum of molecular changes inside the mSC and not sequentially.

Expression of pro-myelinating Transcription Factors (TF) and Epigenetic regulation:

SC development from the pro-myelinating phenotype to a myelinating Schwann cell can be understood in terms of a feedforward cascade of TF expression following radial sorting (Salzer, 2015). Sox2, NFkB and Egr1 are expressed during the later stages of radial sorting. This is followed by the transient expression of Oct6 (Pou3f1) and Brn2 (Pou3f2) in pro-myelinating SC which is then switched off to promote Krox20 expression. Oct6 and Brn2 co-operate and are positive regulators of Krox20. In effect, Oct6 and Brn2 can be considered as markers of pro-myelinating Schwann cells and Krox20 is a marker of mSC. Additionally, expression of Krox20 is also promoted by the NFATc4 and Yin Yang 1 (YY1).

Parallely, Sox10 synergizes with NFATc4 as well Oct6 and Brn2 and it is recruited at the Myelin Specific Enhancer (MSE) site of Krox20 to stimulate the latter's expression. Indeed, Krox20 is regarded as the master myelin gene regulator as it activates the expression of various myelin proteins such as Mpz and Pmp22 (Topilko et al., 1994). This is then followed by the expression of lipogenic transcription factors such as SREBP (Camargo et al., 2009).

Epigenetic changes also take place during the iSC/mSC transition following sorting. Histone deacetylases (such as HDAC1 and HDAC2) which were previously known to mediate the generation of peripheral glia from NCC (see *Generation of Peripheral Glial Cells*) are also implicated in myelination. In more precise terms, HDAC2 but not HDAC1, synergizes with Sox10 to activate the myelin transcription program through Krox20 (Chen et al., 2011; Jacob et al., 2011). Furthermore, Brahma Associated Factor (BAF), a chromatin remodelling factor, also synergizes with Sox10 to drive myelination. SC specific deletion

of Brahma Related Gene product 1 (Brg1) which is the core catalytic unit of BAF, phenocopies Sox10 conditional mutants (Finzsch et al., 2010).

Indeed, after radial sorting, the binary fate adopted by Schwann cells is also intrinsically reinforced by the expression of Sox2 and c-jun (Salzer, 2015). In Remak Schwann cells, the expression of Sox2 and c-jun represses Krox20 and thereby prevents them from activating the myelination cascade. On the contrary, in mSC, the expression of Krox20 needs to be sustained to maintain the myelinating phenotype. This is most likely achieved by a feedforward loop created by Sox10 and the associated factors detailed above. The signalling cascades involved in myelination are detailed in the figure below (Figure 21).

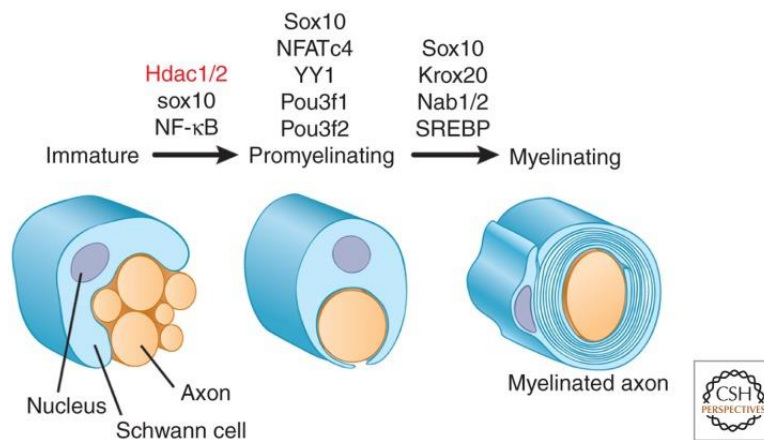


Figure 21: Transcription Factors and epigenetic markers that are involved in the transition of iSC to mSC. Source: (Salzer, 2015).

Intracellular signalling cascades that drive myelination:

The intracellular signalling pathways that drive and sustain myelination are Receptor Tyrosine Kinase pathways that act predominantly downstream of NRG1/ErbB signalling in SC (Monk et al., 2015; Salzer, 2015). They can be briefly classified as follows:

PI3K/Akt/mTOR pathway:

Activation of PI3K pathway exerts its pro-myelinating effect by the downstream phosphorylation of Akt. This drives the activation of the mTOR pathway and results in proper myelination of axons. In line with these observations, SC specific deletion of PTEN, a phosphatase that inhibits downstream Akt activation, results in increased phosphorylation of Akt thereby producing a hyper-myelinating phenotype (Goebbels et al., 2010). However, treatment of these PTEN conditional mutants with Rapamycin (mTOR

inhibitor) reverses many of the aberrant phenotypes observed (Goebbels et al., 2012). Keeping with these observations, it was also observed that SC deletion of mTOR1 and mTOR2 resulted in thinner myelin sheaths (Sherman et al., 2012). Further studies on the mTORC pathway revealed that mTORC1 but not mTORC2 is required for Schwann cell myelination (Norrmen et al., 2014). This was elegantly shown by Norrmen and colleagues through a conditional ablation of *Raptor* (mTORC1 adaptor) which resulted in hypomyelination. However, SC specific ablation of *Rictor* (mTORC2 adaptor) did not elicit the same phenotype. The authors further go ahead and show that mTORC1 drives myelination by regulating the expression of RXR γ . This is followed by the latter's subsequent recruitment at the promoter region of SREBP1c which is a master regulator of lipogenesis.

MAPK Pathway:

MAPK mediates myelination through the activation of Erk1/2 (Newbern et al., 2011). SC specific ablation of Erk1/2 results in SC differentiation deficits and hypomyelination. Similarly, ablation of Shp2, a phosphatase that in turn activates the MAPK pathway in Schwann cells phenocopies ErbB mutants (Grossmann et al., 2009). On the contrary, sustained activation of MAPK pathway by conditional expression of Mek1 results in a hyper-myelinating phenotype (Sheean et al., 2014). Interestingly in this study, it was demonstrated that the activation of MAPK pathway could reverse the effects of mutations affecting NRG/ErbB signalling. In other words, myelination deficits observed in ErbB mutants could indeed be reversed by sustained activation of the MAPK pathway in Schwann cells. Furthermore, one of the target genes activated by MAPK pathway is YY1 which is an important transcription factor required for Krox20 expression (He et al., 2010).

PLC γ /Calcineurin/NFAT Signalling:

Another RTK pathway that is activated by NRG1 is the intracellular Calcineurin pathway. NRG1 signaling results in elevated Calcium levels inside Schwann cells. This activates the phosphatase calcineurin B, which further dephosphorylates NFAT. NFAT then translocates to the nucleus and forms a complex with Sox10 and is recruited at the Myelin Specific Enhancer of Krox20 to promote its expression (Kao et al., 2009). A secondary pathway was also discovered which could potentiate the pro-myelinating effects of NFAT in Schwann cells. Following NRG1 Type III intermembrane proteolysis, the neurons secrete Prostaglandin D2 (PGD2), which acts as a ligand for GPR44 located on the plasma membrane of Schwann cells. This interaction precipitates to canonical NFAT signaling as mentioned above (Trimarco et al., 2014)

cAMP signaling:

cAMP increase in Schwann cells during development can elicit both proliferation of iSC and differentiation of mSC (Monje, 2015). The key difference in these two outcomes depends on how the cAMP is produced and employed in the Schwann cell. The first step of cAMP production is the conversion of ATP to cAMP by Adenylate Cyclase (AC). The most extensively studied AC enzyme in Schwann cells is the transmembrane AC (tAC) which interact with GPCRs such as Gpr126 (Mogha et al., 2013). This classical cAMP activation exerts its effects through PKA activation and ultimately the proliferation of immature Schwann cells, as explained earlier. However, recent studies have also shown the soluble Adenylate Cyclase (sAC) whose mode of action is independent of GPCRs and drugs such as forskolin is also ubiquitously present in Schwann cells (Monje, 2015). Additionally, it has also been demonstrated recently that cAMP action through EPAC (Exchange Protein Activated by cAMP) can specifically drive myelin gene expression (Monje, 2015). Similarly, in cell culture, stimulation of cAMP signaling using Forskolin favors cell proliferation due to its effects on the canonical PKA pathway but addition of 1mM cAMP promotes *in vitro* myelination (Arthur-Farraj et al., 2011). The consensus is that canonical cAMP activation leads to proliferation through PKA pathway whereas Schwann cell differentiation is mediated by EPAC translocation to the nucleus and the cAMP synthesized during differentiation may arise from non-conventional sources such as sAC.

Extracellular signals that promote myelination:

Axonal Regulation through NRG1:

NRG1 signaling governs almost all aspects of SC development and it is crucial for the different transitions that take place therein (Jessen and Mirsky, 2005; Fledrich et al., 2019). Primary observations for the requirement of NRG1 signaling in SC myelination were put forth by Garratt and colleagues who specifically deleted NRG1 Type III receptors, ErbB, in Schwann cells (Garratt et al., 2000). Subsequently, it was found that NRG1 type III isoform is the most crucial for myelination in Schwann cells (Taveggia et al., 2005). Taveggia and colleagues also observed that forced expression of NRG1 Type III in unmyelinated sympathetic neurons resulted in their myelination. Similarly, overexpression of this particular neuregulin isoform in motor neurons also resulted in hypermyelination (Michailov et al., 2004). On the contrary,

haploinsufficiency of NRG1 displayed significant hypomyelination (Michailov et al., 2004; Taveggia et al., 2005; Brinkmann et al., 2008). Hence the consensus on NRG1 signaling is that at threshold levels it drives myelination and disruptions to NRG1 expression can proportionately affect the extent of myelination in the PNS. In keeping with this principle, axons that are destined to be myelinated are always larger and express higher levels of NRG1 Type III (Salzer, 2015). On the contrary, small caliber axons ensheathed by RSC express low amounts of NRG1 Type III given their size but NRG1/ErbB signaling axis is equally important for the formation of remak bundles.

Secretases:

The role of secretases on Schwann cell myelination has been extensively studied in the last two decades. Of note, two secretases (BACE1 and ADAM17), which differentially regulate NRG1 signaling have been of interest to the glial research community. β -secretase BACE1 exerts a promyelinating effect on SC as the cleavage of NRG1 Type III isoform stimulates the RTK pathways discussed in the previous section (Taveggia et al., 2005; Fledrich et al., 2019). However, ADAM17 (also called TACE) cleaves NRG1 Type III in the epidermal growth factor domain and in turn deactivates the canonical NRG1 signaling pathway in SC (La Marca et al., 2011). Inactivation of ADAM17 in Schwann cells accelerates myelination in culture and causes aberrant myelination *in vivo*. These observations give rise to the question if ADAM17 and BACE1 expression in Schwann cells occur at different time points during development to exert their opposite effects on Schwann cell development.

Another secretase that has been studied is ADAM10. *In vitro*, cleavage of NRG1 by ADAM10 promoted myelination but inhibition of ADAM10 does not hamper myelination as long as BACE1 is still active (Luo et al., 2011). Similarly, transgenic mouse models that overexpress ADAM10 or a dominant negative form of the gene do not display any peripheral myelin deficits (Freese et al., 2009).

Notch1 signaling:

Inhibition of Notch signaling is important for the onset of myelination (Woodhoo et al., 2009). This pathway is crucial for the survival of SCP as explained earlier but Notch is systematically downregulated by the expression of Krox20 at the onset of myelination. Correspondingly, forced expression of Notch Intracellular Domain (NICD) at later stages of SC development results in demyelination. (Woodhoo et al., 2009)

Neurotrophins:

Interactions between neuron and glial cells are often mediated by growth factors and proteins called Neurotrophins. In this regard, some well-known neurotrophins such as BDNF, NT3, GDNF and NGF have been studied and are known to impact both Schwann development and myelination of the PNS. For instance, *in vitro* studies on DRG/Schwann cell co-cultures first demonstrated that Neurotrophin 3 (NT3) promotes SC migration and motility by binding to the TrkC receptors on axons and activates the Cdc42/JNK pathway in SCP and iSC (Yamauchi et al., 2003). However, upon the induction of myelination, it was found that this interaction inhibits the synthesis of myelin layers around axons in culture (Cosgaya et al., 2002). Hence, it was postulated that NT3-TrkC interactions are predominant during the SCP and iSC stages but it is downregulated once Schwann cells myelinate. In NT3 null mutants, the sciatic nerve was devoid of myelinated axons. However, the brachial plexus contained Schwann cells that myelinated the nerves properly at birth but as the mice aged, the Schwann cells turned apoptotic (Woolley et al., 2008). This suggests that NT3 might also be implicated in SC survival once it has crossed the pro-myelinating stage *in vivo*.

BDNF binds to its cognate receptor p75NTR present in Schwann cells to promote myelination (Cosgaya et al., 2002). It is to be noted that myelinating Schwann cells downregulate p75NTR expression and only Remak Schwann cells retain its expression. Thus, it is quite probable that BDNF aids in Remak Schwann cell formation during development.

NGF also seems to promote myelination *in vitro* as addition of NGF to DRG/SC cocultures stimulates (Chan et al., 2004). However, it is not clear if this effect is mediated by TrkA on axons or p75NTR expressed in Schwann cells. GDNF, another neurotrophin of glial origins, exerts a pro-myelinating effect on Schwann cells (Höke et al., 2003). However, the action of GDNF is more prominent than that of NGF as increased GDNF exposure also results in the myelination of Remak bundles (Höke et al., 2003).

Cell Adhesion Molecules (Cadm) or Nectin Like Proteins (Necl):

There are multiple ways in which SC and axons interact with each other during development and myelination. NRG1/Signaling is one of the most extensively studied mechanisms followed by the exchange of Neurotrophins as discussed herein. Another means of axo-glial communication occurs through a family of protein called the Cell Adhesion Molecules or Nectin-like proteins (Necl). Of note, both axons and Schwann cells express different kinds of Necl proteins. Axons express high levels of Necl1 and Necl2

whereas Schwann cells express Necl4 and very low levels of Necl2 (Maurel et al., 2007). These proteins are exclusively found in the internodes of mSC and localize at the Schmidt-Lanterman incisures where axonal Necl1 and Necl2 are directly opposed to Schwann cell Necl4 (Maurel et al., 2007). Genetic silencing of Necl4 in DRG/SC cocultures drastically reduced the total number of myelinated axons (Maurel et al., 2007). These results were further supported *in vivo* where dominant negative expression of Necl4 in Schwann cells inhibits myelination suggesting that axo-glial contact during myelination is indeed mediated by Necl4 – Necl1 interaction between Schwann cells and axons respectively (Spiegel et al., 2007). Further evidence for the utility of the Necl4 protein in Schwann cells was provided by Golan and colleagues who specifically deleted Necl4 in SC (Golan et al., 2013). The resulting mutants displayed myelin abnormalities that resembled Charcot-Marie-Tooth neuropathy. Of note, deletion of other Necl types in mice does not give rise to myelination deficits (Golan et al., 2013).

A detailed description of the interplay between the different molecular pathways and extracellular signals is provided below (Figure 22)

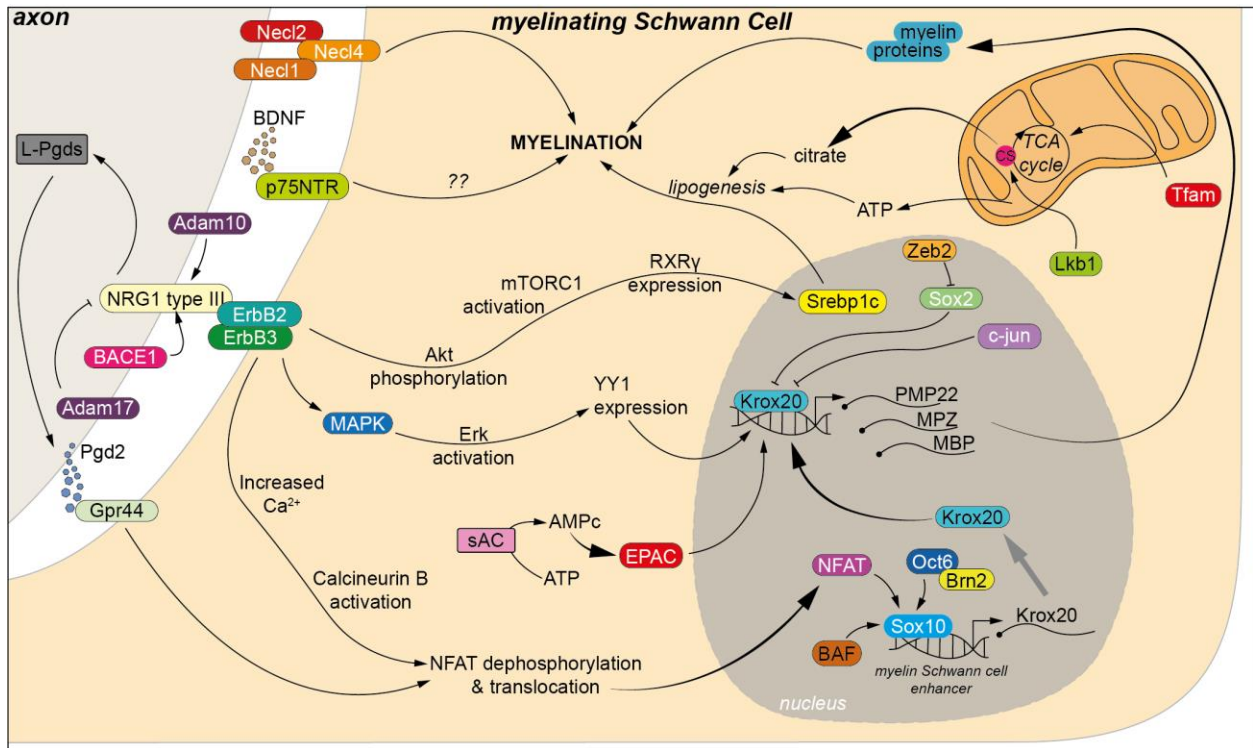


Figure 22. Interplay between different molecular pathways in a myelinating Schwann cell.

Myelination in Schwann cells is majorly governed by NRG1/ErbB2&3 signaling that elicits three fundamental Receptor Tyrosine Kinase Pathways. Firstly, this interaction promotes Akt phosphorylation which then activates mTORC1. This well studied cross-talk between Akt and mTOR pathway results in the expression of RXR γ that then binds to the promoter region of Srebp1c. The latter is a master regulator of fatty acid synthesis that promotes myelin formation. Secondly, NRG1 signaling activates the MAPK cascade that results in the activation of ERK and the concomitant increase in the expression of the pro-myelin transcription factor YY1. YY1 then promotes the expression of Krox20 which governs myelin gene expression. Finally, NRG1 signaling also activates the Calcineurin/NFAT pathway wherein an increase in intracellular Calcium levels activates Calcineurin B phosphatase that in turn promotes NFAT translocation to the nucleus following dephosphorylation. Once inside the Nucleus, NFAT synergizes with Sox10, Oct6 and Brn2 at the Myelin Schwann cell Enhancer site of Krox20 and promotes the latter's expression. On the axonal front, secretases such as BACE1 process NRG1 Type III so as to promote the interaction with ErbB receptors on the Schwann cell. Additionally, it was also shown *in vitro* that ADAM10 can cleave NRG1 Type III to promote the said interaction although the same is not a necessary step *in vivo*. Another α -secretase, ADAM17, cleaves NRG1 Type III at the EGF domain and inhibits its interaction with ErbB. Thus, NRG1 type III processing is plausibly controlled to elicit different outcomes during the course of Schwann cell development. Furthermore, NRG1/ErbB signaling also promotes the expression of Prostaglandin Synthase (L-Pgds) that results in the secretion of Prostaglandin 2 (Pdg2) in the axon-glia interface. These ligands bind to Gpr44 on Schwann cells and reinforce Krox20 expression through the Calcineurin/NFAT axis. Negative regulators of Krox20 expression include Sox2 and c-jun. The former is tightly controlled by Zeb2 which starts inhibiting Sox2 during myelination to permit the expression of Krox20. c-jun, on the other hand, does not inhibit Krox20 during development but its inhibitory action is a pre-require for Schwann cell de-differentiation post injury. On the cellular energy front, cAMP production from ATP is now carried out by soluble Adenyl Cyclase (sAC) that is ubiquitously present in Schwann cells. This drastically increases cAMP levels in the milieu and promotes Krox20 expression through the Exchange Protein Activated by cAMP (EPAC). Furthermore, genes such as Tfam and Lkb1 are implicated in mitochondrial metabolism wherein the former is a master regulator of Mitochondrial gene expression and genes implicated in Oxidative Phosphorylation. Lkb1 regulates Citrate Synthase expression either directly or indirectly and it has been shown to be important for the synthesis of Citrate that acts as a precursor for fatty acid synthesis.

1.1.7 Other cells in the PNS

Apart from Schwann cells, research has also led to the discovery of other cells that are pertinent and play an active role in development and regeneration of peripheral nerves (Richard et al., 2014; Kucenas, 2015; Fontenas and Kucenas, 2017). These cells can be classified into two types – Endoneurial cells and Perineurial cells. This section details their origin and their role in PNS development and myelination.

Perineurial cells

Perineurial cells (previously termed as perineurial fibroblasts in PNS literature), as the word suggests, form the perineurium, which facilitates the compartmentalization of big nerve fascicles in the spinal nerves (Figure 7). They are characterized by the presence of a continuous double basal lamina, pinocytotic vesicles in their cytoplasm and the expression of tight junction proteins (Kucenas, 2015). Furthermore, certain characteristic traits set them apart from conventional fibroblasts. Firstly, fibroblasts have a compact nucleus and a large endoplasmic reticulum that perineurial cells do not have. Secondly, fibroblasts display a single basal lamina but perineurial cells display two layers of basal lamina (Kucenas, 2015). These observations supported the hypothesis that perineurial cells are not fibroblasts or fibroblast-like cells, but they are unique in their structure, morphology, and function.

The origin of perineurial cells is an ongoing topic of research. In mice, past research has shown that a subset of perineurial cells are derived from the Motor Exit Points at the ventral roots of the spinal nerves (Clark et al., 2014). A sub-population of these cells are positive for Nkx2.2, a homeobox domain containing transcription factor that is also implicated in generating derivatives of the CNS (Kucenas et al., 2008). Furthermore, loss of Nkx2.2 in these glial cells disrupts Schwann cell myelination and the formation of Neuromuscular Junctions (Clark et al., 2014). Additionally, all perineurial cells also express tight junction proteins such as Zona Occludens 1 (ZO-1) and glucoprotein Podoplanin (Pdpn) which can be used as markers that can distinguish these cells in the PNS (Clark et al., 2014). However, not all perineurial cells that are Nkx2.2+ express Pdpn (Clark et al., 2014). Nevertheless, all perineurial populations are ZO-1+. This suggests that a population of these cells can also have other origins apart from the CNS such as the mesenchyme. Further research is required to assess the origins of these two different populations of the cells present in the perineurium.

With regard to their functions, these glial cells mediate the exit of motor neurons and their ablation results in aberrant myelination at Motor Exit Points in zebrafish (Kucenas et al., 2008). Together with Boundary Cap cells, Perineurial cells form a population of Glial cells called as the Motor Exit Point (MEP) glia that have crucial implications in the segregation of the PNS and CNS boundaries (Fontenas and Kucenas, 2017, 2018). Perineurial cells are also important in maintaining the structural integrity of developing nerves. This is assured by the communication between SC and perineurial cells during development. Of note, Desert Hedgehog (Dhh) has been implicated in the interaction between SC and perineurial cells (Parmantier et al., 1999; Sharghi-Namini et al., 2006). In Dhh null mice, the perineurial cells invade into the endoneurial space and form many mini fascicles around clusters of axons. Similarly, in Sox10 conditional mutants which exhibit a complete loss of Schwann cell population in peripheral nerves, similar invasion of perineurial cells into the endoneurial space was observed (Finzsch et al., 2010). The authors further state that the absence of SC results in the absence of Dhh signaling and therefore these mutants phenocopy the Dhh null mutants in terms of perineurial ensheathment. Furthermore, perineurial glial have also been implicated in nerve regeneration after injury especially in zebrafish models (Lewis and Kucenas, 2014).

Endoneurial cells:

Endoneurial cells or Endoneurial Fibroblast Like Cells (EFLC) have long been observed in peripheral nerve tissues through early histological studies in the 21st century (Richard et al., 2012). In Electron Microscopy, EFLC look like spindle shaped cells with rectangular cell bodies and have cytoplasmic projections that extend either along the nerve or radially between nerve fibers. They are often localized near endoneurial blood vessels and adjacent to the perineurium in rodents as well as in humans (Figure 23).

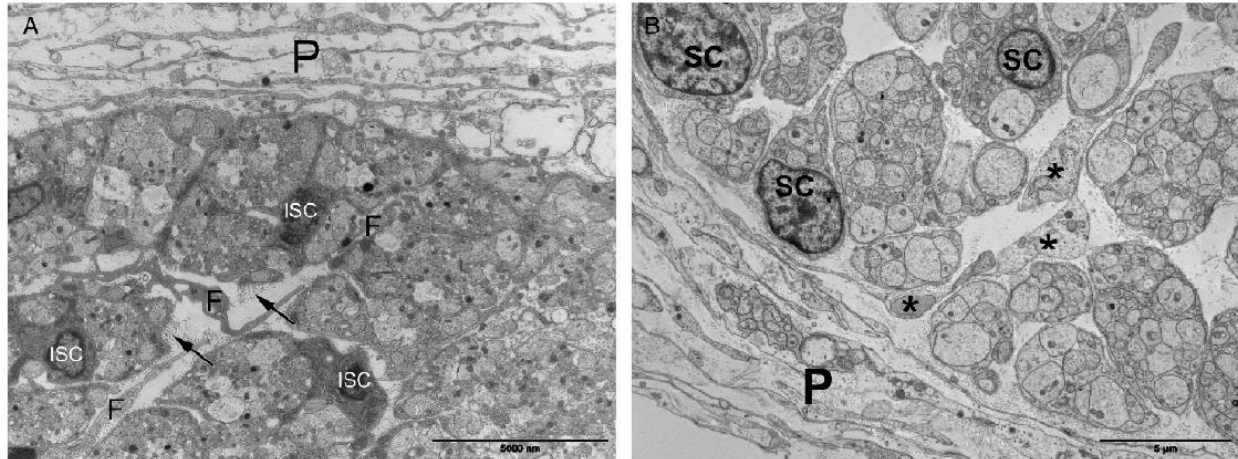


Figure 23: Endoneurial Fibroblast Like Cells in E17 mouse sciatic nerves (Panel A) and E14 weeks human fetal nerves (Panel B). P : Perineurium, ISC : immature Schwann cell, F and * : EFLC. Source: (Richard et al., 2012).

As EFLC do not produce a basal lamina, they can be easily distinguished from Schwann cells and perineurial cells. They are also not tightly packed and therefore do not express any gap junction proteins. Furthermore, they form a reticular network in the endoneurial space and are difficult to spot in ultra-thin electron microscopy sections.

The origin of the EFLC remained a controversial subject until critical observations were put forth by Joseph and colleagues that suggested their Neural Crest origin (Joseph et al., 2004). Using lineage-tracing models of the Neural crest (Wnt1-Cre), they showed that EFLC originate from SCP. A transient SCP glial population which is p75NTR+ve differentiate into two glial populations that become either Dhh+ p75NTR+ve P0+ve (SCP) and Dhh-ve P75NTR-ve Thy1+ (EFLC). They also propose that glial cells that retain contact with axons eventually develop into Schwann cells and the ones that lose contact with axons develop in EFLC (Joseph et al., 2004).

As for the molecular profiles of these cells, all EFLC *in vivo* and *in vitro* are positive for Neuron-Glial Proteoglycan 2 (NG2) and Cluster of Differentiation Marker 34 (CD34) (Richard et al., 2014). A small population of these cells co-express Pdgfr β and Nestin. However, CD34 and NG2 are also expressed by the pericytes that are located in the endoneurial blood vessels, but these two populations can be distinguished by the presence of tight junctions in pericytes as opposed to Endoneurial cells. Interestingly, it was also shown that a small population of perineurial cells also stain positive for NG2 suggesting that they could have Endoneurial origins and properties. Interestingly, the regeneration of the perineurium after surgical insult implicates cells of Endoneurial origin that migrate towards the periphery and

seemingly differentiate into perineurial cells (Yamamoto et al., 2011). Very recently, it was also shown that CD34+ Endoneurial cells behave like mesenchymal progenitors are implicated in mammalian tissue regeneration (Carr et al., 2019). These observations suggest that EFLCs have the potential to generate other cell types during regenerative processes.

The classical functions of EFLC include collagen deposition during development, phagocytosis of myelin debris upon nerve damage, activation of pro-inflammatory cytokine production upon nerve insult, possible interactions with hematogenic macrophages, immune surveillance through expression of MHC II and the production of connective tissue matrix during nerve regeneration (Richard et al., 2012). Thus, Endoneurial cells play an important role in maintaining the structure integrity and normal functioning of the PNS. They are also the first responders to nerve damage in the PNS and are indispensable for nerve regeneration. For this reason, they are also termed as the 'resident immune cells' of the PNS (Richard et al., 2012).

Cells of the nervous vasculature (vasa nervorum):

Peripheral nerves are also innervated with vasculature that runs parallel to the nerve and provides trophic support. Depending on the compartment they innervate, they are categorized into epineurial, perineurial and endoneurial vasculature (Boissaud-Cooke et al., 2015)(Figure 24)

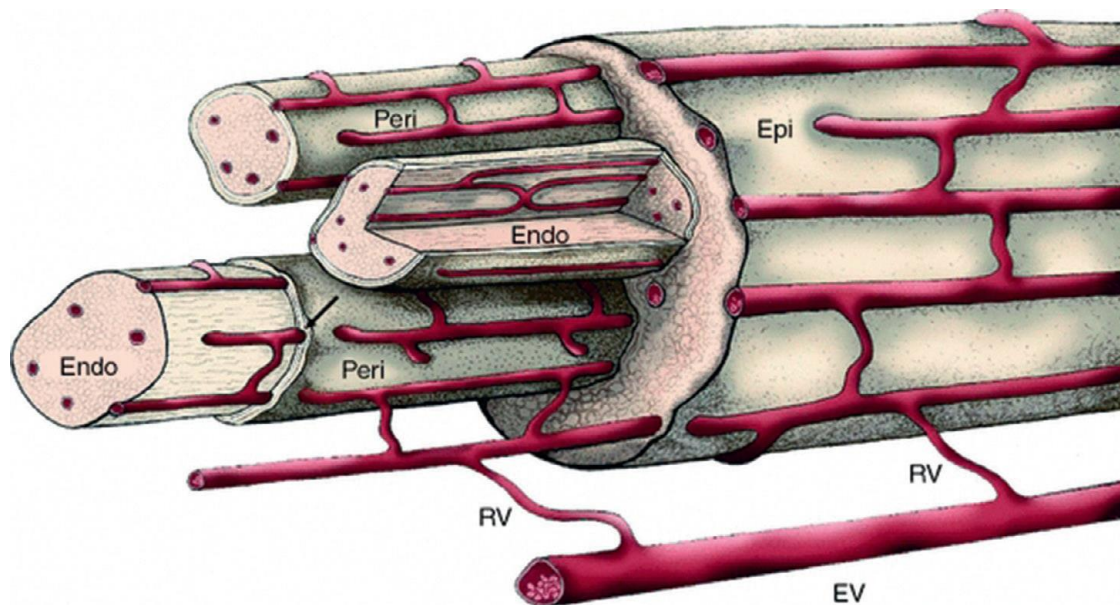


Figure 24: The vasculature present in peripheral nerves. Blood supply is assured to the nerve by external vessels (EV) that run parallel to the nerve along its axis. The EV are connected to the epineurial vessels through Radicular Vessels (RV). The different

compartments of the nerve are well connected by vasculature that ascend and descend between the compartments radially. This gives rise to a longitudinal and radial plexus along the entire nerve with multiple anastomoses between these vascular structures [Source:(Boissaud-Cooke et al., 2015)]

Of note, the endoneurial vasculature that runs through the endoneurium is the one that is in close proximity to the axons, Schwann cells and other cells in the endoneurial matrix. These blood vessels are rather important as they cater to the metabolic requirements of the endoneurial compartment and maintain a homeostatic environment. This is primarily assured the endothelial cells that form the walls of the vasculature. Endothelial cells express tight junction proteins and Claudins that form tight junctions, which in turn form a physical barrier between the vasculature and the nerve. This physical barrier is often termed as the Blood Nerve Barrier (BNB) (Richner et al., 2019). The exchange of nutrients through the BNB occurs predominantly by transcytosis through the endoneurial cells. Additionally, the BNB is reinforced by pericytes that are closely associated to endothelial cells and form an envelope like structure around the endothelial cells (Richner et al., 2019) (Figure 25)

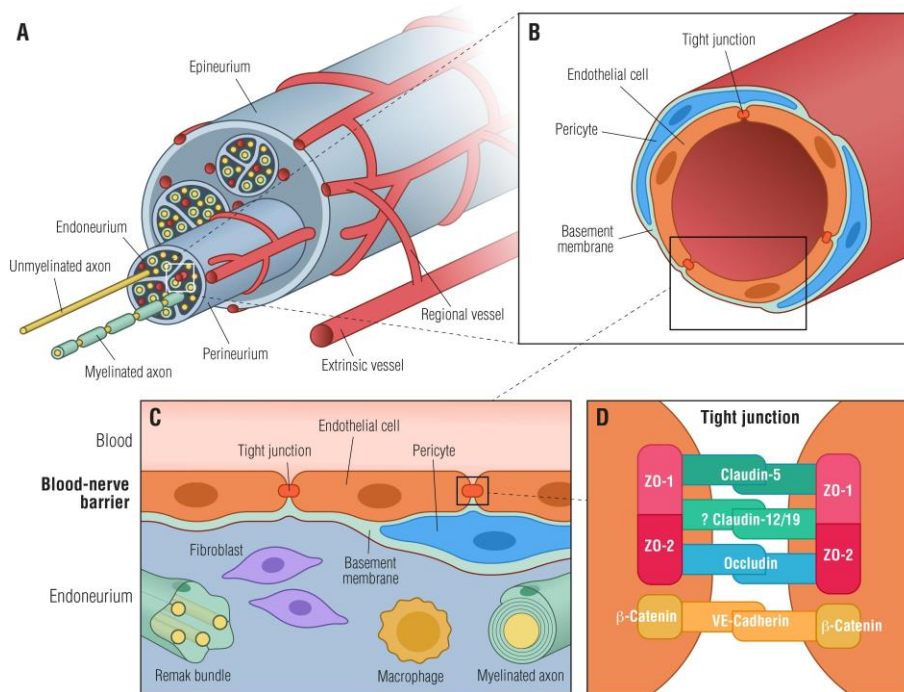


Figure 25: The cellular composition of the Blood Nerve Barrier. A. The overall arrangement of the peripheral nerve with the vasculatures that forms numerous anastomoses both radially and longitudinally along the nerve. B. The cellular composition of an endoneurial blood vessels composed of endothelial cells and pericytes. C. The cellular microenvironment of the endoneurial compartment that is in proximity to a blood vessel. D. The interactions of different tight junction proteins that maintain the structural integrity of these tight junctions. Source ((Richner et al., 2019).

Although the predominant function of the BNB is to provide for a physical separation between the endoneurium and the blood stream, cells of the BNB are known to have other functions. For example, pericytes are known to secrete different Neurotrophins that can potentially regulate neuronal/Schwann cell development and differentiation as explained earlier (Shimizu et al., 2011). Very recently, in an unpublished preprint (Malong et al., 2019), it was reported that the BNB in the endoneurial space is slightly permissive but nerve resident macrophages (Iba1+ & F4/80+) are involved in engulfing any leaks from the BNB. Additionally, the authors also found that pericyte-like cells (CD34+, NG2+ and PDFGR β +) are closely associated to the blood vessels. Given the expression of molecular markers, it is highly probable that these pericytes-like cells are indeed EFLCs. These observations taken together suggests that all these cell types are instrumental in maintaining the structure and function of the BNB.

1.2 Liver X Receptors (LXRs)

1.2.1 Description and Mechanism of Action

The Liver X Receptors (LXRs) are ligand activated transcription factors that belong to the nuclear receptor superfamily. They exist in two isoforms, LXR α and LXR β , which are encoded by two different genes Nr1h3 and Nr1h2, respectively. Nr1h3 is located on chromosome 11 in humans and chromosome 2 in mice and it has 8 exons in humans and 10 exons in mice. The protein product of LXR α weighs about 43kDa in humans and 50kDa in mice. Nr1h2 is located on chromosome 19 in humans and chromosome 7 in mice and it has 10 exons for both the species. The protein product of LXR β weighs approximately about 50kDa for both the species. In mice, LXR β is more ubiquitously expressed, whereas the expression of LXR α is the highest in lipogenic tissues such as the liver (Annicotte et al., 2004).

LXRs were first identified as orphan receptors as their ligands were unknown (Kainu et al., 1996). Further research identified oxidized cholesterol derivatives or oxysterols as natural ligands that can bind and activate LXR (Lehmann et al., 1997). Natural LXR ligands include 20(S)-, 22(R)-, 24(S)-, 25- and 27-hydroxy cholesterol (HC) and 24(S), 25-epoxycholesterol (Gabbi et al., 2014). Further research in the last two decades has also helped in the discovery of synthetic ligands with different specificities to the two isoforms (Komati et al., 2017).

LXRs mechanism of action can occur in two ways – direct activation and transrepression (Figure 20). At the basal state, LXRs forms an obligate heterodimer with Retinoid X Receptor (RXR) and it is recruited at the LXR response Element (LXRE) of target genes. LXRE is a repeat of the sequence 5'-AGGTCA-3' separated by any 4 nucleotides in between (DR4 sequence) present upstream LXR target gene DNA. At this state, the LXR-RXR heterodimer complex recruits co-repressors such as Nuclear Receptor Corepressor (NCoR) or the Silencing Mediator of Retinoic Acid and Thyroid Hormone Receptor (SMRT), thereby preventing the transcription of target genes. However, upon the ligand binding, both the nuclear receptors undergo a conformational change and this liberates the co-repressors and co-activators such as Peroxisome Proliferator Activated Receptor γ (PPAR γ) coactivator-1 α (PGC-1 α), the Steroid Receptor Coactivator-1 (SRC-1) and the Activating Signal Cointegrator-2 (ASC-2) are recruited (Gabbi et al., 2014). The recruitment of co-activators initiates the transcription of target genes such as ATP-Binding Cassette A1 (ABCA1) and Apolipoprotein E (ApoE).

A secondary mode of LXR mechanism occurs through transrepression, which is implicated in the regulation of pro-inflammatory genes. Binding of Ligands to LXR is followed by the SUMOylation by SUMO-2/3 that promotes its interaction with GPS2, a subunit of the N-CoR complex which is recruited by NF- κ B. This binding of LXR to the NCoR complex inhibits the transcription of proinflammatory genes under the control of NF κ B. These two modes of action are described in the following figure (Figure 26).

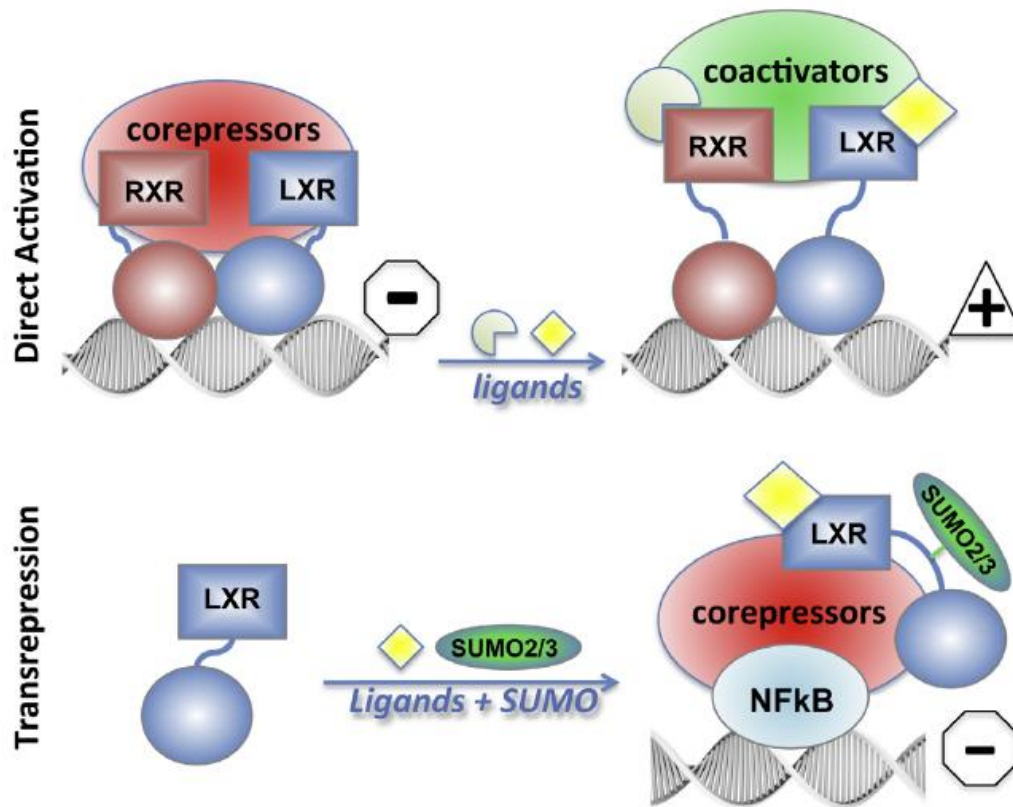


Figure 26: **LXR Mechanism of Action.** The first mode of action is called as direct activation where the heterodimers are first bound to the LXRE of target genes in the presence of Co-Repressors. Upon ligand activation, the co-repressors are released and co-activators take their place thus resulting in the transcription of LXR target genes. The second mode of action is called as transrepression wherein LXR binding to its ligand results in its SUMOylation. The SUMOylated protein then binds to the Co-repressors that are bound to NfκB. This prevents the release of co-repressors from NfκB and prevents the transcription of proinflammatory genes. Source (Gabbi et al., 2014)

LXRs are involved in several physiological processes such as lipid metabolism and homeostasis, inflammation and cholesterol homeostasis (Gabbi et al., 2009). As these nuclear receptors are implicated in such important physiological function they have been intricately linked to a plethora of disorders ranging from Multiple sclerosis, Alzheimer's, Arthritis, autoimmune disorders to skin diseases, metabolic disorders and cancers (Komati et al., 2017). Thus, in the past two decades, LXRs have been extensively studied in different organs systems and cell types and more research is being performed on elucidating their therapeutic roles across different diseases (Komati et al., 2017).

1.2.2 LXRs, Cholesterol Synthesis, Cholesterol Homeostasis and Lipogenesis

In the context of Schwann cell development and myelination, cholesterol synthesis, lipogenesis and the regulation of these biomolecules play a rather important role as these molecules are invariably linked to the production and maintenance of myelin. This section aims to explore this premise from the optic of LXRs and how this nuclear receptor plays a crucial role in the aforementioned molecular processes.

Molecular regulation of Cholesterol synthesis and Lipogenesis:

In almost all cell types, cholesterol and lipids are exclusively produced in the Endoplasmic Reticulum and are shunted to different cellular compartments where they are further processed to generate different derivatives with respective functions. The major molecular regulators of cholesterol and lipid synthesis are Sterol Regulatory Element–Binding Proteins (SREBPs). In mammals, 2 isoforms of SREBPs are known to exist namely SREBP1 and SREBP2 encoded by two separate genes (Horton et al., 2002). However, SREBP1 is expressed as two isoforms – SREBP1a and SREBP1c which are by products of alternative splicing that are expressed in a tissue specific manner. For example, mRNA transcripts from the liver exhibit a 9:1 ratio of SREBP1c:SREBP1a but in the spleen the ratio is reversed. Functionally, SREBP2 uniquely regulates genes implicated in Cholesterol synthesis and SREBP1c uniquely regulates fatty acid synthesis (precursor to lipids) whereas SREBP1a can regulate both these biosynthetic pathways in tissues where it is predominantly expressed (Shimomura et al., 1997; Repa et al., 2000). However, in Schwann cells, it has been categorically demonstrated in three separate studies that SREBP1c and not SREBP1a regulates lipogenesis during Schwann cell development and myelination (de Preux et al., 2007; Verheijen et al., 2009; Norrmén et al., 2014).

The following schematic details the role of SREBP2 and SREBP1c in cholesterol synthesis and lipogenesis respectively (Figure 27).

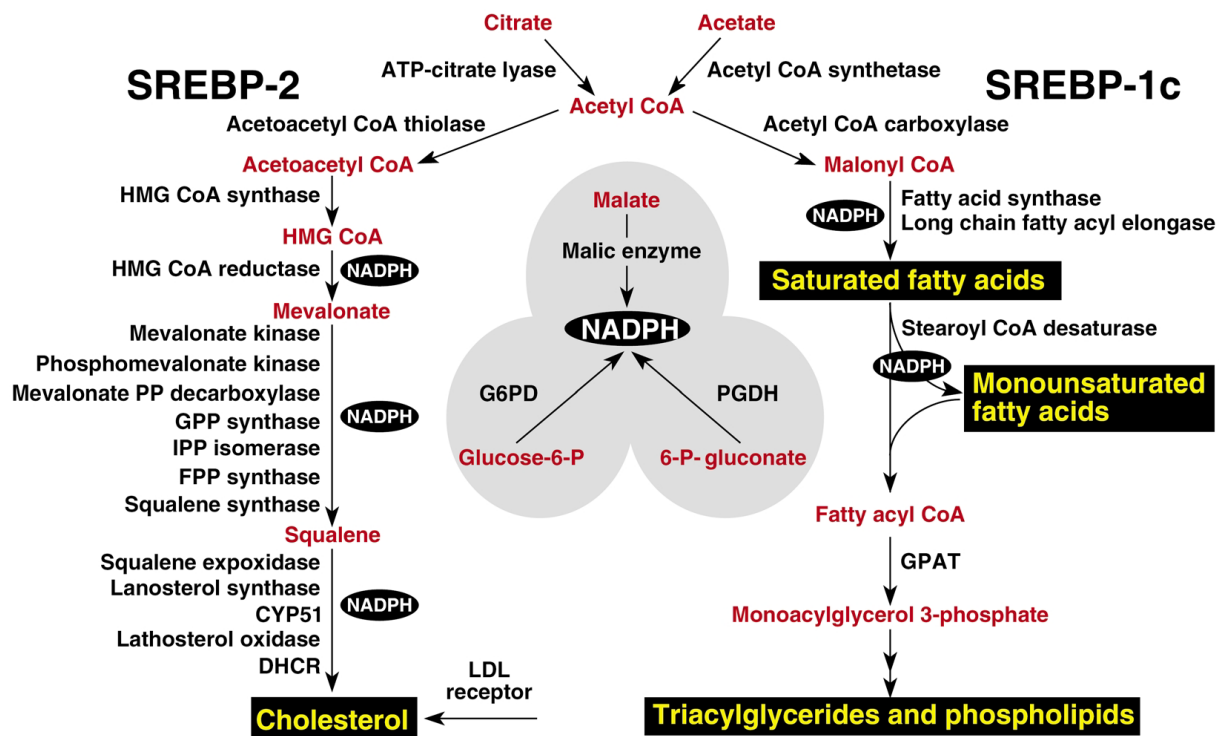


Figure 27: Role of SREBP2 and SREBP1c in cholesterol synthesis and lipogenesis respectively. The common precursor for both cholesterol synthesis and lipogenesis is Acetyl-CoA derived from byproducts of the TCA cycle in mitochondria. The conversion of Acetyl CoA to Acetoacetyl CoA by thiolase directs the former towards Cholesterol synthesis. Acetyl CoA and Acetoacetyl CoA together give rise to HMG CoA, which then undergoes a series of tedious reduction reactions to produce cholesterol. Enzymes such as HMG CoA reductase (HMGCR) and Squalene Synthase (SQS), for example, are under direct transcriptional control of SREBP2. On the other hand, the conversion of Acetyl CoA to Malonyl CoA by Acetyl CoA Carboxylase (ACC) directs the former towards lipogenesis. Malonyl CoA then undergoes a series of reduction reactions to produce fatty acids and triglycerides. Enzymes such as Fatty acid synthase (FASN) and Stearoyl CoA Reductase (SCD) for example, are under direct transcriptional control of SREBP1c. Both these molecular processes require H^+ atoms for the reduction reactions from NADPH which is derived from the pentose phosphate pathway (briefly represented in the center) Source : (Horton et al., 2002)

Role of LXRs in cholesterol homeostasis and lipogenesis

As explained earlier, LXRs are ligand activated Nuclear Receptors and they bind to oxidized cholesterol derivatives or oxysterols, which act as their natural ligands. Different oxysterols are produced from Cholesterols by enzymatic processes or by spontaneous oxidation due to the presence of Reactive Oxygen Species (ROS). The following schematic briefly describes the different oxysterols that are produced through enzymatic and non-enzymatic biochemical mechanisms (Figure 28).

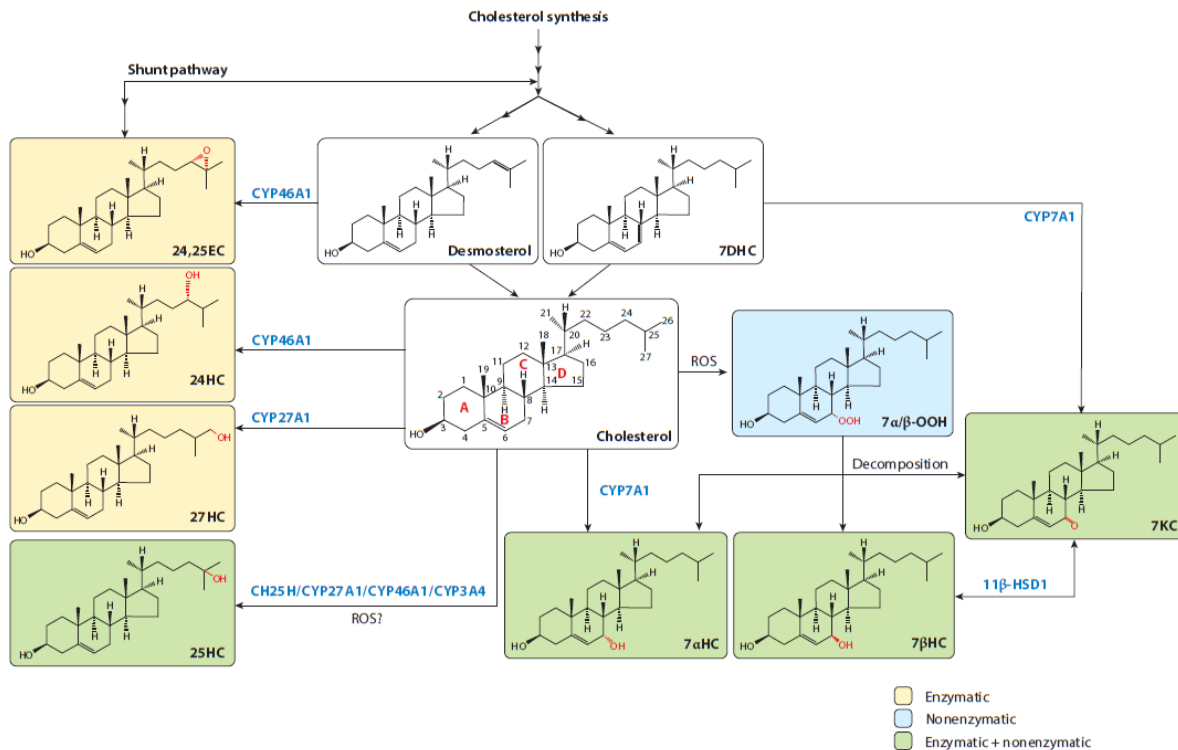


Figure 28: Production of different oxysterols by enzymatic oxidation (through Cytochrome P450 Monoxygenases – Cyp) and non-enzymatic oxidation (ROS and decomposition).

Among these different oxysterol species that are produced, we have previously identified 3 LXR ligands that are expressed in the Peripheral Nervous System. These include 24(S) Hydroxycholesterol, 25-Hydroxycholesterol and 27-Hydroxycholesterol (Makoukji et al., 2011). Although, we also corroborated our findings in a mouse Schwann cell line MSC80, our results are yet to be verified in primary Schwann cells. Nevertheless, though the oxysterol assay was performed using Sciatic Nerve lysates, it is quite probable that these oxysterols potentiate lipogenesis and cholesterol homeostasis in the Schwann cells as they constitute a major proportion of cells in the sciatic nerves.

LXRs are directly implicated in lipogenesis as they regulate the expression of SREBP1c in different cell types (Repa et al., 2000; Rong et al., 2017) and our results on primary Schwann cells also show that LXRβ is the functional isoform that regulates the expression of Srebp1c (refer to Supplementary Results 4.1). However, the natural ligand that potentiates SREBP1c expression in Schwann cells remains to be identified.

On the other hand, much like any other cell type, Schwann cells express SREBP2 to regulate cholesterol synthesis (LeBlanc et al., 2005; Camargo et al., 2009). Cholesterol homeostasis in cells is achieved by a concerted action of LXR target genes and a feedback inhibition loop of Cholesterol synthesis under high sterol conditions. Under physiological conditions, Cholesterol is either synthesized by the canonical SREBP2 pathway or imported into the cells as Cholesterol molecules packaged in Lipoproteins by LDLR. Interestingly, LDLR is also an SREBP2 target gene. Thus, SREBP2 can promote cholesterol synthesis as well as uptake. However, under high sterol conditions, cholesterols naturally give rise to oxysterols as explained earlier or they are converted to Cholesteryl Esters by Acyl-CoA Cholesterol Acyl Transferase (ACAT) or Lecithin Cholesterol Acyl Transferase (LCAT) and stocked in Lipoproteins. Oxysterols activate LXR thus resulting in the expression of target genes such as ABCA1, ApoE and IDOL (Inducible Degradator of LDLR). Among these, ABCA1 and ApoE are membrane bound active transporters of lipoproteins containing cholesterol. IDOL is an E3 ubiquitin ligase that selectively ubiquitinates LDLR and promotes the degradation of the latter. Thus, LXR mediates cholesterol efflux by transporting existing cholesterol out of the cell and at the same time preventing the import of Cholesterol via LDLR. Additionally, oxysterols also inhibit SREBP2 by either binding and retaining the protein in the ER or by inhibiting the activity of key cholesterol biosynthetic enzymes such as HMGCR and SQS. All the genes and pathways mentioned herein have been verified in Schwann cells in physiological as well as pathological contexts (Cermenati et al., 2010, 2012, 2013; Sundaram et al., 2019a; Zhou et al., 2019). Thus, given the current literature on Schwann cells, SREBPs and LXRs, I postulate the following schematic to describe cholesterol homeostasis and lipogenesis in Schwann cells (Figure 29).

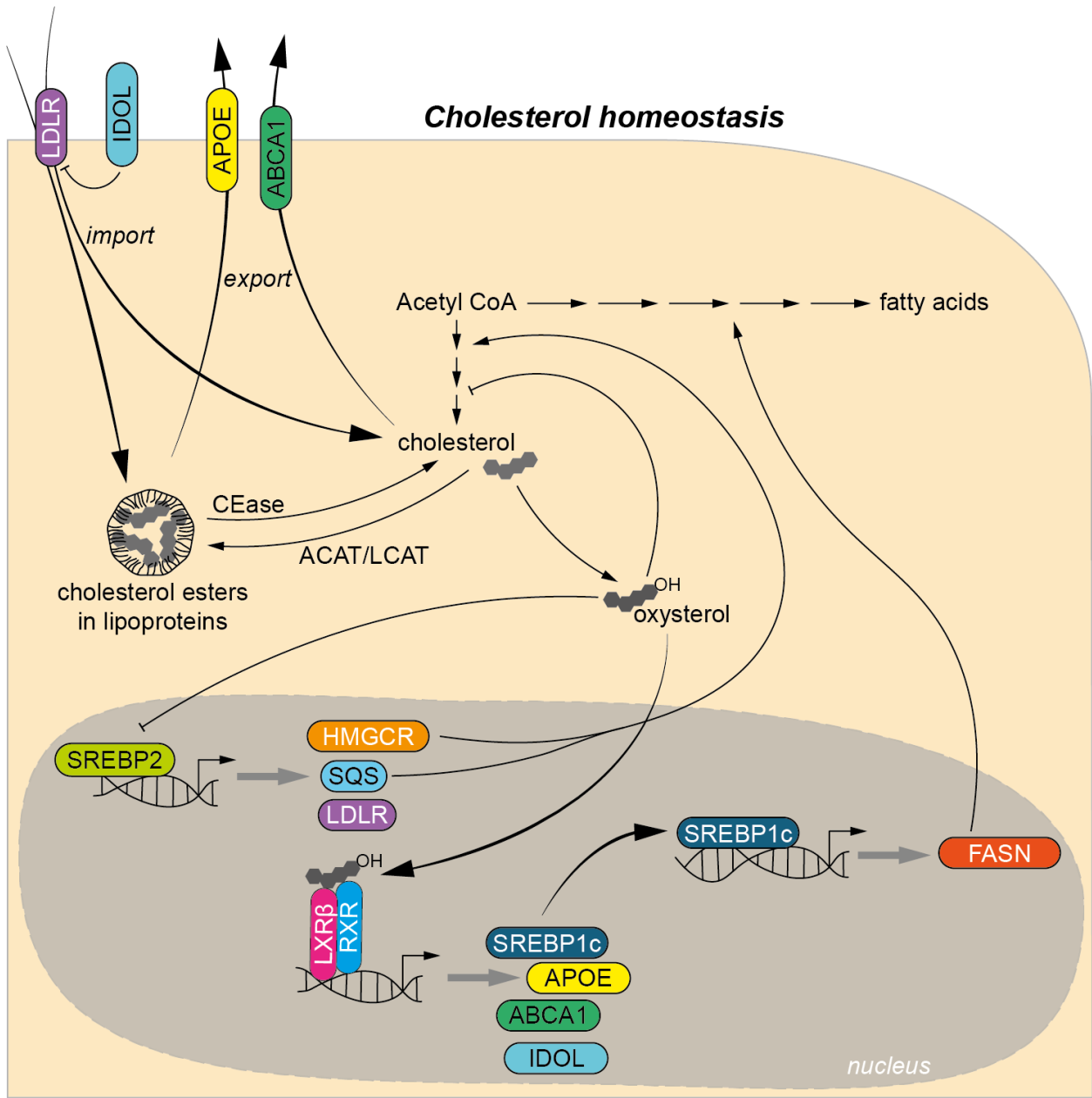


Figure 29. Cholesterol homeostasis in Schwann cells. SREBP2 controls the expression of cholesterol biosynthetic genes such as HMGCR and SQS as well as cholesterol uptake genes such as LDLR. Cholesterols are either converted to oxysterols or converted to cholesteryl esters and stocked in lipoproteins. Oxysterols potentiate LXR activation to stimulate fatty acid synthesis through SREBP1c on the one hand and cholesterol efflux on the other. LXR target genes such as ABCA1 and ApoE aid in cholesterol efflux by active transport across the plasma membrane. IDOL block cholesterol import by ubiquitinating LDLR and thus degrading it.

Sterol Intermediates as LXR ligands

Apart from the conventional oxysterols, certain cholesterol intermediates are known to bind to LXR to potentiate cholesterol efflux (Yang et al., 2006). Of note, desmosterol and zymosterol have been known to bind LXRs in different cells and cell lines. Although, the end result of these interactions is always cholesterol efflux, it is interesting to note that sterol intermediates can indeed bind LXRs. Recently, it was shown that the LXR/SREBP axis can also be stimulated by desmosterol (Magida and Evans, 2018; Muse et al., 2018).

Similarly, catabolic products of another sterol intermediate 7-Dehydrocholesterol (7-DHC) was shown to bind LXRs and partially stimulate cholesterol efflux but inhibit lipogenesis (Endo-Umeda et al., 2014). These observations gives rise to the possibility that tissue specific sterol intermediates can indeed bind to LXRs and thus regulate cholesterol efflux and lipogenesis. Therefore, it is quite probable that certain unconventional LXR ligands exists in Schwann cell and further studies are warranted.

1.2.3 Role of LXRs in the Physiology of the PNS and Related Pathologies

My host laboratory is particularly interested in the implications of LXRs in the myelination of the PNS and CNS. In this regard, they have performed numerous studies trying to elucidate the role of this receptor in the process of myelination (Makoukji et al., 2011; Shackleford et al., 2013; Meffre et al., 2015; Hichor et al., 2018). My doctoral thesis was focused on the elucidation of the role of LXRs in PNS myelination.

In this section, I have detailed the existing literature on LXRs and their implications in PNS physiology and related pathologies. We have recently published a review article that elucidates the role of the nuclear receptor systematically both in sensory neurons as well as Schwann cells. (Sundaram et al., 2019a). Additionally, we have also briefly gleaned into the future avenues of research on all cell types including endoneurial and perineurial cells, which are not rigorously researched even by the glial community. This review of literature has indeed given rise to a lot of scientific questions that I have tried to answer in my doctoral thesis.



Review

Liver X Receptors and Their Implications in the Physiology and Pathology of the Peripheral Nervous System

Venkat Krishnan Sundaram, Charbel Massaad and Julien Grenier *

Faculty of Basic and Biomedical Sciences, Paris Descartes University, INSERM UMRS 1124, 75006 Paris, France

* Correspondence: julien.grenier@parisdescartes.fr; Tel.: +33-1-4286-3887

Received: 25 July 2019; Accepted: 19 August 2019; Published: 27 August 2019



Abstract: Recent research in the last decade has sought to explore the role and therapeutic potential of Liver X Receptors (LXRs) in the physiology and pathologies of the Peripheral Nervous System. LXRs have been shown to be important in maintaining the redox homeostasis in peripheral nerves for proper myelination, and they regulate ER stress in sensory neurons. Furthermore, LXR stimulation has a positive impact on abrogating the effects of diabetic peripheral neuropathy and obesity-induced allodynia in the Peripheral Nervous System (PNS). This review details these findings and addresses certain important questions that are yet to be answered. The potential roles of LXRs in different cells of the PNS are speculated based on existing knowledge. The review also aims to provide important perspectives for further research in elucidating the role of LXRs and assessing the potential of LXR based therapies to combat pathologies of the Peripheral Nervous System.

Keywords: LXR; oxysterol; cholesterol; peripheral nervous system; myelin; schwann cell

1. Introduction

Liver X Receptors (LXRs) are ligand-activated transcription factors that exist in 2 isoforms: LXR α and LXR β encoded in mice by the genes *Nr1h3* and *Nr1h2*, respectively. Although classified as orphan receptors upon discovery, oxidized cholesterol derivatives (oxysterols) such as 20(S)-, 22(R)-, 24(S)-, 25- and 27-hydroxy cholesterol (HC) and 24(S), 25-epoxycholesterols were later found to be their natural ligands [1–5]. Further research in endocrinology over the past two decades has resulted in the identification of many natural and synthetic agonists and antagonists of LXRs with claimed specificities to each of the two isoforms [5].

LXRs have been implicated in several physiological processes such as lipid metabolism and homeostasis, inflammation and cholesterol homeostasis, as well as a plethora of diseases such as Multiple sclerosis, Alzheimer's, Arthritis, and cancers [6–10]. Similarly, the implications of oxysterols are also equally diversified both in physiological and pathological contexts [11].

The implications of LXRs in both the physiology and pathology of the Central Nervous System (CNS) have been extensively studied and reported over the last few years. Seminal and extensive reviews have diligently detailed almost every aspect of LXRs' function in the brain from development to diseases [12–14]. The implication of LXRs in the Peripheral Nervous System (PNS) is a relatively nascent theme of research that is garnering much attention only in the past decade. This review, therefore, aims to assimilate the existing knowledge and also provide certain perspectives on further exploring the role of LXRs in the PNS.

A holistic understanding—of the implications of LXRs and their natural ligands—elicits a clear division of the different components of the PNS. Each specific cell type of the PNS functions differently at a molecular level; making the fatty acids, and cholesterol metabolism in the spinal nerves can require

highly diverse and cell-type-specific actions. Broadly, the PNS can be classified into the following cellular subtypes: Schwann cells, endoneurial cells, perineurial cells, sensory neurons (and their axons originating at the spinal ganglia) [15] (Figure 1).

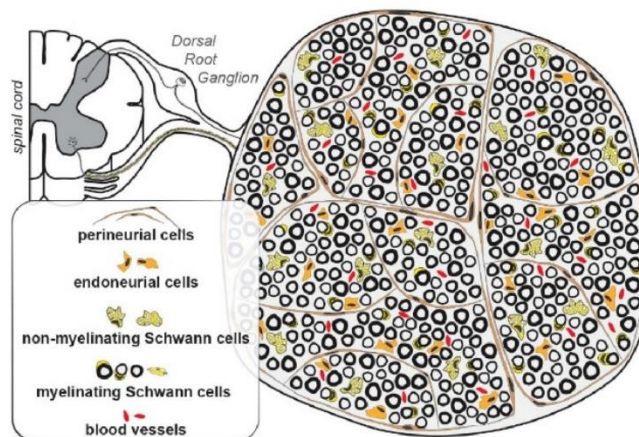


Figure 1. Peripheral nerve cellular structure. Sensory neurons emanating from the dorsal part of the spinal cord with their somata in dorsal root ganglia project their axons towards the spinal cord on the one hand and their peripheral endpoints on the other. Some of these sensory axons are myelinated by Schwann cells, and others are ensheathed by non-myelinating Schwann cells in specific structures called “Remak bundles”. Motor axons emanating from the ventral roots of the spinal cord are wrapped by myelinating Schwann cells. Perineurial cells surround multiple axons and Schwann cells to delineate fascicles. They provide mechanical and structural integrity to these fascicles. Endoneurial cells are dispersed inside the fascicles. They provide major components of the extracellular matrix, perform immune-surveillance, and are implicated in remyelination. The vasculature is composed of endothelial cells surrounded by pericytes that provide the nerve-blood barrier.

The somata of the motor neurons are located in the spinal cord, and only their axons form a part of the PNS. Hence, lipid and cholesterol metabolism, and possible implications of LXRs in motor neuron physiology and associated diseases falls beyond the ambit of this review but have been reviewed elsewhere [16–18]. In the following sections, a survey of literature pertaining to different PNS cell types is detailed along with interesting, yet unanswered, questions, and possible future avenues of research.

2. Schwann Cells

Schwann cells constitute a major portion of the spinal nerves and are by far the most extensively studied glial cells of the peripheral nervous system. They are directly responsible for the production of the myelin sheath around peripheral axons [19]. The composition of myelin and the underlying biochemical and molecular mechanisms of myelination also contribute to a particular interest in studying Schwann cells. So far, the implication of LXRs and oxysterols in Schwann cell physiology has been studied using LXR null mice ($LX\alpha/\beta^{-/-}$ hereafter referred to as LXR double KO or LXRdKO) [20–22].

The first study exploring oxysterol/LXR signaling in Schwann cells revealed that 3 oxysterols well known to be LXR ligands (namely 24(S)-, 25-, and 27-HC) and their corresponding biosynthetic enzymes are present in adult mouse sciatic nerves as well as in a mouse Schwann cell line (MSC80) [20]. Treatment of MSC80 cells with a high concentration of 25-HC or the synthetic LXR ligand T0901317 drastically reduces the expression of two major peripheral myelin genes, myelin protein zero (*Mpz*) and peripheral myelin protein 22 (*Pmp22*), observed through a promoter transactivation assay using constructs of both the myelin genes. Interestingly, *in silico* analysis revealed putative LXR response element (LXRE) sites upstream of these genes, and ChIP analyses confirmed that the stimulation of LXRs increased its occupancy at these sites. Moreover, LXR activation also downregulates key

components of the Wnt/ β Catenin pathway, an important driver of myelination and remyelination of peripheral nerves [23,24].

However, the observations in the sciatic nerve of LXRdKO animals were interestingly different. Firstly, the transcripts of *Mpz* and *Pmp22* were upregulated complementing the results observed in MSC80. However, their protein levels were significantly lower. Moreover, the animals displayed compact but thinner myelin sheaths, possibly due to a reduction of the myelin proteins that help in maintaining the structural integrity of the sheath [25]. This issue opened up the possibility of a secondary indirect mechanism in vivo that resulted in the reduced protein expression of these myelin genes. Upon further inspection, it was found that the systemic ablation of LXRs results in a highly oxidative environment in the sciatic nerve [22]. Indeed, despite a heightened response to oxidative stress through the Nrf2 pathway, anion superoxide production, protein carbonylation, and lipid peroxidation were elevated in the sciatic nerves of LXRdKO animals. Interestingly, younger LXRdKO mice at postnatal day 21 (P21) were not affected, suggesting that the effects of the oxidative insults set in after developmental myelination is almost complete. It was thus hypothesized that in the absence of LXRs, this oxidative stress hampered the processing and the turnover of myelin proteins, especially PMP22 which is known to form dimers due to oxidative damage [26]. This phenomenon possibly leads to progressive hypomyelination during adulthood. The oxidative insults in vivo were abrogated when the mice were treated with N-AcetylCysteine (a potent reactive oxygen species scavenger) between the ages of P21 and 8 weeks. The treated mice exhibited restored protein levels of MPZ and PMP22 coupled with improvements in the thickness of the myelin sheaths and in electrophysiology. Furthermore, LXR stimulation in MSC80 Schwann cells using T0901317 was shown to ramp up the antioxidant response, thereby aiding them in surviving impending oxidative stress induced by a high dose of Tert-butyl Hydroperoxide. These results taken together suggest that LXRs negatively regulate myelin gene expression in peripheral nerves by opposing the driving effect of the Wnt/ β -Catenin pathway. They also aid in maintaining the redox homeostasis in this tissue by stimulating antioxidant cellular responses.

A very recent study, using two different knockout mice models, *PMP22*^{-/-} and ATP Binding Cassette Transporter A1 (*ABCA1*)^{-/-}, demonstrates a direct link between PMP22 and LXR target genes such as ATP Binding Cassette Transporter A1 (*ABCA1*) and Apolipoprotein E (*ApoE*) [27]. Increased accumulation of cholesterol at the perinuclear region of primary *PMP22*^{-/-} mutant Schwann cells was observed in culture along with an accumulation of lipid droplets and vesicles in mutant nerves. These observations were corroborated with a downregulation of certain genes implicated in the Sterol Regulatory Element Binding Protein (SREBP) pathway, notably Fatty Acid Synthase (*FASN*), HMG CoA reductase (*HMGCR*), and Low-Density Lipoprotein Receptor (*LDLR*), possibly because of a cellular response to halt lipogenesis and cholesterol synthesis following their accumulation. Targets of LXR such as *ABCA1* and *ApoE* are possibly upregulated due to the accumulation of cholesterol as these genes are directly responsible for cholesterol efflux from the cell. However, the authors state that they do not see any modulation of LXRs in this phenomenon. The downregulation of the SREBP1c pathway, together with an upregulation of cholesterol efflux genes without any changes to LXR levels, presents a paradoxical situation as both these pathways are positively regulated by LXRs. The *ABCA1*^{-/-} model, on the other hand, has a converse effect with respect to PMP22. While the accumulation of lipid droplets in these mutant nerves comes as no surprise, the authors also show an increase in PMP22 protein levels coupled with improper processing of de novo PMP22 synthesis. Intriguingly, this is in stark contrast to what is observed in an LXR deficient system where the protein levels of PMP22 are downregulated [20,22]. Furthermore, both in primary Schwann cells and nerves, the authors demonstrate that *ABCA1* and PMP22 proteins colocalize and can interact either directly or indirectly in a cholesterol dependent manner, without necessarily implicating LXRs.

In a pathological context, LXR activation has proven to be beneficial as a therapeutic approach to alleviate structural and neurophysiological anomalies of Diabetic Peripheral Neuropathy (DPN) using two distinct pathways [28,29]. In a model of streptozotocin (STZ) induced diabetes, Cermenati

and colleagues first showed that STZ treatment changes the lipid composition of the myelin sheath, with notable differences in phospholipids, fatty acids, and myelin cholesterol [29]. These differences were reversed to control levels upon the treatment of STZ treated rats with a synthetic LXR agonist, GW3965. The authors further describe that the SREBP pathway, which controls lipid biosynthesis, is downregulated in STZ treated animals. SREBP1c (encoded by *Srebf1*) is a transcription factor that is located in the Endoplasmic Reticulum (ER) and shuttles to the nucleus upon activation (referred to as the active form). In STZ treated animals, ER retention was higher, and, upon LXR activation, there was an increase in nuclear translocation, thus resulting in the transcription of lipogenic genes and enzymes. They also show evidence of a restoration in MPZ protein levels, which was previously downregulated due to STZ treatment. This rescue at the molecular level also improves the myelin ultrastructure in the nerve. In another study, the authors also provide evidence of an increase in neurosteroid synthesis upon LXR activation [28]. Neurosteroids have long been known to exert a protective effect and alleviate insults that result from peripheral neuropathy [30–32]. In their study, Cermenati and colleagues showed that STZ induced diabetes is accompanied by a reduction in neurosteroid levels in the nerves that are concomitant with a reduction in the transcript levels of key proteins that regulate steroidogenesis from cholesterol. Notably, they show that the Steroidogenic Acute Regulatory protein (StAR), which transports cholesterol to the mitochondria for steroidogenesis, is directly controlled by LXRs. Additionally, LXR activation increases transcript levels of cytochrome P450 side-chain cleavage (P450scc) and 5 α -reductase, which regulate neurosteroid synthesis. The overall effect of LXR activation resulted in a decrease in diabetic neuropathic insults at the molecular, structural, and functional levels through upregulation of protective neurosteroidogenesis. Figure 2 recapitulates the different physiological and pathological pathways implicating LXRs in Schwann cells.

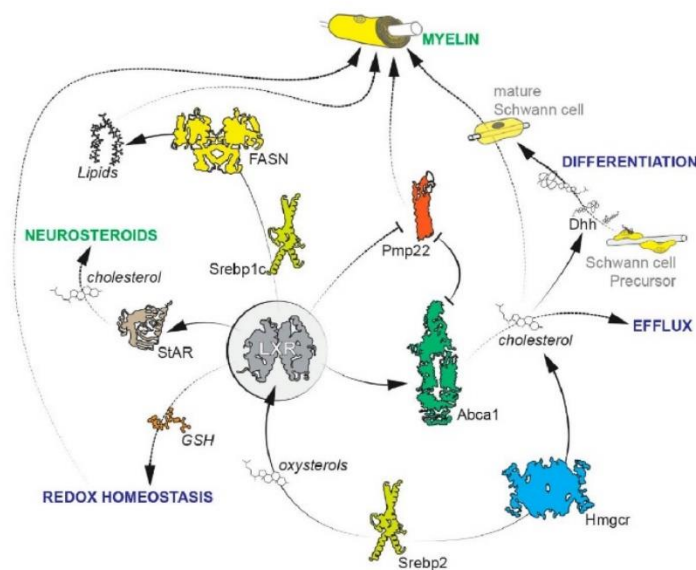


Figure 2. Implication of Liver X Receptors (LXRs) in several cellular pathways of Schwann cell physiology and pathology. LXRs interact with various molecular pathways that directly or indirectly impact (re)myelination. They are direct drivers of myelin gene expression (PMP22) and modulate redox homeostasis through intracellular Glutathione (GSH) levels to maintain myelin integrity. LXRs are also linked to lipid and cholesterol metabolism through the SREBP pathway. They directly regulate lipogenesis through Srebp1c and are in turn regulated by Srebp2 that is known to produce oxysterol LXR ligands to promote cholesterol efflux. Moreover, LXRs regulate neurosteroidogenesis through StAR to protect the nerve against diabetic insults. It is also possible that LXRs participate in Schwann cell development by modulating cholesterol levels in Schwann cell precursors during the processing and secretion of Dhh (refer to the “Perineurial cells” section).

Future Avenues of Research on Schwann Cells

The physiological understanding of the role of LXRs in Schwann cell biology stems from animal models where both the isoforms of LXR are deleted systemically. Although studies point to the possible role of Schwann cells in the resulting phenotype, one cannot negate the impact and the contribution of other systems on the observed phenotype. A thorough understanding of the role of LXRs can be achieved using a Schwann cell-specific knock out. To date, only a few mutant models have targeted cholesterol and fatty acid metabolism in Schwann cells [33–35]. These studies have targeted crucial genes such as Sterol regulatory element-binding protein cleavage (SCAP), Fatty Acid Synthase (FASN), and Squalene Synthase (SQS) in Schwann cells, and all these mouse models develop neuropathy. Nevertheless, these targeted mutations are downstream of the LXR pathway. Although it provides us with a glimpse of what we can expect in an LXR deficient Schwann cell, a Schwann cell-specific knockout of LXRs can possibly result in a similar phenotype or a much severe one given the myriad number of interactions that LXR exhibits with other important metabolic pathways described in previous studies.

Moreover, Schwann cell pathologies open up multiple avenues of research using LXRs. The intricate association between PMP22, LXRs, lipids, and cholesterol explained herein offer unexplored possibilities of using the LXR pathway therapeutically in the treatment of Charcot-Marie-Tooth 1A (CMT1A). CMT1A in humans is characterized by a duplication of Chromosome 17p12 (c17p12), which is a large segment of DNA that encodes the PMP22 protein [36,37]. This results in higher expression levels of PMP22 and compromises the structural and functional integrity of the myelin sheath around peripheral axons. Recently, Fledrich and colleagues have shown that in rodent models of CMT1A, there is a systematic downregulation of lipogenic genes in the nerves [38]. It is interesting to note that PMP22^{-/-} animals exhibit the exact opposite phenotype with accumulation of lipids and cholesterol in Schwann cells [27]. In the CMT1A model, administration of phospholipids improved myelin ultrastructure, electrophysiology, and muscle strength of affected animals. As discussed previously, LXR activation using GW3965 resulted in an overall increase in the expression of lipogenic enzymes altered during STZ induced diabetic peripheral neuropathy [29]. A similar strategy may also prove to be beneficial in CMT1A, given the similarity of the molecular phenotype observed.

Another Schwann cell pathology that is of particular interest to the glial research community is Malignant Peripheral Nerve Sheath Tumor (MPNST), a malignant form of Neurofibromatosis Type 1 (NF1) resulting from a loss of function mutation in the Neurofibromin 1 gene [39,40]. MPNST arise from benign tumors of Schwann cell origin called plexiform neurofibromas in approximately 10% of all afflicted patients [39]. MPNSTs have been characterized with an altered lipid metabolism resulting from increased fatty acid synthesis and fatty acid oxidation—so much, so that fatty acid synthase (FASN) has been suggested to be a targetable metabolic oncogene [41]. Another approach that has rendered positive results is the inhibition of the mTORC pathway [42,43]. From a reductionist perspective, these two strategies seem like two sides of the same coin as mTORC1 is classically known to activate the SREBP pathway that ultimately controls lipogenesis [44,45]. LXRs have also been known to regulate lipogenesis through SREBP1c directly [46–48]. To date, no data exist on the expression levels of LXRs and their lipogenic role, if any, in NF1 tumors, including MPNST. However, inhibition of the LXR pathway to inhibit lipogenesis remains to be explored as a possible therapeutic approach for combating MPNST.

3. Sensory Neurons in the Ganglia

The implications of LXRs in the pathophysiology of sensory neurons has recently been elucidated in two interesting studies [49,50]. In one study conducted on the dorsal root ganglia (DRG), the authors show that LXRs protect Sodium channel 10 alpha subunit (Nav1.8 also called SCN10A) expressing sensory neurons from ER stress and also from mechanical allodynia induced by diet-related obesity [50]. The authors adopt two approaches to demonstrate the same. They first show that western diet fed mice are susceptible to ER stress in the DRG because of increased expression of ER stress markers

C/EBP homologous protein (CHOP), activating transcription factor 4 (ATF4), and the spliced variant of X-box binding protein-1 (sXBP1). Activation of LXRs by the administration of GW3965 to western diet fed mice significantly lowered the expression of these genes along with a concomitant increase in LXR target genes, ABCA1 and ApoE, in the DRG. The activation also proved to be helpful in delaying the onset of induced allodynia. They also observed that saturated fatty acids, such as Palmitate, have the potential to induce ER stress in ex vivo DRG cultures. LXR activation proves to be equally helpful in reducing ER stress in ex vivo cultures. Secondly, and more importantly, the authors adopt cell-specific approaches to show that the absence of LXR α and LXR β in Nav1.8 expressing sensory neurons increases allodynia and thermal sensitivity in these mutants and results in ER stress in DRG both in vivo and ex vivo. These results suggest that the phenotype is indeed driven by LXRs, specifically in Nav1.8 expressing sensory neurons in the DRG.

The second study was conducted in the nodose ganglia of the vagus nerve using the same cell-specific Nav1.8 Recombinase driver to ablate both LXRs. Nav1.8 sensory neurons are also situated in the nodose ganglia [50]. This study is very intriguing because it shows that a cell-specific ablation results in a whole-body phenotype. The authors first confirmed that the mutation has the desired downregulatory effect on LXR target genes *Abca1* and *Srebp1c* in the nodose ganglia. Secondly, when these mutant mice were fed a western diet, they accumulated more cholesterol in the ganglia. However, they did not seem to gain more weight after western diet when compared to controls. This was coupled with lesser body fat accumulation and no difference in lean mass. Upon further inspection, it was revealed that mitochondrial metabolism was upregulated in the brown adipose tissue due to an upregulation of genes such as Uncoupling protein 1 (*Ucp1*) and peroxisome proliferator-activated receptor gamma coactivator 1-alpha (*Pgc1 α*) both at the transcript and protein levels. Additionally, mitochondrial oxidative respiration was also activated in the skeletal muscle. Thus, the authors postulated that the two observations correlate with the observed lack of weight gain in these mutants. Finally, the authors also observed a downregulation in γ synuclein (*Syng*) in the nodose ganglia, a protein that is known to regulate synaptic trafficking and the formation of lipid droplets. They remarked this down-regulation, and the observed phenotype concurs with the total *Syng*^{-/-} mouse model and that the obesity-resistant phenotype is also observed in the LXRdKO mice. The study concluded that regulation of cholesterol and lipid metabolism can have post-synaptic effects in other tissues through yet undiscovered mechanisms.

Future Avenues of Research on Sensory Neurons

Both these studies have been conducted in mice with cell-specific ablation of both LXR α and LXR β . However, the first study does state that the expression levels of both these isoforms are not equal in the ganglia [49]. LXR β expression is classified as “high” and that of LXR α is classified as “moderate”, and the relative difference is not mentioned. Nevertheless, it would be interesting to study which of these isoforms is implicated more in the phenomenon observed. This line of thought is motivated by two key observations. In the CNS, LXR β ^{-/-} mice tend to show more pertinent phenotypes than LXR α ^{-/-} mice, possibly because of the distribution of their expression in different regions [10]. Secondly, our personal observations in the sciatic nerves, Schwann cell-line MSC80, and primary mouse Schwann cells show that the β isoform is expressed much more the α counterpart. Therefore, it is quite possible the LXR β is indeed more important in the physiology of both the CNS and PNS. This hypothesis, however, remains to be verified rigorously.

4. Endoneurial Cells

Endoneurial cells (or endoneurial fibroblast-like cells of peripheral nerves) are multifaceted glial cells which are implicated in various functions such as endoneurial structural integrity, myelin clearance after nerve injury, as well as in mediating immune responses in the peripheral nerves [51,52]. The origin of these cells was highly debated until critical observations were put forth to confirm their neural crest origin, much like Schwann cell precursors [15,53]. Although they have been well

characterized with cell-specific markers in the recent years, the LXR/lipids/cholesterol axis in these cells has not been studied so far, even though these cells are indeed strong candidates.

Firstly, endoneurial cells have been directly implicated in the clearance of myelin debris through phagocytosis [54–56]. The capacity to ingest and clear myelin debris suggests that these cells should have highly functional lipid and cholesterol regulatory mechanisms, especially during nerve regeneration after injury. The role of LXRs, if any, in these mechanisms is yet to be elucidated (Figure 3).

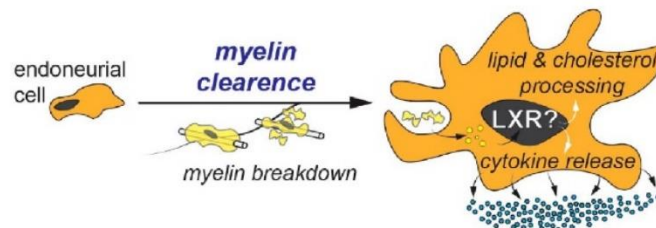


Figure 3. Role of Endoneurial cells in myelin clearance after injury. In response to myelin breakdown, endoneurial cells digest myelin debris through phagocytosis and release cytokines to create a proinflammatory environment. Given the capacity of LXRs to regulate lipid/cholesterol metabolism and immune responses, LXR signaling might play an important role in the physiology of these cells.

Secondly, endoneurial cells are also known to be the first immune responders during nerve injury and participate in creating a proinflammatory environment that favors myelin clearance and axonal regeneration [51]. Consequently, they are sometimes referred to as the “resident macrophages of the peripheral nerve” [57]. Hence, it is quite possible that immune responses mediated by these cells are also regulated by LXRs, given the latter’s implications in inflammation and immunity [8,58].

5. Perineurial Cells

Perineurial cells are cells that align the perineurium of the spinal nerves. They were previously thought to have mesenchymal origins and, hence, were called perineurial fibroblasts [59]. However, recent work from Kucenas and colleagues have reclassified them as perineurial cells originating at the Motor Exit Points (MEP) of the spinal cord [60]. Indeed, MEP glial cells are now studied as a separate family of PNS glial cells originating in the CNS [61,62]. These cells were previously shown to be the target cells of the Desert Hedgehog (Dhh) ligand secreted by Schwann cells during peripheral nerve development [63,64]. Indeed, improper Dhh signaling results in the invasion of the endoneurial space by perineurial cells forming mini-fascicles around groups of myelinated axons.

Interestingly, hedgehog signaling is intrinsically linked to cholesterol, both in the cells that secrete the protein as well as the ones receiving it [65]. In the secreting cell (Schwann cell), the Dhh protein is first cleaved, and a cholesterol moiety is attached to its C terminal. This modification helps in the transport of the protein from the cytosol to the plasma membrane where it is retained before being shunted out of the cell. In the target cell (Perineurial Cells for example), Dhh binds to its receptor Patched1 (PTCH) and releases that latter’s inhibition of Smoothed (SMO), thus activating the downstream signaling cascade of *Dhh* in target cells. The activation of SMO, however, requires the presence of endogenous cholesterol or oxysterols, some of which are potent ligands of LXR [66,67]. Therefore, it is quite probable that perineurial cells also regulate endogenous cholesterol and oxysterols through LXRs and their target genes (Figure 4). Thus, two fundamental questions remain to be answered. Do LXRs modulate cholesterol/oxysterols levels to be permissive for Dhh signaling both from the secreting cell and the target cell? Does Dhh signaling in the nerve occur simultaneously with LXR stimulation to mediate the interaction between Schwann cells and Perineurial cells during development?

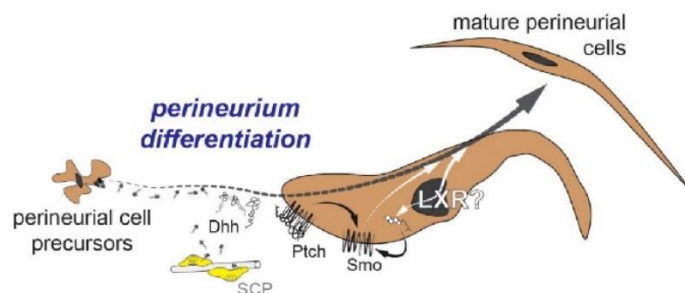


Figure 4. Development of perineurial cells and Desert Hedgehog (Dhh) signaling. Dhh, secreted by Schwann Cell Precursors (SCP), interacts with the Patched (PTCH) receptor at the surface of the perineurial cell precursors. It allows Smoothed (SMO) to be activated to trigger a differentiation program. To be functional, SMO also requires the presence of endogenous cholesterol and oxysterol molecules that are also potent LXR ligands. Therefore, a functional dialogue between these two signaling pathways can be speculated.

6. Discussion

The review so far has considered the implications of LXRs in the physiology and pathology of the Peripheral Nervous System along with associated research questions that are yet to be answered. Cholesterol and lipid metabolism are fundamental biochemical processes that are essentially involved in most cell types of the body. Indeed, the different cells of the PNS utilize these metabolic processes, possibly by the same means, although for different ends. LXRs find themselves at the nexus of these two metabolic processes and, hence, understanding their physiological role in its entirety is crucial for formulating both cellular and generic therapeutic approaches. For instance, stimulating LXRs may render the desired effect of cholesterol efflux through ABCA1 and ApoE, but would also result in increasing lipogenesis through the SREBP pathway if the system permits both. This is one of the main reasons why administering LXR agonists as such as T0901317 or GW3965 for therapy might have the desired effects on the system being studied, but also promote dyslipidemia in the liver and reverse cholesterol transport systemically. Similarly, antagonizing or inhibiting LXRs could result in cholesterol accumulation and would concomitantly decrease lipogenesis in any system.

Certain plausible solutions can be envisaged to tackle this conundrum and to make LXR based therapies more tenable. Fundamental research on identifying which isoform of LXR is necessary and sufficient for a physiological function provides a better framework for designing therapies using isoform-specific agonists or antagonists. For example, in the CNS, LXR β is known to regulate Oligodendrocyte Precursor Cell (OPC) differentiation, prevent adult motor neuron degeneration, and promote ventral midbrain neurogenesis [68–70]. However, LXR α is important for maintaining the blood-brain barrier [71]. Incidentally, it has also been shown that certain LXR β agonists can have the desired effect on cholesterol metabolism without having unacceptable lipogenic effects on the liver [72]. This is mostly because LXR α , but not LXR β , is indispensable for fatty acid and lipogenesis in the liver [73,74]. Therefore, agonizing LXR β as a therapeutic approach is more promising in the context of CNS disorders. In the PNS, the role of the different LXR isoforms is poorly understood in different cells. However, it is quite probable that LXR β is the functionally predominant isoform in the PNS, especially in the context of myelination, given its expression pattern.

Another solution to make successful LXR based therapies is to identify function/cell-specific ligands without any prior knowledge of their specificity to different isoforms. This has been well elucidated in the case of macrophages where desmosterol has been shown to activate cholesterol efflux through LXR in these cells, but not induce lipogenesis in the hepatocytes [75,76]. Identification of such cell or tissue-specific agonists or antagonists in the PNS would be a breakthrough in combatting peripheral nerve disorders and pathologies.

With regard to human pathologies, stimulating LXRs seems to be a possible therapeutic approach for CMT1A. The objective of such an approach would be to counteract the phenotypic decrease in lipogenesis by stimulating the LXR/SREBP1c axis. For NF1 related MPNSTs, the potentiality of LXR based therapies can only be evaluated if the lipogenic role of the nuclear receptor is completely understood both in benign plexiform neurofibromas and MPNSTs. Nevertheless, as increased lipogenesis is a hallmark of MPNST, inhibiting LXRs can be envisaged as a plausible therapeutic approach.

In conclusion, further research in the PNS should be directed towards understanding the role of LXRs at a cellular level in different glial cells of the PNS. Moreover, the identification of the functional isoform in each cell type would provide additional information in our understanding of PNS physiology. Fundamental research is also required in identifying local, tissue-specific natural agonists or antagonists of LXR. These advances would permit us to assess the true potential and promise of LXR based therapies for different pathologies of the PNS.

Author Contributions: V.K.S. and J.G. conducted the literature survey for the review. V.K.S. prepared the outline and wrote the manuscript. C.M. proofread, edited and provided scientific inputs for the redaction. J.G. prepared the figures and revised the manuscript.

Funding: Our research on LXRs was funded by INSERM, CNRS, Paris Descartes University and ANR. The doctoral students who worked on LXRs received their fellowships and funding from the French Ministry of Research and Innovation.

Acknowledgments: We greatly acknowledge Mehdi Hichor, Amalia Trousson, Joelle Makoukji, Ghjuvan Ghjacumu Shackelford, Delphine Meffre, and other colleagues for their work on LXRs over the years.

Conflicts of Interest: The authors declare no conflict of interest.

References

1. Kainu, T.; Kononen, J.; Enmark, E.; Gustafsson, J.Å.; Peltö-Huikko, M. Localization and ontogeny of the orphan receptor OR-1 in the rat brain. *J. Mol. Neurosci.* **1996**, *7*, 29–39. [[CrossRef](#)]
2. Lehmann, J.M.; Kliewer, S.A.; Moore, L.B.; Smith-Oliver, T.A.; Oliver, B.B.; Su, J.L.; Sundseth, S.S.; Winegar, D.A.; Blanchard, D.E.; Spencer, T.A.; et al. Activation of the nuclear receptor LXR by oxysterols defines a new hormone response pathway. *J. Biol. Chem.* **1997**, *272*, 3137–3140. [[CrossRef](#)] [[PubMed](#)]
3. Janowski, B.A.; Willy, P.J.; Devi, T.R.; Falck, J.R.; Mangelsdorf, D.J. An oxysterol signalling pathway mediated by the nuclear receptor LXR α . *Nature* **1996**, *383*, 728–731. [[CrossRef](#)] [[PubMed](#)]
4. Janowski, B.A.; Grogan, M.J.; Jones, S.A.; Wisely, G.B.; Kliewer, S.A.; Corey, E.J.; Mangelsdorf, D.J. Structural requirements of ligands for the oxysterol liver X receptors LXR and LXR. *Proc. Natl. Acad. Sci. USA* **1999**, *96*, 266–271. [[CrossRef](#)] [[PubMed](#)]
5. Komati, R.; Spadoni, D.; Zheng, S.; Sridhar, J.; Riley, K.E.; Wang, G. Ligands of therapeutic utility for the liver X receptors. *Molecules* **2017**, *22*, 88. [[CrossRef](#)] [[PubMed](#)]
6. Wang, B.; Tontonoz, P. Liver X receptors in lipid signalling and membrane homeostasis. *Nat. Rev. Endocrinol.* **2018**. [[CrossRef](#)] [[PubMed](#)]
7. Jakobsson, T.; Treuter, E.; Gustafsson, J.Å.; Steffensen, K.R. Liver X receptor biology and pharmacology: New pathways, challenges and opportunities. *Trends Pharmacol. Sci.* **2012**, *33*, 394–404. [[CrossRef](#)] [[PubMed](#)]
8. Schulman, I.G. Liver X receptors link lipid metabolism and inflammation. *FEBS Lett.* **2017**, *591*, 2978–2991. [[CrossRef](#)] [[PubMed](#)]
9. Lin, C.Y.; Vedin, L.L.; Steffensen, K.R. The emerging roles of liver X receptors and their ligands in cancer. *Expert Opin. Ther. Targets* **2016**, *20*, 61–71. [[CrossRef](#)] [[PubMed](#)]
10. Gabbi, C.; Warner, M.; Gustafsson, J.Å. Minireview: Liver X receptor β : Emerging roles in physiology and diseases. *Mol. Endocrinol.* **2009**, *23*, 129–136. [[CrossRef](#)]
11. Luu, W.; Sharpe, L.J.; Capell-Hattam, I.; Gelissen, I.C.; Brown, A.J. Oxysterols: Old tale, new twists. *Ann. Rev. Pharmacol. Toxicol.* **2016**, *56*, 447–467. [[CrossRef](#)] [[PubMed](#)]
12. Courtney, R.; Landreth, G.E. LXR regulation of brain cholesterol: From development to disease. *Trends Endocrinol. Metab.* **2016**, *27*, 404–414. [[CrossRef](#)] [[PubMed](#)]

13. Wang, L.; Schuster, G.U.; Hultenby, K.; Zhang, Q.; Andersson, S.; Gustafsson, J.A. Liver X receptors in the central nervous system: from lipid homeostasis to neuronal degeneration. *Proc. Natl. Acad. Sci. USA* **2002**, *99*, 13878–13883. [[CrossRef](#)] [[PubMed](#)]
14. Cermenati, G.; Brioschi, E.; Abbiati, F.; Melcangi, R.C.; Caruso, D.; Mitro, N. Liver X receptors, nervous system, and lipid metabolism. *J. Endocrinol. Investig.* **2013**, *36*, 435–443. [[PubMed](#)]
15. Joseph, N.M.; Mukoyama, Y.; Mosher, J.T.; Jaegle, M.; Crone, S.A.; Dormand, E.-L.; Lee, K.F.; Meijer, D.; Anderson, D.J.; Morrison, S.J. Neural crest stem cells undergo multilineage differentiation in developing peripheral nerves to generate endoneurial fibroblasts in addition to Schwann cells. *Development* **2004**, *131*. [[CrossRef](#)] [[PubMed](#)]
16. Verber, N.S.; Shephard, S.R.; Sassani, M.; McDonough, H.E.; Moore, S.A.; Alix, J.J.P.; Wilkinson, I.D.; Jenkins, T.M.; Shaw, P.J. Biomarkers in motor neuron disease: A state of the art review. *Front. Neurol.* **2019**, *10*, 291. [[CrossRef](#)]
17. Abdel-Khalik, J.; Yutuc, E.; Crick, P.J.; Gustafsson, J.Å.; Warner, M.; Roman, G.; Talbot, K.; Gray, E.; Griffiths, W.J.; Turner, M.R.; et al. Defective cholesterol metabolism in amyotrophic lateral sclerosis. *J. Lipid Res.* **2017**, *58*, 267–278. [[CrossRef](#)]
18. Schmitt, F.; Hussain, G.; Dupuis, L.; Loeffler, J.P.; Henriques, A. A plural role for lipids in motor neuron diseases: energy, signaling and structure. *Front. Cell. Neurosci.* **2014**, *8*, 25. [[CrossRef](#)]
19. Jessen, K.R.; Mirsky, R. The origin and development of glial cells in peripheral nerves. *Nat. Rev. Neurosci.* **2005**, *6*, 671–682. [[CrossRef](#)]
20. Makoukji, J.; Shackleford, G.; Meffre, D.; Grenier, J.; Liere, P.; Lobaccaro, J.M.A.; Schumacher, M.; Massaad, C. Interplay between LXR and Wnt/ β -catenin signaling in the negative regulation of peripheral myelin genes by oxysterols. *J. Neurosci.* **2011**, *31*, 9620–9629. [[CrossRef](#)]
21. Hichor, M.; Sampathkumar, N.K.; Montanaro, J.; Borderie, D.; Petit, P.X.; Gorgievski, V.; Tzavara, E.T.; Eid, A.A.; Charbonnier, F.; Grenier, J.; et al. Paraquat induces peripheral myelin disruption and locomotor defects: Crosstalk with LXR and wnt pathways. *Antioxid. Redox Signal.* **2017**, *27*, 168–183. [[CrossRef](#)]
22. Hichor, M.; Sundaram, V.K.; Eid, S.A.; Abdel-Rassoul, R.; Petit, P.X.; Borderie, D.; Bastin, J.; Eid, A.A.; Manuel, M.; Grenier, J.; et al. Liver X receptor exerts a protective effect against the oxidative stress in the peripheral nerve. *Sci. Rep.* **2018**, *8*, 2524. [[CrossRef](#)]
23. Tawk, M.; Makoukji, J.; Belle, M.; Fonte, C.; Trousson, A.; Hawkins, T.; Li, H.; Ghandour, S.; Schumacher, M.; Massaad, C. Wnt/ β -catenin signaling is an essential and direct driver of myelin gene expression and myelinogenesis. *J. Neurosci.* **2011**, *31*, 3729–3742. [[CrossRef](#)]
24. Makoukji, J.; Belle, M.; Meffre, D.; Stassart, R.; Grenier, J.; Shackleford, G.; Fledrich, R.; Fonte, C.; Branchu, J.; Goulard, M.; et al. Lithium enhances remyelination of peripheral nerves. *Proc. Natl. Acad. Sci. USA* **2012**, *109*, 3973–3978. [[CrossRef](#)]
25. Salzer, J.L. Schwann cell myelination. *Cold Spring Harb. Perspect. Biol.* **2015**, *7*, 1–26. [[CrossRef](#)]
26. Hamilton, R.T.; Bhattacharya, A.; Walsh, M.E.; Shi, Y.; Wei, R.; Zhang, Y.; Rodriguez, K.A.; Buffenstein, R.; Chaudhuri, A.R.; Van Remmen, H. Elevated protein carbonylation, and misfolding in sciatic nerve from *db/db* and *Sod1^{-/-}* mice: plausible link between oxidative stress and demyelination. *PLoS ONE* **2013**, *8*, e65725. [[CrossRef](#)]
27. Zhou, Y.; Miles, J.R.; Tavori, H.; Lin, M.; Khoshbouei, H.; Borchelt, D.; Bazick, H.; Landreth, G.E.; Lee, S.; Fazio, S.; et al. PMP22 regulates cholesterol trafficking and ABCA1-mediated cholesterol efflux. *J. Neurosci.* **2019**, *39*, 5404–5418. [[CrossRef](#)]
28. Cermenati, G.; Giatti, S.; Cavaletti, G.; Bianchi, R.; Maschi, O.; Pesaresi, M.; Abbiati, F.; Volonterio, A.; Saez, E.; Caruso, D.; et al. Activation of the liver X receptor increases neuroactive steroid levels and protects from diabetes-induced peripheral neuropathy. *J. Neurosci.* **2010**, *30*, 11896–11901. [[CrossRef](#)]
29. Cermenati, G.; Abbiati, F.; Cermenati, S.; Brioschi, E.; Volonterio, A.; Cavaletti, G.; Saez, E.; De Fabiani, E.; Crestani, M.; Garcia-Segura, L.M.; et al. Diabetes-induced myelin abnormalities are associated with an altered lipid pattern: protective effects of LXR activation. *J. Lipid Res.* **2012**, *53*, 300–310. [[CrossRef](#)]
30. Melcangi, R.C.; Panzica, G.C. Neuroactive steroids: Old players in a new game. *Neuroscience* **2006**, *138*, 733–739. [[CrossRef](#)]
31. Melcangi, R.C.; Garcia-Segura, L.M.; Mensah-Nyagan, A.G. Neuroactive steroids: State of the art and new perspectives. *Cell. Mol. Life Sci.* **2008**, *65*, 777–797. [[CrossRef](#)]

32. Melcangi, R.C.; Garcia-Segura, L.M. Therapeutic approaches to peripheral neuropathy based on neuroactive steroids. *Expert Rev. Neurother.* **2006**, *6*, 1121–1125. [[CrossRef](#)]
33. Montani, L.; Pereira, J.A.; Norrmén, C.; Pohl, H.B.F.; Tinelli, E.; Trötz Müller, M.; Figlia, G.; Dimas, P.; von Niederhäusern, B.; Schwager, R.; et al. De novo fatty acid synthesis by Schwann cells is essential for peripheral nervous system myelination. *J. Cell Biol.* **2018**, *217*, 1353–1368. [[CrossRef](#)]
34. Saher, G.; Quintes, S.; Mobius, W.; Wehr, M.C.; Kramer-Albers, E.M.; Brugger, B.; Nave, K.A. Cholesterol regulates the endoplasmic reticulum exit of the major membrane protein P0 required for peripheral myelin compaction. *J. Neurosci.* **2009**, *29*, 6094–6104. [[CrossRef](#)]
35. Verheijen, M.H.G.; Camargo, N.; Verdier, V.; Nadra, K.; de Preux Charles, A.S.; Médard, J.J.; Luoma, A.; Crowther, M.; Inouye, H.; Shimano, H.; et al. SCAP is required for timely and proper myelin membrane synthesis. *Proc. Natl. Acad. Sci. USA* **2009**, *106*, 21383–21388. [[CrossRef](#)]
36. Valentijn, L.J.; Bolhuis, P.A.; Zorn, I.; Hoogendijk, J.E.; van den Bosch, N.; Hensels, G.W.; Stanton, V.P.; Housman, D.E.; Fischbeck, K.H.; Ross, D.A.; et al. The peripheral myelin gene PMP-22/GAS-3 is duplicated in charcot-marie-tooth disease type 1A. *Nat. Genet.* **1992**, *1*, 166–170. [[CrossRef](#)]
37. Li, J. Caveats in the established understanding of CMT1A. *Ann. Clin. Transl. Neurol.* **2017**, *4*, 601–607. [[CrossRef](#)]
38. Fledrich, R.; Abdelaal, T.; Rasch, L.; Bansal, V.; Schütza, V.; Brügger, B.; Lüchtenborg, C.; Prukop, T.; Stenzel, J.; Rahman, R.U.; et al. Targeting myelin lipid metabolism as a potential therapeutic strategy in a model of CMT1A neuropathy. *Nat. Commun.* **2018**, *9*, 3025. [[CrossRef](#)]
39. Farid, M.; Demicco, E.G.; Garcia, R.; Ahn, L.; Merola, P.R.; Cioffi, A.; Maki, R.G. Malignant peripheral nerve sheath tumors. *Oncologist* **2014**, *19*, 193–201. [[CrossRef](#)]
40. Brohl, A.S.; Kahen, E.; Yoder, S.J.; Teer, J.K.; Reed, D.R. The genomic landscape of malignant peripheral nerve sheath tumors: diverse drivers of ras pathway activation. *Sci. Rep.* **2017**, *7*, 14992. [[CrossRef](#)]
41. Patel, A.V.; Johansson, G.; Colbert, M.C.; Dasgupta, B.; Ratner, N. Fatty acid synthase is a metabolic oncogene targetable in malignant peripheral nerve sheath tumors. *Neuro. Oncol.* **2015**, *17*, 1599–1608. [[CrossRef](#)]
42. Varin, J.; Poulain, L.; Hivelin, M.; Nusbaum, P.; Hubas, A.; Laurendeau, I.; Lantieri, L.; Wolkenstein, P.; Vidaud, M.; Pasmant, E.; et al. Dual mTORC1/2 inhibition induces anti-proliferative effect in NF1-associated plexiform neurofibroma and malignant peripheral nerve sheath tumor cells. *Oncotarget* **2016**, *7*, 35753–35767. [[CrossRef](#)]
43. Johansson, G.; Mahller, Y.Y.; Collins, M.H.; Kim, M.O.; Nobukuni, T.; Perentesis, J.; Cripe, T.P.; Lane, H.A.; Kozma, S.C.; Thomas, G.; et al. Effective in vivo targeting of the mammalian target of rapamycin pathway in malignant peripheral nerve sheath tumors. *Mol. Cancer Ther.* **2008**, *7*, 1237–1245. [[CrossRef](#)]
44. Laplante, M.; Sabatini, D.M. mTORC1 activates SREBP-1c and uncouples lipogenesis from gluconeogenesis. *Proc. Natl. Acad. Sci. USA* **2010**, *107*, 3281–3282. [[CrossRef](#)]
45. Saxton, R.A.; Sabatini, D.M. mTOR signaling in growth, metabolism, and disease. *Cell* **2017**, *168*, 960–976. [[CrossRef](#)]
46. Repa, J.J.; Liang, G.; Ou, J.; Bashmakov, Y.; Lobaccaro, J.M.; Shimomura, I.; Shan, B.; Brown, M.S.; Goldstein, J.L.; Mangelsdorf, D.J. Regulation of mouse sterol regulatory element-binding protein-1c gene (SREBP-1c) by oxysterol receptors, LXRalpha and LXRbeta. *Genes Dev.* **2000**, *14*, 2819–2830. [[CrossRef](#)]
47. Higuchi, N.; Kato, M.; Shundo, Y.; Tajiri, H.; Tanaka, M.; Yamashita, N.; Kohjima, M.; Kotoh, K.; Nakamuta, M.; Takayanagi, R.; et al. Liver X receptor in cooperation with SREBP-1c is a major lipid synthesis regulator in nonalcoholic fatty liver disease. *Hepatology* **2008**, *38*, 1122–1129. [[CrossRef](#)]
48. Rong, S.; Cortés, V.A.; Rashid, S.; Anderson, N.N.; McDonald, J.G.; Liang, G.; Moon, Y.-A.; Hammer, R.E.; Horton, J.D. Expression of SREBP-1c Requires SREBP-2-mediated generation of a sterol ligand for LXR in livers of mice. *Elife* **2017**, *6*. [[CrossRef](#)]
49. Gavini, C.K.; Bookout, A.L.; Bonomo, R.; Gautron, L.; Lee, S.; Mansuy-Aubert, V. Liver X receptors protect dorsal root ganglia from obesity-induced endoplasmic reticulum stress and mechanical allodynia. *Cell Rep.* **2018**, *25*, 271–277. [[CrossRef](#)]
50. Mansuy-Aubert, V.; Gautron, L.; Lee, S.; Bookout, A.L.; Kusminski, C.M.; Sun, K.; Zhang, Y.; Scherer, P.E.; Mangelsdorf, D.J.; Elmquist, J.K. Loss of the liver X receptor LXR α/β in peripheral sensory neurons modifies energy expenditure. *Elife* **2015**, *4*. [[CrossRef](#)]
51. Richard, L.; Topilko, P.; Magy, L.; Decouvelaere, A.V.; Charnay, P.; Funalot, B.; Vallat, J.-M. Endoneurial fibroblast-like cells. *J. Neuropathol. Exp. Neurol.* **2012**, *71*, 938–947. [[CrossRef](#)]

52. Richard, L.; Védrenne, N.; Vallat, J.M.; Funalot, B. Characterization of endoneurial fibroblast-like cells from human and rat peripheral nerves. *J. Histochem. Cytochem.* **2014**, *62*, 424–435. [[CrossRef](#)]
53. Woodhoo, A.; Sommer, L. Development of the schwann cell lineage: From the neural crest to the myelinated nerve. *Glia* **2008**, *56*, 1481–1490. [[CrossRef](#)]
54. Schubert, T.; Friede, R.L. The role of endoneurial fibroblasts in myelin degradation. *J. Neuropathol. Exp. Neurol.* **1981**, *40*, 134–154. [[CrossRef](#)]
55. Stevens, A.; Schabet, M.; Schott, K.; Wiethölter, H. Role of endoneurial cells in experimental allergic neuritis and characterisation of a resident phagocytic cell. *Acta Neuropathol.* **1989**, *77*, 412–419. [[CrossRef](#)]
56. Goodrum, J.F.; Earnhardt, T.; Goines, N.; Bouldin, T.W. Fate of myelin lipids during degeneration and regeneration of peripheral nerve: an autoradiographic study. *J. Neurosci.* **1994**, *14*, 357–367. [[CrossRef](#)]
57. Müller, M.; Stenner, M.; Wacker, K.; Ringelstein, E.B.; Hickey, W.F.; Kiefer, R. Contribution of resident endoneurial macrophages to the local cellular response in experimental autoimmune neuritis. *J. Neuropathol. Exp. Neurol.* **2006**, *65*, 499–507. [[CrossRef](#)]
58. Pascual-García, M.; Valledor, A.F. Biological roles of liver X receptors in immune cells. *Arch. Immunol. Ther. Exp. (Warsz.)* **2012**, *60*, 235–249. [[CrossRef](#)]
59. Bunge, M.; Wood, P.; Tynan, L.; Bates, M.; Sanes, J.R. Perineurium originates from fibroblasts: demonstration in vitro with a retroviral marker. *Science* **1989**, *243*, 229–231. [[CrossRef](#)]
60. Kucenas, S. Perineurial glia. *Cold Spring Harb. Perspect. Biol.* **2015**, *7*. [[CrossRef](#)]
61. Fontenas, L.; Kucenas, S. Livin' on the edge: Glia shape nervous system transition zones. *Curr. Opin. Neurobiol.* **2017**, *47*, 44–51. [[CrossRef](#)]
62. Fontenas, L.; Kucenas, S. Motor exit point (MEP) glia: Novel myelinating glia that bridge CNS and PNS myelin. *Front. Cell. Neurosci.* **2018**, *12*, 333. [[CrossRef](#)]
63. Parmantier, E.; Lynn, B.; Lawson, D.; Turmaine, M.; Namini, S.S.; Chakrabarti, L.; McMahon, A.P.; Jessen, K.R.; Mirsky, R. Schwann cell-derived desert hedgehog controls the development of peripheral nerve sheaths. *Neuron* **1999**, *23*, 713–724. [[CrossRef](#)]
64. Sharghi-Namini, S.; Turmaine, M.; Meier, C.; Sahni, V.; Umehara, F.; Jessen, K.R.; Mirsky, R. The structural and functional integrity of peripheral nerves depends on the glial-derived signal desert hedgehog. *J. Neurosci.* **2006**, *26*, 6364–6376. [[CrossRef](#)]
65. Petrov, K.; Wierbowski, B.M.; Salic, A. Sending and receiving hedgehog signals. *Ann. Rev. Cell Dev. Biol.* **2017**, *33*, 145–168. [[CrossRef](#)]
66. Huang, P.; Nedelcu, D.; Watanabe, M.; Jao, C.; Kim, Y.; Liu, J.; Salic, A. Cellular cholesterol directly activates smoothed in hedgehog signaling. *Cell* **2016**, *166*, 1176–1187. [[CrossRef](#)]
67. Nedelcu, D.; Liu, J.; Xu, Y.; Jao, C.; Salic, A. Oxysterol binding to the extracellular domain of smoothed in hedgehog signaling. *Nat. Chem. Biol.* **2013**, *9*, 557–564. [[CrossRef](#)]
68. Xu, P.; Xu, H.; Tang, X.; Xu, L.; Wang, Y.; Guo, L.; Yang, Z.; Xing, Y.; Wu, Y.; Warner, M.; et al. Liver X receptor β is essential for the differentiation of radial glial cells to oligodendrocytes in the dorsal cortex. *Mol. Psychiatry* **2014**, *19*, 947–957. [[CrossRef](#)]
69. Andersson, S.; Gustafsson, N.; Warner, M.; Gustafsson, J.A. Inactivation of liver X receptor beta leads to adult-onset motor neuron degeneration in male mice. *Proc. Natl. Acad. Sci. USA* **2005**, *102*, 3857–3862. [[CrossRef](#)]
70. Sacchetti, P.; Sousa, K.M.; Hall, A.C.; Liste, I.; Steffensen, K.R.; Theofilopoulos, S.; Parish, C.L.; Hazenberg, C.; Richter, L.Ä.; Hovatta, O.; et al. Liver X receptors and oxysterols promote ventral midbrain neurogenesis in vivo and in human embryonic stem cells. *Cell Stem Cell* **2009**, *5*, 409–419. [[CrossRef](#)]
71. Wouters, E.; de Wit, N.M.; Vanmol, J.; van der Pol, S.M.A.; van het Hof, B.J.; Sommer, D.; Loix, M.; Geerts, D.; Gustafsson, J.A.; Steffensen, K.R.; et al. Liver X receptor alpha is important in maintaining blood-brain barrier function. *Front. Immunol.* **2019**, *10*, 1811. [[CrossRef](#)]
72. Lund, E.G.; Peterson, L.B.; Adams, A.D.; Lam, M.H.N.; Burton, C.A.; Chin, J.; Guo, Q.; Huang, S.; Latham, M.; Lopez, J.C.; et al. Different roles of liver X receptor α and β in lipid metabolism: Effects of an α -selective and a dual agonist in mice deficient in each subtype. *Biochem. Pharmacol.* **2006**, *71*, 453–463. [[CrossRef](#)]
73. Alberti, S.; Schuster, G.; Parini, P.; Feltkamp, D.; Diczfalusy, U.; Rudling, M.; Angelin, B.; Björkhem, I.; Pettersson, S.; Gustafsson, J. Hepatic cholesterol metabolism and resistance to dietary cholesterol in LXR β -deficient mice. *J. Clin. Investig.* **2001**, *107*, 565–573. [[CrossRef](#)]

74. Zhang, Y.; Repa, J.J.; Gauthier, K.; Mangelsdorf, D.J. Regulation of lipoprotein lipase by the oxysterol receptors, LXR α and LXR β . *J. Biol. Chem.* **2001**, *276*, 43018–43024. [[CrossRef](#)]
75. Magida, J.A.; Evans, R.M. Rational application of macrophage-specific LXR agonists avoids the pitfalls of SREBP-induced lipogenesis. *Proc. Natl. Acad. Sci. USA* **2018**, *115*, 5051–5053. [[CrossRef](#)]
76. Muse, E.D.; Yu, S.; Edillor, C.R.; Tao, J.; Spann, N.J.; Troutman, T.D.; Seidman, J.S.; Henke, A.; Roland, J.T.; Ozeki, K.A.; et al. Cell-specific discrimination of desmosterol and desmosterol mimetics confers selective regulation of LXR and SREBP in macrophages. *Proc. Natl. Acad. Sci. USA* **2018**, *115*, E4680–E4689. [[CrossRef](#)]



© 2019 by the authors. Licensee MDPI, Basel, Switzerland. This article is an open access article distributed under the terms and conditions of the Creative Commons Attribution (CC BY) license (<http://creativecommons.org/licenses/by/4.0/>).

1.3. Context of the Doctoral Thesis

As evident from the review, there are a lot of outstanding questions and multiple avenues of research that can be undertaken to further develop our understanding of LXRs in different cells of the Peripheral Nervous System. In my doctoral thesis, I decided to focus on the implication of LXRs specifically in Schwann cell's myelination process.

The first study that I was a part of (in continuation of my Master's Thesis) was trying to establish why LXR null mice (LXR $\alpha/\beta^{-/-}$ hereafter referred to as LXR double KO or LXRdKO) exhibited myelination deficits when they age but did not show any developmental deficits (Hichor et al., 2018). Our experiments demonstrated that systemic loss of LXRs results in a highly oxidative environment that becomes detrimental for the maintenance of myelin sheaths as the mice age. We were also able to empirically show that LXR stimulation can be helpful in combatting oxidative stress in Schwann cells (is it possible to modulate oxidative stress differently?). However, it was unclear if the phenotype that we observed was due to problems arising solely in Schwann cells or if the mutation induced disrupted SC-axon communication and thereby produced myelination deficits. Furthermore, it was also ambiguous if the phenotype is driven by neuronal or other SC extrinsic factors. All these questions arose because we used LXR total mutants and not conditional cell type specific mutants.

Hence, in the beginning of my thesis, we sought to find out if the phenotype can be driven by Schwann cell specific ablation of both LXR isoforms. We used the CRE-Lox recombination system to achieve targeted mutations of LXRs in Schwann cells. In more precise terms, we obtained LXR $\alpha/\beta^{fl/fl}$ mice from Prof. Mangelsdorf (UT Southwestern Medical Center, Dallas, Texas) and we bred these mice with Dhh-Cre mice obtained from JAX.

Dhh, as explained earlier (see Schwann Cell Precursors section), is expressed from the Schwann cell Lineage from the SCP stage. Dhh-cre, therefore, express Recombinase in Dhh⁺ cells at around E12.5 in peripheral nerves (Jaegle et al., 2003). This breeding strategy gave rise to conditional mutants where LXRs are specifically deleted in SCP and by default also in iSC and other derivatives of the Schwann cell lineage. We were hoping for a mild phenotype but much to our surprise, the mice are severely paralyzed in their hind limbs by the time they are weaned. We observed a complete absence of Schwann cells and myelin in peripheral nerves at post-natal stages. Additionally, the ultra-structure of the peripheral nerve

phenocopies Schwann cell targeted Sox10 mutants (Finzsch et al., 2010). These results and other molecular mechanisms that are causative of the observed phenotype are detailed in Chapter 3 (Results section).

Chapter 2: METHODS AND METHODOLOGICAL IMPROVEMENTS

2.1 Methods

Generation of Animal Models and breeding strategy:

LXR α / β ^{f/f} were obtained from the laboratory of Prof. David J Mangelsdorf in the C57Bl6/J background and have been used in earlier studies (Mansuy-Aubert et al., 2015). We bred these mice with the *DhhCre* strain obtained from JAX (Ref: 012929) to obtain LXR α / β ^{f/+}:*DhhCre*. From these heterozygous populations, we selectively bred out either LXR α or LXR β to obtain LXR β ^{f/f}:*DhhCre* and LXR α ^{f/f}:*DhhCre* mice. Control mice (LXR α / β ^{f/f}) were maintained separately in the C57Bl6 background. Pure C57Bl6/J mice (Janvier Labs) were injected into the control mouse line once every 5 generations to avoid genetic drift. Similarly, the control strain (LXR α / β ^{f/f}) was reinjected into the conditional mutant strains every 5 generations to avoid genetic drift. All aspects of Animal breeding and Animal care were in coherence with the internal guidelines of INSERM and Université de Paris and were approved by the ethical committee.

To obtain homozygous LXR β ^{f/f}:*DhhCre* mutants, LXR β ^{f/f} mice were bred with LXR β ^{f/+}:*DhhCre*. Direct breeding of floxed strains was impossible as the homozygous LXR β mutants were paralyzed and could not reproduce. However, the same was possible for LXR α mutants as they did not show any observable phenotype when compared to controls. LXR β ^{f/f}:*DhhCre* mutants were always compared to LXR β ^{f/f} mice for all the experiments used in the study.

Grip Strength Test:

Grip strength was assessed using the BioSeb force gauge dynamometer (BIO-GS3) with rectangular grids. Briefly, mice were placed on the grid on all four limbs until they grasped the grid securely. They were then pulled by their tails along the direction of the axle until all four limbs were released. The maximum force exerted by the mice to stay on the grid was recorded. Each mouse was subjected to 3 successive attempts separated by a 30-minute rest period. Experiments were performed blindly to avoid biases.

Hotplate Test:

The temperature of the electrically heated plate was set at 52°C in compliance with the norms of the Institutional Ethical Committee for Animal Care and Experimentation. Mice were placed on the hot plate for a maximum period of 30 seconds. The time the mice took to respond to the heat, such as licking their

paws or upswing, was recorded. After the response, the mice were immediately placed in a recipient filled with cold water to prevent limb damage. Mice were removed from the hot plate after 30 seconds regardless of their response.

Immunohistochemistry:

Sciatic nerves of mice at stipulated time points were dissected and fixed in 4% PFA for a maximum of 2 hours on ice. Nerves were then washed with PBS1X and dehydrated overnight using 20% sucrose at 4°C. The following day, nerves were embedded in OCT compound (Agar Scientific) and solidified using cold isopentane placed in liquid nitrogen. 12µm transverse cryosections were prepared and placed on APTES (A3648 Sigma) coated slides and air dried for 20 minutes. Sections were then permeabilized using PBS1X containing 0.2% TritonX100, 0.1% Tween20 for 20 minutes at room temperature. Following permeabilization, sections were washed at least twice with PBS1X and blocked using the blocking buffer (2% BSA, 10% Normal Donkey Serum, 0.1% Tween 20 in PBS1X) for 1 hour at room temperature. Sections were then incubated overnight with the necessary primary antibodies diluted in blocking buffer. The following day, sections were washed at least thrice in PBS1X and incubated with secondary antibodies raised in Donkeys (Jackson Immuno-Research) for one hour at room temperature in obscurity. Slides were then washed at least thrice in PBS1X and nuclei were labeled using Hoechst 33342 (5µg/mL). Samples were then washed, air dried in obscurity for 5 minutes and mounted with PermaFluor (Thermo Fisher).

Antibodies:

The following antibodies were used for the IHC analysis in distal sciatic nerve sections.

Primary Antibody	Reference	Concentration	Secondary Antibody	Reference	Concentration
Goat anti-SOX10	AF2864 R&D systems	1/200	Donkey anti-Goat Cy3	705-165-147 Jackson	1/500
Rabbit anti-NFH	AB5539 Merck	1/1000	Donkey anti-Rabbit A488	711-545-152 Jackson	1/1000
Rabbit anti-Krox20	Gift From Prof. Meijer	1/100	Donkey anti-Rabbit A488	711-545-152 Jackson	1/200
Rat anti-ZO1	R26.4C DSHB	1/25	Donkey anti-Rat A647	705-605-147 Jackson	1/100
Chicken anti-MPZ	PZO Aves	1/500	Donkey anti-Chicken Cy3	703-005-155 Jackson	1/1000

Sampling and Image Analysis:

For all IHC experiments, nerves from 3 to 5 mice were analyzed for each group. From each animal, 3 cryosections from different parts of the nerve were prepared and stained with the antibody/chemical reagent. Thus, each group contains 3 to 5 biological replicates. For each biological replicate, 3 technical replicates were generated, and the average of the technical replicates was taken to be the quantification for the biological replicate. IHC confocal images were captured using LSM710 confocal microscope (Leica). Images were captured as z-stacks and analyzed using Fiji (image J). Counting of nuclear stains was performed using macro codes that were generated for each staining. The code script of the macros for each staining is detailed in the supplementary data.

Transmission Electron Microscopy:

Sciatic nerves of mice at different time points were dissected and fixed in KS buffer (4% paraformaldehyde, 2.5% glutaraldehyde in 0.1 M phosphate buffer pH 7.4) overnight. Tissues were then washed in 0.1M phosphate buffer, postfixed in 2% osmium tetroxide, dehydrated in graded ethanol series and embedded

in epoxy resin. For electron microscopy, ultrathin sections (50–90 nm) were cut on an ultramicrotome (8800 Ultratome III; LKB Bromma) and collected on 300-mesh nickel grids. Staining was performed on drops of 4% aqueous uranyl acetate, followed by Reynolds's lead. Ultrastructural analyses were performed in a JEOL jem-1011 electron microscope and digitalized with DigitalMicrograph software. Electron microscopy images were used for calculating the g-ratio and axon perimeter using NIH ImageJ software. At least 100 randomly selected axons were analyzed per animal. At least three animals were used per genotype.

Dissociated DRG cultures:

Dissociated DRG cultures were established from WT and $LXR\beta^{fl}:DhhCre$ animals based according to existing protocols (Kim and Maurel, 2009; Kim and Kim, 2018). A total of 40 DRGs were harvested from each embryo. DRGs were then trypsinized (0.25% Trypsin in HBSS1X) for 30min at 37°C. Trypsinization was stopped using L-15 media containing 10% Horse Serum (Gibco). DRGs were then spun down at 1500 rpm for 5min. The supernatant was removed, and the tissues were resuspended in DRG plating medium (see *Media Compositions*). The tissues were then triturated 10-20 times using flamed Pasteur pipettes until a homogenous cell suspension was obtained. Dissociated DRGs were then plated on 35mm dishes in DRG plating media. The following day the medium was replaced with N2/NGF serum free medium (see *Media Compositions*) to promote neurite growth and Schwann cell proliferation. The cultures were maintained and observed for 1 week.

Primary Schwann cell cultures:

Primary Schwann cell cultures were established from dissociated DRG cultures based on existing protocols with slight modifications (Kim and Maurel, 2009; Kim and Kim, 2018). Briefly, neurite-Schwann cell networks from 1-week old, dissociated cultures were mechanically lifted from the culture plates using a fine 27G^{1/2} needle. They were then digested using Trypsin-Collagenase (0.25% Trypsin & 0.1% Collagenase Type I in HBSS1X). Enzymatic digestion was quenched using Immunopanning media (See *Media Compositions*). The digested cells were briefly triturated 5 – 10 times using Pasteur pipettes and were pelleted using centrifugation. Cells were then resuspended in immunopanning media and incubated for 15 min at 37°C to promote the turnover expression of cell surface markers for efficient immunopanning.

Contaminating fibroblasts were removed by immunopanning based on existing protocols (Lutz, 2014). Briefly, immunopanning dishes coated with Thy1.2 antibody (MCA02R BioRad) were prepared as

described elsewhere(Lutz, 2014). Cells in immunopanning media were then passed through these dishes to selectively pan out Thy1.2+ve contaminating fibroblasts from culture. Schwann cells and neuronal debris that did not adhere to the dishes were then collected and centrifuged. Cells were there resuspended in Schwann cell Growth medium and plated on 60mm PLL-Laminin coated dishes. Media was changed every two days until confluence. Neuronal cells detached and died after two days in culture in the first passage due to the lack of NGF in Schwann cell growth medium. They were washed out subsequently during medium change. Cells were immunopanned once again after the first passage to remove any residual fibroblast contamination and were used for experiments from the second passage.

Media Compositions:

DRG plating media: DMEM with 4.5g/L glucose (Gibco), 10% heat inactivated Horse Serum (Gibco), 1X Glutamax (Gibco), 1X Antibiotic/Antimycotic (Gibco) and 50ng/μL Nerve Growth Factor 2.5S (R&D Systems)

N2/NGF serum free media: DMEM:F12 (Gibco), 1X N2 supplement (Gibco), 1X Glutamax (Gibco), 1X Antibiotic/Antimycotic (Gibco) and 50ng/μL Nerve Growth Factor 2.5S (R&D Systems)

Immunopanning media: DMEM:F12 (Gibco), 10% heat inactivated Horse Serum (Gibco), 1X Glutamax (Gibco), 1X Antibiotic/Antimycotic (Gibco)

Schwann Cell Growth Media: DMEM:F12 (Gibco), 1X Glutamax (Gibco), 1X Antibiotic/Antimycotic (Gibco), 1X N2 supplement (Gibco), 1X B27 Supplement (Gibco), 10ng/μL Neuregulin (396HB R&D Systems), 2.5μM Forskolin (Sigma), 10 ng/mL T3 Salt (Sigma).

Total RNA isolation

Total RNA was extracted from each sample using 1mL of TRIzol reagent (Ambion Life Technologies 15596018) on ice as described in the manufacturer's instructions with slight modifications. Briefly, 100% Ethanol was substituted for Isopropanol to reduce the precipitation of salts. Also, RNA precipitation was carried out overnight at -20°C in the presence of glycogen. The following day, precipitated RNA was pelleted by centrifugation and washed at least 3 times with 70% Ethanol to eliminate any residual contamination. Tubes were then spin dried in vacuum for 5 minutes and RNA was resuspended in 20μL of RNase resuspension buffer containing 0.1mM EDTA, pH 8. RNA was then stored at -80°C till RTqPCR.

RNA quality, integrity and assay

RNA quantity was assayed using UV spectrophotometry on Nanodrop One (Thermo Scientific). Optical density absorption ratios A260/A280 & A260/A230 of the samples were above 1.8 and 1.5, respectively. Furthermore, the extraction protocol used in the study was also validated using Agilent Bioanalyzer (RIN value 9.0 and above).

RTqPCR:

500ng of Total RNA was reverse transcribed with Random Primers (Promega C1181) and MMLV Reverse Transcriptase (Sigma M1302) according to prescribed protocols. Quantitative Real time PCR (qPCR) was

performed using Absolute SYBR ROX 2X qPCR mix (Thermo AB1162B) as a fluorescent detection dye. All reactions were carried out in a final volume of 7 μ l in 384 well plates with 300 nM gene specific primers, around 3.5ng of cDNA (at 100% RT efficiency) and 1X SYBR Master Mix in each well. Each reaction was performed in triplicates. All qPCR experiments were performed on BioRad CFX384 with a No-Template-Control (NTC) to check for primer dimers and a No-RT-Control (NRT) to check for any genomic DNA contamination.

Primer design:

All primers used in the study were designed using the Primer 3 plus software (<https://primer3plus.com/cgi-bin/dev/primer3plus.cgi>). Splice variants and the protein coding sequence of the genes were identified using the Ensembl database (www.ensembl.org). Constitutively expressed exons among all splice variants were then identified using the ExonMine database (<https://imm.medicina.ulisboa.pt/group/exonmine/ack.html>) (Mollet et al., 2010). Primer sequences that generated amplicons spanning two constitutively expressed exons were then designed using the Primer 3 plus software. Detailed information on Primer sequences and amplification efficiencies are described in a previous study (Sundaram et al., 2019b).

Statistical analysis and Data Visualization :

qPCR readouts were analyzed in Precision Melt Analysis Software v1.2. The amplicons were subjected to Melt Curve analysis and were verified for a single dissociation peak at a Melting Temperature (T_m) > 75°C as expected from the primer constructs. Cq values were determined by regression, and the Cq data were exported to Microsoft Excel for further calculations. Each biological sample had 3 technical replicates thereby generating 3 individual Cq values. The arithmetic mean of the triplicates was taken to be the Cq representing the biological sample. The standard deviation (SD) of the triplicates was also calculated and samples that exhibited SD>0.20 were considered inconsistent. In such cases, one outlier Cq was removed to have at least duplicate Cq values for each biological sample and an SD<0.20. Relative expression of genes was quantified using the $2^{-\Delta\Delta C_t}$ method (Livak and Schmittgen, 2001; Schmittgen and Livak, 2008) and data was visualized using Graph Pad Prism v7.0.

2.2 Methodological improvements

2.2.1 Introduction

During my PhD, I have spent a significant amount of time in improving certain methods that have been employed systematically in almost all the studies conducted as a part of my doctorate degree. Of note, I have worked on improving the reliability and reproducibility of qPCR assays that form an integral part of studies undertaken in my host laboratory. qPCR data normalization relies heavily on the choice of reference genes that are presumed to be stable across all samples and experimental conditions, but this is seldom the case. Numerous statistical approaches have been proposed to help researchers choose the best set of reference genes from a predetermined set of candidates. However, these statistical methods often provide conflicting results thus making the data normalization very cumbersome. Therefore, one of the first studies that I conducted aimed to delineate the merits and demerits of these statistical methods so as to devise an integrated qPCR workflow that would render the best choice of reference genes for a given experimental setting. The proposed methodology has been validated and published and is attached in the following sections (Sundaram et al., 2019b).

Furthermore, I also encountered certain technical difficulties in extracting good quality RNA from the sciatic nerve of mice, especially neonates. In fact, peripheral nerves contain high amounts of lipids that jeopardize RNA extraction. This is an issue that is acknowledged in the field and therefore laboratories resort to pooling tissue samples to obtain sufficient quantities of RNA either for RTqPCR or for high-throughput studies. In this regard, I compared different protocols of RNA extraction and proposed a modified version of the Trizol method. I then compared this protocol to other well know RNA extraction methods to exemplify the consistency and the advantages that Trizol offers over other methods even for small sample sizes. The article describing the methodology is attached in the following section (Sundaram et al., 2020, submitted for review).

Finally, I also dedicated a considerable amount of time to establish the protocol for obtaining primary Schwann cells from embryonic dissociated DRG cultures. This method has been a powerful tool to understand the nuances of Schwann cell development *in vitro*. This protocol was first developed in Prof. Nancy Ratner's lab and later modified in Dr. Haesun Kim's lab (Ratner et al., 2005; Kim and Maurel, 2009; Kim and Kim, 2018) . However, these protocols did not efficiently eliminate fibroblast contaminations in

prolonged cultures due to the use of Horse Serum. Therefore, I improved on their method by experimenting on different ways to remove fibroblast contamination in primary cultures and have succeeded in obtaining and culturing highly pure Schwann cells in a defined media that does not require serum supplementation. The technical aspects of my protocol are elaborated in the following sections.

2.2.2 A novel qPCR data analysis workflow for reproducible and reliable results

Context of the study:

The golden standard for qPCR data normalization is through the use reference genes, previously termed as housekeeping genes. However, research in the last two decades has clearly demonstrated that the mRNA expression of these “housekeeping” genes can indeed vary depending on the sample or the experimental condition. To address this issue, numerous statistical methods were proposed in the early 2000s that could help researchers select stable reference genes among a given set of arbitrarily chosen candidates. These methods gained huge popularity with thousands of citations. Subsequently, guidelines were setup to standardize data availability and the methodology used in qPCR assays (Bustin et al., 2009). However, the authors of these guidelines could not agree on a single statistical approach to select the best reference gene(s) for a given experimental condition. Therefore, they proposed the use of at least three different methods for the selection of reference genes.

This proposal led to a different problem as these methods sometimes give rise to highly conflicting results i.e. the reference gene that is ranked the best according to one method was sometimes the least favored by another. Researchers then resorted to averaging the ranks across all methods and chose reference genes based on the overall rank. This approach, in my opinion, is not scientific as each statistical method comes with its own set of assumptions and limitations. Therefore, averaging the ranks would render a sub-optimal assessment of the best reference genes.

Therefore, in this study, my colleagues and I have addressed this issue in the context of longitudinal qPCR data. We analyzed the most common statistical approaches by highlighting their assumptions and limitations using our data. We found that certain methods such as GeNorm and Pairwise ΔC_t are ill suited for longitudinal studies. Furthermore, other methods such as the NormFinder and the Coefficient of Variation (CV) analysis were found to be powerful when used in tandem but not individually. We thus propose a standardized qPCR data analysis workflow for longitudinal datasets using traditional statistical methods such as one-way ANOVA coupled with a combination of CV analysis and Normfinder. The approach proves to be more robust than any of the methods used individually. It is briefly described below (Figure 21).

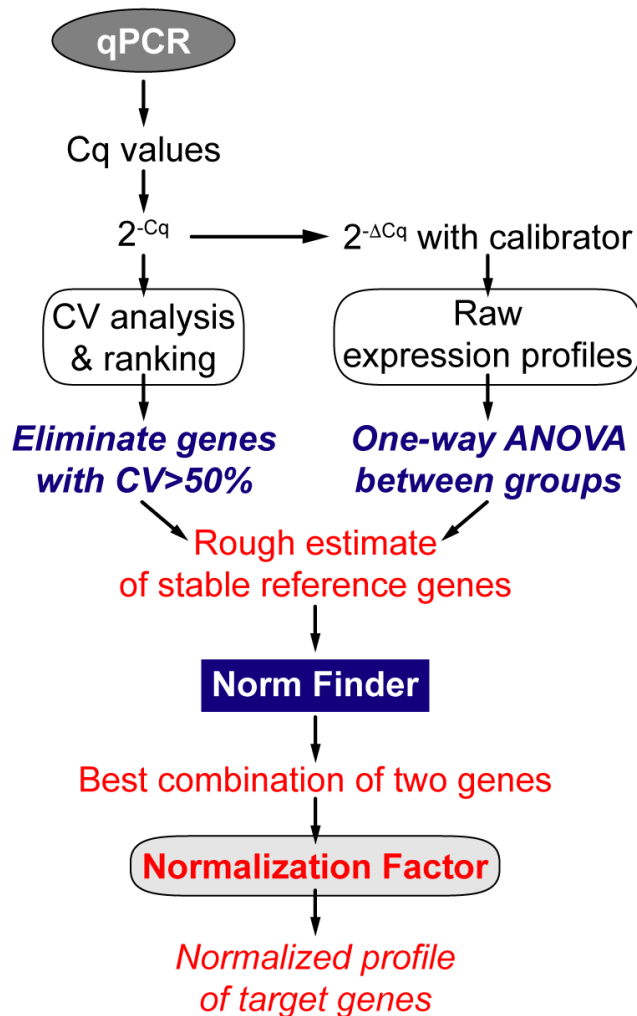


Figure 30: Cq values of all samples and genes are obtained from qPCR, they are linearized, and CV analysis is performed. Parallely, using the experimental calibrator, the raw experimental profiles of all candidate genes are plotted as fold changes ($2^{-\Delta Cq}$). This is followed by One-way ANOVA to assess the variation among all groups. It should be noted that ANOVA is used just to assess if there is significant statistical variation among the means of the groups. It does not assess, by any means, the extent of this variation. Thus, visual representation along with the results of CV analysis and ANOVA can help us obtain a rough estimate of the most stable reference genes. At this stage, genes that exhibit $CV > 50\%$ are removed. The rest of the genes are then subjected to the NormFinder algorithm. The algorithm then ranks the genes based on intergroup and intragroup variation. It also detects the best two genes that can be used for normalization with a grouped stability value. These two genes are then used to calculate a normalizing factor to normalize all target genes. Source: (Sundaram et al., 2019b)

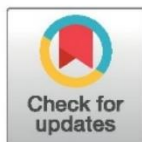
RESEARCH ARTICLE

Optimal use of statistical methods to validate reference gene stability in longitudinal studies

Venkat Krishnan Sundaram¹*, Nirmal Kumar Sampathkumar¹, Charbel Massaad, Julien Grenier

Faculty of Basic and Biomedical Sciences, Paris Descartes University, INSERM UMRS 1124, Paris, France

* These authors contributed equally to this work.

* venkatkrishnan.sundaram@parisdescartes.fr

Abstract

Multiple statistical approaches have been proposed to validate reference genes in qPCR assays. However, conflicting results from these statistical methods pose a major hurdle in the choice of the best reference genes. Recent studies have proposed the use of at least three different methods but there is no consensus on how to interpret conflicting results. Researchers resort to averaging the stability ranks assessed by different approaches or attributing a weighted rank to candidate genes. However, we report here that the suitability of these validation methods can be influenced by the experimental setting. Therefore, averaging the ranks can lead to suboptimal assessment of stable reference genes if the method used is not suitable for analysis. As the respective approaches of these statistical methods are different, a clear understanding of the fundamental assumptions and the parameters that influence the calculation of reference gene stability is necessary. In this study, the stability of 10 candidate reference genes (*Actb*, *Gapdh*, *Tbp*, *Sdha*, *Pgk1*, *Ppia*, *Rpl13a*, *Hsp60*, *Mrpl10*, *Rps26*) was assessed using four common statistical approaches (GeNorm, NormFinder, Coefficient of Variation or CV analysis and Pairwise Δ Ct method) in a longitudinal experimental setting. We used the development of the cerebellum and the spinal cord of mice as a model to assess the suitability of these statistical methods for reference gene validation. GeNorm and the Pairwise Δ Ct were found to be ill suited due to a fundamental assumption in their stability calculations. Highly correlated genes were given better stability ranks despite significant overall variation. NormFinder fares better but the presence of highly variable genes influences the ranking of all genes because of the algorithm's construct. CV analysis estimates overall variation, but it fails to consider variation across groups. We thus highlight the assumptions and potential pitfalls of each method using our longitudinal data. Based on our results, we have devised a workflow combining NormFinder, CV analysis along with visual representation of mRNA fold changes and one-way ANOVA for validating reference genes in longitudinal studies. This workflow proves to be more robust than any of these methods used individually.

OPEN ACCESS

Citation: Sundaram VK, Sampathkumar NK, Massaad C, Grenier J (2019) Optimal use of statistical methods to validate reference gene stability in longitudinal studies. PLoS ONE 14(7): e0219440. <https://doi.org/10.1371/journal.pone.0219440>

Editor: Bjoern Peters, La Jolla Institute for Allergy and Immunology, UNITED STATES

Received: February 25, 2019

Accepted: June 24, 2019

Published: July 23, 2019

Copyright: © 2019 Sundaram et al. This is an open access article distributed under the terms of the [Creative Commons Attribution License](https://creativecommons.org/licenses/by/4.0/), which permits unrestricted use, distribution, and reproduction in any medium, provided the original author and source are credited.

Data Availability Statement: All relevant data are within the manuscript and its Supporting Information files.

Funding: The author(s) received no specific funding for this work.

Competing interests: The authors have declared that no competing interests exist.

Introduction

Relative expression of target genes in qPCR assays require accurate normalization of mRNA quantities using stably expressed internal standards also called reference genes [1]. In theory, such a gene is presumed to be stably expressed across all groups and samples [2]. This is seldom the case. There is no universal reference gene that fulfils this criterion and the choice of a good reference becomes highly subjective depending on several factors such as the sample/tissue type, experimental condition and sample integrity [3,4]. Many statistical methods have been proposed to help researchers identify stable reference genes from a predetermined set of candidates. These statistical approaches determine the stability of these candidates based on a unique set of assumptions and calculations. Therefore, the predictions of these methods can vary rather significantly based on the method used and the experimental setting [5–7]. This observation, to our knowledge, has been constantly neglected in recent studies that validate reference genes. However, to address this issue, researchers average the stability ranks assessed by different methods and calculate an overall “geometric mean rank” [8,9]. Some studies also attribute a weighted rank [10–14]. This approach is rather questionable, as it does not consider the strengths and weaknesses of each method for a given experimental setting.

In this study, we tested the stability of 10 candidate reference genes during early postnatal development of the cerebellum and spinal cord in mice. This experimental setup proves to be a good longitudinal model. The cellular microenvironment is both complex and dynamic complicating the determination of stable reference genes [15–17]. We first observed that the use of arbitrary reference genes gives highly variable profiles of the target gene depending on the reference chosen. Therefore, to identify stable reference genes, we used four different statistical approaches—GeNorm [18], NormFinder [19], Coefficient of Variation analysis (CV) [20] and Pairwise Δ Ct method [21]. However, the stability ranking also varied significantly depending on either the tissue in question or the method used.

Instead of averaging the ranks or attributing a weighted rank, we analyzed the suitability of these methods to identify their respective drawbacks in a longitudinal setting. We find that the ranking of all methods tested except CV analysis are influenced by the presence of genes with high overall variation. Furthermore, GeNorm and the Pairwise Δ Ct method rankings are influenced by the expression pattern of all genes making their ranking inter-dependent. On the other hand, NormFinder and CV analysis prove to be more robust, only when they are used complementarily but not individually. Furthermore, we also report that visual representation of mRNA fold changes followed by One-way ANOVA can also help in stability assessment. Hence, we devised an integrated approach by combining CV analysis, NormFinder and visual representation of mRNA fold changes across experimental groups. We believe that this method provides more accurate estimates of stable reference genes. In summation, our study highlights the importance of choosing the right set of statistical methods and also proposes a sound workflow to validate reference genes in a longitudinal setting.

Results

Normalization with an arbitrary reference gene

To demonstrate the bias in results that arise by using a single arbitrary reference gene, we chose 3 candidate reference genes—*Actb*, *Gapdh* and *Mrpl10* to normalize Myelin Basic Protein (*Mbp*) mRNA expression levels in the cerebellum (Fig 1). *Mbp* levels showed a sudden increase by 35 folds at P10 when normalized to *Gapdh*, peaking at around 50 folds at P15 before coming down to 30 folds at P23. On the contrary, when normalized to *Mrpl10*, *Mbp* expression showed a rather linear relationship with time, gradually increasing from 12 to 41 folds between P10

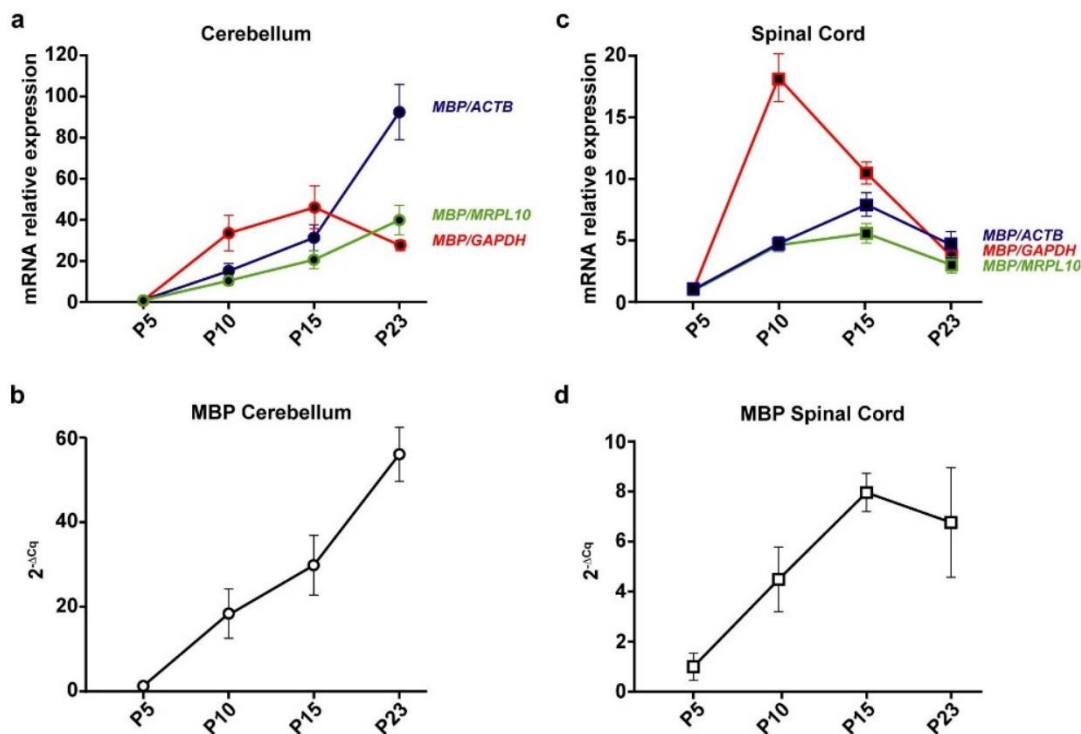


Fig 1. Mbp mRNA levels at post-natal day (P)5, 10, 15 and 23 in the cerebellum and spinal cord. P5 group is the experimental calibrator. (a) Cerebellar Mbp mRNA levels normalized using either Actb, Mrpl10 or Gapdh mRNA quantities. (b) Un-normalized profile of cerebellar Mbp expressed as a fold change of mRNA quantities across groups ($2^{-\Delta Cq}$). (c) Spinal cord Mbp mRNA levels normalized using either Actb, Mrpl10 or Gapdh mRNA quantities. (d) Un-normalised profile of spinal cord Mbp expressed as a fold change of mRNA quantities across groups ($2^{-\Delta Cq}$). Results are expressed as the Mean \pm SD for each time point.

<https://doi.org/10.1371/journal.pone.0219440.g001>

and P23. When normalized to *Actb*, the *MBP* levels increase by 15 and 30 folds at P10 and P15 then shoot up to more than 90 folds at P23. However, the un-normalized profile of *Mbp* using P5 as a calibrator (Fig 1B) shows an almost linear profile increasing from 18 to 56 folds between P10 and P23.

We observed similar contradictions in the spinal cord (Fig 1C). *Mbp* levels normalized to *Gapdh* peak at P10 by 18 folds before reducing gradually to about 3 folds at P23. Normalizing with *Mrpl10* reveals a different kinetic where *Mbp* levels reach a plateau between P10 and P15 (around 4 and 6 folds respectively) before dropping down to 3 folds at P23. Whereas, normalizing with *Actb* reveals yet another profile where *Mbp* levels steadily increase from P5 to P15 in an almost linear fashion and decrease at P23 to around 5 folds. The un-normalised profile of *Mbp* (Fig 1D) however remains linear till P15 and drops at P23.

Raw expression profiles of candidate reference genes

Given the stark differences in *Mbp* expression profiles after normalization with different reference genes, we reasoned that these differences could be induced by intrinsic changes in the mRNA levels of the reference genes during development. To demonstrate this, we calculated the expression profiles of reference genes as fold changes of mRNA quantities across groups using P5 as a calibrator (Figs 2 and 3). These differences in reference gene expression during development could indeed be demonstrated as variations in Cq values across time points. Nevertheless, it should be noted that the Cq values are mere exponents and assessing their

variation across experimental groups does not faithfully recapitulate the extent of variation in actual RNA quantities. Hence, we have represented this data as RNA fold changes ($2^{-\Delta Cq}$) across time points.

The first statistical test to assess stability after visually representing the data was One-way ANOVA to determine if the mean mRNA levels across groups are significantly different from one another. In the cerebellum, 8 of the 10 reference genes tested (*Actb*, *Hsp60*, *Gapdh*, *Sdha*, *Tbp*, *Pgk1*, *Rpl13a* and *Rps26*) showed significant variation in the mRNA levels across time points (Fig 2) Only 2 genes (*Mrpl10*, *Ppia*) showed no significant change. In the spinal cord, all tested genes showed significant variation in mRNA levels across the four time points (Fig 3).

These results taken together with the raw expression profiles of *Mbp* (Fig 1B, Fig 1D) show that intrinsic changes in mRNA levels of reference genes can indeed skew the normalized profile of *Mbp*. As a result, it causes a significant bias in the results and interpretations that ensue thus highlighting the importance of validating reference gene stability in longitudinal studies.

Assessment of expression stability using multiple statistical approaches

The expression stability of candidate reference genes was analyzed in both tissues using four well known statistical methods—CV analysis [20], NormFinder [19], GeNorm [18] and the Pairwise ΔC_t method [21] (Table 1).

CV analysis. The CV analysis estimates the variation in the linearized Cq values (2^{-Cq}) of a reference gene across all samples taken together (S1 Table). CV for each gene is calculated as the ratio of the standard deviation to the mean and it is expressed as a percentage. A lower CV would therefore mean higher stability. CV analysis on the cerebellum samples revealed *Mrpl10*, *Actb* and *Rps26* as the top three stable reference genes. In the spinal cord, the top three reference genes are *Actb*, *Ppia*, *Rps26*.

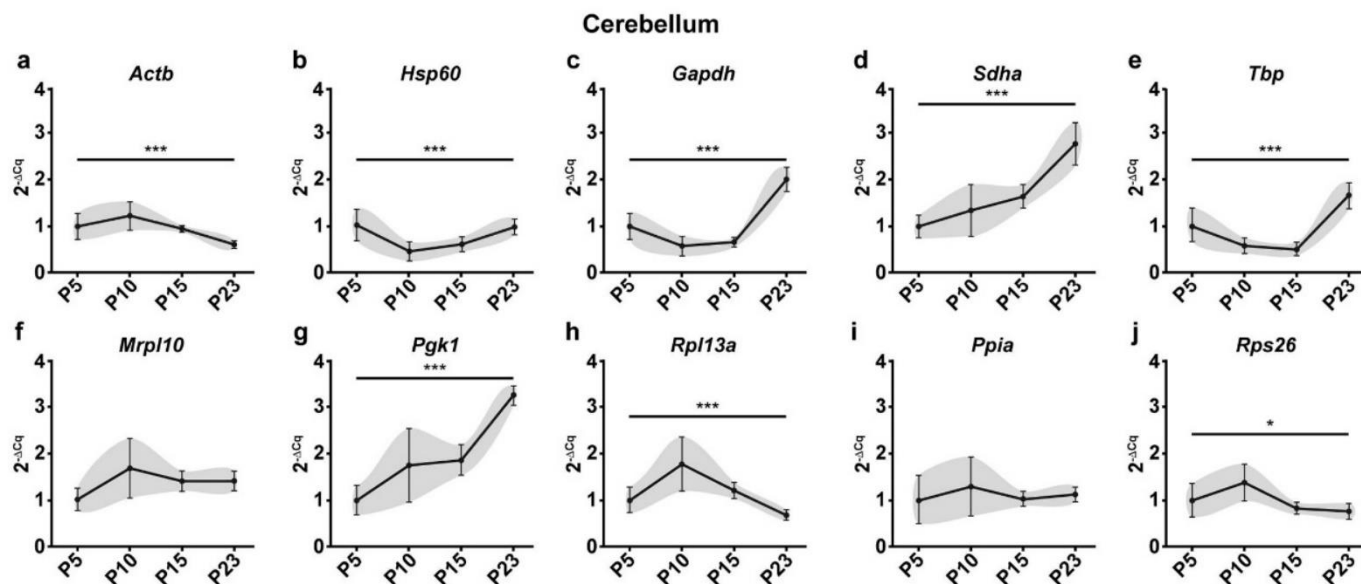


Fig 2. Raw expression profiles of reference genes expressed as fold changes across experimental groups ($2^{-\Delta Cq}$) at P5, 10, 15 and 23 in the cerebellum. P5 group is the experimental calibrator. (a) *Actb*, (b) *Hsp60*, (c) *Gapdh*, (d) *Sdha*, (e) *Tbp*, (f) *Mrpl10*, (g) *Pgk1*, (h) *Rpl13a*, (i) *Ppia* and (j) *Rps26*. Results are expressed as the Mean \pm SD for each time point. One-way ANOVA was performed to assess differences between the means of all groups. Statistical significance is denoted by *** representing P values: *P<0.05, **P<0.01, ***P<0.001. The grey area around each profile denotes the evolution of the intergroup and intragroup variation across time points.

<https://doi.org/10.1371/journal.pone.0219440.g002>

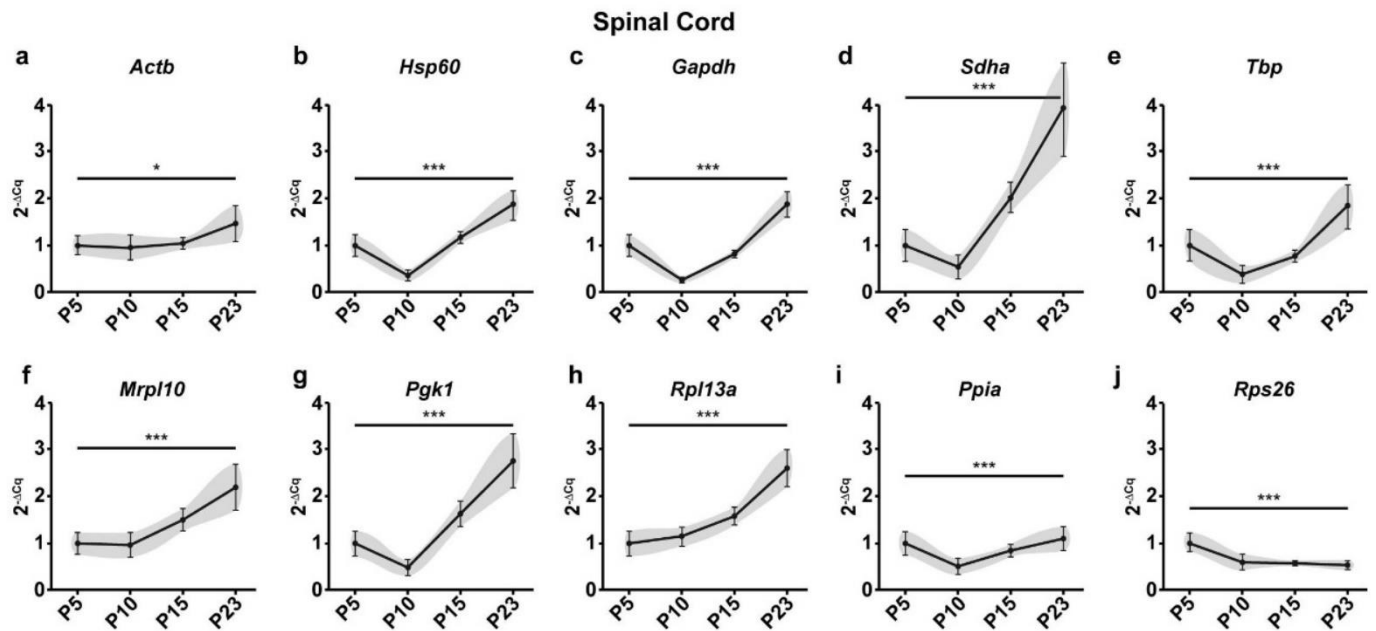


Fig 3. Raw expression profiles of reference genes expressed as fold changes across experimental groups ($2^{-\Delta Cq}$) at P5, 10, 15 and 23 in the spinal cord. P5 group is the experimental calibrator. (a) *Actb*, (b) *Hsp60*, (c) *Gapdh*, (d) *Sdha*, (e) *Tbp*, (f) *Mrpl10*, (g) *Pgk1*, (h) *Rpl13a*, (i) *Ppia* and (j) *Rps26*. Results are expressed as the Mean \pm SD for each time point. One-way ANOVA was performed to assess differences between the means of all groups. Statistical significance is denoted by "*" representing P values: * $P < 0.05$, ** $P < 0.01$, *** $P < 0.001$. The grey area around each profile denotes the evolution of the intergroup and intragroup variation across time points.

<https://doi.org/10.1371/journal.pone.0219440.g003>

NormFinder analysis. We next analyzed our data using NormFinder which uses a model-based approach which calculates the stability of reference genes based on two parameters—the intergroup variation and the intragroup variation. The stability score denoted by the S value is a weighted measure of these two parameters. The most stable reference gene has the least S value. In the cerebellum, NormFinder identified *Ppia*, *Mrpl10* and *Sdha* as the top three stable genes. In the spinal cord, the algorithm identified *Mrpl10*, *Ppia* and *Hsp60* as the top three stable reference genes.

GeNorm analysis. GeNorm calculates stability based on pairwise variation. The rationale is that if two genes vary similarly across all samples, then they are the most stable reference genes for that dataset. All other genes are ranked on their similarity to the expression of the top two genes. The algorithm functions by first identifying two genes with the highest expression agreement and therefore high stability. It then calculates the expression variation of every other gene sequentially with respect to the previous genes chosen. Therefore, the ranking of the GeNorm algorithm always has 2 genes at the top with the same M value followed by other genes with higher M values indicating lower stability. In the cerebellum, the GeNorm algorithm identified *Gapdh* and *Tbp* to be the most stable reference genes followed by *Hsp60*. This is in stark contrast to the genes identified by the previous two methods. In the spinal cord, the most stable reference genes were identified as *Mrpl10* and *Rpl13a* followed by *Pgk1*.

Pairwise ΔC_t analysis. This method works on the same rationale as GeNorm but calculates the stability value (Mean SD) differently. It is calculated as the average standard deviation of the Cq value differences that the gene exhibits with other genes (S2 Table). In the cerebellum, pairwise ΔC_t analysis identified *Mrpl10*, *Ppia* and *Sdha* as the top three most stable reference genes. The ranking of this method and NormFinder are quite similar in the cerebellum.

Table 1. Expression stability of candidate reference genes in cerebellum and spinal cord evaluated using Coefficient of Variation (CV) Analysis, NormFinder, GeNorm and the Pairwise ΔCt method.

Cerebellum											
CV Analysis			Norm Finder			GeNorm			Pairwise ΔCt		
Gene	CV%	Rank	Gene	Stability S	Rank	Gene	Stability M	Rank	Gene	Average SD	Rank
<i>Mrpl10</i>	30.4	1	<i>Ppia</i>	0.31	1	<i>Gapdh</i>	0.37	1	<i>Mrpl10</i>	0.608	1
<i>Actb</i>	31.9	2	<i>Mrpl10</i>	0.33	2	<i>Tbp</i>	0.37	1	<i>Ppia</i>	0.652	2
<i>Rps26</i>	35.3	3	<i>Sdha</i>	0.47	3	<i>Hsp60</i>	0.44	2	<i>Sdha</i>	0.698	3
<i>Ppia</i>	36.8	4	<i>Rps26</i>	0.48	4	<i>Sdha</i>	0.55	3	<i>Rps26</i>	0.699	4
<i>Hsp60</i>	42.6	5	<i>Pgk1</i>	0.49	5	<i>Pgk1</i>	0.59	4	<i>Hsp60</i>	0.745	5
<i>Rpl13a</i>	44.7	6	<i>Hsp60</i>	0.5	6	<i>Mrpl10</i>	0.63	5	<i>Pgk1</i>	0.751	6
<i>Sdha</i>	45.2	7	<i>Actb</i>	0.55	7	<i>Ppia</i>	0.65	6	<i>Actb</i>	0.758	7
<i>Pgk1</i>	47.3	8	<i>Rpl13a</i>	0.58	8	<i>Rps26</i>	0.69	7	<i>Gapdh</i>	0.813	8
<i>Tbp</i>	57.2	9	<i>Gapdh</i>	0.62	9	<i>Actb</i>	0.71	8	<i>Tbp</i>	0.82	9
<i>Gapdh</i>	59.1	10	<i>Tbp</i>	0.68	10	<i>Rpl13a</i>	0.74	9	<i>Rpl13a</i>	0.83	10

Spinal Cord											
CV analysis			Norm Finder			GeNorm			Pairwise ΔCt		
Gene	CV%	Rank	Gene	Stability S	Rank	Gene	Stability M	Rank	Gene	Average SD	Rank
<i>Actb</i>	28.1	1	<i>Mrpl10</i>	0.29	1	<i>Mrpl10</i>	0.19	1	<i>Hsp60</i>	0.535	1
<i>Ppia</i>	32.8	2	<i>Ppia</i>	0.3	2	<i>Rpl13a</i>	0.19	1	<i>Mrpl10</i>	0.536	2
<i>Rps26</i>	36	3	<i>Hsp60</i>	0.3	3	<i>Pgk1</i>	0.39	2	<i>Pgk1</i>	0.544	3
<i>Mrpl10</i>	40.5	4	<i>Rpl13a</i>	0.35	4	<i>Hsp60</i>	0.44	3	<i>Ppia</i>	0.554	4
<i>Rpl13a</i>	42.8	5	<i>Tbp</i>	0.39	5	<i>Tbp</i>	0.46	4	<i>Tbp</i>	0.565	5
<i>Hsp60</i>	49.4	6	<i>Actb</i>	0.44	6	<i>Ppia</i>	0.48	5	<i>Rpl13a</i>	0.593	6
<i>Pgk1</i>	57.7	7	<i>Pgk1</i>	0.45	7	<i>Gapdh</i>	0.51	6	<i>Actb</i>	0.623	7
<i>Tbp</i>	58.6	8	<i>Gapdh</i>	0.5	8	<i>Sdha</i>	0.53	7	<i>Gapdh</i>	0.665	8
<i>Gapdh</i>	59.2	9	<i>Sdha</i>	0.62	9	<i>Actb</i>	0.55	8	<i>Sdha</i>	0.706	9
<i>Sdha</i>	72.1	10	<i>Rps26</i>	0.83	10	<i>Rps26</i>	0.63	9	<i>Rps26</i>	0.934	10

<https://doi.org/10.1371/journal.pone.0219440.t001>

However, in the spinal cord the top three genes were identified as *Hsp60*, *Mrpl10* and *Pgk1*, noticeably different from the NormFinder rankings.

The overall ranking of genes across all methods recapitulated in Table 1 show that the stability ranking of reference genes can indeed vary significantly depending on the tissue studied and the method used for validation. This makes the identification of the best reference genes very cumbersome.

Suitability of validation methods for longitudinal studies

We next analyzed the suitability of these methods in a longitudinal setting highlighting the assumptions of each method and the factors that influence the stability scores.

CV analysis. As mentioned, the CV analysis adopts a direct approach by calculating the variance of a gene across all samples taken together. However, this method does not consider the variation across different time points or groups. For example, *Actb* is ranked 2nd in the cerebellum (Table 1) as it exhibits low overall variation but the profile of the gene (Fig 2A) tells us that it does vary across time points. This is a major concern in a longitudinal study as this method determines variation in just one dimension whereas the dataset exists in two dimensions.

NormFinder analysis. The NormFinder approach is more robust as it calculates the stability based on the intergroup and intragroup variation. However, on inspecting the algorithm

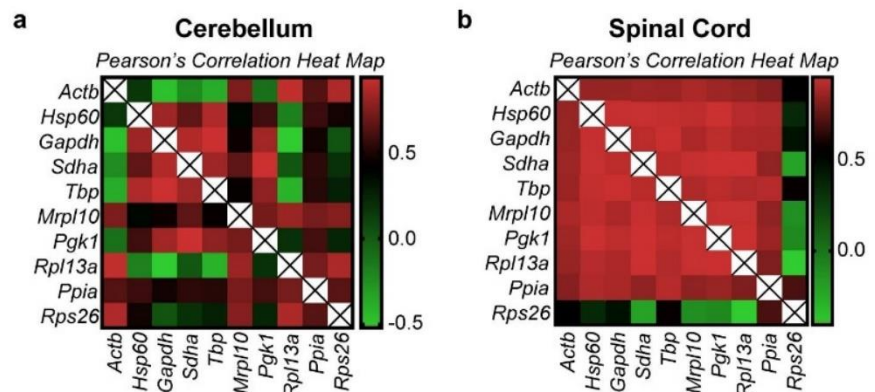


Fig 4. Pearson's correlation heatmap of the linearized Cq values (2^{-Cq}) of all genes. Pearson's correlation of all genes was performed to identify the extent of expression correlation in (a) cerebellum and (b) spinal cord. The colour scheme is denoted next to each heatmap. The numerical values used in the colour scheme represent the Pearson's r score. $r = 0$ (no correlation), $r = +0.5$ (positive correlation), $r = -0.5$ (negative correlation). r values closer to +1 or -1 denote strong positive and negative correlations respectively. The diagonal lines marked with an "X" are indicative of the correlation of a gene with itself and therefore is omitted from analysis.

<https://doi.org/10.1371/journal.pone.0219440.g004>

further, we found that including genes with high overall variation can affect the stability rankings of all the genes. Consider the overall variation of *Actb* in the spinal cord (Fig 3A). It has a CV of 28.1% (Table 1), which is the least among all genes in that group. Furthermore, the profile of *Actb* in the spinal cord is almost flat with minimal variation across groups (Fig 3A). Nevertheless, it is ranked 6th in the NormFinder method. *Hsp60* and *Rpl13a*, on the other hand, with a higher overall variance and significant intergroup variation when compared to *Actb* (Fig 3A, Fig 3B and Fig 3H) are ranked 3rd and 4th. *Hsp60* is in fact attributed the same stability value as *Ppia* which is ranked 2nd. This possible flaw in the algorithm is because of the presence of genes with high overall variations. Hence, the NormFinder algorithm can potentially be improved after identifying and removing genes with high overall variation (See Towards an integrated approach).

GeNorm analysis. The GeNorm algorithm as explained earlier ranks genes based on pairwise correlation. Hence, there is a possibility that this method could estimate correlated and co-regulated genes to be highly stable. To validate the rankings of this algorithm we performed Pearson's correlation on the linearized Cq values of all genes and samples (Fig 4, S3 Table and S4 Table). We observed two distinct patterns of correlation in the cerebellum and the spinal cord, the cerebellum being more heterogeneous. In the spinal cord, almost all genes tested exhibit a positive correlation except *Actb* which correlates less and *Rps26* which exhibits negative correlation with most of the other genes. This is also evident from the raw expression profiles where we see that the raw expression profiles in the cerebellum are heterogeneous (Fig 2). In the spinal cord, however, all the reference genes seem to have a similar profile except for *Actb* and *Rps26* (Fig 3).

Interestingly, the highest correlation in the cerebellum dataset was observed in *Gapdh/Tbp* with a Pearson's r score of 0.937. This gene pair is ranked first in the GeNorm analysis (Table 1) but have the highest overall variation in the group (CV = 59.1% and 57.2%). In the spinal cord, however, the top two genes according to GeNorm are *Mrpl10/Rpl13a* while the highest correlation is observed in *Sdha/Pgk1* with a Pearson's r score of 0.97. Intriguingly, the genes that are classed below—*Pgk1*, *Hsp60* and *Tbp* have CV values of 57.8%, 49.4% and 58.6%, which are among the highest in the spinal cord group. This is because of their

expression agreement with the top two genes. Seemingly stable genes such as *Ppia* (CV = 32.8%, Fig 3I) and *Actb* (CV = 28.1%, Fig 3A) are pushed to the lower half of the ranking (Table 1).

These results suggest that GeNorm tends to favor highly correlated genes in a heterogeneously correlated set of genes (cerebellum dataset). In a less heterogeneous dataset (spinal cord) the ranking does not concur with the overall stability of the genes across samples assessed by visual representation (Fig 3) and CV analysis (Table 1). These results taken together show that GeNorm's ranking can be influenced by the extent of correlation in the dataset. This exclusion of possibly stable genes by GeNorm because of negative or less correlation was indeed foreseen by Anderson and colleagues when they proposed the NormFinder model. We find that to be true in our analysis.

Pairwise Δ Ct Analysis. The pairwise Δ Ct approach seems to work better in a heterogeneously correlated set of genes. The rankings of NormFinder and the pairwise Δ Ct methods are rather identical in the cerebellum. However, in the spinal cord apart from *Mrpl10* the other top genes—*Pgk1* and *Hsp60*—show high variation across samples as explained earlier. The limitations of this method can also be observed in the spinal cord. *Actb*, which shows a rather flat profile (Fig 3A) is very distinct when compared to the others. It correlated very little with other genes (Fig 4B and S4 Table). This increases the difference in the Cq values between *Actb* and others resulting in a high Mean SD (stability value) thereby attributing it with a lower rank. Therefore, although a gene varies very little across samples and groups, the pairwise Δ Ct approach might attribute it with a lower rank if the profiles of the other genes are different. The same argument is also true for *Rps26* in the spinal cord (Fig 3J and Fig 4B)

In conclusion, we find that the ranking of all the methods except CV analysis is influenced by the inclusion of genes with high overall variation. Additionally, the pairwise expression stability methods (GeNorm and Pairwise Δ Ct) could produce misleading results depending on the profile of the highly variable genes together with the extent of expression correlation between all the genes.

Towards an integrated approach

The first step towards an integrated approach was to remove genes with high overall variance. CV analysis calculates the overall variance of each gene and it is the only method where the stability ranking of a gene is not influenced by others. We therefore used this method to objectively identify genes with high overall variance. We defined a threshold of CV = 50%. Genes that exhibit a CV above this value are taken to be highly variable and are excluded from further analysis. In the cerebellum, *Gapdh* and *Tbp* were removed and in the spinal cord *Gapdh*, *Tbp*, *Pgk1* and *Sdha* were removed from analysis. We next determined how this exclusion impacts the stability ranking of NormFinder, GeNorm and the Pairwise Δ Ct approach in both tissues (Table 2).

Ranking changes in NormFinder. As expected, exclusion of highly variable genes changed the overall ranking of the NormFinder algorithm in the cerebellum (Table 2). Although the top two genes remained the same, the ranking of other genes changed. *Sdha*, *Hsp60* and *Pgk1* that were ranked higher than *Actb* (Table 1) now obtained ranks lower than *Actb* (Table 2). The top three genes after exclusion of *Gapdh* and *Tbp* were identified as *Mrpl10*, *Ppia* and the third position is shared between *Rps26* and *Actb*. The most stable genes identified by NormFinder after exclusion (Table 2) concurs with the CV analysis (Table 1) and with the expression profiles of the genes (Fig 2A, Fig 2E, Fig 2I and Fig 2J) wherein the most stable genes exhibit minimal variation across time points.

Table 2. Revised rankings of candidate reference genes in cerebellum and spinal cord using NormFinder, GeNorm and the Pairwise Δ Ct method.

Cerebellum								
Norm Finder			GeNorm			Pairwise Δ Ct		
Gene	Stability S	Rank	Gene	Stability M	Rank	Gene	Average SD	Rank
<i>Mrpl10</i>	0.19	1	<i>Actb</i>	0.3	1	<i>Mrpl10</i>	0.529	1
<i>Ppia</i>	0.21	2	<i>Rpl13a</i>	0.3	1	<i>Ppia</i>	0.598	2
<i>Rps26</i>	0.45	3	<i>Rps26</i>	0.33	2	<i>Rps26</i>	0.614	3
<i>Actb</i>	0.45	4	<i>Mrpl10</i>	0.4	3	<i>Actb</i>	0.65	4
<i>Rpl13a</i>	0.47	5	<i>Ppia</i>	0.46	4	<i>Rpl13a</i>	0.703	5
<i>Sdha</i>	0.51	6	<i>Sdha</i>	0.57	5	<i>Sdha</i>	0.714	6
<i>Pgk1</i>	0.52	7	<i>Pgk1</i>	0.62	6	<i>Pgk1</i>	0.756	7
<i>Hsp60</i>	0.64	8	<i>Hsp60</i>	0.67	7	<i>Hsp60</i>	0.823	8

Spinal Cord								
Norm Finder			GeNorm			Pairwise Δ Ct		
Gene	Stability S	Rank	Gene	Stability M	Rank	Gene	Average SD	Rank
<i>Ppia</i>	0.22	1	<i>Mrpl10</i>	0.19	1	<i>Mrpl10</i>	0.472	1
<i>Mrpl10</i>	0.25	2	<i>Rpl13a</i>	0.19	1	<i>Ppia</i>	0.49	2
<i>Actb</i>	0.28	3	<i>Actb</i>	0.32	2	<i>Actb</i>	0.494	3
<i>Rpl13a</i>	0.35	4	<i>Ppia</i>	0.39	3	<i>Rpl13a</i>	0.537	4
<i>Hsp60</i>	0.48	5	<i>Hsp60</i>	0.47	4	<i>Hsp60</i>	0.68	5
<i>Rps26</i>	0.64	6	<i>Rps26</i>	0.58	5	<i>Rps26</i>	0.78	6

In the cerebellum, *Gapdh* and *Tbp* were excluded from analysis. In the spinal cord, 4 genes—*Sdha*, *Gapdh*, *Tbp* and *Pgk1* were excluded from analysis

<https://doi.org/10.1371/journal.pone.0219440.t002>

In the spinal cord, similar changes were observed. *Ppia* was now ranked above *Mrpl10* and these two were identified as the top two (Table 2). However, the third rank was now attributed to *Actb*. *Hsp60*, which was previously third finds itself in the lower half of the ranking. Again, the top three genes identified exhibit low overall variation in the spinal cord and their profiles exhibit minimal variation across timepoints (Fig 3A, Fig 3F and Fig 3I).

This indeed shows that exclusion of highly variable genes potentially improves the performance of the NormFinder method and can help in improving the quality of the results.

Ranking changes in GeNorm. The changes observed in GeNorm were more drastic in the cerebellum. The new rankings were almost the inverse of the previous rankings (Tables 1 and 2) with *Actb/Rpl13a* now identified as the most stable genes followed by *Rps26*, *Mrpl10* and *Ppia*. These results, although astonishing, made sense when interpreted with the raw expression profiles (Fig 2). In the absence of *Gapdh* and *Tbp*, the algorithm has chosen *Actb/Rpl13a* to be the most stable. Notice how the profiles of these two genes are very similar (Fig 2A and Fig 2H). The genes ranked just below also have as similar profile to these two. In effect, the previous GeNorm rankings (Table 1) were based on genes that had profiles similar to *Gapdh/Tbp* (U shaped curve) whereas the new rankings are based on genes with the exact inverted profile exhibited by *Actb* and *Rpl13a*. This change in ranking brings to evidence the possible biases that can occur when using GeNorm in a heterogeneously correlated data set.

In the spinal cord, however, the changes were not so drastic. The top two genes *Mrpl10/Rpl13a* remained the same (Tables 1 and 2). Nevertheless, the genes that were ranked below showed some noticeable change. *Actb* and *Ppia* are now ranked above *Hsp60*. In the spinal cord, most of the genes are correlated (Fig 4B) and their profiles look alike except *Rps26* (Fig 3J). Therefore, the top two genes did not change even after the exclusion of the highly variable genes. However, in the absence of these genes, the profile of *Actb* (Fig 3A) now looks more like

Mrpl10/Rpl13a than *Ppia* or *Hsp60* (Fig 3B, Fig 3E, Fig 3H and Fig 3I). This is a possible reason for the change in ranks observed.

These results taken together yet again show that GeNorm results can prove to be highly biased depending on the correlation observed in the dataset and the expression agreement between candidate genes.

Ranking changes in Pairwise Δ Ct method

In the cerebellum, the changes observed are very similar to the changes observed in the NormFinder algorithm (Table 2). *Mrpl10* and *Ppia* are still ranked as the top two. However, *Actb* and *Rpl13a* are now ranked above *Sdha*, *Pgk1* and *Hsp60*. Indeed, the removal of *Gapdh* and *Tbp* decreased the difference in Cq values between *Actb* and other genes thereby leading to lower Mean SD (higher ranks). The same is true for *Rpl13a*. Similarly, genes that resembled *Gapdh* and *Tbp* were now pushed to the bottom as their profiles look much different from the top ranked reference genes. In other words, the difference between their Cq values and the others have increased across all samples. Interestingly, the ranking of the Pairwise Δ Ct method and NormFinder seem to concur a lot both before and after exclusion of highly variable genes (Tables 1 and 2).

However, in the spinal cord, which shows high extent of homogenous correlation, the changes are rather significant. The top two genes now are *Mrpl10* and *Ppia*. This is followed by *Actb*. *Hsp60* which was ranked 1st before exclusion (Table 1) is now close to the bottom of the ranking along with *Rps26* (Table 2). The reason for this change is the same as stated for the cerebellum. Removal of genes with high overall variation results in genes that had a similar profile to the genes removed being classed lower. However, this also depends on the similarity of the rest of the genes with the profile of the new highly ranked genes. This is a significant hurdle as the ranking of genes becomes inter dependent even after the removal of highly variable genes. In the spinal cord, the ranking of this method after exclusion concurs with NormFinder (Table 2), that was previously not the case (Table 1).

Discussion

As each method analyzed in the study has its own advantages and drawbacks, using any of these methods alone would not be enough to have bias-free results. Neither would averaging the ranks of genes determined from all these methods. Hence, there is a need to devise an integrated approach that is based on the suitability of the method in a longitudinal setting.

Among the different methods tested in this developmental study, we find that the methods that rely on pairwise variation (GeNorm and Pairwise Δ Ct method) are ill suited for reference gene validation. However, it should be noted that the predictions of the Pairwise Δ Ct method did improve after the exclusion of highly variable genes. Nevertheless, the ranking inter-dependency does pose a major problem for a longitudinal study.

Regarding the other two methods, the major drawback of the CV analysis is that it does not factor in the variation between groups but can however determine the absolute overall variation. The major drawback of the NormFinder method is that the stability ranking of the method is influenced by genes with high overall variation. It can however calculate stability based on both intergroup and intragroup variation. Hence, using these two methods in tandem would negate their respective drawbacks. It goes without saying that visual representation of the raw expression profiles is also an additional tool that can be used to validate the findings of these two methods.

Taking all these factors into account, we propose an integrated approach that uses CV analysis, visual representation (with ANOVA) and NormFinder to assess the best set of reference

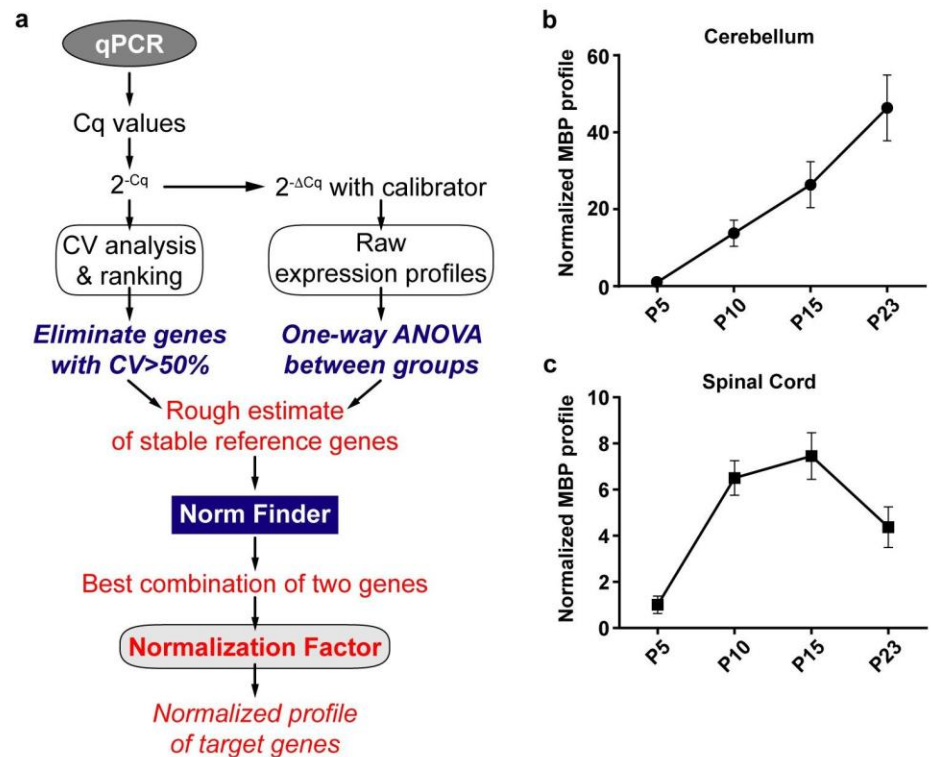


Fig 5. Integrated approach to determine the best reference genes in a longitudinal study. (a) Proposed qPCR Workflow (b) Normalized Mbp expression profile in the cerebellum using *Ppia* and *Mrpl10*. (c) Normalized Mbp expression profile in the spinal cord using *Ppia* and *Mrpl10*.

<https://doi.org/10.1371/journal.pone.0219440.g005>

genes for a longitudinal study (Fig 5). This method also recapitulates the method used in this study.

Once the Cq values of all samples and genes are obtained from qPCR, they are linearized, and CV analysis is performed. Parallely, using the experimental calibrator, the raw experimental profiles of all candidate genes are plotted as fold changes ($2^{-\Delta Cq}$). This is followed by One-way ANOVA to assess the variation among all groups. It should be noted that ANOVA is used just to assess if there is significant statistical variation among the means of the groups. It does not assess, by any means, the extent of this variation. Thus, visual representation along with the results of CV analysis and ANOVA can help us obtain a rough estimate of the most stable reference genes. At this stage, genes that exhibit $CV > 50\%$ are removed. The rest of the genes are then subjected to the NormFinder algorithm. The algorithm then ranks the genes based on intergroup and intragroup variation. It also detects the best two genes that can be used for normalization with a grouped stability value. These two genes are then used to calculate a normalizing factor to normalize all target genes.

In our study, the integrated approach detected *Mrpl10* and *Ppia* as the two best genes in both tissues with a grouped stability of $S = 0.17$ in the cerebellum and $S = 0.11$ in the spinal cord. Nevertheless, we cannot be sure if the same genes would be the best references if another time point was added or if one of the time points studied here is removed. This limitation indeed exists for all reference gene validation studies. In other words, the best reference gene (s) identified by any study using any method is only suitable for that experimental setting and cannot be extrapolated.

Apart from the parameters that have been identified in this study that contribute to the suitability of a method, certain other factors are to be considered while constructing a validation study. Indeed, simple factors such as the total sample size and number of candidate reference genes play an important role on the suitability of a statistical method [22]. Similar issues have been detailed and standard guidelines have been established to facilitate standardization and reproducibility of qPCR assays [23].

A notable limitation of this study is the choice of the candidate reference genes. The candidates were chosen as they have been conventionally used for normalization of differential expression in the Central Nervous System. This means that we could have potentially excluded unknown and undiscovered stable references. A more thorough approach would be to choose candidate genes from high-throughput data to avoid this inherent bias [24–26].

In this study we analyzed four commonly used statistical methods. Indeed, other methods have been proposed to validate reference genes. Notably, the RefFinder [10] and the Best-Keeper [27] algorithms have been used commonly in a multitude of studies that validate reference genes. Although we have not used them in our study, we have identified some key issues in their approaches. The RefFinder is a combinatory method that takes into consideration the stability rankings of GeNorm, NormFinder, BestKeeper and the Pairwise Δ Ct method. Depending on the rankings of the candidate genes across these different algorithms, it attributes an ordinal “weight” for each candidate gene. The final rankings are then computed as the geometric mean of the weighted rankings. We emphasize that such an approach is not scientifically sound as it does not consider the merits and demerits of these algorithms in a longitudinal setting. We therefore find that the rankings of the RefFinder tool is merely arithmetic in nature and has no intrinsic scientific rigor or validity. This observation has also been pointed out previously by De Spiegelaere and colleagues in their study [22].

The BestKeeper algorithm assesses stability based on Pearson’s correlation of candidate gene Cq values with the BestKeeper Index. Firstly, the algorithm eliminates genes that it considers highly variable by calculating the Standard Deviation of candidate gene Cq values across all samples. The authors define a threshold of SD = 1 cycle (RNA quantity difference by a factor of 2). Any gene that exhibits SD > 1 is deemed highly variable and removed from further analysis.

We remark that this threshold of SD = 1 is too lenient as it is calculated using just the Cq values where the actual fold changes in RNA quantities are underestimated. From our data (S5 Table), we find that genes that exhibit SD < 1 (below BestKeeper Threshold) in Cq values can exhibit CV values (of 2^{-Cq}) well above 50% which we believe is indicative of high variation in RNA fold changes. In turn, this elimination process based solely on variation in Cq values can decrease the robustness of the algorithm as it is dependent on the elimination of highly variable genes. We have also observed using our data that the Pearson’s correlation analysis (the core of the BestKeeper algorithm) of Cq values are largely different from the correlation analysis of 2^{-Cq} values with significant differences in Pearson’s r score. As minor changes in Cq values can imply huge changes in RNA quantities, correlation analysis of Cq values would produce a biased assessment of the actual correlation present in RNA quantities. We thus believe that this algorithm can potentially be improved by taking these factors into consideration.

Finally, the integrated approach proposed in this study is only applicable for a longitudinal setting. How these methods fare in cross sectional studies remains to be explored. However, the approach proposed in this study addresses an important observation that has been constantly made but systematically overlooked in validation studies. Our integrated approach, in effect, is contradictory to previously held notions that all statistical approaches are applicable to any experimental setting and that a minimum of three different statistical approaches are

Each reaction was performed in triplicates. All qPCR experiments were performed on BioRad CFX384.

Primer design

All primers used in the study were designed using the Primer 3 plus software (<https://primer3plus.com/cgi-bin/dev/primer3plus.cgi>). Splice variants and the protein coding sequence of the genes were identified using the Ensembl database (www.ensembl.org). Constitutively expressed exons among all splice variants were then identified using the ExonMine database (www.imm.fm.ul.pt/exonmine/). Primer sequences that generated amplicons spanning two constitutively expressed exons were then designed using the Primer 3 plus software. For detailed information on Primer sequences refer to [Table 3](#).

Amplification efficiencies

The amplification efficiencies of primers were calculated using serial dilution of cDNA molecules. Briefly, cDNA preparations from Cerebella and Spinal cords from different age groups of mice were pooled and serially diluted three times by a factor of 10. qPCR was then performed using these dilutions and the results were plotted as a standard curve against the respective concentration of cDNA. Amplification efficiency (E) was calculated by linear regression of standard curves using the following equation

$$E = 10^{-\frac{1}{\text{slope of the standard curve}}}$$

Table 3. Details of the primer sequences used in the study.

GENE	Gene Name	Refseq ID	Sequence	Primers	Primer length	Amplicon length	Efficiency
<i>Actb</i>	<i>Actin Beta</i>	NM_007393.5	Forward	ATGGTGGGAATGGGTGAGAAG	21 bp	94 bp	98%
			Reverse	TGCCATGTCTCAATGGGGTAC	20 bp		
<i>Gapdh</i>	<i>Glyceraldehyde-3-phosphate dehydrogenase</i>	NM_001289726.1	Forward	GTGGACCTCATGGCCTACAT	20 bp	125 bp	97%
			Reverse	TGTGAGGGAGATGCTCAGTG	20 bp		
<i>Hsp60</i>	<i>Heat Shock Protein Family D Member 1</i>	NM_001356512.1	Forward	AGCACGCTGGTTTGAACAG	20 bp	132 bp	97%
			Reverse	TTCTCCAACACTGCACCAC	20 bp		
<i>Tbp</i>	<i>TATA Box Binding Protein</i>	NM_013684.3	Forward	CAGCAGTTCAGTAGCTATGAGC	22 bp	129 bp	101%
			Reverse	CTCTGCTCTAACTTTAGCACCTG	23 bp		
<i>Mrp10</i>	<i>Mitochondrial Ribosomal Protein L10</i>	NM_026154.3	Forward	AGCTGCGGAAACACAAGATC	20 bp	97 bp	100%
			Reverse	AAAAGGGGTAGCAGGTTTCG	20 bp		
<i>Sdha</i>	<i>Succinate Dehydrogenase Complex Subunit A</i>	NM_023281.1	Forward	AGAAAGGCCAAATGCAGCTC	20 bp	131 bp	96%
			Reverse	GTGAGAACAAGAAGGCATCAGC	22 bp		
<i>Pgk1</i>	<i>Phosphoglycerate Kinase 1</i>	NM_008828.3	Forward	ACGGTGTGCCAAAATGTCG	20 bp	150 bp	105%
			Reverse	TTGGAACAGCAGCCTTGATC	20 bp		
<i>Rpl13a</i>	<i>Ribosomal Protein L13a</i>	NM_009438.5	Forward	TACGCTGTGAAGGCATCAAC	20 bp	88 bp	102%
			Reverse	TTGGTATTCATCCGCTTCCG	20 bp		
<i>Ppia</i>	<i>Peptidylprolyl Isomerase A</i>	NM_008907.1	Forward	GGCAAATGCTGGACCAAAC	19 bp	149 bp	105%
			Reverse	CATTCTGGACCCAAAACG	19 bp		
<i>Rps26</i>	<i>Ribosomal Protein S26</i>	NM_013765.2	Forward	TGCCATCCATAGCAAGGTTG	20 bp	129bp	93%
			Reverse	AAACGGCCTCTTTACATGGG	20 bp		
<i>Mbp</i>	<i>Myelin Basic Protein</i>	NM_001025259.2	Forward	ACTCACACACGAGAACTACCC	21 bp	118 bp	98%
			Reverse	GGTGTTCGAGGTGTCACAATG	21 bp		

<https://doi.org/10.1371/journal.pone.0219440.t003>

Primer pairs that exhibited an Amplification Efficiency (E) of 1.93 to 2.05 (93% - 105%) and an R^2 value (Determination Coefficient) of 0.98 or above were chosen for this study.

qPCR data analysis & visualization

qPCR readouts were analyzed in Precision Melt Analysis Software v1.2. The amplicons were subjected to Melt Curve analysis and were verified for a single dissociation peak at a Melting Temperature (T_m) $> 75^\circ\text{C}$ as expected from the primer constructs. The Cq data was exported to Microsoft Excel for further calculations. Each biological sample had 3 technical replicates thereby generating 3 individual Cq values. The arithmetic mean of the triplicates was taken to be the Cq representing the biological sample. The standard deviation (SD) of the triplicates was also calculated and samples that exhibited $SD > 0.25$ were considered inconsistent. In such cases, one outlier Cq was removed so as to have at least duplicate Cq values for each biological sample and an $SD < 0.25$.

Statistical analysis

Statistical analysis for reference gene validation was performed using R software packages and Microsoft Excel. GeNorm [18] analysis was performed using the ReadqPCR and NormqPCR packages in R [29]. Normfinder [19] analysis was performed using NormFinder for R (<https://moma.dk>). Co-efficient of Variance Analysis was performed in Microsoft Excel. The Cq values were first transformed to a linear scale (linearization) by calculating 2^{-Cq} for each sample. CV analysis was then performed on 2^{-Cq} values (S1 Table). Pairwise ΔCt analysis was also performed in Microsoft Excel (S2 Table).

To assess statistical difference in RNA quantities between groups, One-way ANOVA was performed in Graph Pad Prism v7.0. Pearson's correlation matrix of reference genes and the heat maps were also generated in Graph Pad Prism v7.0.

The normalization factor was determined by first calculating the arithmetic mean of the Cq values from the 2 best genes determined by the workflow. The mean Cq values were linearized and then used to normalize target genes using the $2^{-\Delta\Delta\text{Ct}}$ method [30,31]. The P5 group was used as the experimental calibrator. Data was visualized using Graph Pad Prism v7.0.

Supporting information

S1 Table. CV analysis example. The Cq values of all samples are linearized. The CV is then calculated as the ratio of the SD to the mean of the linearized Cq values. It is expressed as a percentage. A lower CV value would mean lower variation across samples and therefore higher stability.

(DOCX)

S2 Table. Pairwise ΔCt analysis example. The table shows the stability calculation by the Pairwise ΔCt method for *Actb*. It is a table of Cq value differences between *Actb* and all the other genes. Each row represents a sample and each column represents a gene. The difference in Cq values between *Actb* and the others is first calculated across all samples. Therefore, the first column has 0s (difference in Cq of *Actb* with itself) Next, the standard deviation of the differences is calculated at the end of each column indicated by SD. The stability value (Average SD) of *Actb* is then calculated as the arithmetic mean of these standard deviations.

(DOCX)

S3 Table. Pearson's correlation matrix for the cerebellum.

(DOCX)

S4 Table. Pearson's correlation matrix for the spinal cord.
(DOCX)

S5 Table. Raw qPCR output data.
(XLSX)

Acknowledgments

The authors did not receive any specific funding for this study. The authors would like to thank Paris Descartes University and INSERM. V.K.S. and N.K.S. received their PhD fellowships from the French Ministry of Research and Innovation. The authors would like to acknowledge Céline Becker and Claire Mader (Saints-Pères Animal Facility) for the breeding and management of the animals used in the study.

Author Contributions

Conceptualization: Venkat Krishnan Sundaram, Nirmal Kumar Sampathkumar.

Formal analysis: Venkat Krishnan Sundaram, Nirmal Kumar Sampathkumar.

Investigation: Venkat Krishnan Sundaram, Nirmal Kumar Sampathkumar.

Methodology: Venkat Krishnan Sundaram.

Validation: Charbel Massaad, Julien Grenier.

Visualization: Julien Grenier.

Writing – original draft: Venkat Krishnan Sundaram.

Writing – review & editing: Nirmal Kumar Sampathkumar, Charbel Massaad, Julien Grenier.

References

1. Bustin SA. Absolute quantification of mRNA using real-time reverse transcription polymerase chain reaction assays [Internet]. *Journal of Molecular Endocrinology*. 2000. Available: <http://www.endocrinology.org>
2. Thellin O, Zorzi W, Lakaye B, De Borman B, Coumans B, Hennen G, et al. Housekeeping genes as internal standards: use and limits [Internet]. *Journal of Biotechnology*. 1999. Available: www.elsevier.com/locate/jbiotec
3. Kozera B, Rapacz M. Reference genes in real-time PCR. *J Appl Genet*. Springer Berlin Heidelberg; 2013; 54: 391–406. <https://doi.org/10.1007/s13353-013-0173-x> PMID: 24078518
4. Dheda K, Huggett JF, Chang JS, Kim LU, Bustin SA, Johnson MA, et al. The implications of using an inappropriate reference gene for real-time reverse transcription PCR data normalization. *Anal Biochem*. Academic Press; 2005; 344: 141–143. <https://doi.org/10.1016/J.AB.2005.05.022> PMID: 16054107
5. Lee JM, Roche JR, Donaghy DJ, Thrush A, Sathish P. Validation of reference genes for quantitative RT-PCR studies of gene expression in perennial ryegrass (*Lolium perenne* L.). *BMC Mol Biol*. BioMed Central; 2010; 11: 8. <https://doi.org/10.1186/1471-2199-11-8> PMID: 20089196
6. Langnaese K, John R, Schweizer H, Ebmeyer U, Keilhoff G. Selection of reference genes for quantitative real-time PCR in a rat asphyxial cardiac arrest model. *BMC Mol Biol*. BioMed Central; 2008; 9: 53. <https://doi.org/10.1186/1471-2199-9-53> PMID: 18505597
7. Spinsanti G, Panti C, Bucalossi D, Marsili L, Casini S, Frati F, et al. Selection of reliable reference genes for qRT-PCR studies on cetacean fibroblast cultures exposed to OCs, PBDEs, and 17 β -estradiol. *Aquat Toxicol*. Elsevier; 2008; 87: 178–186. <https://doi.org/10.1016/J.AQUATOX.2008.01.018> PMID: 18339435
8. Cheung TT, Weston MK, Wilson MJ. Selection and evaluation of reference genes for analysis of mouse (*Mus musculus*) sex-dimorphic brain development. *PeerJ*. PeerJ, Inc; 2017; 5: e2909. <https://doi.org/10.7717/peerj.2909> PMID: 28133578

9. Freitag D, Koch A, Lawson Mclean A, Kalff R, Walter J. Validation of Reference Genes for Expression Studies in Human Meningiomas under Different Experimental Settings. *Mol Neurobiol. Molecular Neurobiology*; 2017; 1–11. <https://doi.org/10.1007/s12035-015-9635-y>
10. Xie F, Xiao P, Chen D, Xu L, Zhang B. miRDeepFinder: a miRNA analysis tool for deep sequencing of plant small RNAs. *Plant Mol Biol. Springer Netherlands*; 2012; 80: 75–84. <https://doi.org/10.1007/s11103-012-9885-2> PMID: 22290409
11. Perez LJ, Rios L, Trivedi P, D'Souza K, Cowie A, Nzirorera C, et al. Validation of optimal reference genes for quantitative real time PCR in muscle and adipose tissue for obesity and diabetes research. *Sci Rep. Nature Publishing Group*; 2017; 7: 3612. <https://doi.org/10.1038/s41598-017-03730-9> PMID: 28620170
12. Kang Y, Wu Z, Cai D, Lu B. Evaluation of reference genes for gene expression studies in mouse and N2a cell ischemic stroke models using quantitative real-time PCR. *BMC Neurosci. BioMed Central*; 2018; 19: 3. <https://doi.org/10.1186/s12868-018-0403-6> PMID: 29390963
13. Rydbirk R, Folke J, Winge K, Aznar S, Pakkenberg B, Brudek T. Assessment of brain reference genes for RT-qPCR studies in neurodegenerative diseases. *Sci Rep. Nature Publishing Group*; 2016; 6: 37116. <https://doi.org/10.1038/srep37116> PMID: 27853238
14. Mallona I, Lischewski S, Weiss J, Hause B, Egea-Cortines M. Validation of reference genes for quantitative real-time PCR during leaf and flower development in *Petunia hybrida*. *BMC Plant Biol. BioMed Central*; 2010; 10: 4. <https://doi.org/10.1186/1471-2229-10-4> PMID: 20056000
15. Fu Y, Rusznák Z, Herculano-Houzel S, Watson C, Paxinos G. Cellular composition characterizing post-natal development and maturation of the mouse brain and spinal cord. *Brain Struct Funct. Springer Berlin Heidelberg*; 2013; 218: 1337–1354. <https://doi.org/10.1007/s00429-012-0462-x> PMID: 23052551
16. Hughes EG, Appel B. The cell biology of CNS myelination. *Curr Opin Neurobiol.* 2016; 39: 93–100. <https://doi.org/10.1016/j.conb.2016.04.013> PMID: 27152449
17. Bercury KK, Macklin WB. Dynamics and mechanisms of CNS myelination. *Dev Cell. Elsevier*; 2015; 32: 447–58. <https://doi.org/10.1016/j.devcel.2015.01.016> PMID: 25710531
18. Vandesompele J, De Preter K, Pattyn F, Poppe B, Van Roy N, De Paepe A, et al. Accurate normalization of real-time quantitative RT-PCR data by geometric averaging of multiple internal control genes. *Genome Biol.* 2002; 3: RESEARCH0034. <https://doi.org/10.1186/gb-2002-3-7-research0034> PMID: 12184808
19. Andersen C, Jensen J, Orntoft T. Normalization of Real - Time Quantitative Reverse Transcription - PCR Data: A Model - Based Variance Estimation Approach to Identify Genes Suited for Normalization, Applied to Bladder and Colon Cancer Data Sets. *Cancer Res.* 2004; 64: 5245. <https://doi.org/10.1158/0008-5472.CAN-04-0496> PMID: 15289330
20. Boda E, Pini A, Hoxha E, Parolisi R, Tempia F. Selection of Reference Genes for Quantitative Real-time RT-PCR Studies in Mouse Brain. *J Mol Neurosci. Humana Press Inc*; 2009; 37: 238–253. <https://doi.org/10.1007/s12031-008-9128-9> PMID: 18607772
21. Silver N, Best S, Jiang J, Thein SL. BMC Molecular Biology Selection of housekeeping genes for gene expression studies in human reticulocytes using real-time PCR. 2006; <https://doi.org/10.1186/1471-2199-7-33>
22. De Spiegelaere W, Dern-Wieloch J, Weigel R, Schumacher V, Schorle H, Nettersheim D, et al. Reference gene validation for RT-qPCR, a note on different available software packages. *PLoS One.* 2015; 10: 1–13. <https://doi.org/10.1371/journal.pone.0122515> PMID: 25825906
23. Bustin SA, Benes V, Garson JA, Hellemans J, Huggett J, Kubista M, et al. The MIQE Guidelines: Minimum Information for Publication of Quantitative Real-Time PCR Experiments. 2009; <https://doi.org/10.1373/clinchem.2008.112797> PMID: 19246619
24. Eisenberg E, Levanon EY. Human housekeeping genes, revisited. *Trends Genet. Elsevier*; 2013; 29: 569–74. <https://doi.org/10.1016/j.tig.2013.05.010> PMID: 23810203
25. Hoang VLT, Tom LN, Quek X-C, Tan J-M, Payne EJ, Lin LL, et al. RNA-seq reveals more consistent reference genes for gene expression studies in human non-melanoma skin cancers. *PeerJ. PeerJ, Inc*; 2017; 5: e3631. <https://doi.org/10.7717/peerj.3631> PMID: 28852586
26. Zhou Z, Cong P, Tian Y, Zhu Y. Using RNA-seq data to select reference genes for normalizing gene expression in apple roots. <https://doi.org/10.1371/journal.pone.0185288> PMID: 28934340
27. Pfaffl MW, Tichopad A, Prgomet C, Neuvians TP. Determination of stable housekeeping genes, differentially regulated target genes and sample integrity: BestKeeper—Excel-based tool using pair-wise correlations. *Biotechnol Lett.* 2004; 26: 509–15. Available: <http://www.ncbi.nlm.nih.gov/pubmed/15127793> PMID: 15127793
28. Jacob F, Guertler R, Naim S, Nixdorf S, Fedier A, Hacker NF, et al. Careful Selection of Reference Genes Is Required for Reliable Performance of RT-qPCR in Human Normal and Cancer Cell Lines.

- Huang S, editor. PLoS One. Public Library of Science; 2013; 8: e59180. <https://doi.org/10.1371/journal.pone.0059180> PMID: [23554992](https://pubmed.ncbi.nlm.nih.gov/23554992/)
29. Perkins JR, Dawes JM, McMahon SB, Bennett DLH, Orengo C, Kohl M. ReadqPCR and NormqPCR: R packages for the reading, quality checking and normalisation of RT-qPCR quantification cycle (Cq) data. BMC Genomics. 2012; 13. <https://doi.org/10.1186/1471-2164-13-296> PMID: [22748112](https://pubmed.ncbi.nlm.nih.gov/22748112/)
 30. Schmittgen TD, Livak KJ. Analyzing real-time PCR data by the comparative C(T) method. Nat Protoc. 2008; 3: 1101–8. Available: <http://www.ncbi.nlm.nih.gov/pubmed/18546601> PMID: [18546601](https://pubmed.ncbi.nlm.nih.gov/18546601/)
 31. Livak KJ, Schmittgen TD. Analysis of relative gene expression data using real-time quantitative PCR and the $2^{-\Delta\Delta CT}$ Method. Methods. 2001; 25: 402–408. <https://doi.org/10.1006/meth.2001.1262> PMID: [11846609](https://pubmed.ncbi.nlm.nih.gov/11846609/)

Supplementary Data sets:

The supplementary data sets of this study could not be presented due to space restrictions. They are available as excel documents online at

<https://journals.plos.org/plosone/article?id=10.1371/journal.pone.0219440>

Perspectives:

The findings of this study were presented at the qPCR/NGS conference 2019 held in TUM Munich as a poster. The conference concluded that RNA-seq data should be a prerequisite to select suitable candidate reference genes. We, however, are of the opinion that the statistical methods used for reference gene validation are more important than the pre-selection of 'ideal' candidates from RNA-seq data.

We are in the process of exploring this hypothesis using RNA-seq data from two tissues: the liver and the sciatic nerve of mice at P3 and P21. Using RNA-seq, we have shortlisted suitable candidate reference genes in both tissues. Using our qPCR workflow, we are now comparing their efficacy in data normalization. We are also comparing their efficiency to that of a standard set of reference genes used in the study elucidated herein.

Our hypothesis is that the selection of 'good' candidate reference genes from RNA seq does not offer a significant advantage over traditional reference genes if both are subjected to the same workflow that determines the best reference genes from a given set of candidates. The article that summarizes this study is currently under preparation and will be submitted by fall 2020.

2.2.3 Extracting sufficient amounts of RNA from mouse sciatic nerves across all ages

Context of the study:

Extracting sufficient amounts of RNA from peripheral nerves proves to be cumbersome process as the tissue is enriched in lipids (from the myelin sheath) and collagens (from the Extra-Cellular-Matrix). Lipids hinder tissue lysis and homogenization at the cellular level and collagens can entrap nucleic acids thus posing two major hurdles in isolating total RNA from sciatic nerves. Furthermore, in neonates (till P3 – P4), the tissue size is too small, thereby rendering scanty amounts of RNA for downstream applications. Hence, it is common practice to pool different biological replicates to obtain sufficient yields. This, however, is disadvantageous if the study aims to quantify intrinsic gene expression variation in a given population. Hence, the primary objective of the study was to devise an RNA extraction protocol that can render sufficient yields (greater than 500ng) from mouse sciatic nerves irrespective of the age and the tissue size.

We demonstrate that the use of the Trizol method with significant modifications can render consistent and sufficient yields of RNA from sciatic nerves starting from P0 mice to any postnatal age. We have compared our protocol to another liquid phase extraction proposed originally by Prof. Sacchi and colleagues (Chomczynski and Sacchi, 1987) as well a popular silica column based extraction kit (mirVana from Ambion Technologies). We compared each protocol based on criteria such as absorbance ratios, yield consistency across UV spectrophotometry assays (Nanodrop) and Florescence assays (Agilent Bioanalyzer) and an additional validation using RTqPCR.

Our results demonstrate that the Trizol method renders consistent and copious yields across all post-natal timepoints. Furthermore, RNA extracted through Trizol shows very little difference in total yield when measured through Nanodrop and Bioanalyzer. In the other two methods, we observe that the Nanodrop concentrations are highly overestimated when compared to the Bioanalyzer estimates. This issue is probably because of the co-precipitation of free nucleotides in the other two methods. In Trizol samples, however, the co-precipitation is negligible and thus the concentration estimates across the two methods only vary by a small margin. These results are detailed in the article attached in the following pages (Sundaram et al 2020, submitted)

A step-by-step depiction of our modified protocol is described in the figure below (Figure 22)

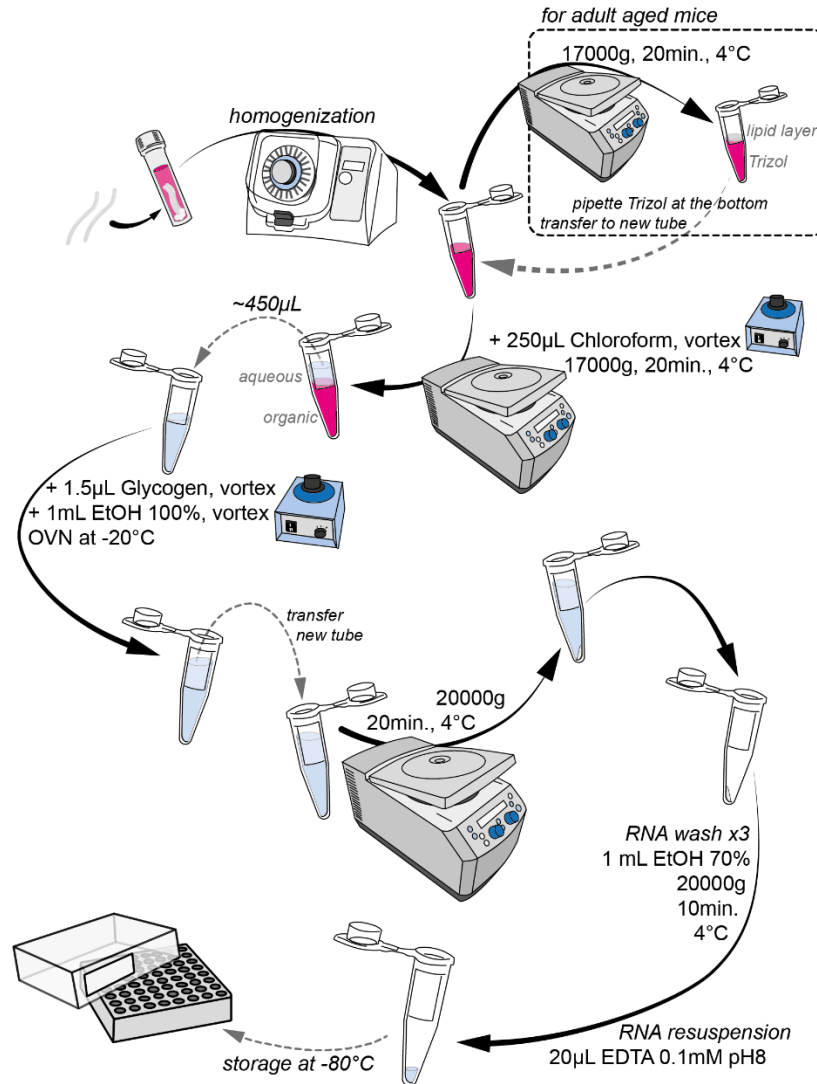


Figure 22: Detailed description of the different steps of RNA extraction from Sciatic Nerves using Trizol. Tissues are harvested from mice and immediately placed in 1mL of Trizol solution in Fisherband Tubes. They are then incubated for 10 minutes on ice. Next, samples are homogenized in a bead mill homogenizer. Tissue homogenates are then transferred to a new eppendorf tube (1.5mL). For adult and aged mice, a preliminary centrifugation step is performed with the lysates to bring the lipid layer to the top. Trizol is then pipetted out from the bottom carefully and transferred to a new tube. 250µL of Chloroform is added to the lysate and the tubes are vortexed for 15sec – 30sec. Samples are then placed at room temperature for 3 minutes followed by centrifugation at 17000g for 20 minutes at 4°C. The organic phase separates from the aqueous phase post centrifugation. The aqueous phase, which contains the RNA is then carefully transferred to a new tube. 1.5µL of glycogen is added to each sample and the tubes are briefly vortexed. This is followed by the addition of 1mL 100% Ethanol and the tubes are again vortexed briefly. The samples are then placed at -20°C overnight to facilitate RNA precipitation. The following day, the contents of the tube are transferred to a new one followed by centrifugation at 20000g for 20 min at 4°C. The supernatant is decanted, and the pellet is washed with 70%

Ethanol at least thrice before being dried in a speed-vac. Dry RNA is then resuspended in 20 μ L of RNA resuspension buffer (0.1mM EDTA, pH 8) and stored at -80°C till RTqPCR. Source: (Sundaram et al 2020, submitted for review)

Triz'Old is gold : A reliable and efficient method to extract total RNA from mouse sciatic nerves across all ages

Venkat Krishnan Sundaram ^{1*}, Rasha Barakat ^{1,2}, Nirmal Kumar Sampathkumar ¹, Julien Grenier ¹, Franck Letourneur ², Laure Weill ^{1*}

1. INSERM U1124, Faculty of Basic and Biomedical Sciences, Campus Saint Germain Des Prés, Université de Paris, Paris, France
2. INSERM U1016, Institut Cochin, Paris, France

*Corresponding Authors:

Venkat Krishnan Sundaram
venkatkrishnan.sundaram@parisdescartes.fr

Laure Weill
laure.weill@parisdescartes.fr

Author Contributions:

VKS and RB designed the study. VKS, NKS, RB and FL performed the experiments. VKS analyzed the results and wrote the manuscript. LW validated the methodology and provided scientific inputs. JG prepared the figures. All authors reviewed and edited the manuscript. LW and VKS prepared the final draft for submission.

Acknowledgements:

We thank Maja Adamsen and Claire Mader from the *Animal House Core Facility* of BioMedTech (INSERM US36/CNRS UMS2009) for the handling of mice used in the study. We also thank the *Cyto2BM Molecular Biology Platform* of BioMedTech Facilities for the research equipment and other services pertaining to the generation of qPCR data. We also thank the Genomic Platform at Institut Cochin, Paris for the quality control of RNA samples. Finally, we thank Dr. Robert Fledrich for his valuable suggestions to standardize tissue harvesting and optimize tissue homogenization.

Funding:

No specific funding was sought for this study. VKS and NKS were funded by a PhD fellowship from the French Ministry of Research and Innovation and Université de Paris. RB was funded by CNRS Lebanon and a doctoral contract from INSERM U1016, Institut Cochin, Paris.

Conflict of interest:

The authors declare that there is no conflict of interest.

Abstract:

The sciatic nerve is extensively used in murine models that aim to study Schwann cell development, peripheral myelination, and associated pathologies. Quantifying differential gene expression through RTqPCR and RNA-seq forms an integral part of such studies. However, the extraction of total RNA from sciatic nerves for these applications proves to be difficult and results in inconsistent yields owing to the fact that the tissue is rich in lipids and collagens. Therefore, the primary objective of this study was to devise an RNA extraction protocol that renders sufficient and consistent yield of total RNA across all postnatal ages in mice. We have developed a modified version of the Trizol method that satisfies all the fundamental quality requirements for downstream applications such as RTqPCR and RNA-seq. Furthermore, we compared our protocol to two other methods that have been employed in previous studies. All the methods were subjected to stringent validation criteria such as RNA purity, integrity and yield consistency. The extracted RNA was also subjected to RTqPCR as an additional validation step. Using our data, we highlight the merits and drawbacks of each method along with the potential pitfalls in employing these protocols. Taking these insights into consideration, we exemplify the efficiency of the modified Trizol protocol and the advantages it offers on multiple fronts for downstream applications.

Keywords: RNA extraction, Trizol, Schwann cell, Sciatic Nerve, RTqPCR, RNA-seq

Introduction:

Peripheral nerve development and myelination are complex molecular processes that elicit a concerted effort of multiple molecular pathways implicating numerous genes (Woodhoo and Sommer, 2008; Monk et al., 2015). In peripheral neuropathies and demyelinating diseases, the molecular mechanisms and the regulation of associated genes are disrupted, thereby leading to disease progression. Therefore, identifying and quantifying such alterations in gene expression through RTqPCR and RNA-seq forms an integral part of a multitude of studies on peripheral nerves.

The most crucial outcome of RNA extraction is to obtain good quality RNA that is devoid of any chemical contaminants from the extraction process. Furthermore, it is also essential to obtain RNA with high integrity that can then be used for sequencing. The quality of the isolated RNA is quickly assessed by determining the spectrophotometric absorbance of the sample at 230nm, 260nm, 280nm and then calculating the A260/A230 & A260/A280 ratios. Highly pure RNA exhibits values around 1.8 – 2.0 for both these ratios. Lower values of A260/A230 and A260/A280 indicate contamination with guanidine salts and proteins, respectively. These contaminants hamper the quantification of RNA as well as downstream applications such as RTqPCR (Schrader et al., 2012). Therefore, the quality of the isolated RNA is of prime importance especially if amplification or sequencing is envisaged as a downstream application.

The extraction of total RNA from the sciatic nerve is rather unwieldy and it results in poor/inconsistent yields due to a couple of reasons. The cellular anatomy of the nerve reveals two major cell types: Schwann cells that produce the lipid-rich myelin sheath around axons and other fibroblast-like glial cells that produce collagen to maintain the structural integrity of the nerves (Shellswell et al., 1979; Morell and Quarles, 1999; Chen et al., 2015) (**Figure 1**). Therefore, the tissue, by virtue of its molecular composition, is considered highly fibrous and lipid rich thus presenting with two major hurdles in the isolation of good quality RNA. Lipids hinder tissue disruption and facilitate coprecipitation of contaminants such as phenols and polysaccharides with RNA (Cirera, 2013; Lan et al., 2013). Collagen and proteoglycans, on the other hand, can entrap nucleic acids and thus result in poor yields if RNA is extracted using phase separation (Groppe and Morse, 1993; Wang and Stegemann, 2010). Moreover, in neonates between P0 (Postnatal day 0) and P3, the tissue mass is extremely small and hence it is common practice to pool different biological replicates to obtain copious amounts of RNA. This practice, however, proves to be disadvantageous if the study aims to quantify inherent biological variations of a given population. Therefore, the primary objective of this study was to devise an RNA extraction protocol that can render sufficient yields of RNA for RTqPCR and RNA-seq, irrespective of the age and tissue size.

To this end, we have modified the conventional Trizol method to render sufficient amounts of total RNA for RTqPCR and RNA-seq. We then compared our method to a modified version of the original Guanidium-Acid-Phenol-Chloroform method proposed by Dr. Chomczynski and Prof.

Sacchi (Chomczynski and Sacchi, 1987) and a commercially available column extraction kit (mirVana kit) that is gaining more popularity and is often used in peripheral nerve studies involving microRNAs (Yu et al., 2012; Wu and Murashov, 2013; Phay et al., 2015). Numerous parameters such as the yield consistency, RNA integrity (Agilent Bioanalyzer), A260/A280 ratio and A260/A230 ratio were taken into consideration to validate each method. The extracted RNA was also subjected to RTqPCR to check for the expression of two reference genes: β -Actin (*Actb*) and TATA-Box Binding Protein (*Tbp*) in order to assess how the quality of RNA extracted using these different methods played a role in this downstream application. Our results highlight the potential challenges that are involved in using these protocols and based on our data we find that our modified Trizol method renders sufficient and consistent yields across all ages and satisfies the fundamental RNA quality/integrity requirements for both RTqPCR and RNA-seq.

Submitted for Review

Materials and Methods:

Animals, Tissue Harvesting and Tissue homogenization:

C57Bl6/J mice at different timepoints were obtained from our animal breeding facility. Adult mice were first anesthetized with isoflurane and sacrificed using cervical dislocation. Neonatal mice were sacrificed using decapitation. Sciatic nerves from both the hind limbs were harvested and immediately subjected to tissue homogenization in Fisherbrand™ Bead Mill 24 Homogenizer (Fisher 15515799) using appropriate tubes (2mL Tubes with 2.8mm ceramic beads, Fisher 15565799). Homogenization was carried out using the following settings – Speed = 4.5, Cycles = 3, Time = 10sec, Duration = 1min30sec. Tissue lysis was carried out in different chaotropic lysis buffers as detailed in the following section. All aspects of animal care and animal experimentation were performed in accordance with the relevant guidelines and regulations of INSERM and Université de Paris (authorization APAFIS#7405-2016092216181520).

Total RNA isolation :

TRIzol Extraction :

Tissue homogenates were transferred to a new tube and placed on ice for 5 minutes. Next, RNA was extracted mostly in accordance with the manufacturer's instructions with slight modifications. A detailed schematic of the protocol along with the different modifications and suggestions are provided in Figure 4B. Briefly, 100% Ethanol was substituted for Isopropanol to reduce the precipitation of salts. Also, RNA precipitation was carried out overnight at -20°C in the presence of glycogen. The following day, precipitated RNA was pelleted by centrifugation and washed at least 3 times with 70% Ethanol to eliminate any residual contamination. Tubes were then spin dried in vacuum and RNA was resuspended in 20µL of RNA resuspension buffer (EDTA 0.1mM, pH 8.0). RNA was then stored at -80°C till RT-PCR.

Guanidine-Acid Phenol-Chloroform Extraction (APC method):

Nerves were placed in 500µL of lysis buffer (4M GuSCN, 0.1 M beta-mercaptoethanol, 0.5% N-lauryl sarcosine, 25 mM Na-citrate, pH 7) on ice (Chomczynski and Sacchi, 1987). This lysis buffer can be prepared in-house or purchased commercially (Ambion 8540G21). Samples were then homogenized as described above. The homogenates were then transferred to a new tube. 50 µL of 2M Na Acetate pH 4.5 (Fischer Scientific 50-843-077) were added to the lysate and briefly vortexed. Samples were again placed on ice for 10 minutes. Next, 500µL of Acid Phenol:Chloroform (Ambion 10095904) was added to the lysate and the samples were thoroughly vortexed for 15s. The tubes were then centrifuged at 20000g for 20 min at room temperature. From the resulting separation of phases, the aqueous phase on top (approx. 400µL) was transferred to a new tube. 1.5µL of glycogen (Sigma G1767) was added to these tubes followed by 1mL of 100% Ethanol. Samples were briefly vortexed and placed at -20°C overnight.

The following day, precipitated RNA was pelleted by centrifugation and washed at least 3 times with 70% Ethanol to eliminate any residual contamination. Tubes were then spin dried in vacuum and RNA was resuspended in 20µL of RNA resuspension buffer (EDTA 0.1mM, pH 8.0). RNA was then stored at -80°C till RT-PCR.

mirVana miRNA isolation kit (Ambion Life Technologies AM1560):

Total RNA (including miRNA) was extracted using the column kit according to manufacturer's instructions with no modifications.

RNA quality, integrity and assay:

RNA quantity was assayed using UV spectrophotometry on Nanodrop One (Thermo Scientific). Optical density absorption ratios A260/A280 & A260/A230 of the samples were measured along with the respective yields. RNA integrity was also assessed using Agilent Bioanalyzer.

RTqPCR:

500ng of Total RNA was reverse transcribed with Random Primers (Promega C1181) and MMLV Reverse Transcriptase (Sigma M1302) according to prescribed protocols. Quantitative Real time PCR (qPCR) was performed using Absolute SYBR ROX 2X qPCR mix (Thermo AB1162B) as a fluorescent detection dye. All reactions were carried out in a final volume of 7µl in 384 well plates with 300 nM gene specific primers, around 3.5ng of cDNA (at 100% RT efficiency) and 1X SYBR Master Mix in each well. Each reaction was performed in triplicates. All qPCR experiments were performed on BioRad CFX384 with a No-Template-Control (NTC) to check for primer dimers and a No-RT-Control (NRT) to check for any genomic DNA contamination.

Primer design:

All primers used in the study were designed using the Primer 3 plus software (<https://primer3plus.com/cgi-bin/dev/primer3plus.cgi>). Splice variants and the protein coding sequence of the genes were identified using the Ensembl database (www.ensembl.org). Constitutively expressed exons among all splice variants were then identified using the ExonMine database (<https://imm.medicina.ulisboa.pt/group/exonmine/ack.html>) (Mollet et al., 2010) Primer sequences that generated amplicons spanning two constitutively expressed exons were then designed using the Primer 3 plus software. Detailed information on Primer sequences and amplification efficiencies are described in a previous study (Sundaram et al., 2019).

Statistical analysis and Data Visualization :

qPCR readouts were analyzed in Precision Melt Analysis Software v1.2. The amplicons were subjected to Melt Curve analysis and were verified for a single dissociation peak at a Melting Temperature (T_m) > 75°C as expected from the primer constructs. Cq values were determined by regression and the Cq data was exported to Microsoft Excel for further calculations. Each biological sample had 3 technical replicates thereby generating 3 individual Cq values. The arithmetic mean of the triplicates was taken to be the Cq representing the biological sample. The

standard deviation (SD) of the triplicates was also calculated and samples that exhibited $SD > 0.20$ were considered inconsistent. In such cases, one outlier Cq was removed to have at least duplicate Cq values for each biological sample and an $SD < 0.20$. Relative expression of genes was quantified using the $2^{-\Delta\Delta C_t}$ method (Livak and Schmittgen, 2001; Schmittgen and Livak, 2008). The Trizol group was used as the experimental calibrator and data was visualized using Graph Pad Prism v7.0.

Transmission Electron Microscopy (TEM) :

Adult mice were deeply anesthetized by intraperitoneal injection of 40 mg/kg ketamine and 30 mg/kg xylazine and then intracardially perfused with 4% paraformaldehyde, 2.5% glutaraldehyde in 0.1M phosphate buffer, pH 7.4. Tissues were dissected and immersed in the same fixative solution at 4°C overnight, washed in phosphate buffer, post fixed in 2% osmium tetroxide, dehydrated in graded ethanol series and embedded in epoxy resin. For electron microscopy, ultrathin sections (50–90 nm) were cut on an ultramicrotome (8800 Ultratome III; LKB Bromma) and collected on 300-mesh nickel grids. Staining was performed on drops of 4% aqueous uranyl acetate, followed by Reynolds's lead. Ultrastructural analyses were performed in a JEOL jem-1011 electron microscope and digitalized with Digital Micrograph software.

Results

RNA yield and Purity:

We first extracted RNA from Post-natal day 7 (P7) mice using the three different methods (Trizol, mirVana and Acid Phenol Chloroform – abbreviated as APC). The yield and purity of the samples were measured by UV Spectrophotometry on Nanodrop One and the results are detailed in **Figure 2**.

In terms of total RNA yield, Trizol extraction renders 190.3 ± 7 ng/ μ L (mean \pm SD) and mirVana fares a little poorer at 179.3 ± 37.9 ng/ μ L (**Figure 2A**). The best yield, however, is obtained using the APC method which renders 349.9 ± 18 ng/ μ L (**Figure 2A**). In terms of consistency, we find that the Trizol method fares the best as it exhibits the least variance among all the three. We would also like to note that ample care was taken to standardize tissue harvesting and no palpable differences exist in the amount of tissue dissected from mice. Hence, the variations observed in the yield can be safely attributed to the intrinsic efficacy of these methods and it is not due to any experimental errors.

We further observed that all the three methods are efficient in removing protein contamination from the extracted RNA. They exhibited A260/A280 ratios between 1.7 to 2.0 (**Figure 2B**). The best results were however achieved from the mirVana method which showed the highest A260/A280 ratio.

With respect to guanidine contamination, APC method fares the best with the highest A260/A230 ratio of 2.12 ± 0.15 (mean \pm SD) (**Figure 2C**). Trizol method is the second best at 1.69 ± 0.3 . The highest variation and significantly lower purity is observed in the mirVana method which stands at 1 ± 0.45 (**Figure 2C**). We next assessed RNA integrity of all the samples extracted using the three methods using Agilent Bioanalyzer and the results are summarized in the table below (**Table 1**).

Trizol samples exhibit RIN values from 8.5 to 9.2. MirVana RIN values range from 9.4 to 10 and APC RIN values range from 8.9 to 10 (**Table 1**). These results suggest that the integrity of the mirVana and the APC samples are relatively better than the Trizol samples. However, all the three methods show RIN values above 8 suggesting that all these samples exhibit adequate RNA integrity for downstream applications such as RTqPCR and RNA-seq.

Validation by RTqPCR:

We next sought to compare each method using RTqPCR by amplifying the expression of two commonly used reference genes *Actb* and *Tbp*. Based on the results from UV spectrophotometry, we reasoned that if equal quantity of RNA (500ng) is reverse transcribed, we should obtain similar Cq values for these genes across all the three methods. However, much to our surprise, we observed significant differences in Cq values (and therefore mRNA quantities) for both *Actb* and *Tbp* across the three methods (**Figure 3A, Figure 3B, Supplementary Table S1**).

In Trizol samples, *Actb* was detected from 16.6 ± 0.27 cycles (mean \pm SD) and *Tbp* was detected at 24.87 ± 0.3 cycles. In the mirVana samples, *Actb* was detected from 17.35 ± 0.36 cycles and *Tbp* was detected from 25.83 ± 0.38 cycles. Similarly, in APC samples, *Actb* was detected from 17.76 ± 0.27 cycles and *Tbp* was detected from 26.27 ± 0.26 cycles (**Supplementary Table S1**).

These differences in Cq values indeed could not result from the differences in the purity or the integrity of these samples. This is because APC samples which exhibit the highest purity (**Figure 2B, 2C and Table 1**), shows significantly higher Cq values when compared to the Trizol group which exhibits relatively lower purity. Moreover, although these differences in Cq values look negligible at first glance, the true extent of this variation is revealed when the data is represented as fold changes with the Trizol group used as the experimental calibrator (**Figure 3A, Figure 3B**). We see that *Actb* expression in the mirVana group is reduced by one-thirds and that of the APC group is reduced by half (**Figure 3A**). A similar and almost congruent reduction in *Tbp* expression is also observed in mirVana and APC groups (**Figure 3B**).

To explain such drastic differences, we cautiously analyzed our raw data to root out any experimental errors during RTqPCR. Upon inspection, we observed that RNA concentrations determined by Nanodrop and Bioanalyzer do not concur especially in the mirVana and the APC groups (**Figure 3C and Supplementary Table S2**). In general, RNA concentrations assessed by Bioanalyzer are lower than that of Nanodrop, but the difference is more pronounced in the mirVana and the APC samples. In the Trizol group, Nanodrop concentrations are estimated to be 1.2 ± 0.1 (mean \pm SD) folds higher than Bioanalyzer values whereas in the mirVana and the APC, the fold increase is 3.3 ± 0.4 and 4.7 ± 1.1 folds respectively (**Supplementary Table 2**).

As we performed RTqPCR based on Nanodrop concentrations, we wanted to ascertain if the differences in RNA quantity used for reverse transcription could potentially cause the Cq value changes in qPCR among the three groups. Therefore, we recalculated the total amount of RNA that was used in reverse transcription based on the Bioanalyzer concentrations (**Supplementary Table S3**). We then plotted these RNA quantities as fold-differences with respect to the Trizol group (experimental control) (**Figure 3D**). This is was done in order to compare the revised fold-differences in RNA quantities used for RTqPCR with the qPCR fold changes observed in *Actb* and *Tbp* among the three groups.

The revised RNA quantities expressed as fold-differences seemed to concur with the fold changes observed in qPCR (**Figure 3A, 3B and 3D**). Consequently, to validate our observation, we performed a correlation analysis (Spearman's correlation) between the qPCR fold-changes and the revised RNA fold-differences across all samples and methods. The results of this analysis are detailed in the correlation matrix below (**Table 2**).

We observe that the *Actb* and *Tbp* expression positively correlates with the revised RNA quantity fold-differences across all methods ($r = 0.82$ and $r = 0.80$ respectively). As expected, we also observe an almost perfect correlation between *Actb* and *Tbp* ($r = 0.98$) qPCR results across the three methods.

These results, taken together, show that Nanodrop drastically overestimates the concentration of RNA in mirVana and APC samples. Furthermore, qPCR results demonstrate that the bioanalyzer concentration values are more reliable than Nanodrop and care must be employed while constructing RTqPCR experiments especially if RNA is extracted by the mirVana kit or the APC method.

Reliability of the Trizol Method:

Although RNA quantification by Nanodrop is not reliable when compared to the bioanalyzer, the Trizol method offers an advantage on two fronts. Firstly, the RNA yield from Trizol extraction is the highest when compared to the other two methods as indicated by the Bioanalyzer results (**Figure 3C**). Secondly, the consistency of the yield is also conserved irrespective of the method employed for RNA quantification.

In the Trizol samples, the intragroup variation in RNA yield assessed through Nanodrop is 3.7% (co-efficient of variation) and that of Bioanalyzer is marginally higher at 8.5% (**Supplementary Table S2**). This pales in comparison to mirVana samples whose intragroup variation is 21% in Nanodrop and 27% in Bioanalyzer. Although the differences in yield variation between Nanodrop and Bioanalyzer are quite similar in the mirVana group, a variation of more than 20% in the yield is rather high. As for the APC samples, this difference in yield variation is more flagrant as they exhibit an intragroup variation of 5.2% in Nanodrop but a staggering 24.4% in Bioanalyzer. These results taken together suggest that the Trizol method produces the highest and the most consistent yields. Additionally, the differences in yield variation is the least between Nanodrop and Bioanalyzer in the Trizol group.

Subsequently, we assayed the RNA yield from the Trizol method from sciatic nerves harvested from mice at P0, P7, P21 and 8 weeks (**Figure 3E**) without pooling nerves from different mice. On an average, at P0 we obtain 629.2ng (N=5, 14.3% variation), at P7 we obtain 3805.3 ng (N=5, 3.7% variation), at P21 we obtain 3501.5ng (N=5, 6.6% variation), at 8 weeks we obtain 3000.7 ng (N=4, 6.8% variation). Our data thus demonstrates that the extraction of total RNA using Trizol renders sufficient yields in neonates as well as in adult mice.

Discussion:

The primary objective of this study was to set up an RNA extraction protocol for mouse sciatic nerves that can render consistent and abundant yields irrespective of the tissue size. We have shown that the use of the conventional Trizol protocol caters to this objective. However, the protocol needs to be adapted to the sciatic nerve which is a tissue that is enriched in lipids and collagens. We have also observed that the use of this protocol as per the manufacturer's instructions does not guarantee consistent yields across all ages.

A step by step approach of our modified version is described in Figure 4B. During the optimization of this protocol, we encountered several difficulties in isolating the aqueous phase without retrieving contaminants from the interphase that is enriched with lipids. This problem often occurs in adult nerves (aged 8 weeks and above) where the interphase forms a white opaque deposit on the walls of the tube thus blinding the observer's view on the separation of the aqueous phase above (containing RNA) and the organic phase below (enriched in DNA and proteins). This issue, however, did not arise in young or neonatal mice. The plausible reason can be attributed to the fact that younger mice (aged between P0 and P21) do not possess completely formed myelin sheaths which account for the majority of the lipid content in the sciatic nerve (Jessen and Mirsky, 2005; Salzer, 2015).

To circumnavigate this issue, we performed a preliminary centrifugation step after tissue homogenization and before the addition of chloroform. This brings the lipid layer to the top of the homogenate. The homogenate is then carefully pipetted out from the bottom and transferred to a new tube before continuing with the protocol. This troubleshooting method is often practiced while extracting RNA from the adipose tissue which is also highly enriched in lipids (Cirera, 2013).

One of the crucial steps of RNA extraction from the sciatic nerve is tissue disruption and homogenization. We initially used the RETSCH MM300 homogenizer with 5mm stainless steel beads and we observed that the tissues were not completely disrupted even after 3 cycles at 20Hz. We then switched to the Fisherbrand™ Bead Mill 24 Homogenizer with 2.8mm ceramic beads and we could substantially increase tissue disruption and homogenization. Moreover, incubation of the nerves in Trizol for 10 minutes on ice prior to homogenization improved tissue disruption. In adult or aged mice, sciatic nerves can also be cut into smaller pieces using microdissection Vannas scissors immediately after placing them in tubes containing Trizol. This step ensures complete homogenization and prevents left-over tissue aggregates after lysis.

During RNA precipitation, we replaced isopropanol with ethanol for two reasons. As the precipitation process occurs overnight at -20°C in the presence of glycogen, the use of ethanol would reduce the co-precipitation of salts and also enhance the precipitation of smaller RNA species such as microRNA (Farrell, 2010). This would ensure that our protocol also caters to researchers who would like to study miRNA expression and regulation in peripheral nerves.

A noteworthy limitation of the proposed method is that the maximum yield that is obtained is around 3µg of RNA even from adult mice. Although the tissue mass increases rather significantly as mice age, it has no bearing on the total yield after P7 (**Figure 3E**). This is due to the fact that the tissue becomes more fibrous and lipid rich with age due to the deposition of collagen and an increase in the myelin sheath thickness. Fibrous tissues pose a major hurdle in RNA extraction as they hinder tissue disruption at the cellular level (Peeters et al., 2016; Reimann et al., 2019). However, despite this drawback, the amount of RNA extracted is largely sufficient for downstream applications.

Another observation that requires explanation is the discrepancies that we observed in the quantification of RNA between Nanodrop and Bioanalyzer in the mirVana and APC samples (**Figure 3C**). We believe that the overestimation by Nanodrop is due to UV absorbance of an unknown molecule at 260nm that eventually skews the results. This issue is possibly due to the co-precipitation of free nucleotides (dNTPs) along with RNA molecules in the mirVana and the APC methods. The absorbance of these free dNTPs is picked up by the nanodrop at 260nm and hence it overestimates the actual amount of RNA present. Our reasoning is also supported by the fact that APC samples show the highest concentration values in Nanodrop (Figure 2A) as they are subjected to overnight precipitation as opposed to the mirVana samples where precipitation is performed at the bench for a few minutes and the RNA is retrieved by silica based spin columns. This explains why the overestimation due to the presence of dNTPs is moderate in mirVana samples but very high in APC samples (**Figure 3C**). It should be noted that both these methods employ similar lysis buffers followed by Acid Phenol Chloroform to separate and retrieve the aqueous phase. In Trizol however, we think that the amount of dNTPs that are co-precipitated with RNA are significantly lower and hence the Nanodrop and Bioanalyzer estimates differ only by a small margin (**Figure 3C**). Besides, Bioanalyzer does not quantify RNA based on spectrophotometry but the quantification is achieved through fluorescence. In a conventional Bioanalyzer setup, RNA molecules are electrophoretically passed through microchannels that are filled with fluorescent RNA intercalants. The fluorescence is then measured for large RNA molecules that bind to the intercalants thus resulting in specific fluorescence peaks for specific RNA populations at specific locations along the microchannel after electrophoresis. The instrument then computes an integrity score (RIN) based on the fluorescence profile of the separated RNA populations. It also computes the total RNA concentration based on the overall fluorescence. Therefore, free dNTPs that are present in the sample either do not bind to these intercalants or they emit feeble amounts of fluorescence that fall below the detection threshold of the Bioanalyzer. Thus, the methodological difference in assaying RNA quantities coupled with the presence of dNTPs in the mirVana and APC samples could possibly explain the differences observed in RNA quantification between Nanodrop and Bioanalyzer.

Additionally, we also looked at the kind of acetate salts used for RNA precipitation in all the three methods since the kind of salt used for nucleic acid precipitation can influence the co-precipitation of free dNTPs (Farrell, 2010). All three methods use Sodium Acetate in an acidic pH (around 4.0) which increases the chances of co-precipitating free nucleotides (Farrell, 2010).

However, should our dNTP hypothesis be true, it is intriguing as to why the Trizol method coprecipitates lesser dNTPs than the other two methods. Thus, further investigation is required to confirm the provenance of this variation in RNA quantification between Nanodrop and Bioanalyzer.

Nevertheless, despite the minor drawbacks in terms of the total yield and discrepancies in RNA quantification between methods, Trizol extraction proves to be reliable in terms of total RNA yield and consistency in neonatal as well as adult mouse sciatic nerves.

Submitted for Review

Figures and Figure Legends:

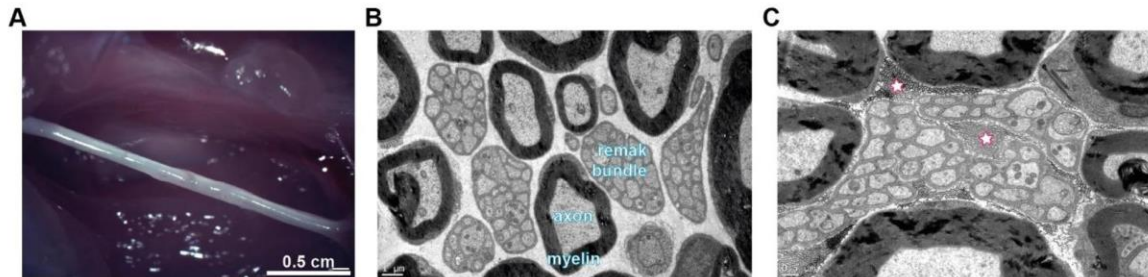


Figure 1 : Cellular composition of the sciatic nerve.

(A) The macroscopic view of an adult 8-week-old nerve during dissection. The nerve appears as an opaque fibrous tissue that is situated between the muscles of the hindlimbs. The nerve is first separated from surrounding tissue and is dissected distally at the level of the gastrocnemius muscle. The second incision is made proximally near the spinal cord where the sciatic emerges near the lumbar vertebrae L4 and L5 in mice (Rigaud et al., 2008). Scale bar = 0.5cm

(B) An electron micrograph of a sciatic nerve transverse section (8 weeks old). The cellular anatomy of the nerve reveals two distinct types Schwann cells enwrapping axons. The myelin sheath and the axonal body are depicted for a given axon/schwann cell unit. Smaller axons are ensheathed in a cellular matrix and packed into distinct structures called as Remak Bundles. These small axonal bundles are wrapped by non-myelinating Schwann cells. Scale bar = 1um

(C) A magnified image of the Extra Cellular Matrix (ECM) around Schwann cells. Small circular structures are dispersed in the ECM around schwann cells. These are collagen deposits (depicted by an asterisk) synthesized by other glial cells in the endoneurial space. The fibres are concentrated in specific locations and extend longitudinally along the nerve. Scale bar = 0.5um

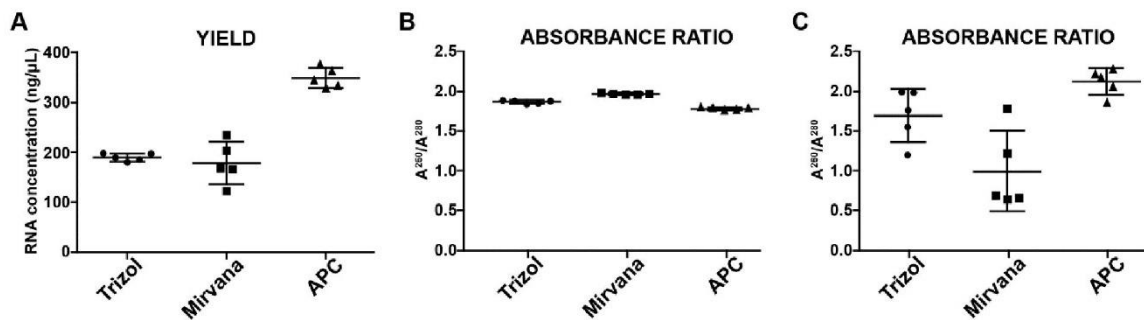


Figure 2 : RNA yield and purity of P7 sciatic nerves measured using Nanodrop One.

(A) Concentration of RNA (ng/uL) across the three different protocols of RNA extraction using Trizol, mirVana kit and the conventional Acid Phenol Chlorofom (APC). RNA was extracted from P7 nerves and was resuspended in a final volume of 20uL.

(B) Optical Density (OD) absorbance ratio A₂₆₀/A₂₈₀. Nucleic Acids absorb UV radiation at a wavelength of 260nm and proteins absorb at 280nm. This ratio is computed to assess the amount of RNA with respect to the amount of proteins that hinder downstream applications such as RTqPCR. A₂₆₀/A₂₈₀ ratios above 1.8 are exhibited samples are enriched in nucleic acids.

(C) Optical Density (OD) absorbance ratio A₂₆₀/A₂₃₀. Chemical contaminants such as Guanidine salts and phenol absorb UV radiation at 230nm. This ratio is computed to assess the amount of RNA with respect to the amount of chemical contaminants. A₂₆₀/A₂₃₀ ratios above 1.8 are exhibited by samples that contain relatively sparing amounts of chemical contaminants from the extraction process.

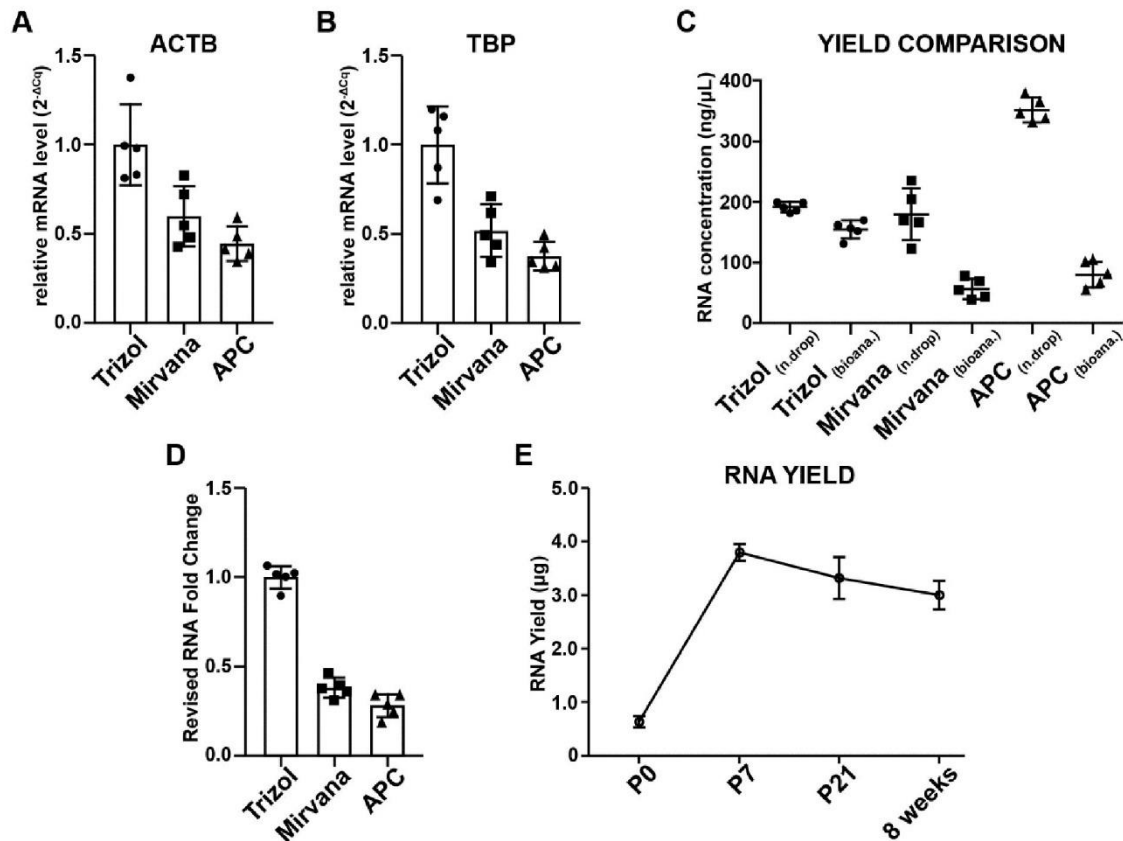


Figure 3 : Validation of RNA extraction by RTqPCR.

RNA extracted from the three methods were subjected to RTqPCR to check for the expression of *Actb* and *Tbp*.

(A) Relative expression of *Actb* across the three different protocols. Cq values were linearized and expressed as fold changes ($2^{-\Delta Cq}$) with respect to the Trizol group that is used as the experimental calibrator. Data is represented as histograms with the mean and error bars that signify the Standard Deviation.

(B) Relative expression of *Tbp* across the three different protocols. Cq values were linearized and expressed as fold changes ($2^{-\Delta Cq}$) with respect to the Trizol group that is used as the experimental calibrator. Data is represented as histograms with the mean and error bars that signify the Standard Deviation.

(C) A comparative analysis of RNA quantification between Nanodrop and Bioanalyzer across the three different methods. Bioanalyzer RNA concentrations are always lower than the nanodrop assessments. The difference is more pronounced in the mirVana group and the APC group. Data is represented with the mean and the error bars denoting the standard deviation.

(D) Revised RNA quantities used for RTqPCR. Based on the Bioanalyzer values, the amount of RNA used for RTqPCR was recalculated. The revised RNA amounts are expressed as fold differences with respect to the Trizol group that is used as the experimental calibrator. Data is represented as histograms with the mean and error bars that signify the Standard Deviation.

(E) RNA yield of the Trizol method across different developmental timepoints from Post Natal Day 0 (P0) to 8 weeks.

Submitted for Review

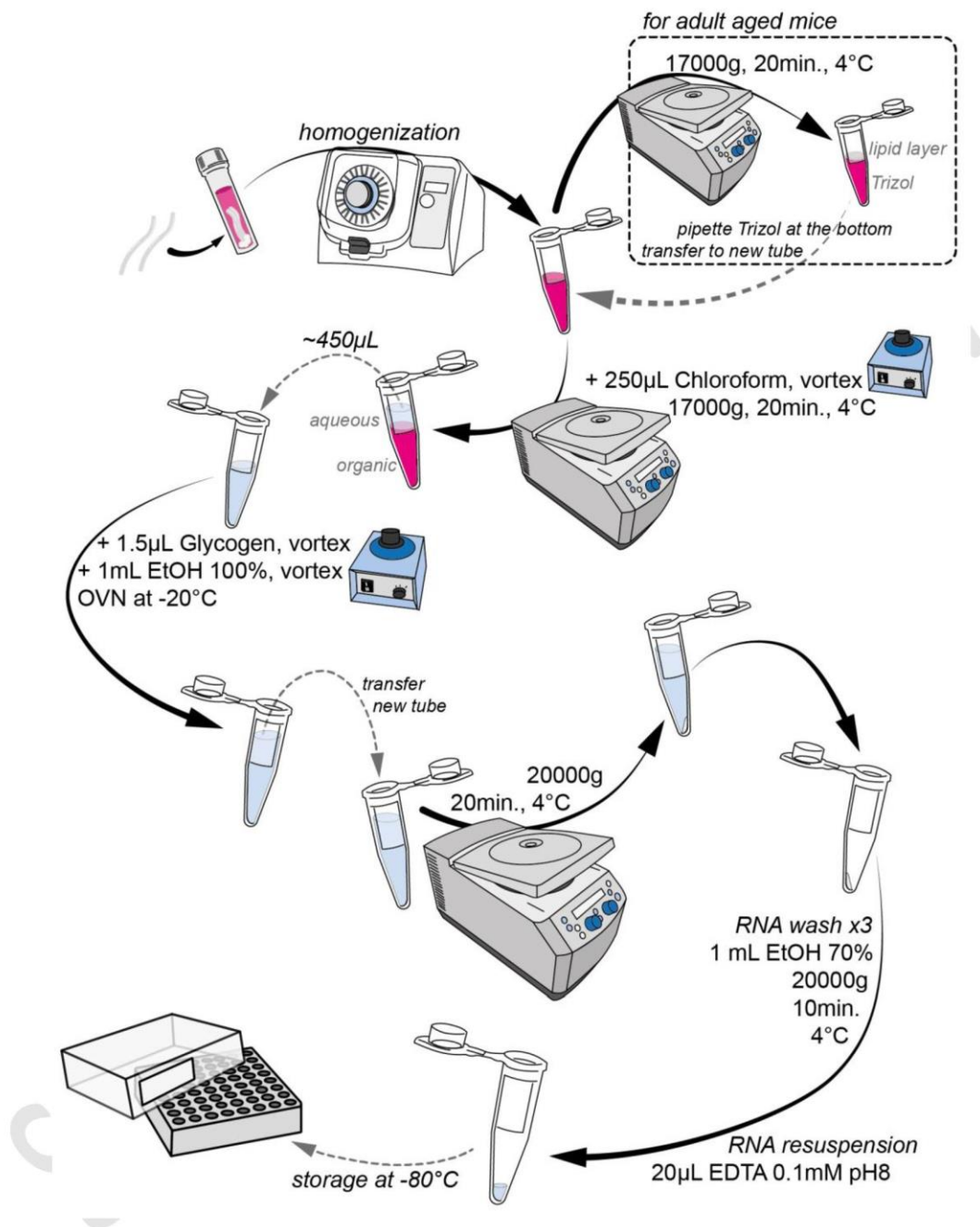


Figure 4: A step-by-step depiction of the Trizol protocol with modifications

Detailed description of the different steps of RNA extraction from Sciatic Nerves using Trizol. Tissues are harvested from mice and immediately placed in 1mL of Trizol solution in Fisherband Tubes. They are then incubated for 10 minutes on ice. Next, samples are homogenized in a bead mill homogenizer. Tissue homogenates are then transferred to a new eppendorf tube (1.5mL). For adult and aged mice, a

preliminary centrifugation step is performed with the lysates to bring the lipid layer to the top. Trizol is then pipetted out from the bottom carefully and transferred to a new tube. 250 μ L of Chloroform is added to the lysate and the tubes are vortexed for 15sec – 30sec. Samples are then placed at room temperature for 3 minutes followed by centrifugation at 17000g for 20 minutes at 4°C. The organic phase separates from the aqueous phase post centrifugation. The aqueous phase which contains the RNA is then carefully transferred to a new tube. 1.5 μ L of glycogen is added to each sample and the tubes are briefly vortexed. This is followed by the addition of 1mL 100% Ethanol and the tubes are again vortexed briefly. The samples are then placed at -20°C overnight to facilitate RNA precipitation. The following day, the contents of the tube are transferred to a new one followed by centrifugation at 20000g for 20 min at 4°C. The supernatant is decanted, and the pellet is washed with 70% Ethanol at least thrice before being dried in a speed-vac. Dry RNA is then resuspended in 20 μ L of RNA resuspension buffer (0.1mM EDTA, pH 8) and stored at -80°C till RTqPCR.

Submitted for Review

Tables and Table Legends:

Table 1

<i>Sample</i>	<i>RIN</i>
<i>Trizol_1</i>	<i>9</i>
<i>Trizol_2</i>	<i>8.8</i>
<i>Trizol_3</i>	<i>8.4</i>
<i>Trizol_4</i>	<i>8.5</i>
<i>Trizol_5</i>	<i>9.2</i>
<i>Mirvana_1</i>	<i>9.4</i>
<i>Mirvana_2</i>	<i>9.8</i>
<i>Mirvana_3</i>	<i>10</i>
<i>Mirvana_4</i>	<i>9.9</i>
<i>Mirvana_5</i>	<i>9.9</i>
<i>APC_1</i>	<i>8.9</i>
<i>APC_2</i>	<i>10</i>
<i>APC_3</i>	<i>10</i>
<i>APC_4</i>	<i>9.7</i>
<i>APC_5</i>	<i>9.6</i>

Table 1: Assessment of RNA integrity using Agilent Bioanalyzer. 5µL of each sample was placed on RNA-Nanochips. RNA was then electrophoretically separated into different rRNA populations. The fluorescence of each rRNA population is measured by the instrument and based on the fluorescence profile and the intactness of the rRNA populations, the instrument computes an RNA Integrity Number (RIN) for each sample. RIN scores above 8 signify that the sample can be further used for sequencing or RTqPCR. Samples with no RNA degradation present with a perfect RIN score of 10.

Table 2

Spearman's r Matrix	<i>Actb</i> Fold changes	<i>Tbp</i> Fold Changes	RNA fold difference (Revised)
<i>Actb</i> Fold changes	n/a	0.98	0.82
<i>Tbp</i> Fold changes	0.98	n/a	0.80
RNA fold difference (Revised)	0.82	0.80	n/a

P-Value Matrix	<i>Actb</i> Fold changes	<i>Tbp</i> Fold Changes	RNA fold difference (Revised)
<i>Actb</i> Fold changes	n/a	3.88E-09	3.54E-04
<i>Tbp</i> Fold changes	3.88E-09	n/a	6.46E-04
RNA fold difference (Revised)	3.54E-04	6.46E-04	n/a

Table 2: Spearman's correlation matrix to compare qPCR results with the revised RNA quantities (based on Bioanalyzer estimates) used for RTqPCR. The actual amount of RNA used for RTqPCR was recalculated using the Bioanalyzer values and expressed as fold differences with respect to the Trizol group. These fold differences were correlated to the qPCR fold changes of *Actb* and *Tbp* using Spearman's correlation. The correlation matrix of Spearman's *r* values along with the corresponding P values for each comparison is detailed in the table. R values closer to 1 indicate strong positive correlation between the datasets. P values lesser than 0.05 are considered statistically significant. The correlation of the datasets with themselves are denoted by 'n/a' and are omitted from analysis.

References

- Chen, P., Cescon, M., and Bonaldo, P. (2015). The Role of Collagens in Peripheral Nerve Myelination and Function. *Mol. Neurobiol.* 52, 216–225. doi:10.1007/s12035-014-8862-y.
- Chomczynski, P., and Sacchi, N. (1987). Single-step method of RNA isolation by acid guanidinium thiocyanate-phenol-chloroform extraction. *Anal. Biochem.* 162, 156–159. doi:10.1016/0003-2697(87)90021-2.
- Cirera, S. (2013). Highly efficient method for isolation of total RNA from adipose tissue. *BMC Res. Notes* 6, 472. doi:10.1186/1756-0500-6-472.
- Farrell, R. E. (2010). *RNA Methodologies: Laboratory Guide for Isolation and Characterization*. doi:10.1016/B978-0-12-374727-3.00025-5.
- Groppe, J. C., and Morse, D. E. (1993). Isolation of Full-Length RNA Templates for Reverse Transcription from Tissues Rich in RNase and Proteoglycans. *Anal. Biochem.* 210, 337–343. doi:10.1006/abio.1993.1205.
- Jessen, K. R., and Mirsky, R. (2005). The origin and development of glial cells in peripheral nerves. *Nat Rev Neurosci* 6, 671–682. doi:10.1038/nrn1746 [pii]\n10.1038/nrn1746.
- Lan, T., Yao, B., Shen, Y., and Wang, X. (2013). Isolation of high-quality total RNA from lipid-rich seeds. *Anal. Biochem.* 438, 11–13. doi:10.1016/J.AB.2013.03.012.
- Livak, K. J., and Schmittgen, T. D. (2001). Analysis of relative gene expression data using real-time quantitative PCR and the $2^{-\Delta\Delta CT}$ Method. *Methods* 25, 402–408. doi:10.1006/meth.2001.1262.
- Mollet, I. G., Ben-Dov, C., Felício-Silva, D., Grosso, A. R., Eleutério, P., Alves, R., et al. (2010). Unconstrained mining of transcript data reveals increased alternative splicing complexity in the human transcriptome. *Nucleic Acids Res.* 38, 4740–4754. doi:10.1093/nar/gkq197.
- Monk, K. R., Feltri, M. L., and Taveggia, C. (2015). New insights on schwann cell development. *Glia* 63, 1376–1393. doi:10.1002/glia.22852.
- Morell, P., and Quarles, R. H. (1999). Characteristic Composition of Myelin. Available at: <https://www.ncbi.nlm.nih.gov/books/NBK28221/> [Accessed November 30, 2017].
- Peeters, M., Huang, C. L., Vonk, L. A., Lu, Z. F., Bank, R. A., Helder, M. N., et al. (2016). Optimisation of high-quality total ribonucleic acid isolation from cartilaginous tissues for real-time polymerase chain reaction analysis. *Bone Jt. Res.* 5, 560–568. doi:10.1302/2046-3758.511.BJR-2016-0033.R3.
- Phay, M., Kim, H. H., and Yoo, S. (2015). Dynamic Change and Target Prediction of Axon-Specific MicroRNAs in Regenerating Sciatic Nerve. *PLoS One* 10, e0137461. doi:10.1371/journal.pone.0137461.
- Reimann, E., Abram, K., Köks, S., Kingo, K., and Fazeli, A. (2019). Identification of an optimal method for extracting RNA from human skin biopsy, using domestic pig as a model system. *Sci. Rep.* 9, 1–10. doi:10.1038/s41598-019-56579-5.
- Rigaud, M., Gemes, G., Barabas, M.-E., Chernoff, D. I., Abram, S. E., Stucky, C. L., et al. (2008).

- Species and strain differences in rodent sciatic nerve anatomy: Implications for studies of neuropathic pain. *Pain* 136, 188–201. doi:10.1016/j.pain.2008.01.016.
- Salzer, J. L. (2015). Schwann cell myelination. *Cold Spring Harb. Perspect. Biol.* 7, 1–26. doi:10.1101/cshperspect.a020529.
- Schmittgen, T. D., and Livak, K. J. (2008). Analyzing real-time PCR data by the comparative C(T) method. *Nat. Protoc.* 3, 1101–8.
- Schrader, C., Schielke, A., Ellerbroek, L., and Johne, R. (2012). PCR inhibitors - occurrence, properties and removal. *J. Appl. Microbiol.* 113, 1014–1026. doi:10.1111/j.1365-2672.2012.05384.x.
- Shellswell, G. B., Restall, D. J., Duance, V. C., and Bailey, A. J. (1979). Identification and differential distribution of collagen types in the central and peripheral nervous systems. *FEBS Lett.* 106, 305–308. doi:10.1016/0014-5793(79)80520-7.
- Sundaram, V. K., Sampathkumar, N. K., Massaad, C., and Grenier, J. (2019). Optimal use of statistical methods to validate reference gene stability in longitudinal studies. *PLoS One* 14, e0219440. doi:10.1371/journal.pone.0219440.
- Wang, L., and Stegemann, J. P. (2010). Extraction of high quality RNA from polysaccharide matrices using cetyltrimethylammonium bromide. *Biomaterials* 31, 1612–8. doi:10.1016/j.biomaterials.2009.11.024.
- Woodhoo, A., and Sommer, L. (2008). Development of the Schwann cell lineage: From the neural crest to the myelinated nerve. *Glia* 56, 1481–1490. doi:10.1002/glia.20723.
- Wu, D., and Murashov, A. K. (2013). MicroRNA-431 regulates axon regeneration in mature sensory neurons by targeting the Wnt antagonist Kremen1. *Front. Mol. Neurosci.* 6, 35. doi:10.3389/fnmol.2013.00035.
- Yu, B., Zhou, S., Wang, Y., Qian, T., Ding, G., Ding, F., et al. (2012). Mir-221 and mir-222 promote Schwann cell proliferation and migration by targeting LASS2 after sciatic nerve injury. *J. Cell Sci.* 125, 2675–2683. doi:10.1242/jcs.098996.

Submitted for Review

Perspectives :

This article has been submitted to *Frontiers in Cellular Neuroscience* Section : Non-Neuronal cells as a 'Method' article. It is currently under peer review. In the meantime, we are also working on understanding why the other two protocols exhibit RNA yield differences when measured using UV spectrophotometry and fluorescence. We hypothesized that the differences arise due to the co-precipitation of free nucleotides (NTPs). This can be due to the use of Sodium Acetate as the primary salt for RNA precipitation (Farrell, 2010). To test our hypothesis, we are now using 5M Ammonium Acetate which is known to obstruct the co-precipitation of nucleotides with RNA. This could greatly enhance the utility of the other two methods and provide tangible solutions for labs that have invested in purchasing the mirVana and other silica-column based RNA isolation kits.

We are also verifying if the RNA extracted from Trizol also comprises of microRNA (miR) populations. This would greatly enhance the utility of our protocol and cater to the needs of a broader research community that is interested in studying gene regulation by miRs in peripheral nerves. These improvements will either be appended to this study during the peer review process or will be published as a separate follow-up study in the coming months.

2.2.4 Establishing highly pure primary immature Schwann cell cultures from embryonic DRG cultures

Context of the Study:

Primary Schwann cell cultures offer the unique possibility of studying the nuances of Schwann cell proliferation, survival, and differentiation *in vitro*. Traditionally, primary cultures were established from neonatal mouse sciatic nerves aged between P0 and P4 (Lutz, 2014; Irigoyen et al., 2018). However, this method demands the use of sciatic nerves pooled from multiple mice of the same genotype to have sufficient yields in order to perform cell culture experiments. Nevertheless, this exigency proves to be a disadvantage when dealing with mutant animals from the same litter. Often, multiple simultaneous breedings are required to generate enough number of mutant animals for extracting immature Schwann cells from their sciatic nerves. To overcome this hurdle, Kim, Ratner and colleagues developed a protocol to extract immature Schwann cells from Embryonic dissociated Dorsal Root Ganglia (DRG) cultures from embryos aged between E12.5 to E13.5 (Ratner et al., 2005; Kim and Maurel, 2009; Kim and Kim, 2018). Briefly, this protocol employs dissociated DRG cultures from mouse embryos that are maintained in culture for 1 week. Schwann cells being to appear and proliferate on developing neurites. At the end of 1 week *in vitro*, neurites and contaminating fibroblasts are eliminated from culture and pure Schwann cells are retrieved.

This method offers the advantage of obtaining 0.5 million immature Schwann cells (iSC) / embryo and does not require the use of multiple embryos to get enough yields. Therefore, each embryo can generate Schwann cells that can then be treated as individual biological replicates. However, the proposed methodology does not guarantee pure Schwann cell cultures as contaminating fibroblasts are often found to invade and expand during successive passages. This is also true for Schwann cell cultures established from neonatal sciatic nerves.

Hence, the aim of this study was to compare different methods of fibroblast elimination from Schwann cell cultures during the first couple of passages to ensure highly pure monocultures. We compared three different protocols of fibroblast elimination from cultures and based on empirical evidence, we have found that one of the three methods to be highly efficient in removing fibroblast in under two passages. The study is presently underway to delineate the advantages and drawbacks of

different methods to eliminate fibroblasts. The following sections briefly summarize the different aspects of the study along with the associated questions and perspectives.

Elimination of Fibroblasts using Cytosine Arabinoside (AraC) treatment:

AraC is an antimetabolic agent that exerts cytostatic and cytotoxic effects by interfering in DNA replication during the S-Phase of cell cycle. Its effects are more pronounced in rapidly multiplying cells in culture. In Schwann cell cultures with contaminating fibroblasts, AraC treatment (10 μ M) is used in combination with standard DMEM medium supplemented with 10% Bovine or Horse Serum and Glutamine for period of 48h – 72h. In this media, Schwann cells do not multiply due to the absence of soluble Neuregulin that is normally added to expand Schwann cell populations. However, fibroblasts thrive in this media and therefore are subjected to the cytotoxic effects of AraC.

Empirical observations and hypothesis:

We observed that this method is not efficient in eradicating fibroblasts. Significant amounts of fibroblasts are observed in phase contrast microscopy (fibroblasts exhibit a flattened morphology whereas Schwann cells are spindle shaped and bipolar) even after the treatment. These fibroblasts proliferate further during successive passages and cause significant infiltration.

Secondly, we also observed a drastic reduction in Schwann cell numbers post treatment. This leads us to believe that Schwann cells indeed proliferate at lower levels in serum containing media without soluble neuregulin. This results in collateral genotoxicity from AraC treatment on Schwann cell populations.

Thirdly, we hypothesize that cultivating Schwann cells in serum supplemented media changes the basal expression of known Schwann cell markers at the RNA level. Our hypothesis is that Schwann cells in culture adopt a ‘repair’ Schwann cell like phenotype in the presence of serum. *In vivo*, the cells are insulated from the serum through the blood nerve barrier that is ensured by pericytes and endothelial cells of the vasculature. However, during peripheral nerve injury/insult, Schwann cells directly come in contact with serum proteins and other growth factors that can possibly help them in adopting the ‘repair’ Schwann cell phenotype to promote nerve regeneration and remyelination (Liu et al., 2014; Jessen and Mirsky, 2016, 2019b; Su-chun Ho et al., 2017). Thus, we postulate that the use of serum in Schwann cell

cultures can induce a paradigm shift in the expression of markers associated with Schwann cell development and peripheral nerve repair. We are presently verifying this hypothesis using RNA-seq and qPCR.

Elimination of Fibroblasts using Complement Mediated Cytotoxicity:

Another protocol that is widely used is complement-mediated cytotoxicity. Briefly, this method employs the tagging of fibroblasts in culture using an Antibody raised against CD90 protein that is localized in the membranes of fibroblasts. Then the media is substituted with Rabbit Complement Serum (1/5th titer) and the cultures are treated for up to 2 hours. The complement serum contains proteins that bind to the CD90 antibody and induce cell lysis rapidly through the formation of the Membrane Attack Complex (MAC) (Courtois et al., 2012).

Empirical observations:

Yet again, we find that this method is not very efficient in removing fibroblasts from culture and residual amounts of fibroblasts expand during successive passaging. However, contrary to AraC treatment we did not observe any reduction in Schwann cell numbers post treatment, but we did observe that Schwann cells proliferate rather slowly after treatment during the 1st passage.

Elimination of Fibroblasts using Immunopanning:

The last protocol that we tried is immunopanning. This method also employs the use of CD90 antibodies, but it is not cytotoxic to the cells. Briefly, Schwann cell cultures with fibroblasts are incubated in suspension over polystyrene plastic dishes (not cell culture grade) that are coated with the CD90 antibody. During the incubation, fibroblasts adhere to the cell dish due to the antibody and Schwann cells remain afloat. After about 30 minutes of incubation, the suspension is retrieved leaving behind the fibroblasts attached to the dishes. The Schwann cells in suspension are then cultured in separate dishes. The fibroblasts left behind in the dishes can then be trypsinized and placed in culture separately. Thus, this method offers the possibility of culturing fibroblasts and Schwann cells separately.

Empirical observations:

By far, we find that this method is the most efficient in removing fibroblasts from culture and we could establish highly pure Schwann cell cultures that are devoid of fibroblasts. However, we did notice that the immunopanning process also targets Schwann cells due to non-specific binding of Schwann cells to the CD90 antibody. This is mostly due to the fact that we use a monoclonal mouse anti-CD90. We are now improving the immunopanning protocol using CD90 antibodies raised in other species. Additionally, we are also optimizing the immunopanning suspension medium with different concentrations of BSA and

neuregulin so as to prevent non-specific binding and also keep the Schwann cells alive during the treatment. Nevertheless, even after the loss of a few Schwann cells during panning, this method proves to be the most efficient in removing fibroblast contamination from Schwann cell cultures.

Perspectives:

The empirical observations are now being tested using ICC and qPCR. The results are currently being generated and this study will be ready for publication in a few months. Our objective is to detail different methodological considerations that need to be examined while performing Schwann cell primary cultures. The study also aims to standardize Schwann cell cultures so as to render results from multiple studies comparable.

Chapter 3: RESULTS

3.1 LIVER X RECEPTORS PROTECT SCHWANN CELLS FROM OXIDATIVE DAMAGES

Context of the Study:

My host laboratory has been working on elucidating the role of Liver X Receptors in the context of myelination both in the CNS and the PNS (Makoukji et al., 2011; Shackleford et al., 2013). These studies revealed that both LXR isoforms (LXR α and LXR β) are expressed in the sciatic nerves (Makoukji et al., 2011). They employed total LXR α/β ^{-/-} mutants (LXRdKO, refer to '*Context of the Doctoral Thesis*') to elucidate the role of these nuclear receptors in peripheral myelination. The studies first confirmed the presence of 3 endogenous LXR ligands, 24S-Hydroxycholesterol (24S-HC), 25-Hydroxycholesterol (25-HC) and 27-Hydroxycholesterol (27-HC) along with expression of their respective biosynthetic enzymes in adult sciatic nerves and an immortalized Schwann cell line MSC80 (Makoukji et al., 2011). Furthermore, activation of LXRs using 25-HC or a synthetic LXR ligand TO9 in MSC80 reduced the mRNA expression of myelin genes such as Myelin Protein Zero (*Mpz*) and Peripheral Myelin Protein 22 (*Pmp22*). Putative LXR binding sites upstream of these two genes were identified suggesting that LXRs might be involved in the negative regulation of myelin gene expression possibly by transrepression. Furthermore, the study also demonstrated that this negative regulation is likely because LXR stimulation also downregulates components of the Wnt/ β Catenin pathway which is essential for both myelination and remyelination (Makoukji et al., 2012; Grigoryan et al., 2013). In summation, LXRdKO mice exhibited an upregulation of *Mpz* and *Pmp22* at the RNA level, complementing the results in the MSC80 cell line. However, their protein levels were downregulated and these animals displayed thinner myelin sheaths and electrophysiological deficits in adults (8-week-old mice) (Hichor et al., 2018).

Thus, my first study pertaining to LXRs was conducted on these animals to explain the discrepancy between the level of *Pmp22* and *Mpz* RNA and protein expression (Hichor et al., 2018). To this end, we explored the redox homeostasis of the sciatic nerves in these animals based on a microarray analysis that revealed multiple hits pertaining to genes implicated in redox homeostasis mediated by Nuclear factor erythroid 2-related factor (*Nfe2l2* also commonly known as *Nrf2*). Further investigation revealed that the

absence of LXRs gives rise to oxidative stress in peripheral nerves, which in turn resulted in the aggregation of *Pmp22* thus lowering its protein expression. Interestingly, these mice do not exhibit any behavioral or ultrastructural anomalies till P21 suggesting that the oxidative insults do not affect developmental myelination. To test this observation, these mice were treated with N-Acetyl Cysteine (NAC), an antioxidant, between the ages of P21 and 8 weeks. Treatment with NAC counteracted the oxidative stress generated in these mice and restored myelin protein levels back to normal. Furthermore, we also observed functional recovery of myelin sheath thickness in the sciatic nerves of treated animals coupled with electrophysiological improvements. To understand the role of LXRs in combating the oxidative stress, we used a mouse Schwann line (MSC80) to demonstrate that stimulation of LXRs using a pharmacological agonist (TO9) protects these cells from an acute oxidative stress induced by Tert-Butyl Hydroperoxide (tBHP) in cell culture. These results taken together, suggest that LXRs play a protective role against oxidative stress in the Schwann cells of the peripheral nerve.

SCIENTIFIC REPORTS

OPEN

Liver X Receptor exerts a protective effect against the oxidative stress in the peripheral nerve

Received: 6 June 2017
Accepted: 16 January 2018
Published online: 06 February 2018

Mehdi Hichor¹, Venkat Krishnan Sundaram¹, Stéphanie A. Eid¹, Ronza Abdel-Rassoul¹, Patrice X. Petit¹, Didier Borderie¹, Jean Bastin¹, Assaad A. Eid², Marin Manuel³, Julien Grenier¹ & Charbel Massaad¹

Reactive oxygen species (ROS) modify proteins and lipids leading to deleterious outcomes. Thus, maintaining their homeostatic levels is vital. This study highlights the endogenous role of LXRs (LXR α and β) in the regulation of oxidative stress in peripheral nerves. We report that the genetic ablation of both LXR isoforms in mice (LXRdKO) provokes significant locomotor defects correlated with enhanced anion superoxide production, lipid oxidization and protein carbonylation in the sciatic nerves despite the activation of Nrf2-dependant antioxidant response. Interestingly, the reactive oxygen species scavenger N-acetylcysteine counteracts behavioral, electrophysical, ultrastructural and biochemical alterations in LXRdKO mice. Furthermore, Schwann cells in culture pretreated with LXR agonist, TO901317, exhibit improved defenses against oxidative stress generated by tert-butyl hydroperoxide, implying that LXRs play an important role in maintaining the redox homeostasis in the peripheral nervous system. Thus, LXR activation could be a promising strategy to protect from alteration of peripheral myelin resulting from a disturbance of redox homeostasis in Schwann cell.

Liver X Receptors (LXR α and LXR β) belong to the nuclear receptor superfamily of ligand-activated transcription factors. They regulate target gene expression by binding to specific responsive elements and are implicated in metabolic processes such as cholesterol turnover, inflammation as well as pathologies such as cancer and neurodegenerative diseases¹. Natural ligands of LXRs are oxysterols (*i.e.* 24(S)-hydroxycholesterol (24(S)-OH) or 25-hydroxycholesterol (25-OH)), produced either through auto-oxidation or enzymatic oxidation of cholesterol. Synthetic ligands of LXR, like TO901317, have also been discovered and are known to be potent activators of the LXR pathway.

Previous studies have shown that mice where both LXR isoforms (LXR α and LXR β) are deleted (LXR double KO or LXRdKO) exhibit altered lipid homeostasis in the brain resulting in neuronal loss, astrocytic proliferation, disorganized myelin sheaths and lipid accumulation in specific brain regions that participates in locomotor defects highlighted in these animals^{2,3}. We also observed that LXRdKO mice have thinner myelin sheaths surrounding axons of the sciatic nerve^{4,5}. Importantly, LXR inhibition enhanced myelin gene transcripts but decreased the amount of myelin proteins, suggesting post-translational modifications, detrimental for peripheral myelin integrity.

Oxidative stress has been recently shown to alter the structure of myelin proteins in several diabetic peripheral neuropathies⁶. In particular, PMP22 misfolding and aggregation provokes demyelination and nerve conduction velocity reduction. In line with this, our team recently showed that a burst of oxidative stress induced by Paraquat provokes a dramatic alteration of myelin structure in the sciatic nerves⁷. Indeed, because of their high reactivity, reactive oxygen species (ROS) modify the structure and therefore the physiological functions of proteins and lipids. Thus, maintaining normal cellular ROS levels is essential. The excessive production of ROS or the decrease of antioxidant defenses is rather a hallmark characteristic in the pathogenesis of diseases such as diabetes, atherosclerosis and neurodegeneration^{8,9}. Hence, compounds that exhibit anti-oxidative effects, triggering the intracellular cascade of protective pathways, may offer a promising strategy for therapeutic applications¹⁰.

¹Paris Descartes University, INSERM UMR-S 1124, Faculty of Basic and Biomedical Sciences, 45 rue des Saints-Pères, 75270, Paris Cedex 6, France. ²American University of Beirut, Department of Anatomy, Cell Biology and Physiological Sciences, PO Box 11-0236, Riad El-Solh, 1107 2020, Beirut, Lebanon, Beirut, Lebanon. ³Centre de Neurophysiologie, Physiologie et Pathologie, Université Paris Descartes, CNRS UMR 8119, Paris, France. Correspondence and requests for materials should be addressed to C.M. (email: charbel.massaad@parisdescartes.fr)

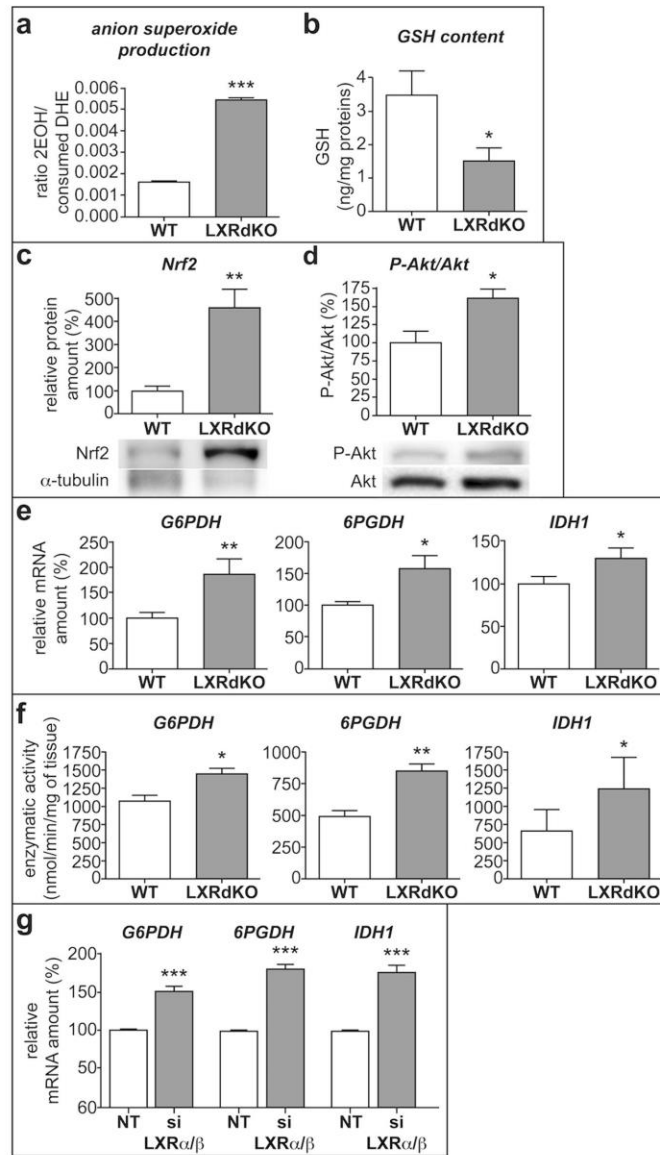


Figure 1. LXR ablation provokes oxidative stress in sciatic nerve. Sciatic nerves from either 8 week-old WT or LXRdKO mice were extracted. **(a)** Anion superoxide production quantified by DHE assay using HPLC. **(b)** GSH assay in WT and LXRdKO animals. **(c)** Representative western blots (cropped gels) of nerve lysate detecting Nrf2 **(d)** Akt and P-Akt proteins. All quantifications were normalized to alpha-tubulin. **(e)** mRNA quantification by RT-qPCR of antioxidant genes. Transcript levels were normalized to GAPDH expression both in control and LXRdKO animals. **(f)** Enzymatic activity assay of antioxidant genes. The activities of these enzymes were normalized to tissue weight. **(g)** mRNA levels of antioxidant response genes in MSC80 transfected with both siLXR α and siLXR β quantified by RT-qPCR. Transcript levels were normalized to GAPDH expression both in Non-Targeting controls and siLXR-transfected cells. Results represent the means \pm SEM of at least three independent experiments for transfection and 5 animals per group for the other experiments. ** $P < 0.01$ and * $P < 0.05$ *** $P < 0.001$ assessed by Student's *t* test.

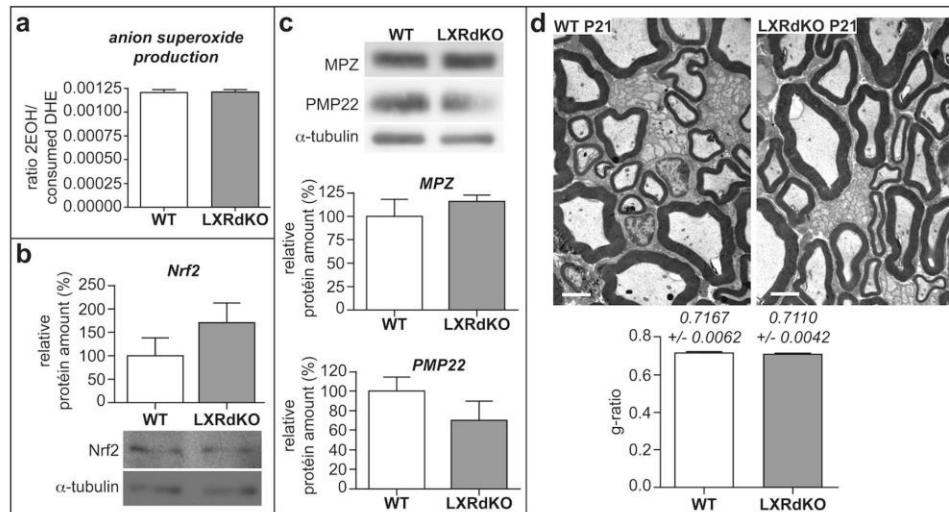


Figure 2. Ablation of LXR does not alter normal myelination and redox status during development. Sciatic nerves from either 21-day-old WT or LXRdKO mice were used for the experiments. (a) Anion superoxide production quantified by DHE assay using HPLC. Representative western blots (cropped gels) of nerve lysate detecting Nrf2 (b), PMP22 and MPZ (c) proteins. All quantifications were normalized to alpha-tubulin. (d) Electron microscopy images of ultrathin (50–90 nm) sciatic nerve cross-sections of WT and LXRdKO P21 mice. Myelin thickness estimated by g-ratio (inner over outer perimeter of myelinated axons). Results represent the means \pm SEM of at least 5 animals per group. Statistical significance was assessed by a Student's *t* test.

Nuclear factor (erythroid-derived 2)-like 2 (Nrf2), also known as NFE2L2, is commonly involved in the transcriptional regulation of genes encoding antioxidant proteins, among which Glucose-6-phosphate dehydrogenase (G6PDH), Isocitrate dehydrogenase 1 (IDH1) and 6-phosphogluconate dehydrogenase (6-PGDH)¹¹. These enzymes protect cells from oxidative stress by regenerating nicotinamide adenine dinucleotide phosphate (NADPH). NADPH, in turn, plays a pivotal role in the regeneration of reduced glutathione (GSH), one of the most important reducers of ROS. Hence, the Nrf2 signaling pathway can be considered as a key driver of cellular antioxidant defenses. Studies have clearly shown that deletion of Nrf2 impairs functional recovery, reduces clearance of myelin debris and axonal re-myelination after peripheral nerve injury¹². Besides, activation of Nrf2 pathway is suggested as a new therapeutic strategy for neurodegenerative diseases¹³.

The aim of this study is to understand the role of both LXR isoforms in the modulation of the redox status of myelinating Schwann cells. LXR genetic ablation provokes locomotor defects in adult mice accompanied by an elevation of oxidative stress in the sciatic nerve. The accumulation of oxidative insults (lipid peroxidation and protein carbonylation) led to myelin sheaths alterations that can be prevented by treating LXRdKO mice with the ROS scavenger N-acetylcysteine (NAC). Furthermore, we show that the LXR agonist TO901317 protects Schwann cells from ROS by enhancing the antioxidant response through Nrf2 target genes. Therefore, we highlight the potency of LXRs as new therapeutic targets to prevent oxidative stress-mediated peripheral myelin alteration.

Results

LXR knockout induces oxidative stress and antioxidant responses in the sciatic nerve. We first quantified the oxidative state in the sciatic nerves of adult LXRdKO mice. A 3-fold increase of anion superoxide production was observed (Fig. 1a) while the amount of GSH was decreased by 50% when we compared LXRdKO mice to WT (Fig. 1b). We measured the expression level of Nrf2 protein, a redox-sensitive transcription factor that controls the transcriptional activity of antioxidant enzymes. We observed a significant 2-fold increase of Nrf2 protein amount in LXRdKO nerves when compared to WT (Fig. 1c). Interestingly, we observed a parallel stimulation of the survival pathway Akt known to be an upstream effector of Nrf2 signaling^{14,15}. The ratio of P-Akt/Akt was enhanced by 2.5-fold in the sciatic nerves of LXRdKO animals (Fig. 1d). Consequently, both the RNA expression level and the enzymatic activities of the major Nrf2 target genes (*i.e.* G6PDH, 6PGDH and IDH1) were enhanced in the nerves of LXRdKO animals (Fig. 1e and f, respectively). We observed similar results *in vitro* using the mouse Schwann cell-line MSC80. The down-regulation of the expression of both LXR α and LXR β by selective siRNA increased antioxidant gene expression by approximately 50% (Fig. 1g). Altogether, these results show that the absence of LXRs alters the redox homeostasis in Schwann cells and elicits an antioxidant response in the sciatic nerves of adult LXRdKO mice.

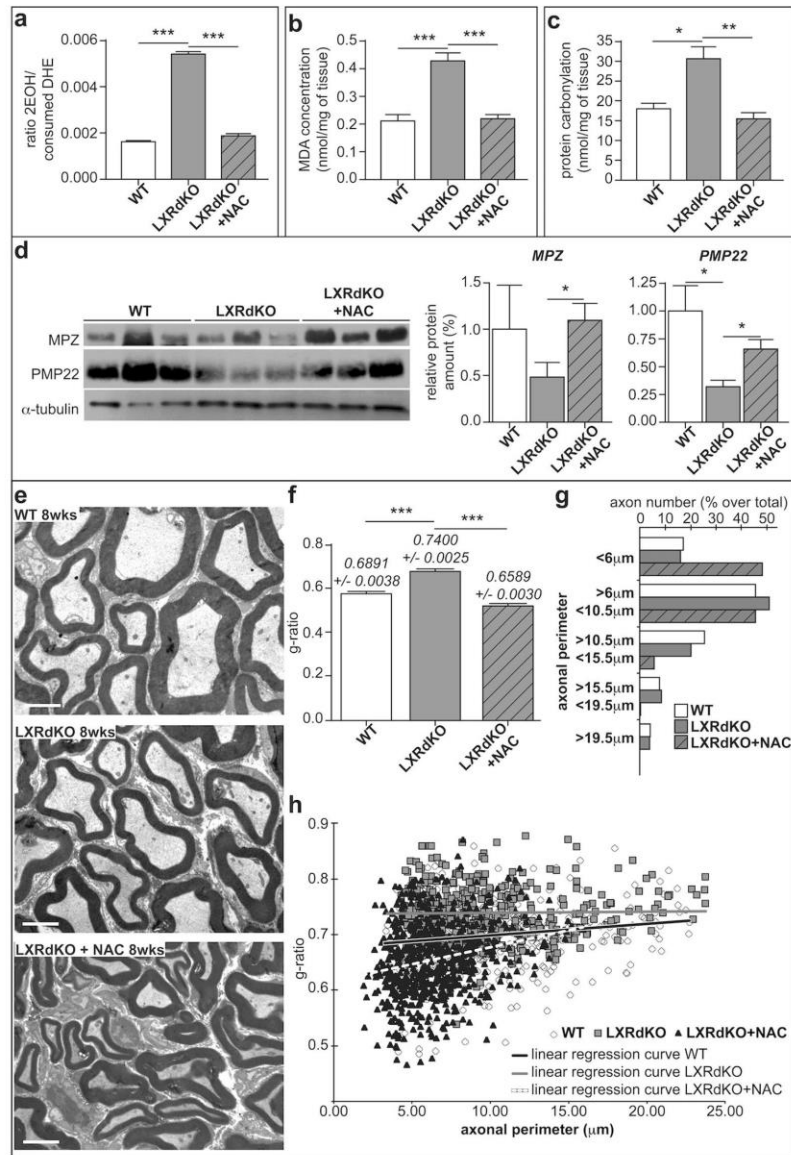


Figure 3. N-acetylcysteine treatment markedly attenuates myelin status alteration in LXRdKO mice. Sciatic nerves from either 8-week-old WT or LXRdKO or NAC-Treated LXRdKO mice were used for these experiments. **(a)** Anion superoxide production quantified by DHE assay using HPLC. **(b)** Lipid peroxidation assay through malonaldehyde (MDA) quantification. **(c)** Protein carbonylation assay. **(d)** Representative western blots (cropped gels) of nerve lysate detecting PMP22 and MPZ proteins. All quantifications were normalized to alpha-tubulin. **(e)** Electron microscopy images of ultrathin (50–90 nm) sciatic nerve cross-sections of WT, LXRdKO or NAC-Treated LXRdKO mice. **(f)** Myelin thickness estimated by g-ratio. Results represent the means \pm SEM of at least 5 animals per group. Statistical significance was assessed by Tukey's post hoc test after ANOVA. **(g)** Myelinated axon size distribution in the sciatic nerves of WT, LXRdKO and LXRdKO + NAC. **(h)** Plotted g-ratio analysis as a function of the axonal perimeter. Linear regression curve is shown in black for WT, grey for LXRdKO and white dashed line for LXRdKO + NAC animals. Results represent the means \pm SEM of at least 5 animals per group. Statistical significance was assessed by a Student's *t* test.

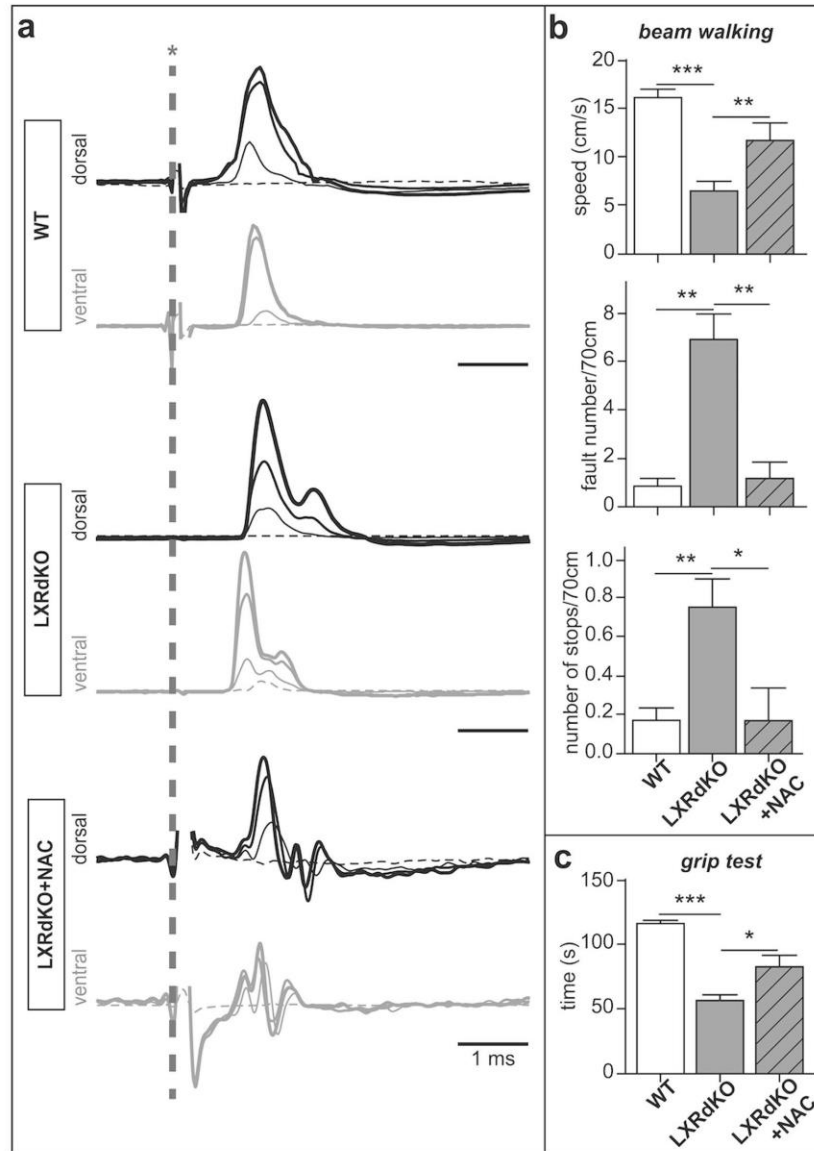


Figure 4. N-acetylcysteine treatment counteracts functional defects in LXRdKO mice. (a) Nerve conduction of WT, LXRdKO or LXRdKO + NAC animals. Representative responses recorded from L4 dorsal (top traces) and ventral (bottom traces) roots following electrical stimulation of the sciatic nerve at different stimulation intensities in WT mice, LXRdKO mice, and LXRdKO mice treated with NAC. The vertical dashed line with an asterisk indicated the time of the stimulation. Each trace is the average response (average of 10–15 sweeps) to stimulation at increasing intensities (dashed line trace, threshold intensity, thinner trace, stimulation at $1.2 \times$ threshold, slightly thicker trace, stimulation at $1.75 \times$ threshold, and the thickest trace is the maximum response at $2-3 \times$ threshold). The stimulation artifacts were truncated. (b) Beam walking test results measuring speed, number of faults and the number of stops while moving along the beam. (c) Grip test results measuring the total time the mice remain suspended from a horizontal bar. Results were obtained across three trials sessions. Results are the mean \pm SEM of 5–7 animals per group; * $P < 0.05$; ** $P < 0.01$; *** $P < 0.001$ by Tukey's post hoc test after ANOVA.

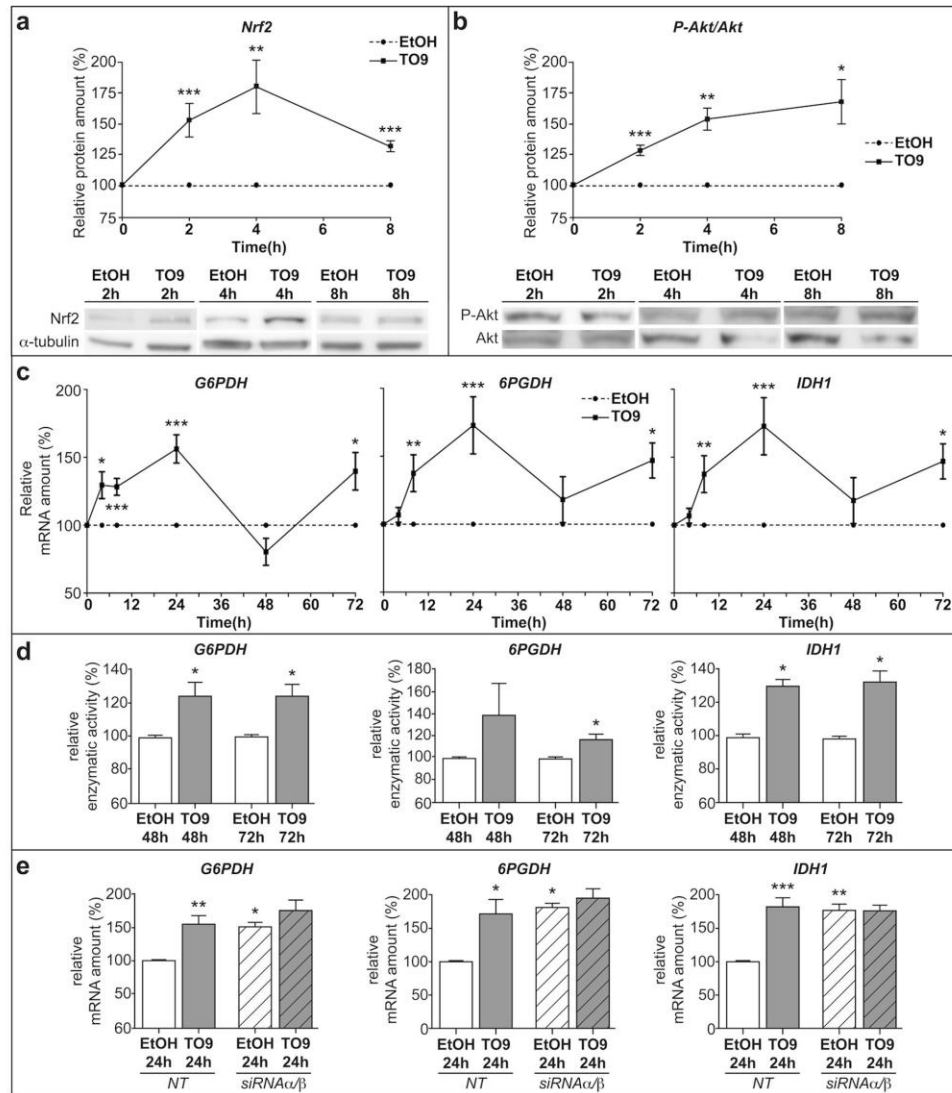


Figure 5. LXR activation by TO901317 regulates anti-oxidant enzyme expression in Schwann cells. MSC80 cells were treated either with TO9 (10 μ M) or vehicle (Ethanol) for 2h, 4h, and 8h. Total proteins were extracted at the specified time points followed by Western Blotting. (a) Expression profile of Nrf2 protein quantified through western blots (cropped gels). All blots were normalized to alpha-tubulin expression. (b) Phosphorylation profile of Akt protein (Ratio P-Akt/Akt) quantified through western blots (cropped gels). All blots were normalized to alpha-tubulin expression. (c) mRNA expression profile of antioxidant response genes across 72h. Transcript levels were normalized to GAPDH expression. Results represent the means \pm SEM of at least three independent experiments. * $P < 0.05$, ** $P < 0.01$ and *** $P < 0.001$ assessed by Tukey's post *hoc* test after ANOVA. (d) Enzymatic activity of antioxidant response genes at 48h and 72h. Enzymatic activity is normalized to tissue weight. (e) MSC80 cells were transfected with either non-target siRNA (NT) or siRNA directed against LXR α and LXR β . 48 hours after transfection, cells were treated either with TO9 (10 μ M) or vehicle (Ethanol) for 24h. mRNA levels of G6PDH, 6PGDH and IDH1 were assessed through RT-qPCR and normalized to GAPDH expression. Results represent the means \pm SEM of at least three independent experiments. * $P < 0.05$, ** $P < 0.01$, *** $P < 0.001$ assessed by Student's *t* test.

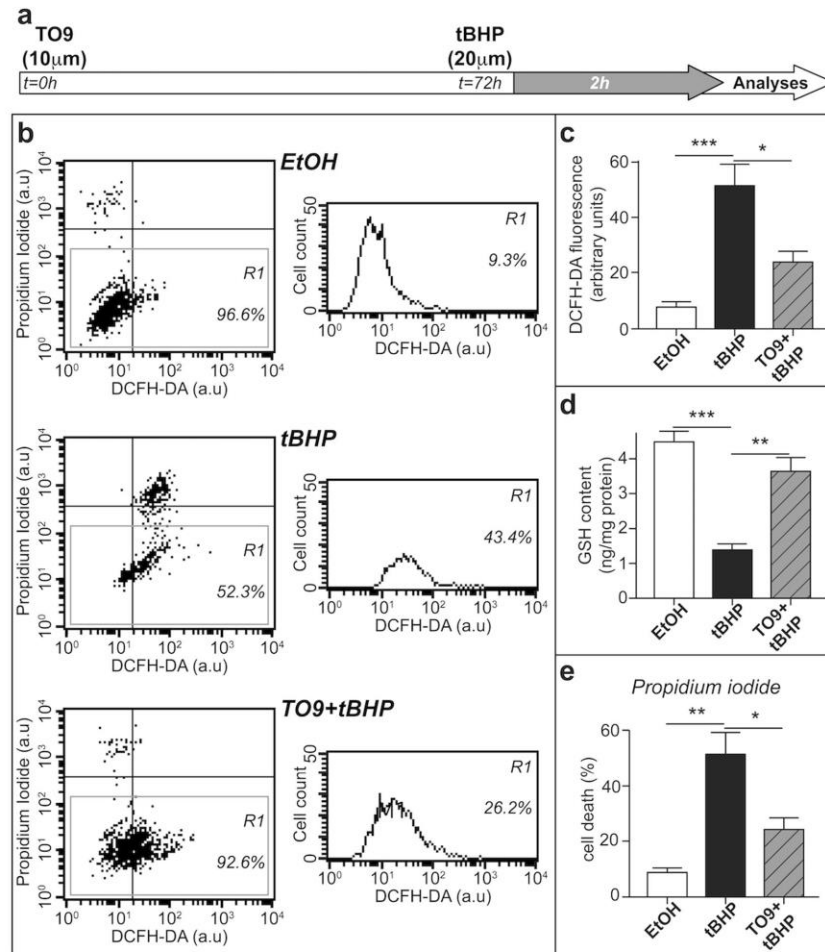


Figure 6. LXR activation reduces ROS generation and cytotoxicity *in vitro*. MSC80 cells were pre-incubated with either TO9 or vehicle control for 72 h and then subjected to tert-butyl hydroperoxide (tBHP) treatment during 2 h. **(a)** Schematic time scale representation of the experiment performed. **(b)** Representative FACS analysis results for each condition (Vehicle control Ethanol: EtOH, Tertbutyl hydroperoxide: tBHP and TO9 + tBHP treatment) X axis represents DCFH-DA fluorescence and Y-Axis represents PI fluorescence. The scatter plot represents the entire population of cells with their respective DCFH-DA and PI fluorescence. The R1 gate considers only live cells to quantify DCFH-DA fluorescence and excludes dead cells. **(c)** Oxidative stress assessed by DCFH-DA fluorescence across 3 individual FACS experiments. **(d)** GSH assay results after tBHP treatment. Cell death assessed by PI fluorescence across 3 individual FACS experiments. Results are presented as the mean \pm SD values of three independent experiments. * $P < 0.05$, ** $P < 0.01$, *** $P < 0.001$ by Tukey's post hoc test after one-way ANOVA when compared with control.

Ablation of LXR does not alter myelination and redox status during development. We then inquired if the knockout of LXR isoforms alters oxidative status and myelin structure from the early stages of sciatic nerve myelination. Interestingly, we observed that anion superoxide production was not affected at the end of the myelination process (post-natal day 21, P21) in the sciatic nerves of LXRdKO animals (Fig. 2a). Furthermore, Nrf2 expression was not significantly modified (Fig. 2b) and neither Myelin Protein Zero (MPZ) nor PMP22 protein amounts were altered when compared to WT mice (Fig. 2c). Finally, electron microscopy analyses of sciatic nerve ultrathin sections at P21 did not reveal any changes in myelin thickness (Fig. 2d) [calculated by g-ratio: inner over outer perimeter of myelinated axons]. These data reveal that the alteration of redox status in LXRdKO are not concomitant with myelin development but appears after the end of this process.

N-acetylcysteine treatment markedly attenuates the myelin alteration in LXRdKO mice. Since LXRdKO exhibited myelin modifications at 8 weeks, it is likely that chronic elevation of oxidative stress leads to the accumulation of oxidative damage. Therefore, we treated LXRdKO mice with the anti-oxidant ROS scavenger N-acetylcysteine (NAC) from P21 (before the emergence of myelin abnormalities) to 8 weeks and investigated both redox status and the extent of myelin structure.

NAC treatment efficiently abolished oxidative stress as revealed by quantifying superoxide production by HPLC (Fig. 3a). Oxidative stress can damage nerve structure through lipid peroxidation and protein carbonylation that we assayed in the sciatic nerves by quantifying the formation of malonaldehyde (MDA) (Fig. 3b) and carbonyls (Fig. 3c), respectively. We observed that the level of MDA in the sciatic nerves of LXRdKO mice was increased by almost 2-folds when compared to WT mice. Notably, lipid peroxidation was totally reversed after NAC administration (Fig. 3b). Similarly, we found a significant increase in the overall level of protein carbonyls by almost 70% in sciatic nerve of LXRdKO mice that was reversed in the nerves of NAC-treated LXRdKO animals (17 nmol/mg of protein for WT and NAC-treated LXR dKO vs 31 nmol/mg protein for LXRdKO) (Fig. 3c).

Since accumulation of oxidative insults can lead to protein degradation, we assessed peripheral myelin levels in the sciatic nerves of WT, LXRdKO and NAC-treated LXRdKO mice (Fig. 3d). LXR extinction led to a decrease of both MPZ and PMP22 protein levels (−50% for MPZ, and −75% for PMP22). Interestingly, NAC treatment brought back myelin protein levels to normal. We pushed forward the analysis of the consequences of ROS generation on myelin integrity and evaluated sciatic nerve myelin ultrastructure by electron microscopy (Fig. 3e). Sciatic nerves of LXRdKO mice displayed thinner myelin sheaths as indicated by a higher g-ratio than WT mice (Fig. 3f). Interestingly, treatment of LXRdKO mice with NAC led to a significant decrease of the sciatic nerve g-ratio, bringing it even lower than in WT. LXR ablation provoked a modest shift in the size of myelinated axons (Fig. 3g), with fewer axons measuring between 10.5 and 15.5 μm of perimeter (20% over total axon number in LXRdKO animals vs 25% in WT animals) to the benefit of smaller ones (50% of the total axonal population sized between 6 and 10.5 μm vs 45% in WT). Notably, NAC administration deeply modifies axon caliber distribution in the sciatic nerves of treated animals. Indeed, high-caliber myelinated axons appear almost absent in the sciatic nerves of NAC-treated LXRdKO animals to the benefit of small-caliber myelinated axons of less than 6 μm of perimeter. Despite an altered axonal caliber distribution in WT, LXRdKO and NAC treated LXRdKO animals, the total number of myelinated axons remained almost the same (16.67 \pm 5.79 for WT, 15.22 \pm 5.47 for LXRdKO and 15.55 \pm 6.42 per 500 μm^2 for NAC Treated LXRdKO animals). Finally, the analysis of plotted g-ratio as a function of the axonal perimeter shows that the alteration of myelin thickness is more severe in small caliber axons (Fig. 3h). In addition, we also reveal that this category of smaller axons appears hypermyelinated in the sciatic nerves of NAC-treated LXRdKO animals.

N-acetylcysteine treatment reverts the deleterious effect of LXR ablation on nerve conduction and locomotion. We assessed the functional consequences of myelin changes in the sciatic nerves of WT and LXRdKO animals treated or not with NAC by assessing nerve conduction (Fig. 4a). On WT mice, stimulation of the sciatic nerve produced a single peak with a short latency on both dorsal and ventral roots. In LXRdKO animals, although sciatic stimulations initially generated a peak at roughly the same latency as in WT mice, they also produced a second peak at longer latency, indicating that a significant proportion of large myelinated fibers in both the dorsal and ventral roots had a reduced conduction velocity compared to controls. Treatment with NAC had complex effects on LXRdKO mice, with three peaks appearing on the response to sciatic stimulation. Although the first peak retained roughly the same latency as in the controls and LXRdKO mice, the second peak tended to have a slightly shorter latency than the second peak observed in LXRdKO mice. Furthermore, a third peak was visible, with a longer latency than both preceding peaks. We think that this third peak corresponds to fibers that, in LXRdKO mice, were conducting too slowly to be synchronized and were therefore unable to produce a measurable peak in the response. These fibers appeared to become faster and more synchronized due to the protective effects of NAC.

Peripheral myelin alterations also led to severe locomotor deficits and muscular weakness that were evaluated using the beam walking test and the grip test, respectively (Fig. 4b and c). We analyzed the ability of WT and LXRdKO animals treated or not with NAC to remain upright and to walk on an elevated and narrow beam. We observed that LXRdKO mice walked the distance twice slower than the control animals (15 cm/sec for WT mice vs 7 cm/sec for LXRdKO mice). Interestingly, NAC-treated animals crossed the beam twice faster than the non-treated LXRdKO mice. Moreover, the number of foot slips made by LXRdKO animals was significantly increased by 6-fold when compared to WT mice, but was brought back to normal following NAC treatment. Furthermore, we noted a 3-fold augmentation in the number of stops made by LXRdKO animals that was decreased to WT level after NAC administration (0.2 stop/70 cm for WT and NAC-treated LXRdKO vs 0.7 stop/70 cm for LXRdKO). Finally, we evaluated the muscular strength and fatigue using the grip test and showed that the NAC-treated LXRdKO mice were able to hold on to the rod using their forelimbs much longer than the LXRdKO mice (Fig. 4c). Indeed, while WT mice succeeded to hold on for over 120 seconds, LXRdKO mice remained suspended for less than 50 seconds while the NAC-treated LXRdKO animals were able to hold on for about 80 seconds.

These results point-out that the absence of LXRs in mice leads to increased ROS production in the sciatic nerve that alters cellular constituents and compromises myelin integrity. This oxidative stress participates in electrophysiological and locomotion defects that could be reversed by treating the mice with N-Acetylcysteine.

LXR activation by TO901317 regulates anti-oxidant enzyme expression in Schwann cells. Our findings indicate that LXRs signaling could be a major actor in the modulation of redox status in the nerve and suggest its relevance for the treatment of oxidative stress related disorders. Consequently, we questioned whether

LXR activation by TO901317 (TO9) could modulate Nrf2 signaling in a mouse Schwann cell-line (MSC80). Western-blot experiments showed that Nrf2 protein levels increased after TO9 treatment (between 2 h to 8 h) (Fig. 5a). Akt survival pathway, upstream effector of Nrf2, was also activated after incubation with TO9. Indeed, Akt phosphorylation was increased by 25% after 2 h, and reached its sustained maximum activation level after 4 hours until at least 8 hours of TO9 treatment (Fig. 5b).

Nrf2 activation by TO9 is followed by the stimulation of anti-oxidant genes: G6PDH, 6PGDH and IDH1 (Fig. 5c). TO9 treatment caused a time-dependent increase of G6PDH, 6PGDH and IDH1 transcripts after 4 and 8 h of treatment, with a peak activity seen at 24 h with 60% increase. An induction in the enzymatic activities of G6PDH, 6PGDH and IDH1 was observed (Fig. 5d). Interestingly, the knockdown of LXRs by siRNA in MSC80 abrogated the activation of antioxidant genes by TO9 (Fig. 5e), confirming that TO9-mediated antioxidant response in Schwann cells requires the presence of LXRs. Altogether these results show that TO9 can trigger cellular antioxidant responses and could be potent enough to alleviate ROS-mediated deleterious outcomes in Schwann cells.

LXR activation reduces ROS generation and cytotoxicity *in vitro*. We finally investigated whether LXR activation by TO9 could protect Schwann cell-line from the deleterious effects of increased ROS production. We pre-treated MSC80 with TO9 for 72 h before provoking ROS production by *tert*-butyl hydroperoxide (tBHP) (Fig. 6a). We quantified ROS production and cell death by flow cytometry (using DCFH-DA and propidium iodide staining, Fig. 6b) and observed that TO9 pre-treatment was able to dampen ROS production (Fig. 6c). The cells appear to be well prepared to fight against the oxidative stress. Indeed, the amount of GSH was decreased by almost 60% after tBHP treatment, and that TO9 pre-treatment brought back GSH concentration to control levels (Fig. 6d). Moreover, TO9 treatment is able to prevent cell death elicited by tBHP treatment (Fig. 6e) as observed through decreased PI fluorescence.

Discussion

LXR activation is classically known to have beneficial outcomes for the treatment of several chronic diseases through anti-inflammatory effects and regulation of cholesterol homeostasis^{16–20}. For example, LXR activation affects Parkinson disease progression by modulating the cytotoxic functions of microglia²¹ and attenuates diabetic neuropathy by stimulating neuroprotective steroid synthesis¹⁶. LXRs have also been exploited as potential targets for oxidative stress disorders that provoke myocardial dysfunctions in diabetic db/db model mice^{22,23}.

In this study, we established that LXRs have an anti-oxidant potential in Schwann cells and in the peripheral nerve. We detected an increased anion superoxide production in the sciatic nerves of LXRdKO mice. We also observed a concomitant augmentation in lipid peroxidation and protein carbonylation along with a drop in reduced glutathione, hallmarks of many chronic neurodegenerative diseases²⁴. Previously, our team showed that the knock-out of LXRs reduced the thickness of myelin sheaths in the sciatic nerves of adult animals^{4,5}. This phenotype was accompanied by a down regulation of myelin protein levels despite a stimulation of their respective transcripts. Here, we provide evidence that the myelin disorder observed could be linked to altered redox status in the sciatic nerves of LXRdKO animals, leading to accumulation of oxidative insults responsible of peripheral myelin progressive alteration. Indeed, in young LXRdKO animals (P21) neither the alteration of myelin structure nor the activation of cellular responses to oxidative stress was detectable. Thus, the compromised myelin integrity observed in adult LXRdKO mice is not initiated at birth but develops after the end of the myelination process (P21). The oxidative environment produced by the loss of LXR function coupled with an overexpression of myelin genes can presumably induce accumulation of modified cellular constituents as the animal grows and progressively compromises myelin integrity. This plausible cause-effect explanation is indeed verified when we administered the antioxidant molecule, NAC, to LXRdKO mice from P21 until P56 (8 week-old). A 5-week long treatment with this ROS scavenger allowed the mice to recover from locomotor impairment elicited by LXR genetic ablation, together with a normalization of both sciatic lipid peroxidation and protein carbonylation levels.

Besides, NAC treatment led to profound changes in axonal topology within the sciatic nerves of LXRdKO animals. A dramatic increase of the number of small and hypermyelinated axons were observed at the expense of large caliber axons that were missing. In fact, we previously demonstrated that LXRs signaling is a negative driver of myelination in the PNS^{4,5}. Thus, myelin genes are stimulated in the absence of LXRs. Attenuation of the oxidative stress due to NAC administration prevented the accumulation of oxidative insults that could participate in myelin degradation, thereby inducing hypermyelination of certain type of axons. The shift in sciatic axonal topology was unraveled when we analyzed the nerve conduction velocity. LXRdKO animals exhibited faults in transmitting rapid nervous influx accounting for their locomotor defects. NAC-treated animals exhibited a more complex scheme, with the appearance of shifted faster peaks that could compensate for the loss of large, fast axons, through the recruitment of small, hypermyelinated axons. Those could allow a faster transmission of the influx and improve fine locomotion behavior we highlighted in NAC-treated LXRdKO animals. Altogether, we have shown here that the locomotor defects observed in LXRdKO mice could be reversed upon an antioxidant treatment with NAC from P21, before the emergence of oxidative stress and alteration of myelin status. These observations underline the deleterious consequences of the accumulation of oxidative damage^{25,26}. Moreover, the functional, cellular and molecular recovery initiated by NAC suggest a direct link between increased ROS production and myelin damage accumulation in the peripheral nerves in the absence of LXRs. However, these alterations in myelin status could also be attributed to axonal diameter changes. Indeed, several signaling pathways govern the tight crosstalk between Schwann cells and axons. For instance, it is well known that axonal Neuregulin-1 interacts with ErbB receptor on myelinating Schwann cells to command myelin thickness²⁷. In fact, the NAC treatment leading to a shift in sciatic axonal topology could in turn affect myelination.

Dynamic changes are seen in the Nrf2 pathway in patients as well as in animal models of aging and disease²⁸. Akt/Nrf2 pathway has already been implicated in neuroprotection against oxidative stress damage in the

CNS. Indeed, Lee and colleagues showed that an inhibition of the molecular hub PI3K/Akt pathway provokes the downregulation of Nrf2 signaling and subsequent oxidative stress in mouse hippocampal HT22 cells²⁹. In LXRdKO nerves, enzymes implicated in glutathione metabolism are stimulated, but the extent of endogenous activation of Nrf2 is not sufficient to combat the overload of oxidative stress. Interestingly, both LXR inhibition in mice and LXR activation by TO9 in Schwann cells stimulated Nrf2 signaling through Akt survival pathway. These results are in accordance with recent studies showing that exogenous activation of Nrf2 pathway has neuroprotective effects in fighting against sciatic nerve oxidative stress damage in streptozotocin-induced diabetic rats^{30,31}. Moreover, deletion of Nrf2 also impairs functional recovery, reduces clearance of myelin debris and decreases axonal remyelination after peripheral nerve injury¹².

Furthermore, when MSC80 cells were treated with LXR agonist, TO9, we observed a stimulation of the enzymatic antioxidant response sufficient enough to counteract the deleterious effects of *tert*-butylhydroperoxide, a potent pro-oxidant molecule. Hence, following LXR activation in Schwann cells, we were able to stimulate anti-oxidant defenses to dampen ROS production and subsequent alteration of cellular constituents causing cell death.

We previously revealed that LXR agonists are encouraging candidates for the treatment of central myelin disorders as they were able to stimulate myelin gene expression and cellular maturation to increase remyelinating efficacy³. Here we show that LXR activation could also be a promising strategy to reduce oxidative stress-induced damages by activating an anti-oxidant response in the peripheral nervous system. Therefore, this study helps to better understand the importance of LXRs in the modulation of cellular redox status in the peripheral nerve and paves way for developing promising avenues for the treatment of oxidative stress disorders based on LXR modulation.

Methods

All methods were performed in accordance with the relevant guidelines and regulations of INSERM and Université Paris Descartes.

Animals and *in vivo* experiments. LXRdKO mice and their wild-type (WT) controls were maintained on a mixed strain background (C57BL/6:129 Sv) and housed in a temperature-controlled room with a 12 h light/dark cycle. All experiments were performed on age-matched male mice (8 weeks old). Animals were fed *ad libitum* with water. N-acetylcysteine (NAC) treatment was administered in a 0.1% drinking water solution during five weeks to independent groups of LXRdKO mice from P21 to P56 (8 week-old mice). Sciatic nerves were collected and frozen either in liquid nitrogen or isopentane. All aspects of animal care were approved by the National Ethic Committee (No. 2016092216181520).

Cell culture and treatment. The mouse SC line (MSC80) was maintained in Dulbecco's minimal essential medium (DMEM) supplemented with 10% decomplexed fetal calf serum (Hyclone-Perbio), 1% penicillin, 1% streptomycin (Gibco) and 1% Glutamine (Gibco). All cultures were grown at 37 °C in a humidified atmosphere of 5% CO₂. MSC80 cells were treated with TO901317 (Tocris) at the concentration of 10 μM in DMEM.

Transient transfections. Cells were transiently transfected with siLXRs (Dharmacon) using Effecten reagent (Effecten Transfection Reagent, Qiagen). One day prior to the transfection, MSC80 cells (1.5×10^5 cells/well) were cultured on 6-well plates and incubated in the DMEM culture medium containing 10% heat inactivated fetal calf serum. Sixteen hours post transfection, the medium was replaced by DMEM or DMEM containing TO901317 (10 μM) or vehicle (Ethanol).

Behavioral tests. *Rod test.* Mice were trained to walk along a horizontal rod (70 cm long, 3 cm diameter) placed at an elevation of 30 cm on a bench. The mice were taught to move from a platform on one end to the goal box on the other. Once the mice had succeeded in reaching the goal box several times with the help of investigator, the test was recorded in three trials. Mice that fell were returned to the position they fell from with a maximum time of 60 s allowed on the beam. The speed, the number of times the mice slipped on the rod, the number of falls and stops were measured. A high definition digital camera was used to film the experiment.

Grip test. The time spent holding onto a thin metal rod suspended in midair was calculated. Each mouse was subjected to 3 successive attempts separated by a 10-minute rest period. All tests were made blind, the group assignment being unknown to the observers.

Sciatic nerve conduction velocity measurement. 8 week-old mice were anesthetized with isofluorane. Once surgical plane was reached, the mouse was transferred to a heating pad and anesthesia was continued through a gas mask. The right sciatic nerve was dissected free, cut distally, and placed on a bipolar stimulation electrode. A laminectomy was then performed on vertebral segments L1-L5. The L4 dorsal ganglion was identified and the L4 dorsal and ventral roots were dissected and cut close to the spinal cord. Each root was placed on a recording electrode. The sciatic nerve was stimulated at 1 Hz at increasing stimulation intensities while afferent and antidromic efferent volleys were recorded on the dorsal and ventral root, respectively. At the end of the experiment, mice were killed with an overdose of pentobarbital.

Lipid peroxidation. Lipid peroxidation assay kit (Abcam ab118970) was used to detect malonaldehyde (MDA) present in samples as per the manufacturer's instruction with slight modifications. Detailed description can be found in Supplemental Methods.

Protein carbonylation. Sciatic nerves were homogenized in 5–10 ml of 100 mM Tris, pH 7.4 and then, tissues were centrifuged at 10000 g for 15 min at 4 °C. The supernatant was removed and stored on ice. Protein concentration of each sample was determined by DC assay (BIORAD) and adjusted between 5–10 mg/ml. 200 µl of each sample was mixed with 200 µl of 10 mM DNPH in 2 N HCl or with 200 µl of 2 N HCl alone for the blank and incubated at room temperature for 1 h in the dark. Samples were frequently vortexed every 15 min. Proteins were precipitated with 20% trichloroacetic acid (w/v), vortexed and centrifuged (13,000 g for 3 min). The pellet was washed three times with 1 ml ethanol-ethyl acetate (1:1 v/v) before re-dissolving in 1 ml of 6 M guanidine HCl in 20 mM potassium phosphate adjusted to pH 2.3 with trifluoroacetic acid. The absorbance was measured in the supernatant at 360 nm and carbonyl content was calculated, using the molar absorption coefficient of 22,000 M⁻¹cm⁻¹ relative to protein concentration.

GSH measurement. Intracellular reduced glutathione (GSH) levels from sciatic nerves and MSC80 cells were measured by the Glutathione assay kit (Sigma Aldrich CS1020) as per the manufacturer's instructions.

Western blot. Frozen sciatic nerves from adult mice were homogenized using a Bead Mill Homogenizer (RETSCH MM300) in RIPA buffer [25 mM Tris•HCl pH 7.6, 150 mM NaCl, 1% NP-40, 1% sodium deoxycholate, 0.1% SDS] supplemented with Protease Inhibitor Cocktail. (Roche) The lysates were centrifuged at 12000 g for 15 min at 4 °C and protein content in the supernatant was assessed using the RC DC protein assay kit (Bio-Rad) with BSA (2 mg/ml) as standard. Equal quantities of Sciatic Nerve or MSC80 protein lysates were separated on 12% SDS-PAGE and blotted onto polyvinylidene difluoride (PVDF) membranes. Nonspecific binding sites in the transblots were blocked with 5% Bovine Serum Albumin (Sigma) in Tris Buffer Saline 1 × with 0.1% Tween 20 (Invitrogen) for at least an hour. Membranes were then incubated at 4 °C overnight with the following primary antibodies diluted in a mixture of BSA 5%/TBS- Tween 0.1%: Rabbit polyclonal PMP22 antibody (Abcam, 1:1000), P0 antibody (Abcam, 1:750), Nrf2 antibody (Abcam, 1:100), Phospho-Akt Serine 473 antibody (Abcam, 1:1000), Akt antibody (Abcam, 1:1000), α -tubulin antibody (Abcam, 1:10000). The membranes were then washed and incubated at room temperature for 1 h with the appropriate secondary antibody (HRP conjugated Goat Anti-Mouse or Anti-Rabbit IgG at 1:20000, Millipore) diluted in 5% BSA/TBS-0.1% Tween followed by ECL Plus Western Blot Detection (GE Healthcare). Protein bands were detected using ImageQuant LAS 4000 imager (GE healthcare) and quantified using NIH Image J Software.

Transmission electron microscopy. Eight-week-old and P21 mice were deeply anesthetized by intraperitoneal injection of 40 mg/kg ketamine and 30 mg/kg xylazine and then intracardially perfused with 4% paraformaldehyde, 2.5% glutaraldehyde, and 0.1 M phosphate buffer, pH 7.4. Tissues were dissected and immersed in the same fixative solution at 4 °C overnight, washed in phosphate buffer, postfixed in 2% osmium tetroxide, dehydrated in graded ethanol series and embedded in epoxy resin. For electron microscopy, ultrathin sections (50–90 nm) were cut on an ultramicrotome (8800 Ultratome III; LKB Bromma) and collected on 300-mesh nickel grids. Staining was performed on drops of 4% aqueous uranyl acetate, followed by Reynolds's lead. Ultrastructural analyses were performed in a JEOL jem-1011 electron microscope and digitalized with DigitalMicrograph software. Electron microscopy images were used for calculating the g-ratio and axon perimeter using NIH ImageJ software. At least 100 randomly selected axons were analyzed per animal. At least three animals were used per genotype. Healthy axons were defined based on the presence of intact membranes and the normal complement of organelles.

RT-qPCR experiments. Total RNA from sciatic nerves or cultured MSC80 was obtained using TRIzol Plus RNA purification Kit (Thermo Fischer Scientific). One microgram was reverse transcribed with random primers (Promega) and reverse transcriptase MMLV-RT (Invitrogen). PCR experiments were performed using TaqDNA polymerase (Promega) and specific primer sequences (Eurofins). Quantitative real-time PCR was performed with standard protocols using SYBRGreen ROX Mix (ABgene) as a fluorescent detection dye in ABI PRISM 7000. For a final reaction volume of 7 µl, 300 nM primers and 20 ng of reverse-transcribed RNA were used in 384-well plates. Each reaction was performed in triplicate, and the mean of at least three independent experiments was calculated. The melt curve analyses were used to characterize amplicons and to check for contamination. Relative mRNA quantities were normalized to the GAPDH mRNA level and expression fold change was calculated using the $\Delta\Delta C_t$ method. Refer to Supplementary Table 1 for primer sequences.

Enzymatic activity assays (G6PDH, 6PGDH, IDH assay). Frozen cells or sciatic nerves were collected and homogenized in 50 µl of resuspension buffer. 3 µl of each sample were added to 200 µl of either:

- (i) G6PDH buffer (100 mM AMP-OL pH 9.4, 1 mM of Glucose-6-Phosphate, 50 µM of NADP⁺, 0.5 mM of EDTA and 0.02% BSA)
- (ii) 6PGDH buffer (50 mM Tris acetate buffer pH 8.1, 1 mM of 6-phosphogluconate, 50 µM of NADP⁺, 0.1 mM of EDTA and 0.05% BSA)
- (iii) IDH buffer (50 mM Tris HCl buffer pH 8.2, 2 mM of isocitrate 1 mM of NADP⁺, 0.2 mM of MnCl₂ and 0.05% BSA)

In these assays, enzymatic activities are proportional to the concentration of NADPH produced from NADP⁺ reduction³². The fluorescence signal was read every 2 minutes for a total time of 20 minutes in a plate reader (TECAN) at Ex/Em = 340 nm/460 nm. Enzymatic activity is expressed in nanomoles of NADPH produced per min normalized to tissue weight.

Assessment of cytosolic ROS and cell death using flow cytometry. Flow cytometry experiments were performed on a FACS Calibur flow cytometer (Becton Dickinson, San Jose, CA, USA). Cellular oxidative stress was measured by flow cytometry using dichloro-dihydro-fluorescein diacetate (DCFH-DA) assay (Molecular Probes by Life technologies, D-399). MSC80 cells (250000 cells/well in 6-well plates) were pretreated with T0 for 72 h followed by 2 h of tert-butyl hydroperoxide (tBHP 20 μ M) treatment to induce ROS production. After tBHP treatment, the cells were washed, collected and incubated with 0.5 μ M DCFH-DA for 30 min at 37 °C. After DCFH-DA incubation the cells were centrifuged and resuspended again in 1 ml of PBS with 1 μ l of PI solution (50 μ g/ml, Life technologies) followed by flow cytometry. A total of 10,000 events were recorded with a flow rate of less than 200 cells/second for each assay. Data analysis was performed using BD Cell Quest Pro Software.

In situ detection of superoxide by HPLC. HPLC experiments were performed on Jasco HPLC system, LC-2000 plus series as previously described^{10,11}. For a detailed protocol refer to supplementary methods.

References

1. Radhakrishnan, A., Ikeda, Y., Kwon, H. J., Brown, M. S. & Goldstein, J. L. Sterol-regulated transport of SREBPs from endoplasmic reticulum to Golgi: Oxysterols block transport by binding to Insig. *Proc. Natl. Acad. Sci.* **104**, 6511–6518 (2007).
2. Andersson, S., Gustafsson, N., Warner, M. & Gustafsson, J.-A. Inactivation of liver X receptor beta leads to adult-onset motor neuron degeneration in male mice. *Proc. Natl. Acad. Sci. USA* **102**, 3857–62 (2005).
3. Meffre, D. *et al.* Liver X receptors alpha and beta promote myelination and remyelination in the cerebellum. *Proc. Natl. Acad. Sci. USA* **112**, 7587–92 (2015).
4. Makoukji, J. *et al.* Interplay between LXR and Wnt/ β -catenin signaling in the negative regulation of peripheral myelin genes by oxysterols. *J. Neurosci.* **31**, 9620–9 (2011).
5. Shackelford, G. *et al.* Differential regulation of Wnt/ β -catenin signaling by Liver X Receptors in Schwann cells and oligodendrocytes. *Biochem. Pharmacol.* **86**, 106–114 (2013).
6. Hamilton, R. T. *et al.* Elevated protein carbonylation, and misfolding in sciatic nerve from db/db and Sod1(–/–) mice: plausible link between oxidative stress and demyelination. *PLoS One* **8**, e65725 (2013).
7. Hichor, M. *et al.* Paraquat Induces Peripheral Myelin Disruption and Locomotor Defects: Crosstalk with LXR and Wnt Pathways. *Antioxid. Redox Signal. ars* **2016.6711**. <https://doi.org/10.1089/ars.2016.6711> (2016).
8. Barateiro, A., Brites, D. & Fernandes, A. Oligodendrocyte Development and Myelination in Neurodevelopment: Molecular Mechanisms in Health and Disease. *Curr. Pharm. Des.* **22**, 656–79 (2016).
9. Lu, X.-L. *et al.* Paeonolol protects against MPP(+)-induced neurotoxicity in zebrafish and PC12 cells. *BMC Complement. Altern. Med.* **15**, 137 (2015).
10. Serini, S. & Calviello, G. Reduction of Oxidative/Nitrosative Stress in Brain and its Involvement in the Neuroprotective Effect of n-3 PUFA in Alzheimer's Disease. *Curr. Alzheimer Res.* **13**, 123–34 (2016).
11. Espinosa-Diez, C. *et al.* Antioxidant responses and cellular adjustments to oxidative stress. *Redox Biol.* **6**, 183–97 (2015).
12. Zhang, L., Johnson, D. & Johnson, J. A. Deletion of Nrf2 impairs functional recovery, reduces clearance of myelin debris and decreases axonal remyelination after peripheral nerve injury. *Neurobiol. Dis.* **54**, 329–38 (2013).
13. Denzer, I., Münch, G. & Friedland, K. Modulation of mitochondrial dysfunction in neurodegenerative diseases via activation of nuclear factor erythroid-2-related factor 2 by food-derived compounds. *Pharmacol. Res.* **103**, 80–94 (2016).
14. Qi, H., Han, Y. & Rong, J. Potential roles of PI3K/Akt and Nrf2–Keap1 pathways in regulating hormesis of Z-ligustilide in PC12 cells against oxygen and glucose deprivation. *Neuropharmacology* **62**, 1659–1670 (2012).
15. Wang, L., Chen, Y., Sternberg, P. & Cai, J. Essential Roles of the PI3 Kinase/Akt Pathway in Regulating Nrf2-Dependent Antioxidant Functions in the RPE. *Investig. Ophthalmology Vis. Sci.* **49**, 1671 (2008).
16. Cermenati, G. *et al.* Activation of the liver X receptor increases neuroactive steroid levels and protects from diabetes-induced peripheral neuropathy. *J. Neurosci.* **30**, 11896–901 (2010).
17. Sandireddy, R., Yerra, V. G., Areti, A., Komirishetty, P. & Kumar, A. Neuroinflammation and oxidative stress in diabetic neuropathy: futuristic strategies based on these targets. *Int. J. Endocrinol.* **2014**, 674987 (2014).
18. Xu, P. *et al.* LXR agonists: New potential therapeutic drug for neurodegenerative diseases. *Mol. Neurobiol.* **48**, 715–728 (2013).
19. Verheijen, M. H. G. *et al.* SCAP is required for timely and proper myelin membrane synthesis. *Proc. Natl. Acad. Sci. USA* **106**, 21383–8 (2009).
20. Sandireddy, R., Yerra, V. G., Komirishetty, P., Areti, A. & Kumar, A. Fisetin Imparts Neuroprotection in Experimental Diabetic Neuropathy by Modulating Nrf2 and NF- κ B Pathways. *Cell. Mol. Neurobiol.* **36**, 883–92 (2016).
21. Marwarha, G., Rhen, T., Schommer, T. & Ghribi, O. The oxysterol 27-hydroxycholesterol regulates α -synuclein and tyrosine hydroxylase expression levels in human neuroblastoma cells through modulation of liver X receptors and estrogen receptors—relevance to Parkinson's disease. *J. Neurochem.* **119**, 1119–36 (2011).
22. Fang, D. *et al.* Endoplasmic reticulum stress leads to lipid accumulation through upregulation of SREBP-1c in normal hepatic and hepatoma cells. *Mol. Cell. Biochem.* **381**, 127–37 (2013).
23. He, Q. *et al.* Liver X receptor agonist treatment attenuates cardiac dysfunction in type 2 diabetic db/db mice. *Cardiovasc. Diabetol.* **13**, 149 (2014).
24. Rebrin, I., Kamzalov, S. & Sohal, R. S. Effects of age and caloric restriction on glutathione redox state in mice. *Free Radic. Biol. Med.* **35**, 626–35 (2003).
25. Gan, N. *et al.* Sulforaphane activates heat shock response and enhances proteasome activity through up-regulation of Hsp27. *J. Biol. Chem.* **285**, 35528–36 (2010).
26. Dong, Y. *et al.* Activation of the Liver X Receptor by Agonist TO901317 Improves Hepatic Insulin Resistance via Suppressing Reactive Oxygen Species and JNK Pathway. *PLoS One* **10**, e0124778 (2015).
27. Michailov, G. V. *et al.* Axonal Neuregulin-1 Regulates Myelin Sheath Thickness. *Science (80-)*. **304**, 700–703 (2004).
28. Gan, L. & Johnson, J. A. Oxidative damage and the Nrf2-ARE pathway in neurodegenerative diseases. *Biochim. Biophys. Acta - Mol. Basis Dis.* **1842**, 1208–1218 (2014).
29. Lee, D.-S., Ko, W., Kim, D.-C., Kim, Y.-C. & Jeong, G.-S. Cudarflavone B provides neuroprotection against glutamate-induced mouse hippocampal HT22 cell damage through the Nrf2 and PI3K/Akt signaling pathways. *Molecules* **19**, 10818–31 (2014).
30. Yang, X. *et al.* Mechanism of Tang Luo Ning effect on attenuating of oxidative stress in sciatic nerve of STZ-induced diabetic rats. *J. Ethnopharmacol.* **174**, 1–10 (2015).
31. Yang, X. *et al.* Tangleuning, a traditional Chinese medicine, attenuates *in vivo* and *in vitro* diabetic peripheral neuropathy through modulation of PERK/Nrf2 pathway. *Sci. Rep.* **7**, 1014 (2017).
32. Passonneau, J. V., Lowry, O. H. & Lowry, O. H. *Enzymatic analysis: a practical guide.* (Humana Press, 1993).

Acknowledgements

This work was funded by INSERM, CNRS, Paris Descartes University, ANR. M.H. and V.K.S. received PhD fellowships from the French Ministry of Research (MNRT). We greatly acknowledge Claire Mader from the Animal Facility of the Saints Pères, and A. Schmitt from the Cochin Imaging Facility and S. Dupuy from the Saints-Pères Flow Cytometer Facility.

Author Contributions

M.H., V.K.S. performed the experiments and analyzed the data. S.A.E., R.A.R., P.X.P., D.B., J.B., M.M. and A.A.E. performed experiments. J.G. prepared the figures and corrected the article. C.M. conceived the experiments and wrote the manuscript.

Additional Information

Supplementary information accompanies this paper at <https://doi.org/10.1038/s41598-018-20980-3>.

Competing Interests: The authors declare that they have no competing interests.

Publisher's note: Springer Nature remains neutral with regard to jurisdictional claims in published maps and institutional affiliations.



Open Access This article is licensed under a Creative Commons Attribution 4.0 International License, which permits use, sharing, adaptation, distribution and reproduction in any medium or format, as long as you give appropriate credit to the original author(s) and the source, provide a link to the Creative Commons license, and indicate if changes were made. The images or other third party material in this article are included in the article's Creative Commons license, unless indicated otherwise in a credit line to the material. If material is not included in the article's Creative Commons license and your intended use is not permitted by statutory regulation or exceeds the permitted use, you will need to obtain permission directly from the copyright holder. To view a copy of this license, visit <http://creativecommons.org/licenses/by/4.0/>.

© The Author(s) 2018

Perspectives:

Although this study provides preliminary evidence to the protective role of LXRs in Schwann cells against oxidative stress, the provenance of the latter remained elusive. In other words, we could not identify the causative agents of the oxidative stress in the sciatic nerves of LXRdKO mice. As the myelin protein and the myelin sheath were impacted, we speculated that the resulting phenotype was due to the ablation of the nuclear receptor in Schwann cells. To test this hypothesis, we generated a Schwann cell specific Knockout of LXR α and LXR β by crossing floxed strains of the nuclear receptor with Desert Hedgehog-Cre (Dhh-Cre) mice. The resulting mutants exhibited an ablation of LXR α and LXR β from the SCP stage of Schwann cell development. Much to our surprise, we observed a drastic phenotype in LXR α/β ^{f/f}: DhhCre mice

We next decided to selectively breed out LXR α or LXR β from these mutants to generate ablation of both the isoforms separately. We observed that LXR α ^{f/f}:DhhCre do not exhibit any phenotype but the phenotype of LXR β ^{f/f}:DhhCre faithfully recapitulated the phenotype of LXR α/β ^{f/f}: DhhCre mice both at the behavioral and histological levels. Thus, we concluded that the β isoform of the nuclear receptor is indispensable from Schwann cells and focused our research on LXR β ^{f/f}:DhhCre (LXR β ScKO) . The observations on these Schwann Cell specific mutants form the core of the research that I conducted in my doctoral thesis. These results along with future avenues of research are detailed in the following sections.

3.2 LXR β IS INDISPENSABLE FOR THE SURVIVAL OF SCHWANN CELL PRECURSORS IN DEVELOPING SPINAL NERVES

3.2.1 Validation of the model:

The LXR β gene is composed of 10 exons with the coding region that begins at exon 3 (**Figure 1A**). Therefore, the LoxP sites were inserted upstream of Exon 3 and downstream of exon 7. This region contained by the LoxP sites codes for the DNA-Binding Domain (DBD) and the Ligand-Binding Domain (LBD) of the LXR β protein. Thus, recombinase mediated excision of this targeted region would indeed result in the deletion of the functionally important domains of the LXR β gene.

As Schwann cells are absent in LXR β SckO nerves, we devised an indirect approach to validate the model. To confirm that the targeted mutation of LXR β in Schwann cells has the desired molecular effect, we isolated Primary Schwann Cells from LXR $\beta^{f/f}$ (Control) animals and treated them with TAT-Cre Recombinase (1 μ M) for 2 hours. The exogenous addition Recombinase, resulted in a drastic reduction of LXR β transcripts, most notably the regions between exons 4,5 and 7,8 which codes for the DNA binding and ligand binding domain (**Figure 1B**). Of note, the expression of Exon 1 and 2 remained unchanged suggesting that LXR β does not control its own expression. Furthermore, we also observed the downregulation of LXR β target gene ABCA1 (**Figure 1B**). These results show that the targeted insertion of LoxP sites in the LXR β gene results in the desired effect of LXR β ablation upon Cre recombinase action. Furthermore, we also observe that LXR β is the major activator of ABCA1 in SC cultures.

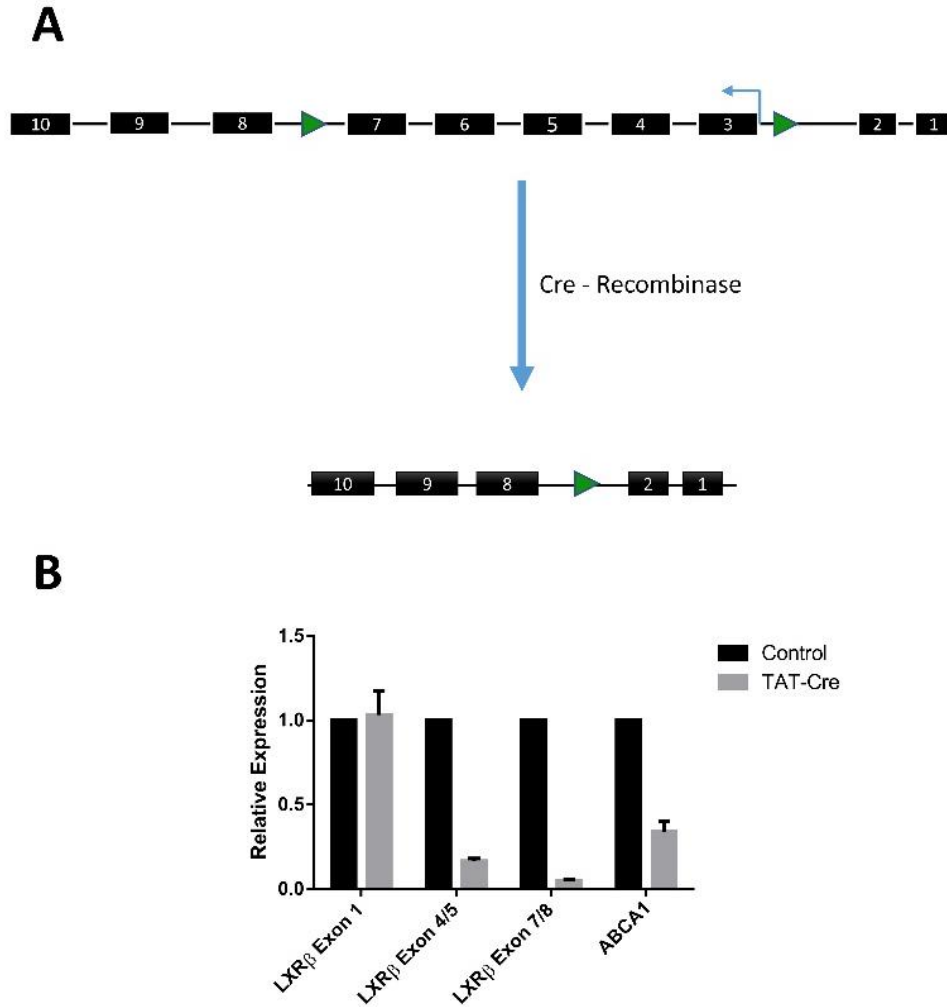


Figure 1: **Validation of the model.** (A) *LoxP* sites in the *LXR β* gene are inserted upstream of exon 3 and downstream of exon 7. *Cre*-mediated excision would result in the deletion of exons 3 to 7 that code for the DBD and LBD. Truncated expression of *LXR β* is theoretically not possible due to the absence of a start codon in the remaining fragment. (B) Primary Schwann cells from the *LXR β ^{fl/fl}* strain were treated with TAT-*Cre* (exogenous recombinase) at 1 μ M for 4 hours. TAT-*Cre* treatment of control *LXR β ^{fl/fl}* primary Schwann cells resulted in the deletion of the region flanked by the *LoxP* sites as assessed through qPCR using primers that specifically amplified regions spanned by Exon 1, Exon 4 and 5, Exons 7 and 8. *Cre* treatment also resulted in the downregulation of *LXR β* target gene *ABCA1*.

3.2.2 Phenotypic description of LXR β ScKO animals:

LXR β ScKO animals were born in the expected mendelian ratios. WT (LXR $\beta^{f/f}$) and mutant animals are indistinguishable for the first 2 weeks after birth. By postnatal day 21 (P21), the mutants developed paralysis of the hind limbs and the movement of their forelimbs were reduced. The paralysis in the caudal region progressed as mice aged and we observed a complete loss of tail movement by the time they were 8 weeks old. Between 8 and 20 weeks, they drastically lost weight and they developed severe motor coordination deficits. They also developed a hunched back and suffered from palpitations and shortness of breath, which are clinical signs of peripheral neuropathy. All mutant mice died at around 7 months. The Kaplan-Meier survival graphs for the mutants are shown in **Figure 2A**.

Owing to the severe apparent locomotor deficits observed in adult LXR β ScKO animals, we first analyzed their muscular strength at 8 weeks. The grip strength (all limbs) of LXR β ScKO was drastically reduced to about 90 grams (force) whereas age matched WT (LXR $\beta^{f/f}$) animals displayed about 200 grams (force) on average (**Figure 2B**). Furthermore, the mutant mice were insensitive to the hot plate test whereas the control animals reacted to heat at around 20 seconds on a hot plate (**Figure 2C**). When we dissected the mutant mice at 8 weeks, we observed that the sciatic nerves were thinner and translucent, and we could see through the tissue whereas, in the control animals, the nerves appeared thicker and opaque (**Figure 2D**).

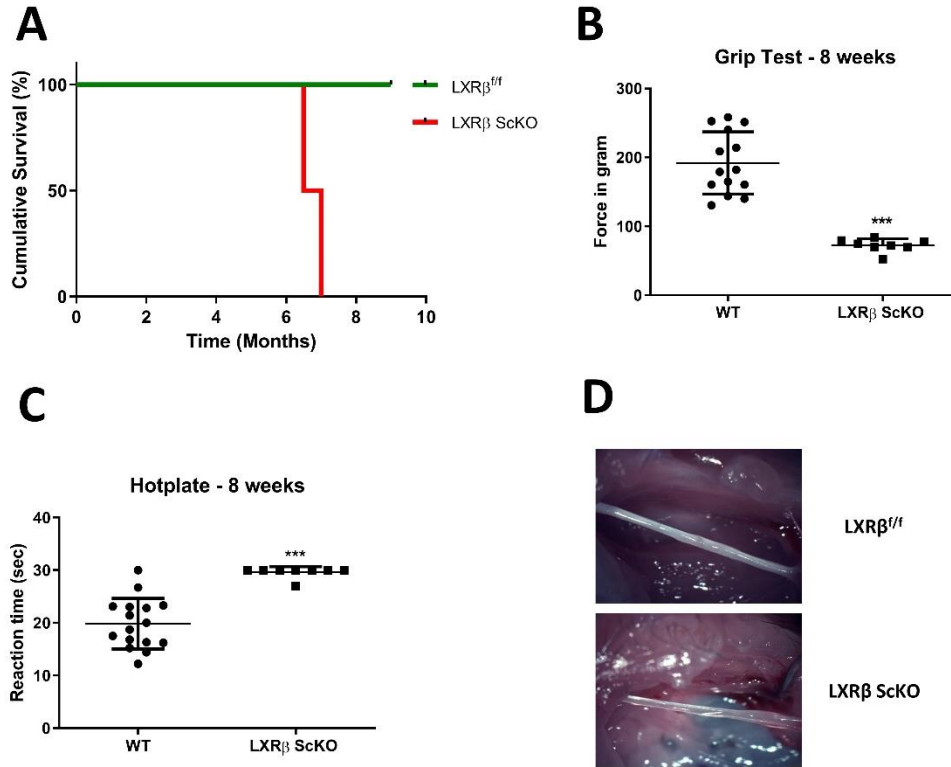


Figure 2: **Phenotypic description of the animals.** (A) Kaplan Meier Survival graphs for controls and mutants. All mutant animals died around 7 months. (B) Assessment of muscular strength using the Grip strength test of adult 8-week-old mice. Mice were placed on a grill plate that was connected to a dynamometer. Once mice latched on to the grill, they were pulled by their tails and the force exerted to hold on to the grill was measured. (C) Adult mice were placed on a hotplate at 52°C. The time taken for the mice to sense the heat (paw licks) was measured. Mice that did not sense the heat were removed from the hotplate after 30 secs for ethical reasons. (D) Macroscopic view of sciatic nerve dissection of control and mutant animals.

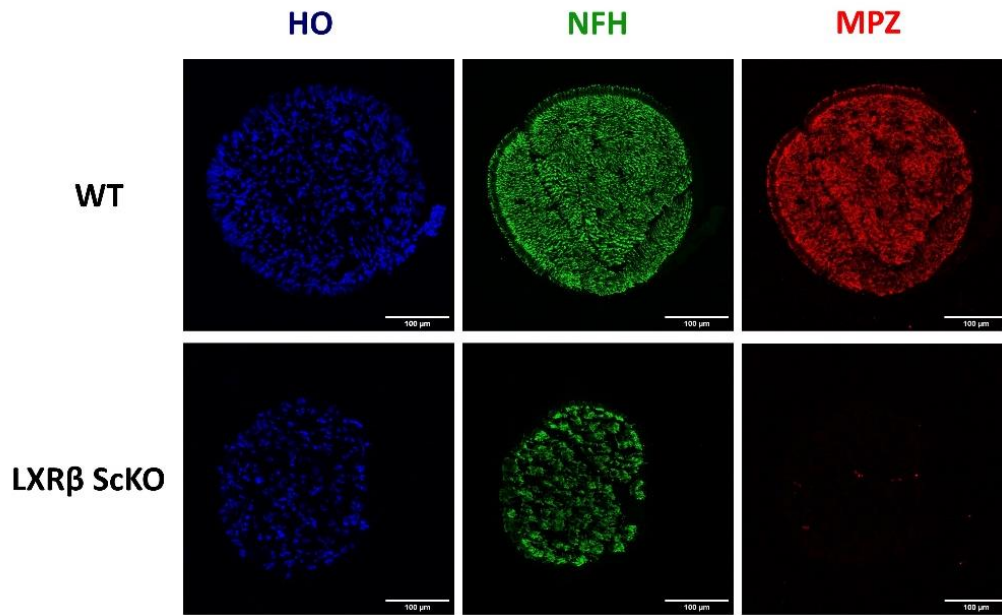
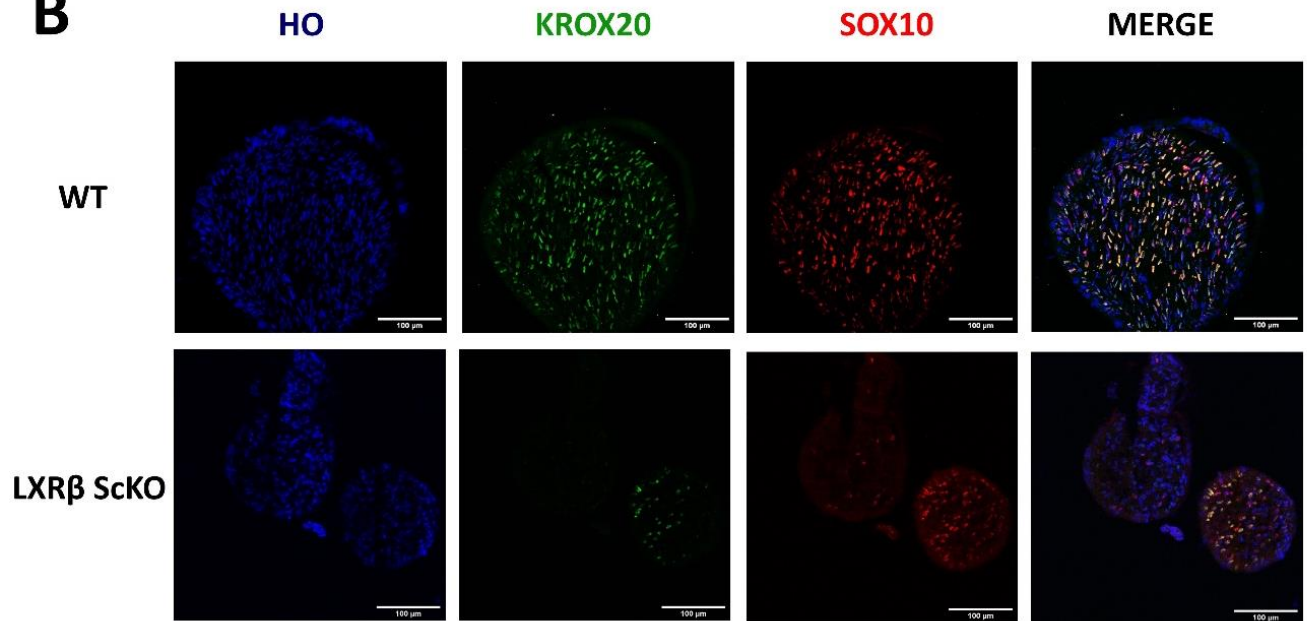
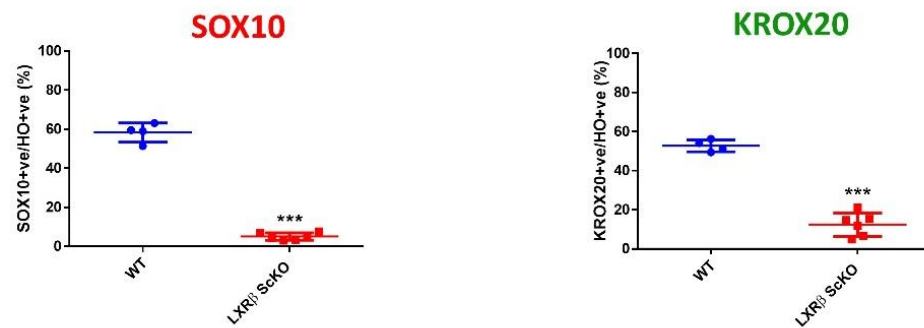
3.2.3 Immunohistochemical analysis of younger mice reveals a drastic reduction in myelin content and Schwann cell numbers

We next performed an Immunohistochemical analysis on the sciatic nerves of younger mice aged P10. Upon dissecting, we first noticed that the nerves of the mutant mice looked underdeveloped and resembled neonatal nerves. This could be either a reduction in cell numbers or a default in myelination or a combination of both. Therefore, to ascertain the cause, the distal sciatic nerve cross sections were stained with antibodies against Neurofilament (NFH – axonal marker), Myelin Protein Zero (MPZ – myelinating Schwann cell maker), SRY-Box Transcription Factor 10 (SOX10 – Neural Crest Derivative marker) and Early growth response protein 2 (EGR2 also called KROX20-myelinating Schwann cell marker) (**Figure 3**).

We first observed that the diameter of cross sections of the LXR β ScKO nerves was reduced comparing to control mice recapitulating our empirical observations of sciatic nerve after dissection (**Figure 3A**). Furthermore, in mutant mice we observed a very faint and sparse staining for MPZ whereas the control mice showed a uniform staining across the entire section suggesting that either the Schwann cells did not myelinate effectively or there were reduced number of Schwann cells (**Figure 3A**).

We looked for the expression of Krox20 which is uniquely expressed in myelinating Schwann cells from birth (Topilko et al., 1994). In control animals, the percentage of Krox20+ cells averaged at $53 \pm 3\%$ (mean \pm SD) whereas in mutant mice, the proportion of Krox20+ cells was significantly lower at $12 \pm 5\%$ (**Figure 3C**). These results taken together suggest that the sciatic nerves of LXR β ScKO mice show a drastic reduction in MPZ levels due to a reduction in Krox20+ve Schwann cells. However, we wanted to assess if Schwann cells were arrested at the pre-myelinating stage or if the mutant nerves had lesser number of Schwann cells to begin with. Therefore, we looked at the total number of Neural Crest derivatives in the peripheral nerves by staining for SOX10 (**Figure 3B**). In control mice, the percentage of SOX10+ cells averaged at $58 \pm 4\%$ (mean \pm SD) whereas in mutants this proportion was significantly reduced to $5 \pm 2\%$ (**Figure 3C**). As SOX10 is a pan neural crest marker, it accounts for all the derivatives of neural crest cells which include both myelinating and non-myelinating Schwann cells as well as Endoneurial Fibroblast Like Cells (EFLCs) (Joseph et al., 2004; Richard et al., 2014). These results suggested that the sciatic nerves of LXR β ScKO mice are largely depleted of Schwann cells as early as Post-natal day 10 (P10).

Our results suggest that the phenotype observed in mutant mice is largely driven by a reduction in the total number of Schwann cells at P10. Consequently, we observe a reduction in the cross sectional diameter of the nerves. The absence of Schwann cells also results in the absence of myelinating Schwann cells and therefore the nerve is very sparsely myelinated.

A**B****C**

*Figure 3: Immunohistochemical analysis of the sciatic nerves from WT and mutant animals at P10. (A) Distal sciatic nerve cross-sections were immunostained to detect Neurofilament heavy chain (NFH – axonal marker) and Myelin Protein Zero (MPZ – myelinating Schwann cell marker) in WT and mutants. Nuclei were stained with Hoechst dye (HO), Scale Bar = 100µm; (B) Distal sciatic nerve cross-sections were immunostained for Krox20 (Myelinating Schwann cell Marker) and Sox10 (pan neural crest marker). Nuclei were stained with Hoechst dye (HO), Scale Bar = 100µm; (C) Data representation of the proportion of cells that were immuno-positive for SOX10 and KROX20 in WT and mutant animals. Non-parametric Mann-Whitney test was performed to analyze statistical differences between the groups and P values are represented as follows: P<0.05: *, P<0.01: **, P<0.001: ***.*

3.2.4 The histochemical phenotype of LXR β SckO nerves is not completely homogenous

While performing histochemical analyses of mutant sciatic nerves, we observed that the phenotype was not homogenous. We observed two phenotypes that we have named moderate and severe (**Figure 4**). In the moderate type, we observed that there were sparse but significant amounts of myelin that are concentrated in a single vesicle of the nerve. In the severe phenotype, we observed that there was no myelin present (**Figure 4**). Furthermore, this difference in the phenotypes presented itself laterally and along the proximo-distal axis i.e. the dissymmetry of the severity was observed in the proximal and distal sections of the same nerve as well as between the right and the left sciatic nerve of the same animal.

Thus, we sought to determine the frequency of such phenotypes in postnatal animals at P10 (**Figure 4**). We analyzed six mutants at P10. The right and the left sciatic nerves from each mouse were sectioned at the proximal and the distal regions. The moderate phenotype was ascribed to the section when the myelinated region of the nerve covers between 50% - 70% of the total area of the section. Conversely, the severe phenotype was ascribed to the section when the Mpz staining covers less than 10% of the total area. Furthermore, across all animals, Mpz staining in the moderate phenotype did not cover more than 70% of the total section area.

Our results indicated that the moderate phenotype presented itself in only 30% of all cases (**Table 1**). Moreover, along the proximo-distal axis, the moderate phenotype was observed 4 out of 7 times in the distal region and 3 out of 7 times in the proximal region.

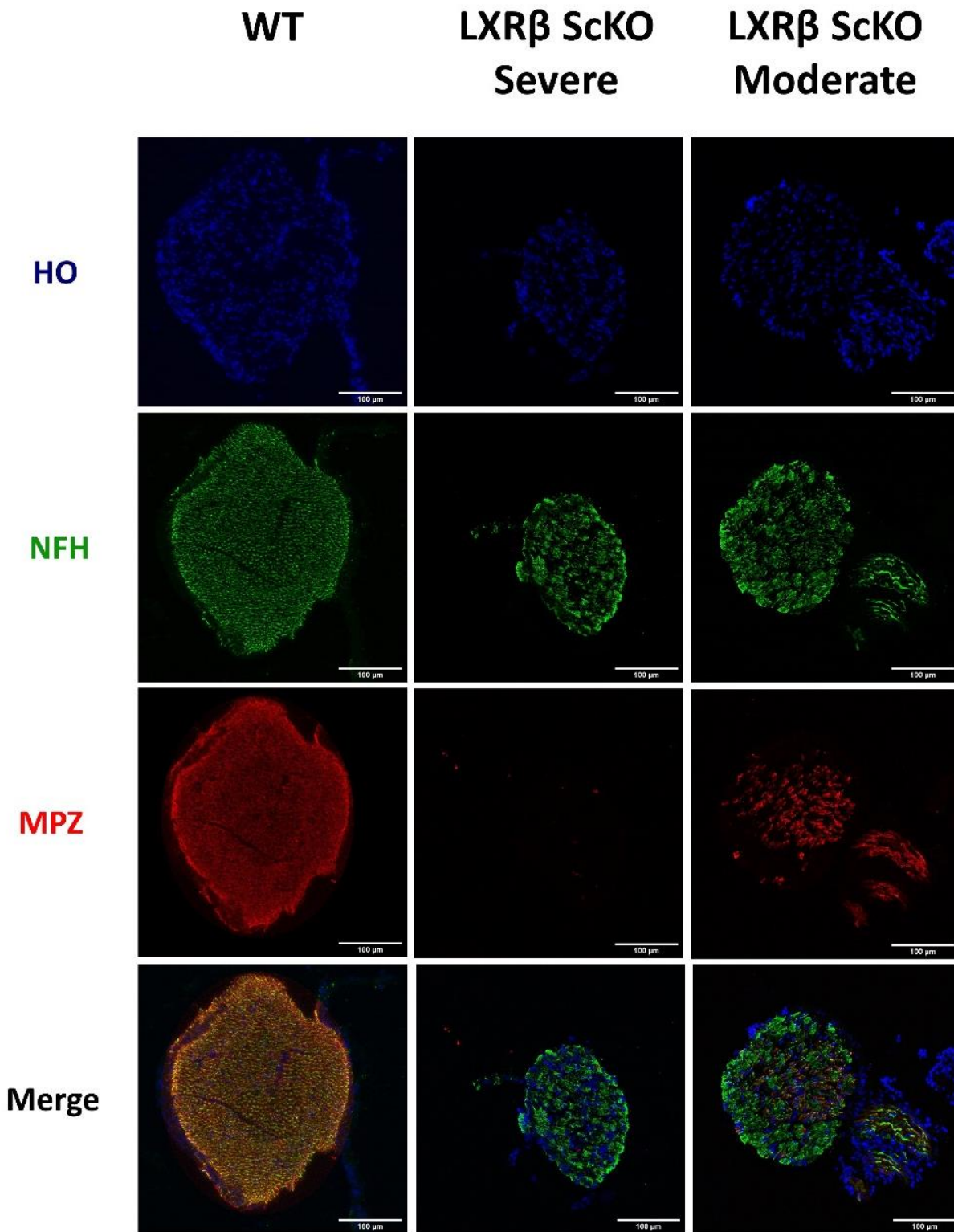


Figure 4: Description of the moderate and the severe phenotype in LXR6 ScKO sciatic nerves at P10. Distal sciatic nerve cross sections were immunostained to detect Neurofilament heavy chain (NFH – axonal marker) and Myelin Protein Zero (MPZ – myelinating Schwann cell marker) in WT and mutants. Nuclei were stained with Hoechst dye (HO), Scale Bar = 100µm. The phenotype was ascribed using the area covered by MPZ staining. If MPZ was found to cover more than 50% of the total cross sectional area, the section was ascribed the ‘moderate phenotype’. If MPZ was found to cover less than 10% of the total cross sectional area, the section was ascribed the ‘severe phenotype’.

Animal	Lateral Side	Region	Phenotype
1	Left	Distal	Severe
		Proximal	Severe
	Right	Distal	Severe
		Proximal	Severe
2	Left	Distal	Moderate
		Proximal	Severe
	Right	Distal	Severe
		Proximal	Severe
3	Left	Distal	Severe
		Proximal	Severe
	Right	Distal	Moderate
		Proximal	Moderate
4	Left	Distal	Moderate
		Proximal	Severe
	Right	Distal	Severe
		Proximal	Severe
5	Left	Distal	Severe
		Proximal	Moderate
	Right	Distal	Moderate
		Proximal	Severe
6	Left	Distal	Moderate
		Proximal	Severe
	Right	Distal	Severe
		Proximal	Severe

	Occurrence	% Occurrence
Moderate phenotype	7	29.2
Severe phenotype	17	70.8
Total Number of sections	24	

Table 1: Occurrence of the severe and moderate phenotypes in P10 mutant sciatic nerves. For each nerve, three technical replicates at an interval of 0.1 cm from each other were analyzed both at the proximal and at the distal regions for MPZ expression. A 'Moderate phenotype' was ascribed to the region if MPZ expression covered between 50% - 70% of the total section area across all technical replicates and a 'severe phenotype' was ascribed to the region if MPZ expression covered less than 10% of the total

section area across all technical replicates. The phenotypes are summarized in the table at the bottom and the occurrences are represented as a percentage.

3.2.5 Ultrastructure analysis reveals a paradigm shift in the cellular anatomy of the sciatic nerve

Given the dramatic reduction of Schwann cells in the mutant mice, we next looked at the sciatic nerve ultrastructure using TEM to assess the consequential ramifications arising from the lack of Schwann cells in LXR β ScKO mice. At P10, we found that the axons are aggregated, and they are surrounded by cytoplasmic extensions of an unknown cell type (**Figure 5**). On the contrary, axons in control mice have been segregated and myelinated by Schwann cells. As the mutant mice age, these cytoplasmic extensions tightly ensheathed axonal bundles and segregated different axonal bundles from one another (**Figure 5**).

In control mice, however, Schwann cells increased the myelin sheath thickness around the axons and we also observed the two distinct Schwann cell populations – myelinating and Remak Schwann cells. As expected, we did not observe the two different Schwann cell populations in mutant nerves. This rearrangement of the cellular anatomy persisted as mice age further with no signs of improvement in terms of myelin sheath production or the segregation of axons (**Figure 5**). The mice were thus euthanized at 20 weeks due to ethical considerations.

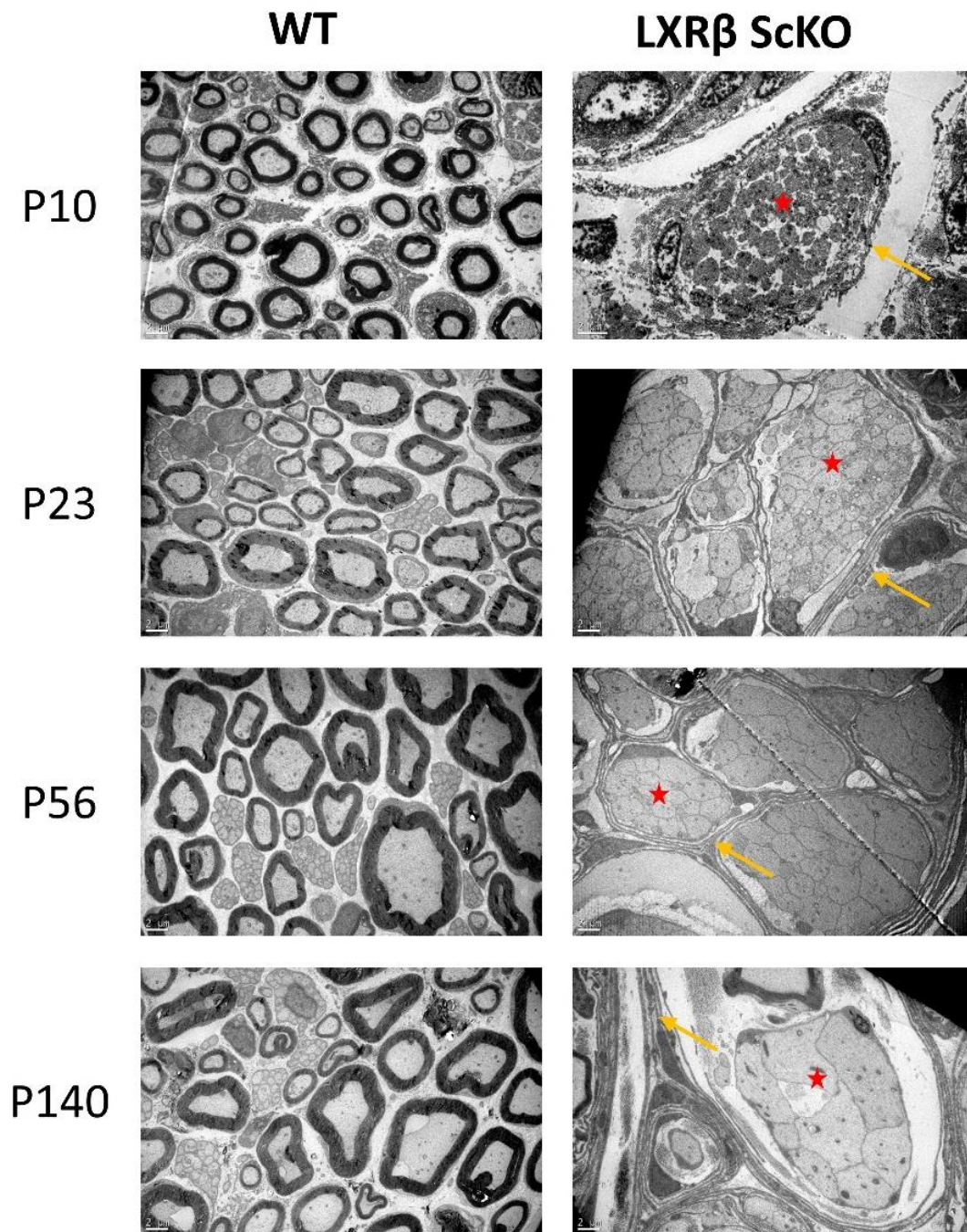


Figure 5: Transmission Electron Microscopy (TEM) of ultra-thin distal sciatic nerve sections of WT and mutant animals. TEM was performed on mice aged 10 days (P10), 23 days (P23), 56 days (8 weeks) and 140 days (20 weeks). WT nerves showed physiological features such as myelinating and non-myelinating Schwann cells. Mutant nerves exhibited abnormal features such as axonal aggregates (Red star) that are ensheathed by cytoplasmic extensions of an unknown cell type (yellow arrows) across all ages observed. Scale bar = 2 μ m (located on the bottom left)

3.2.6 Perineurial cells invade into the Endoneurial space in the absence of Schwann cells

Our observations of electron microscopy images from mutant sciatic nerves prompted us to hypothesize that an unknown cell type ensheaths axonal bundles in LXR β ScKO mice. These cells could not originate from the neural crest as mutant nerves displayed a huge reduction in Sox10+ cells. Furthermore, these cytoplasmic extensions of the unknown cell type resembled the perineurial sheath that normally delineate nerve fascicles in physiological conditions (Kucenas, 2015) (**Figure 6**).

Thus, we speculated that the perineurial cells indeed invaded into the Endoneurial space and proliferated in LXR β ScKO nerves. To test this hypothesis, we checked for the expression of Tight Junction Protein 1 (Tjp1 also called as Zonula Occludens 1 or ZO1) which is a marker of perineurial cells in control and mutant nerves at P10 (**Figure 6**). At P10, we observed that ZO1 is primarily localized to the periphery of the nerve fascicles in control nerves (**Figure 6A**) with traces of ZO1+ cells in the endoneurium, possibly from pericytes and endothelial cells of the vasculature, which also express ZO1. However, in mutant animals we observed that the protein is localized in the periphery as well as in the endoneurial space (**Figure 6A**) forming a clear circular pattern over unmyelinated axons. This pattern of expression is also observed in P23 mice (**Figure 6B**). These results taken together suggested that the perineurial cells invaded and expanded in the endoneurial space in the absence of Schwann cells in LXR β ScKO mice. This phenomenon was also observed in *Krox20GFP (DT)⁺*, *HtPA:Cre* mice where Schwann cells are killed embryonically with Diphtheria Toxin *in vivo* (Coulpier et al., 2010).

Indeed, during Schwann cell development especially at the SCP, Schwann cells secrete Dhh that binds to hedgehog receptors in the perineurial cells and restricts their localization towards the periphery of nerve fascicles (Parmantier et al., 1999; Sharghi-Namini et al., 2006). In our mutant model, the lack of Schwann cells does not permit this dialogue through Dhh signaling and the perineurial cells invade into the endoneurial space. A similar phenotype is also observed in *Dhh^{-/-}* mutants but this mutation does not influence the survival of Schwann cells (Parmantier et al., 1999).

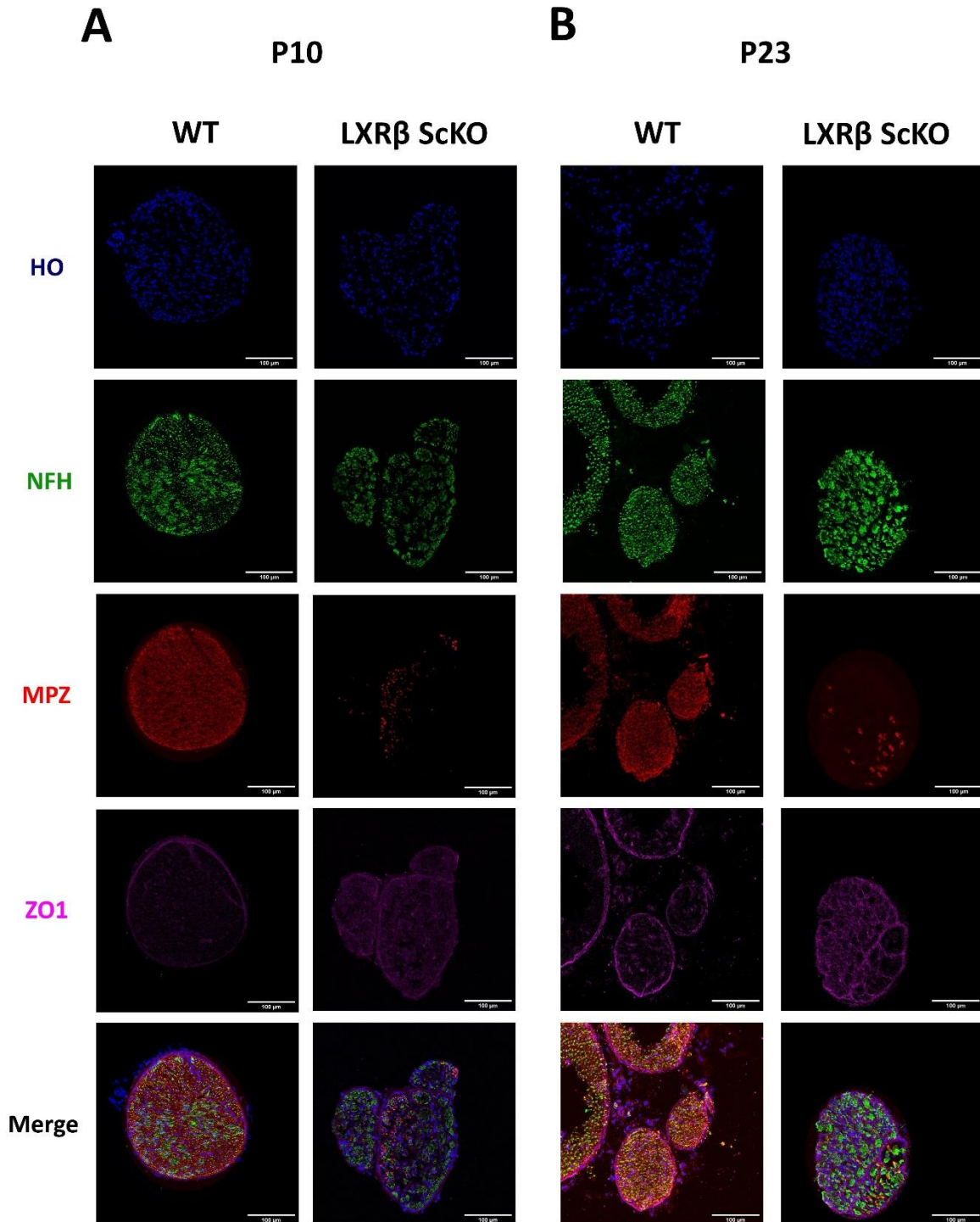


Figure 6: Immunohistochemical analysis of WT and mutant distal sciatic nerves at P10 and P23. Distal sciatic nerve sections were immunostained to detect Neurofilament Heavy chain (NFH – axonal marker), Myelin Protein Zero (MPZ – Myelinating Schwann cell marker), Zona Occludens 1 (ZO1 – Perineurial cell marker). Nuclei were stained with the Hoechst dye (HO). Scale bar = 100 μ m

3.2.7 Schwann cells disappear embryonically in LXR β ScKO animals

To ascertain the time window when Schwann cells disappear from peripheral nerves of LXR β ScKO animals, we performed IHC at Post Natal Day 0 (P0) (**Figure 7**). We looked for the expression of Sox10 to verify if Schwann cells are present in the mutant nerves at birth. Similar to P10 mutant nerves, the cross-sectional area of P0 mutant nerves were smaller than their respective controls. Additionally, we also observed a drastic reduction in SOX10+ cells in mutant nerves suggesting that the mice are born with reduced Schwann cell numbers (**Figure 7A**). Furthermore, we also observed that TEM images of mutant nerves recapitulated the phenotype of postnatal time points, which is characterized by the ensheathment of axonal bundles by perineurial cells (**Figure 7B**). These results suggested that LXR β ScKO mice are born with reduced Schwann cell numbers and that perineurial cells probably start enheathing axonal bundles during embryonic development. However, these observations also give rise to two possibilities. LXR β might be involved in the survival of either iSC or SCP.

At E18.5 during development, SCP have differentiated into iSC and radial sorting of axons has already begun. Our TEM images suggest that in mutant nerves radial sorting has not taken place and thus we can postulate that Schwann cells are absent from the developing nerves right from the SCP stage (after Dhh expression) or at the iSC stage.

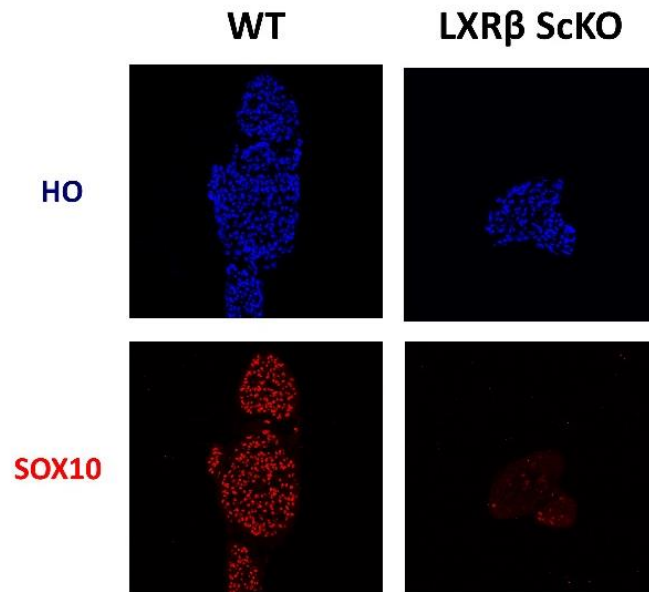
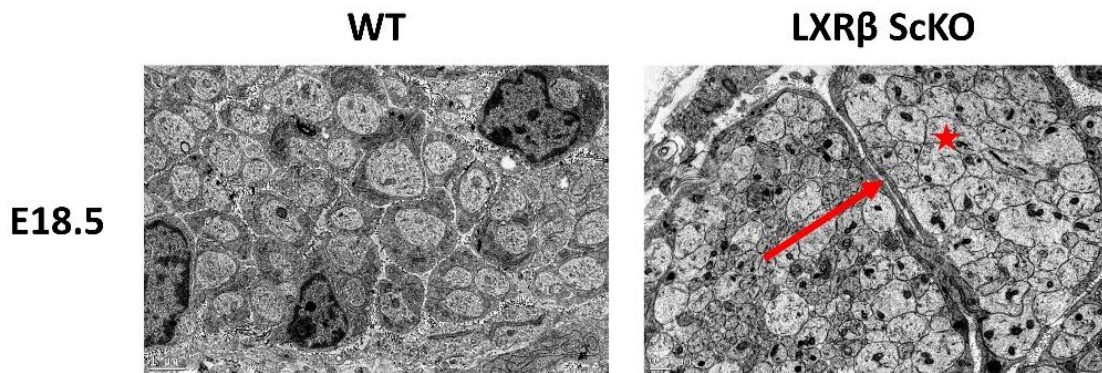
A**B**

Figure 7: IHC and TEM analysis of WT and mutant perinatal sciatic nerves. (A) Distal sciatic nerves at P0 were immunostained for Sox10 expression. Mutant mice were born with very little NCC derivatives whereas the WT mice exhibited many Sox10+ cells; (B) TEM analysis of WT and mutant sciatic nerves at E18.5 (one day before birth). WT sections displayed axons that have formed a one on one relationship with Schwann cells whereas mutant sciatic nerves exhibited axonal aggregates (red star) that were ensheathed by cytoplasmic extensions of Perineurial cells presumably (red arrow). Scale Bar = 1 μ m.

3.2.8 Retracing Schwann cell developmental transitions in embryonic dissociated DRG cultures

Following the results obtained, we wanted to determine the embryonic time window where LXR β ScKO Schwann cells either died or halted their proliferation. To this end, we employed embryonic dissociated Dorsal Root Ganglia (DRG) cultures, which recapitulate embryonic Schwann cell development. However, there were no existing data on how these *in vitro* cultures correlate with *in vivo* development notably the transition of SCP to iSC. In developing spinal nerves, SCP appear at the DRG at around E11.5 and being migrating on nascent axons at between E12.5 to E13.5 (Jacob, 2015). However, from *ex vivo* and *in vitro* cultures, DRGs were extracted from the embryos at E13.5. These dissociated DRGs gave rise to neurons and Schwann cells in culture and this culture system recapitulated *in vivo* development albeit with a time difference. Our primary goal was to determine this phase difference and thereby ascertain the exact time period where SCP that migrate on neurites transition into iSC in culture.

To this end, we assessed the expression of different Schwann cell markers and compared them to high throughput data generated on embryonic spinal nerves and Schwann cells *in vivo*. These results have been documented in the form of an article that is presently being peer reviewed. The article is presented in the following pages and the salient results are described below:

- 1. Between DIV1 (Days in vitro 1) and DIV3, SCP had begun to appear on nascent neurites.**
- 2. Between DIV3 and DIV5, SCP migrated and proliferated on neurites.**
- 3. Between DIV5 and DIV7, SCP underwent the transition into iSC.**

In developing nerves, SCP appeared at E11.5. They migrated and proliferated on nascent axons between E11.5 to E15.5. At around E15.5 the SCP begun their transition into iSC and at around E17.5 most of the SCP have successfully transitioned into iSC. This comparative study provided us with a strong inferential framework to compare DRG cultures established from Control and LXR β ScKO animals.

1 **Retracing Schwann cell developmental transitions in embryonic**
2 **dissociated DRG cultures**

3 **Venkat Krishnan Sundaram^{1*}, Rasha Barakat^{1,2}, Charbel Massaad¹, Julien Grenier^{1*}**

4 1. Université de Paris, INSERM UMR 1124, Faculty of Basic and Biomedical Sciences, Paris,
5 France.

6 2. Université de Paris, INSERM UMR 1016, Institut Cochin, Paris, France.

7

8 ***Correspondance :**

9 Venkat Krishnan SUNDARAM

10 venkatkrishnan.sundaram@parisdescartes.fr

11 <https://orcid.org/0000-0001-6024-6959>

12

13 Julien GRENIER

14 julien.grenier@parisdescartes.fr

15 <https://orcid.org/0000-0002-1897-1329>

16

Under Review

17

18 **Author Contributions:**

19 CM, JG and VKS designed the study. VKS and RB performed the experiments. VKS analyzed the
20 results and wrote the manuscript. CM validated the methodology. JG prepared the figures. All authors
21 reviewed and edited the manuscript. JG and VKS prepared the final draft for submission.

22

23 **Acknowledgements:**

24 The authors thank Maja Adamsen and Claire Mader from the *Animal House Core Facility* of BioMedTech
25 (INSERM US36/CNRS UMS2009) for the handling of mice used in the study. We also thank the *Cyto2BM*
26 *Molecular Biology Platform* of BioMedTech Facilities for the research equipment and other services
27 pertaining to the generation of qPCR data.

28

29 **Funding:**

30 No specific funding was sought for this study. VKS is funded by a PhD fellowship from the French Ministry
31 of Research and Innovation and Université de Paris. RB is funded by a doctoral contract from INSERM
32 U1016, Institut Cochin, Paris.

33

34 **Conflict of interest:**

35 The authors declare that there is no conflict of interest.

36 **Abstract:**

37 Embryonic Dissociated Dorsal Root Ganglia cultures are often used to investigate the role of novel
38 molecular pathways or drugs in Schwann cell development and myelination. These cultures largely
39 recapitulate the order of cellular and molecular events that occur in Schwann cells of embryonic nerves.
40 However, the timing of Schwann cell developmental transitions, notably the transition from Schwann Cell
41 Precursors to immature Schwann cells, has not been estimated so far in this culture system. In this study,
42 we use RTqPCR to determine the expression profiles of Schwann cell developmental genes during the
43 first week of culture. We first identified stable reference genes that show minimal variation across different
44 experimental time points. Consequently, we normalized the mRNA profiles of Schwann cell
45 developmental genes using the best internal reference genes. We then compared our data to the
46 expression profiles of these genes in developing spinal nerves elaborated in numerous high-throughput
47 and lineage tracing studies. This comparison helped in identifying that Schwann Cell Precursors
48 transition into immature Schwann Cells between the 5th and 7th day *in vitro*. In effect, our data allows for
49 a better understanding and interpretation of DRG culture experiments especially in studies that aim to
50 elucidate the role of a novel gene in Schwann Cell development and myelination.

51

52 **Keywords:** Dissociated DRG cultures, Schwann Cell Precursors, immature Schwann Cells,
53 Development, RTqPCR

Under Review

54 Introduction:

55 Dissociated Dorsal Root Ganglia (DRG) cultures from mouse embryos have long been utilized as a
56 resourceful model for exploring the nuances of Schwann cell development *in vitro* (Taveggia and Bolino,
57 2018). The co-culture system provides a solid experimental framework to study different aspects of
58 Schwann cell development such as proliferation, migration, differentiation and myelination of neurites
59 (Päiväläinen et al., 2008; Taveggia and Bolino, 2018). Furthermore, it holistically recapitulates the
60 different aspects of Schwann cell development that is observed *in vivo*. Hence, dissociated DRG cultures
61 form an indispensable part of studies that aim to understand the role of a novel gene in Schwann cell
62 development and differentiation.

63 It is well known that temporal differences exist between Schwann cell development in Dissociated DRG
64 cultures and in developing spinal nerves. In developing spinal nerves of mice, Neural Crest Cells (NCC),
65 destined to a glial fate, differentiate into Schwann Cell Precursors (SCP) and appear in the DRGs at
66 around E11 (Jacob, 2015). Then, SCPs start migrating on nascent axons between E12.5 and E13.5 to
67 populate their peripheral targets. However, at around E15.5 in mice, SCP transition into immature
68 Schwann cells (iSC) that further differentiate into myelinating and non-myelinating Schwann cells
69 perinatally (Monk et al., 2015; Fledrich et al., 2019; Jessen and Mirsky, 2019).

70 Nevertheless, these observations cannot be used to extrapolate the timing of Schwann cell
71 developmental transitions *in vitro* because of certain technical reasons. Firstly, the DRGs are dissected
72 from mouse embryos towards the end of the 2nd week of gestation (E12.5 or E13.5). At this stage, SCP
73 *in vivo* have started departing from the DRGs and begun migrating on developing axons (Jessen et al.,
74 1994; Jessen and Mirsky, 2005). However, once dissected and dissociated, the DRG cells give rise to
75 sensory neurons and Schwann cell precursors once again *in vitro* (Ratner et al., 2005; Kim and Maurel,
76 2009; Kim and Kim, 2018). This is rendered possible because of a reservoir of Neural Crest Cells located
77 inside the DRGs that re-differentiate and populate the culture. Therefore, a significant portion of *in vivo*
78 development is repeated in cell culture albeit with a phase difference. Our objective in this study was to
79 better understand these temporal differences in cocultures in an effort to provide a better experimental
80 and inferential framework.

81 In this research report, we have used RTqPCR to delineate the expression profiles of developmental
82 genes that are expressed in SCP and iSC (*Dhh, Mpz, Cnp, Plp, Mbp, Krox20, Cad19 and Tfp2a*). Their
83 expression pattern was determined in dissociated DRG cultures during the first 7 Days *in vitro* (DIV) at
84 regular intervals of 48 hours. In order to produce robust and reproducible qPCR data, we first sought to
85 identify stable reference genes from 10 candidates
86 (*Actb, Gapdh, Tbp, Sdha, Pfkfb3, Ppia, Rpl13a, Hsp60, Mrpl10, Rps26*) using a data analysis workflow
87 that we developed recently (Sundaram et al., 2019). This step is crucial as the cell culture environment
88 is dynamic with different cell populations undergoing proliferation and differentiation simultaneously.
89 Hence, arbitrary choice of reference genes without assessing their stability could possibly render biased
90 expression profiles.

91 We next determined the expression profile of the developmental genes and compared them to their
92 profiles *in vivo*. Previous high-throughput studies in Neural Crest Cells and their derivatives in the
93 Peripheral Nervous System have generated extensive data on the differential expression of genes during
94 Schwann Cell development (Buchstaller et al., 2004; D'Antonio et al., 2006). Additionally, we also
95 compared our data to numerous lineage tracing and gene expression studies performed in developing
96 spinal nerves. This analysis helped us in determining the time window where SCP transition into iSC in
97 Dissociated DRG cultures. Indeed, understanding the developmental transitions of Schwann cells in
98 cocultures is crucial for designing rigorous cell culture experiments on Schwann cell development and *in*
99 *vitro* myelination assays using different Schwann cell mutants.

100 **Materials and methods:**

101 **Animals and Tissue Harvesting**

102 Timed pregnant C57Bl6/J mouse at E13.5 was purchased from Janvier Labs. The pregnant mouse was
103 first anesthetized with isoflurane and sacrificed using cervical dislocation. A total of 5 embryos were
104 surgically removed and placed in ice-cold L-15 media. DRGs were harvested from these embryos based
105 on existing protocols (Kim and Kim, 2018; Taveggia and Bolino, 2018). All aspects of animal care and
106 animal experimentation were performed in accordance with the relevant guidelines and regulations of
107 INSERM and Université de Paris (authorization APAFIS#7405-2016092216181520).

108 **Dissociated DRG cultures**

109 A total of 40 DRGs were harvested from each embryo. DRGs were then trypsinized (0.25% Trypsin in
110 HBSS1X) for 30min at 37°C. Trypsinization was stopped using L-15 media containing 10% Horse Serum
111 (Gibco). DRGs were then spun down at 1500 rpm for 5min. The supernatant was removed, and the
112 tissues were resuspended in DRG plating medium (refer to *Media Compositions*). The tissues were then
113 triturated 10-20 times using flamed Pasteur pipettes until a homogenous cell suspension was obtained.
114 Dissociated DRGs were then plated on 12 well plates for each time point –DIV1 (*Days In Vitro* 1), DIV3,
115 DIV5, DIV7. 40 DRGs from each embryo were plated into 8 wells at approximately 5 dissociated DRGs
116 per well. 2 wells were assigned to each time point. The cells were first plated with DRG plating medium
117 for 16h. The following day the medium was replaced by N2/NGF serum free medium to promote neurite
118 growth and Schwann cell proliferation.

119 **Media Compositions**

120 *DRG plating media*: DMEM with 4.5g/L glucose (Gibco), 10% heat inactivated Horse Serum (Gibco), 1X
121 Glutamax (Gibco), 1X Antibiotic/Antimycotic (Gibco) and 50ng/μL Nerve Growth Factor 2.5S (R&D
122 Systems)

123 *N2/NGF serum free media*: DMEM:F12 (Gibco), 1X N2 supplement (Gibco), 1X Glutamax (Gibco), 1X
124 Antibiotic/Antimycotic (Gibco) and 50ng/μL Nerve Growth Factor 2.5S (R&D Systems)

125 **Total RNA isolation**

126 Total RNA was extracted from each sample using 1mL of TRIzol reagent (Ambion Life Technologies
127 15596018) on ice as described in the manufacturer's instructions with slight modifications. Briefly, 100%
128 Ethanol was substituted for Isopropanol to reduce the precipitation of salts. Also, RNA precipitation was
129 carried out overnight at -20°C in the presence of glycogen. The following day, precipitated RNA was
130 pelleted by centrifugation and washed at least 3 times with 70% Ethanol to eliminate any residual
131 contamination. Tubes were then spin dried in vacuum for 5 minutes and RNA was resuspended in 20μL
132 of RNA resuspension buffer containing 0.1mM EDTA, pH 8. RNA was then stored at -80°C till RTqPCR.

133 **RNA quality, integrity and assay**

134 RNA quantity was assayed using UV spectrophotometry on Nanodrop One (Thermo Scientific). Optical
135 density absorption ratios A260/A280 & A260/A230 of the samples were above 1.8 and 1.5, respectively.
136 The yield (mean ± SD) for each time point is as follows: DIV1 (26.74 ± 2.57 ng/μL), DIV3 (61.3 ± 8.01
137 ng/μL), DIV5 (51.86 ± 10.8 ng/μL), and DIV7 (77.34 ± 24.04 ng/μL). Furthermore, the extraction protocol
138 used in the study was also validated using Agilent Bioanalyzer (RIN value 9.0 and above).

139 **RTqPCR**

140 500ng of Total RNA was reverse transcribed with Random Primers (Promega C1181) and MMLV
141 Reverse Transcriptase (Sigma M1302) according to prescribed protocols. Quantitative Real time PCR

142 (qPCR) was performed using Absolute SYBR ROX 2X qPCR mix (Thermo AB1162B) as a fluorescent
143 detection dye. All reactions were carried out in a final volume of 7 μ l in 384 well plates with 300 nM gene
144 specific primers, around 3.5ng of cDNA (at 100% RT efficiency) and 1X SYBR Master Mix in each well.
145 Each reaction was performed in triplicates. All qPCR experiments were performed on BioRad CFX384
146 with a No-Template-Control (NTC) to check for primer dimers and a No-RT-Control (NRT) to check for
147 any genomic DNA contamination.

148 **Primer design**

149 All primers used in the study were designed using the Primer 3 plus software
150 (<https://primer3plus.com/cgi-bin/dev/primer3plus.cgi>). Splice variants and the protein coding sequence
151 of the genes were identified using the Ensembl database (www.ensembl.org). Constitutively expressed
152 exons among all splice variants were then identified using the ExonMine database
153 (<https://imm.medicina.ulisboa.pt/group/exonmine/ack.html>) (Mollet et al., 2010) Primer sequences that
154 generated amplicons spanning two constitutively expressed exons were then designed using the Primer
155 3 plus software. For detailed information on Primer sequences used in the study, refer to the
156 supplementary table S3.

157 **Amplification efficiencies**

158 The amplification efficiencies of primers were calculated using serial dilution of cDNA molecules. Briefly,
159 cDNA preparations from all the time points were pooled and serially diluted three times by a factor of 10.
160 qPCR was then performed using these dilutions and the results were plotted as a standard curve against
161 the respective concentrations of cDNA. Amplification efficiency (E) was calculated by linear regression
162 of standard curves using the following equation:

$$163 \quad E = 10^{-(1/\text{slope of the standard curve})}$$

164 Primer pairs that exhibited a theoretical Amplification Efficiency (E) of 1.9 to 2.1 (95% - 105%) and an R²
165 value (Determination Coefficient) of 0.98 and above were chosen for this study.

166 **Statistical analysis and Data Visualization**

167 qPCR readouts were analyzed in Precision Melt Analysis Software v1.2. The amplicons were subjected
168 to Melt Curve analysis and were verified for a single dissociation peak at a Melting Temperature (T_m) >
169 75°C as expected from the primer constructs. The C_q data was exported to Microsoft Excel for further
170 calculations. Each biological sample had 3 technical replicates thereby generating 3 individual C_q values.
171 The arithmetic mean of the triplicates was taken to be the C_q representing the biological sample. The
172 standard deviation (SD) of the triplicates was also calculated and samples that exhibited SD>0.20 were
173 considered inconsistent. In such cases, one outlier C_q was removed to have at least duplicate C_q values
174 for each biological sample and an SD<0.20.

175 Statistical analyses for reference gene validation were performed according to our qPCR data analysis
176 workflow (Sundaram et al., 2019). Briefly, 10 conventional reference genes were chosen for the study.
177 The C_q values of these genes were first linearized and the Coefficient of variation (CV) for each gene
178 was calculated (Supplementary Table S1). As all the genes exhibited CV < 50%, they were subsequently
179 screened through the NormFinder algorithm in R (<https://moma.dk>) (Andersen et al., 2004). The algorithm
180 predicted *Tbp* and *Ppia* to be the most stable references. The normalization factor was then determined
181 as the mean C_q value of *Tbp* and *Ppia* for each sample (Supplementary Table S2). Relative expression
182 of target genes was quantified using the 2^{- $\Delta\Delta$ C_q} method (Livak and Schmittgen, 2001; Schmittgen and
183 Livak, 2008). DIV1 group was used as the experimental calibrator and data was visualized using Graph
184 Pad Prism v7.0.

185 To assess statistical difference in relative RNA quantities between groups, One-way ANOVA was
186 performed in Graph Pad Prism v7.0. If statistical significance was observed between the means of the
187 groups, Tukey's post hoc was performed to compare all the 4 groups with each other. The alpha value
188 threshold was set at 5% and the P-values are represented as follows: P<0.05 - *, P<0.01 - **, P<0.001 -
189 ***.

Under Review

190 **Results:**

191

192 **Progression of dissociated DRG cultures:**

193 We first documented the progression of the culture at Days *in Vitro* (DIV) 1, DIV3, DIV5 and DIV7 using
194 phase-contrast microscopy. At DIV 1, we observed a very sparse population of dissociated cells that
195 comprised of precursors to neurons, Schwann cells and fibroblasts (**Figure 1A**). At DIV3, however, we
196 could see a neurite network gradually being formed with small bead-shaped cells located on top of
197 neuronal extensions. These cells are presumably migratory Schwann cell precursors (**Figure 1B**). The
198 neurites then grew out and established a well-connected network by DIV5 (**Figure 1C**). Schwann cells
199 now densely populated neurites. Flattened Fibroblast like cells were also observed below the Neurite-
200 Schwann cell network. Not much difference was observed between DIV5 and DIV7 except that more
201 connections were established in the neurite-Schwann cell network (**Figure 1D**). From these
202 observations, we could only deduce that Schwann cell precursors appear between DIV1 and DIV3. The
203 transition of SCP to iSC could not be established, as we did not observe any significant morphological
204 changes in the cells attached to the developing neurites as observed *in vivo* (Jessen and Mirsky, 2019).

205 **Determination of stable reference genes for normalization:**

206

207 As a prerequisite to determine the expression profiles of Schwann cell developmental genes using
208 RTqPCR, we first identified suitable reference genes for our experimental setting. We chose 10 candidate
209 reference genes and used our data analysis workflow (Sundaram et al., 2019) to determine the two most
210 stable reference genes across all the time points under consideration.

211 Briefly, we first calculated the Co-efficient of Variation (CV) of the linearized Cq values of reference
212 genes. All reference genes exhibited CV values lesser than 50% (**Table 1 and Supplementary Table**
213 **S1**) indicating that they can all be screened by the NormFinder algorithm without compromising its
214 robustness (Sundaram et al., 2019). Consequently, the Normfinder algorithm predicted *Tbp* and *Ppia* as
215 the most stable reference genes with an S value of 0.16 followed by others with higher S values indicating
216 lower stability (**Table 1**). The algorithm also determines the best combination of two genes for more
217 accurate normalization. In this regard, the algorithm predicted the combination of *Tbp* and *Ppia* as the
218 best with a grouped S value of 0.11 (**Table 1**).

219 **Expression profiles of Schwann cell developmental genes:**

220 We then determined the expression profiles our target genes using *Tbp* and *Ppia* as internal references
221 (**Figure 2**). All target genes tested showed considerable variation across the time points when analyzed
222 with one-way ANOVA (**Figure 2A – 2H**) To determine differences among groups, we performed Tukey's
223 Post Hoc test.

224 *Dhh* showed a stark 14-fold increase between DIV1 and DIV3 (**Figure 2A**). Although the profile seemed
225 to project a downward trajectory after DIV3, the levels of *Dhh* did not vary significantly between DIV3 and
226 DIV7. *Mpz* displayed an initial spike between DIV 1 and DIV3 by about 12 folds, which was similar to
227 *Dhh*. However, the quantity of *Mpz* gradually increased and reached about 17 folds at DIV7 (**Figure 2B**).

228 *Cnp* expression increased by about 7-folds between DIV1 and DIV3 and maintained a stable profile till
229 DIV7 (**Figure 2C**). *Plp* showed an initial peak at DIV3 by about 7-folds, which was comparable to that of
230 *Cnp*. However, *Plp* expression momentarily dropped at DIV5 and reached a plateau by DIV7 (**Figure**
231 **2D**).

232 *Mbp* displayed a modest but statistically significant increase by 2-folds between DIV1 and DIV3 (**Figure**
233 **2E**). However, the expression did not increase significantly beyond DIV3. *Krox20* expression did not vary

234 significantly between DIV1 to DIV5 (**Figure 2F**). However, at DIV7 we observed a sudden spike by about
235 4-folds.

236 *Cad19* expression increased almost linearly between DIV1 and DIV5 (**Figure 2G**). However, between
237 DIV5 and DIV7, we observe a drop in its expression level. *Tfap2a* maintains a flat profile from DIV1 and
238 DIV3 (**Figure 2H**). It begins to decline after DIV3 and drops significantly to about 0.5 folds at DIV7.

239 **Comparison of *in vitro* and *in vivo* expression profiles:**

240 We then compared the *in vitro* expression profiles with the profiles of the genes assessed from previous
241 gene profiling studies on the Schwann cell lineage (Buchstaller et al., 2004; D'Antonio et al., 2006). We
242 also consulted seminal reviews on Schwann cell developmental markers (Jessen et al., 1994; Jessen
243 and Mirsky, 2005; Woodhoo and Sommer, 2008; Monk et al., 2015) and other gene-specific expression
244 profiling studies to gain a holistic understanding of the literature. A summary of the current consensus
245 on the expression profiles of these genes *in vivo* along with the relevant literature is presented in **Figure**
246 **3**.

247 The expression of *Dhh*, *Mpz* and *Mbp* is upregulated in SCP at around E12.5 in mice (Jessen and Mirsky,
248 2005; Woodhoo and Sommer, 2008). In DRG cultures, *Dhh*, *Mpz* and *Mbp* expression is increased at
249 DIV3, confirming our observation that SCP appears between DIV1 and DIV3 (**Figure 2A and 2B**).
250 Interestingly, the profile of *Dhh* after DIV3 shows some minor differences with its expression *in vivo*. In
251 developing nerves, *Dhh* expression is upregulated during the SCP/iSC transition where it reaches a
252 plateau (Parmantier et al., 1999; Buchstaller et al., 2004; Sharghi-Namini et al., 2006). In culture, the
253 expression seemed to decrease progressively as cells progress from DIV3 to DIV7, albeit the differences
254 are not statistically significant (**Figure 2A**). On the contrary, *Mpz* expression between DIV3 and DIV7
255 complies perfectly with *in vivo* data (Blanchard et al., 1996; Lee et al., 1997; Buchstaller et al., 2004).
256 *Mpz* expression increases gradually between DIV3 and DIV7 (**Figure 2B**).

257 The profile of *Mbp* concurs with its profile *in vivo* with minor differences. In embryonic nerves, *Mbp*
258 expression is detected primarily in SCP at around E12.5 and keeps increasing till E18.5 (Paratore et al.,
259 2002; Buchstaller et al., 2004). In DRG culture at DIV3, *Mbp* expression is increased and reached a
260 plateau at DIV5 (**Figure 2E**).

261 *Plp* is expressed in migrating neural crest cells and Schwann cell Precursors (Timsit et al., 1992;
262 Buchstaller et al., 2004). In developing nerves, *Plp* expression increases in schwann cells between E12.5
263 and E18.5. (Buchstaller et al., 2004). In DRG cultures, increase in *Plp* expression at DIV3 concurs with
264 *in vivo* data. However, a momentary but significant drop of *Plp* expression is observed between DIV3
265 and DIV5 but it marginally increases again at DIV7 (**Figure 2D**).

266 Data on *Cnp* expression in SCP of embryonic nerves is inconclusive. We analyzed three separate studies
267 that sought to trace *Cnp* expression in the PNS (Gravel et al., 1998; Yuan et al., 2002; Deng et al., 2014).
268 One study demonstrated that *Cnp* is expressed in the satellite cells of DRGs at E14.5 and at the ventral
269 roots at E17.5 but did not comment on its expression in SCPs (Deng et al., 2014). The other two studies
270 dealt with post-natal time points. Nonetheless, our observations suggest that *Cnp* mRNA is expressed in
271 SCP at DIV3 in culture. This observation, however, needs to be verified *in vivo*.

272 *Krox20* is expressed at two different time points during the development of the PNS (Topilko et al., 1994;
273 Voiculescu et al., 2000; Coulpier et al., 2010). At around E10.5, it is first expressed in the boundary cap
274 cells that are located at the dorsal and ventral roots. This is followed by its expression as SCP transition
275 into iSC at around E15.5. It is one of the genes used in the study that can categorically distinguish
276 between SCP and iSC. In our study, *Krox20* expression does not change significantly between DIV1 and
277 DIV5. We then see a sudden spike in its expression between DIV5 and DIV7 suggesting that SCP
278 transition to iSC in this time-period (**Figure 2F**).

279 To test this hypothesis, we further looked at the expression profile of *Tfap2a*, which is expressed in NCC
280 and SCP but not in iSC (Stewart et al., 2001)(**Figure 2H**). The downregulation of this transcription factor
281 is indeed required for SCP to transition into iSC in developing nerves (Stewart et al., 2001; Jacob, 2015).
282 Consistent with this observation, *Tfap2a* levels drop by 50% between DIV5 and DIV7 thus providing
283 further evidence of the SCP/iSC transition between DIV5 and DIV7. Moreover, we also assayed the
284 expression levels of *Cad19*, which is the only known gene that is uniquely expressed in SCP but not in
285 NCC or iSC (Jessen and Mirsky, 2005, 2019; Takahashi and Osumi, 2005). *Cad19* expression *in vitro*
286 was the highest around DIV3 and DIV5 but it reduced again at DIV7 reaching to levels comparable to
287 DIV3.

288 Taken together, these results give a clear picture of Schwann cell developmental transitions *in vitro*. We
289 thus conclude that SCP appear between DIV1 and DIV3. Between DIV3 and DIV5, SCP proliferate and
290 migrate on nascent neurites. At DIV5, SCP begin their transition into iSC and at DIV7 most of the cells
291 present on neurites are iSC.

Under Review

292 **Discussion:**

293 The objective of this study was to determine the SCP/iSC transition in DRG-SC cocultures using the
294 mRNA expression profiles of Schwann cell developmental genes (*Dhh*, *Mpz*, *Cnp*, *Plp*, *Mbp*, *Krox20*,
295 *Cad19*, *Tfap2a*). We first identified stable reference genes to normalize the expression of the target
296 genes and determine their profiles. In this study, we have determined *Ppia* and *Tbp* to be the best
297 combination of reference genes to normalize qPCR data in dissociated DRG cultures before the
298 induction of myelination. From the normalized profiles of developmental genes, we sought to estimate
299 the time window where SCP transition to iSC in this culture system.

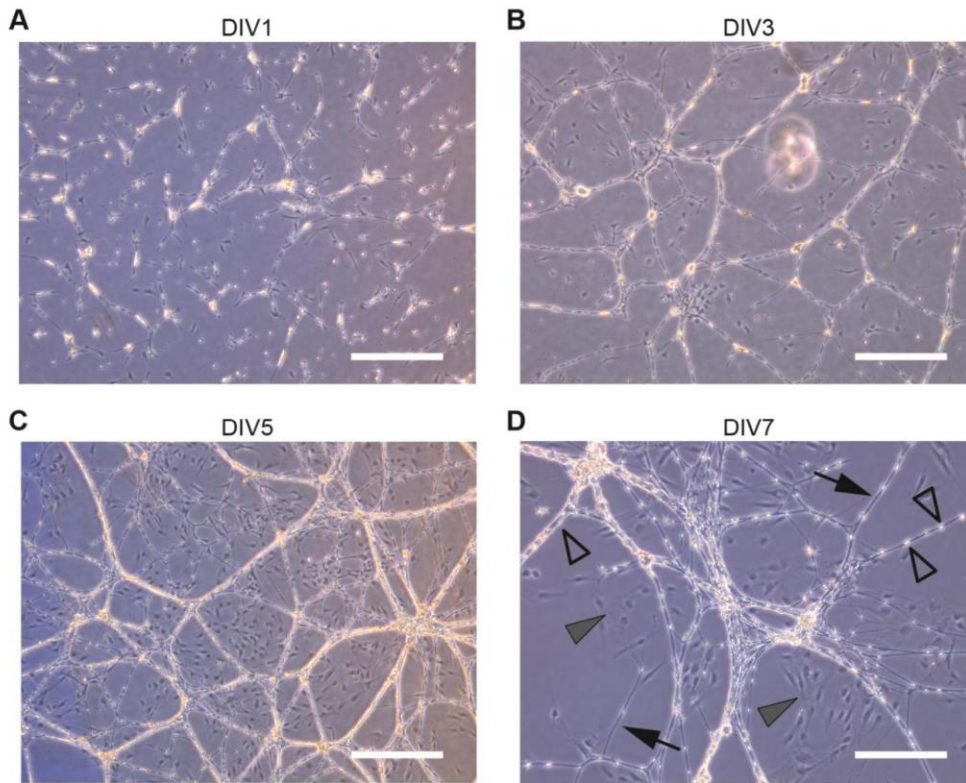
300 Our data seem to largely comply and concur with the order of molecular events observed in embryonic
301 spinal nerves. However, we pinpoint certain differences in genes such as *Dhh* and *Plp*. We believe that
302 such differences exist due to innate differences between DRG cultures and developing nerves. For
303 instance, SCP which transition into iSC at around E15.5 further differentiate into promyelinating and
304 Remak Schwann cells after radially sorting large caliber axons from smaller ones gradually between
305 E18.5 and P10 (Jessen and Mirsky, 2005; Monk et al., 2015; Fledrich et al., 2019). This is accompanied
306 by an intrinsic change in the expression of Schwann cell developmental genes. *Dhh*, for example, is not
307 expressed in Remak Schwann cells but its expression is maintained in myelinating Schwann cells
308 postnatally (Sharghi-Namini et al., 2006). Similarly, the expression of *Plp* and other myelin related genes
309 such as *Mbp* and *Mpz* is further upregulated in myelinating Schwann cells but not in remak cells (Jessen
310 and Mirsky, 2005; Woodhoo and Sommer, 2008; Salzer, 2015). This is primarily because *Krox20* drives
311 the expression of myelin genes in myelinating cells and its expression in Remak cells is downregulated
312 (Svaren and Meijer, 2008; Woodhoo et al., 2009). Hence, our data on DRG-SC cocultures can only be
313 compared and contrasted to *in vivo* data up until the appearance of iSC in embryonic nerves between
314 E15.5 to E17.5. Further comparison with *in vivo* data can be possible if we assess the expression of
315 these genes using *in vitro* myelination assays. Myelination in coculture can be induced by the addition of
316 Ascorbic Acid (Päiväläinen et al., 2008). Conventionally, ascorbic acid is added at DIV7, which concurs
317 with the molecular profiles of iSC at DIV7 (highest RNA expression of *Krox20*, *Mpz*, *Mbp* and *Plp* coupled
318 with the downregulation of *Tfap2a* and *Cad19*). Thus, deducing the profiles of these genes in myelination
319 assays can further help in comparing *in vitro* and *in vivo* data beyond the SCP/iSC transition.

320 A notable limitation of our study is that we performed qPCR assays with total RNA extracted from all the
321 cell types in the coculture system. Although most of our target genes are uniquely expressed in the
322 Schwann cell lineage, certain genes such as *Tfap2a* and *Cad19* are not unique to Schwann cells. *Tfap2a*
323 expression has also been documented in sensory neurons (Donaldson et al., 1995; Schmidt et al., 2011).
324 However, in DRG-SC cocultures, the total number of sensory neurons pales in comparison to Schwann
325 cells largely because neuronal cells do not actively proliferate in culture as opposed to SCP or iSC.
326 Hence, it is safe to conclude that the difference we observed in *Tfap2a* expression at DIV7 is largely
327 contributed by SCP transitioning into iSC. This is also supported by the concomitant increase in *Krox20*
328 levels.

329 Similarly, *Cad19* mRNA is also detected in satellite glial cells (SGC) attached to the neuronal soma
330 (Takahashi and Osumi, 2005). Interestingly, *Cad19* expression is retained in SGC postnatally but it is
331 turned down in SCP as they transition to iSC in nerves (George et al., 2018). In culture, SGC are present
332 attached to neuronal soma. However, their proportion is very minimal when compared to Schwann cells.
333 This is mostly because their proliferation is intrinsically dependent on neuronal size and numbers
334 (Hanani, 2005; George et al., 2018). Hence, although *Cad19* levels drop significantly between DIV5 and
335 DIV7, it remains detectable in sufficient amounts even at DIV7 as its expression is retained in SGC.

336 Nevertheless, despite these minor limitations, our data provides conclusive evidence that the SCP/iSC
337 transition occurs between DIV5 and DIV7. This information serves as a powerful frame of reference to
338 design, execute and comprehend coculture experiments using WT mice or other Schwann cell mutants.

Under Review

Figures and Figure Legends

340

341

342 **Figure 1: Progression of Dissociated DRG cultures between the first (DIV1) and the**
 343 **seventh (DIV7) day of culture.**

344

345 Dissociated DRG cells form an extensive network comprised of neurites, Schwann Cells and
 346 fibroblasts.

347

348 (A) 1 day after plating - DIV1, spindle-shaped neuronal precursors start to form neurite
 349 outgrowths. (5X Magnification, Scale Bar = 500 μ m).

350 (B) 3 days after plating - DIV3, neurites extend and start to form a mesh like network.
 351 Refringent cells attached to the neurites are presumably SCP. Few fibroblasts grow on
 352 the bottom of the culture dish beneath the neurite network. (5X Magnification, Scale Bar
 353 = 500 μ m).

354 (C) 5 days after plating – DIV5, the neurite network is well established and connected. An
 355 increase in Schwann cells attached to the neurites is visible when compared to DIV3.
 356 Fibroblasts also proliferate in the same time. (5X Magnification, Scale Bar = 500 μ m).

357 (D) 7 days after plating – DIV7, the neurite-Schwann cell network now spans the entire dish
 358 and all neuronal extensions are covered with Schwann cells. Black arrows indicate
 359 neurite extensions. Hollow arrowheads indicate Schwann cells that appear bright under
 360 phase contrast. Grey arrowheads indicate flattened fibroblasts that proliferate beneath
 361 the network. (10X magnification, Scale Bar = 250 μ m).

362

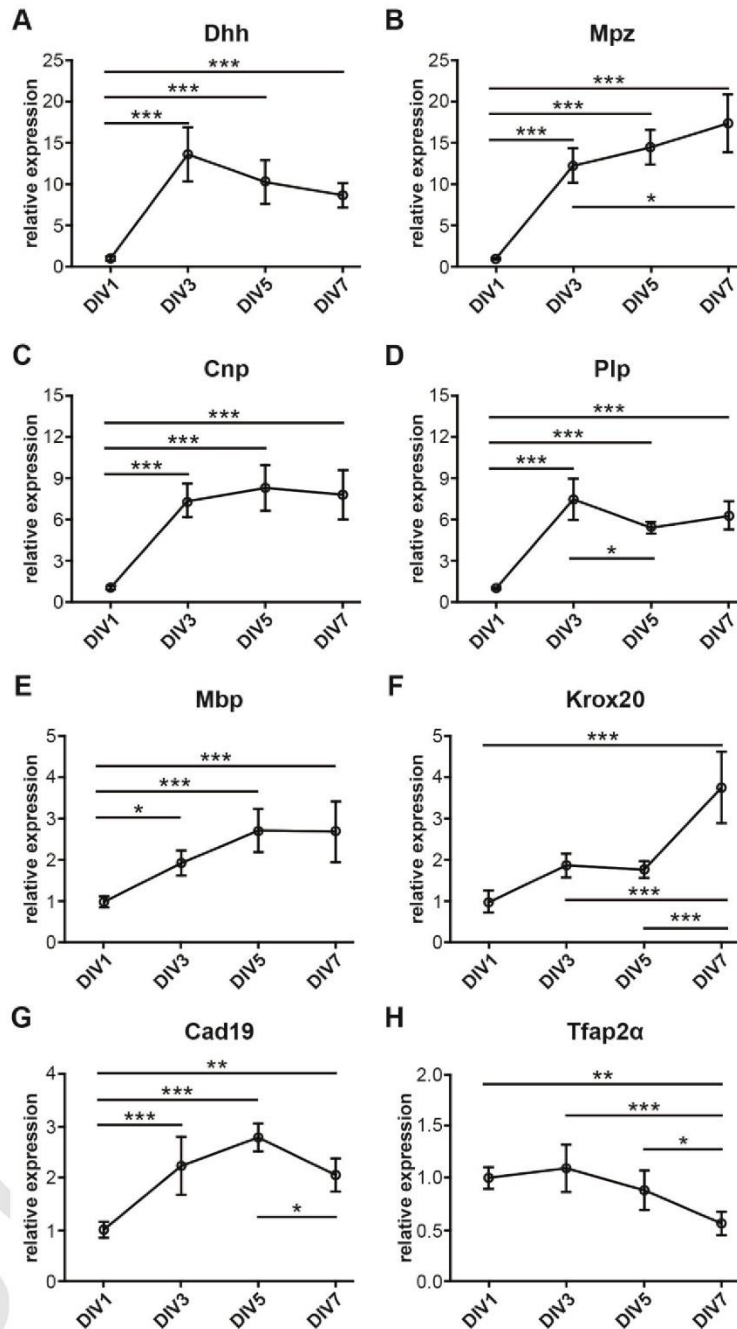


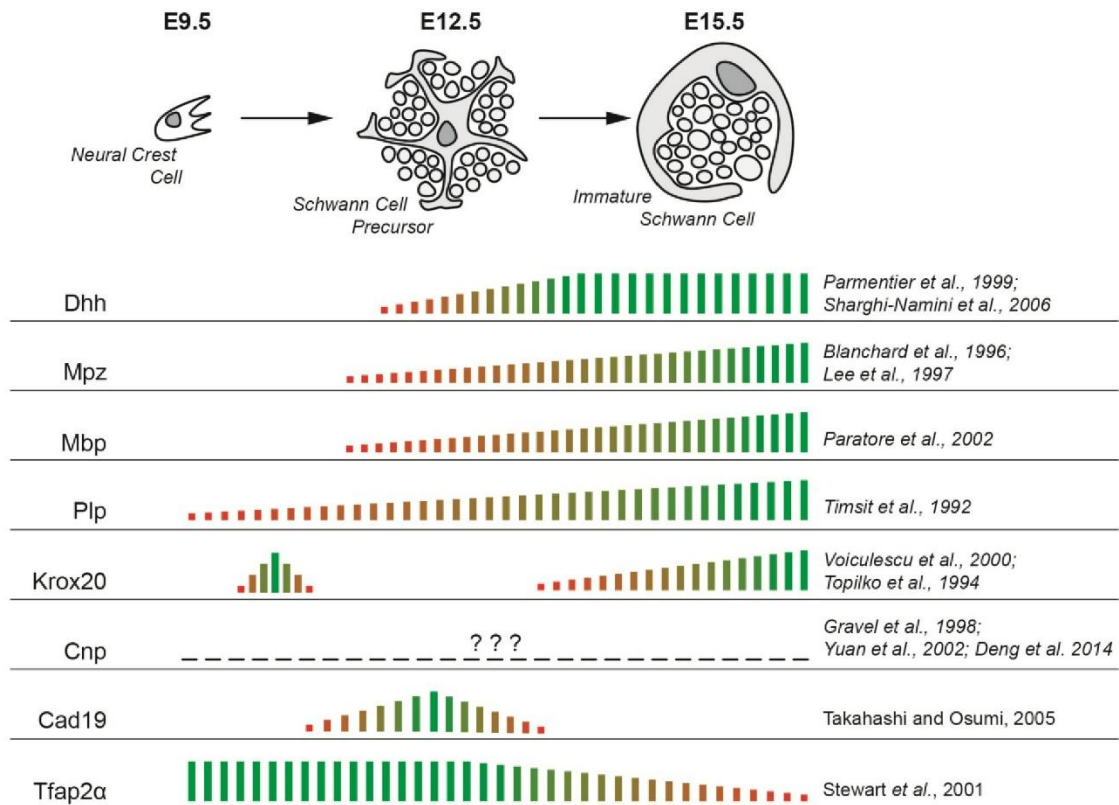
Figure 2: Relative expression of Schwann cell developmental genes during the first week of culture at regular intervals of 48 hours.

Expression profiles of Dhh (A), Mpz (B), Cnp (C), Plp (D), Mbp (E), Krox20 (F), Cad19 (G) and Tfap2α (H) are shown relative to DIV1, which was used as the experimental calibrator. Ppia/Tbp were used as reference genes for normalization. To assess differences across timepoints, one-way ANOVA was performed followed by Tukey's Post Hoc analysis to compare all the 4 groups with each other. The alpha value threshold was set at 5% and the P-values are represented as follows: * for P<0.05, ** for P<0.01 and *** for P<0.001. Statistically significant comparisons are

363
364
365
366
367
368
369
370
371
372
373

374 highlighted with horizontal lines spanning the groups under comparison. Group comparisons
375 that are not highlighted with horizontal lines do not exhibit any statistically significant differences.

Under Review



376
377
378
379
380

Figure 3: Expression levels of Schwann cell developmental genes in vivo as the transition from SCP to iSC.

381 The expression levels are expressed as horizontal bars with increasing height indicating higher
382 expression levels. This representation is based on microarray data (Buchstaller et al., 2004) and
383 other high-throughput data (D'Antonio et al., 2006). Additionally, relevant gene profiling and
384 lineage tracing studies are indicated for each gene. Dhh expression begins at the SCP stage
385 and reaches a plateau at the iSC stage. Mpz and Mbp expression is detected at the SCP slightly
386 before the expression of Dhh. Plp is expressed in migrating neural crest cells that are destined
387 towards a glial fate. Krox20 expression occurs in two distinct waves – the first in Boundary Cap
388 Cells that arise from NCC at around E10. The second wave occurs when SCP transition into
389 iSC at E15.5 in embryonic nerves of mice. Cnp expression in the glial lineage is not well
390 documented barring a couple of studies that have documented its expression in satellite glial
391 cells and ventral spinal roots. Cad19 is the only gene know so far that is uniquely expressed in
392 SCP but not in iSC or NCC. Tfp2α is a transcription factor that is expressed from migrating
393 NCC to SCP stages before being downregulated in iSC.

394 **Tables and Table Legends**

395 **Table 1**

396

CV analysis		NormFinder		NormFinder- Best pair of genes	
Gene	CV%	Gene	Stability Value (S)	Gene	Stability Value (S)
SDHA	23.66	PPIA	0.16	TBP/PPIA	0.11
MRPL10	23.89	TBP	0.16	HSP60/PPIA	0.14
PPIA	25.53	HSP60	0.22	HSP60/GAPDH	0.15
TBP	25.73	GAPDH	0.24	HSP60/TBP	0.16
GAPDH	29.12	RPL13A	0.24	GAPDH/TBP	0.18
RPL13A	30.94	MRPL10	0.34	GAPDH/PPIA	0.18
PGK1	35.13	ACTB	0.37	TBP/RPL13A	0.18
HSP60	36.29	SDHA	0.38	RPL13A/PPIA	0.18
RPS26	40.15	RPS26	0.39	HSP60/RPL13A	0.19
ACTB	47.27	PGK1	0.44	GAPDH/RPL13A	0.22

397

398 **Table 1: Determination of stable reference genes for qPCR assays on DRG-SC**
 399 **cocultures during the 1st week.**

400

401 Coefficient of Variation analysis (CV analysis) calculates the overall variation of RNA expression
 402 across all samples and time points. It is used to identify genes with high overall variation
 403 (CV>50%). Such genes can decrease the performance of the Normfinder algorithm (Sundaram
 404 et al., 2019). Normfinder determines the stability of a reference as a weighted measure of its
 405 intergroup and intragroup variation (Andersen et al., 2004). The S value calculated by
 406 Normfinder ranks the genes from the most to the least stable with the former exhibiting the
 407 lowest S value. The method also predicts the best combination of two reference genes that can
 408 produce robust qPCR data. In our dataset, Tbp/Ppia combination is found to be the best.
 409

410 **References:**

- 411
- 412 Andersen, C., Jensen, J., and Orntoft, T. (2004). Normalization of Real Time Quantitative Reverse
413 Transcription PCR Data : A Model Based Variance Estimation Approach to Identify Genes Suited
414 for Normalization , Applied to Bladder and Colon Cancer Data Sets. *Cancer Res.* 64, 5245.
415 doi:10.1158/0008.
- 416 Blanchard, A. D., Sinanan, A., Parmantier, E., Zwart, R., Broos, L., Meijer, D., et al. (1996). Oct-6
417 (SCIP/Tst-1) is expressed in Schwann cell precursors, embryonic Schwann cells, and postnatal
418 myelinating Schwann cells: comparison with Oct-1, Krox-20, and Pax-3. *J. Neurosci. Res.* 46,
419 630–40. doi:10.1002/(SICI)1097-4547(19961201)46:5<630::AID-JNR11>3.0.CO;2-0.
- 420 Buchstaller, J., Sommer, L., Bodmer, M., Hoffmann, R., Suter, U., and Mantei, N. (2004). Efficient
421 Isolation and Gene Expression Profiling of Small Numbers of Neural Crest Stem Cells and
422 Developing Schwann Cells. *J. Neurosci.* 24, 2357–2365. doi:10.1523/JNEUROSCI.4083-03.2004.
- 423 Couplier, F., Decker, L., Funalot, B., Vallat, J. M., Garcia-Bragado, F., Charnay, P., et al. (2010).
424 CNS/PNS boundary transgression by central glia in the absence of schwann cells or Krox20/Egr2
425 function. *J. Neurosci.* 30, 5958–5967. doi:10.1523/JNEUROSCI.0017-10.2010.
- 426 D’Antonio, M., Michalovich, D., Paterson, M., Droggiti, A., Woodhoo, A., Mirsky, R., et al. (2006). Gene
427 profiling and bioinformatic analysis of Schwann cell embryonic development and myelination. *Glia*
428 53, 501–515. doi:10.1002/glia.20309.
- 429 Donaldson, L. F., McQueen, D. S., and Seckl, J. R. (1995). Induction of transcription factor AP2 mRNA
430 expression in rat primary afferent neurons during acute inflammation. *Neurosci. Lett.* 196, 181–
431 184. doi:10.1016/0304-3940(95)11870-3.
- 432 Fledrich, R., Kungl, T., Nave, K. A., and Stassart, R. M. (2019). Axo-glia interdependence in peripheral
433 nerve development. *Development* 146. doi:10.1242/dev.151704.
- 434 George, D., Ahrens, P., and Lambert, S. (2018). Satellite glial cells represent a population of
435 developmentally arrested Schwann cells. *Glia* 66, 1496–1506. doi:10.1002/glia.23320.
- 436 Hanani, M. (2005). Satellite glial cells in sensory ganglia: From form to function. *Brain Res. Rev.* 48,
437 457–476. doi:10.1016/j.brainresrev.2004.09.001.
- 438 Jacob, C. (2015). Transcriptional control of neural crest specification into peripheral glia. *Glia* 63, 1883–
439 1896. doi:10.1002/glia.22816.
- 440 Jessen, K. R., Brennan, A., Morgan, L., Mirsky, R., Kent, A., Hashimoto, Y., et al. (1994). The Schwann
441 cell precursor and its fate: A study of cell death and differentiation during gliogenesis in rat
442 embryonic nerves. *Neuron* 12, 509–527. doi:10.1016/0896-6273(94)90209-7.
- 443 Jessen, K. R., and Mirsky, R. (2005). The origin and development of glial cells in peripheral nerves. *Nat*
444 *Rev Neurosci* 6, 671–682. doi:nm1746 [pii]n10.1038/nm1746.
- 445 Jessen, K. R., and Mirsky, R. (2019). Schwann cell precursors; multipotent glial cells in embryonic
446 nerves. *Front. Mol. Neurosci.* 12, 69. doi:10.3389/fnmol.2019.00069.
- 447 Kim, H. A., and Maurel, P. (2009). “Primary Schwann Cell Cultures,” in (Humana Press), 253–268.
448 doi:10.1007/978-1-60761-292-6_15.
- 449 Kim, J., and Kim, H. A. (2018). “Isolation and expansion of Schwann cells from transgenic mouse
450 models,” in *Methods in Molecular Biology* (Humana Press Inc.), 39–48. doi:10.1007/978-1-4939-
451 7649-2_3.
- 452 Lee, M. J., Brennan, A., Blanchard, A., Zoidl, G., Dong, Z., Taberner, A., et al. (1997). P0 is
453 constitutively expressed in the rat neural crest and embryonic nerves and is negatively and
454 positively regulated by axons to generate non- myelin-forming and myelin-forming Schwann cells,
455 respectively. *Mol. Cell. Neurosci.* 8, 336–350. doi:10.1006/mcne.1996.0589.

- 456 Livak, K. J., and Schmittgen, T. D. (2001). Analysis of relative gene expression data using real-time
457 quantitative PCR and the $2^{-\Delta\Delta CT}$ Method. *Methods* 25, 402–408. doi:10.1006/meth.2001.1262.
- 458 Mollet, I. G., Ben-Dov, C., Felício-Silva, D., Grosso, A. R., Eleutério, P., Alves, R., et al. (2010).
459 Unconstrained mining of transcript data reveals increased alternative splicing complexity in the
460 human transcriptome. *Nucleic Acids Res.* 38, 4740–4754. doi:10.1093/nar/gkq197.
- 461 Monk, K. R., Feltri, M. L., and Taveggia, C. (2015). New insights on schwann cell development. *Glia*
462 63, 1376–1393. doi:10.1002/glia.22852.
- 463 Päiväläinen, S., Nissinen, M., Honkanen, H., Lahti, O., Kangas, S. M., Peltonen, J., et al. (2008).
464 Myelination in mouse dorsal root ganglion/Schwann cell cocultures. *Mol. Cell. Neurosci.* 37, 568–
465 578. doi:10.1016/j.mcn.2007.12.005.
- 466 Paratore, C., Hagedorn, L., Floris, J., Hari, L., Kléber, M., Suter, U., et al. (2002). Cell-intrinsic and cell-
467 extrinsic cues regulating lineage decisions in multipotent neural crest-derived progenitor cells. *Int.*
468 *J. Dev. Biol.* 46, 193–200. Available at: <http://www.ncbi.nlm.nih.gov/pubmed/11902683> [Accessed
469 April 18, 2020].
- 470 Parmantier, E., Lynn, B., Lawson, D., Turmaine, M., Namini, S. S., Chakrabarti, L., et al. (1999).
471 Schwann cell-derived Desert hedgehog controls the development of peripheral nerve sheaths.
472 *Neuron* 23, 713–24. Available at: <http://www.ncbi.nlm.nih.gov/pubmed/10482238> [Accessed July
473 18, 2019].
- 474 Ratner, N., Williams, J. P., Kordich, J. J., and Kim, H. A. (2005). Schwann Cell Preparation from Single
475 Mouse Embryos: Analyses of Neurofibromin Function in Schwann Cells. *Methods Enzymol.* 407,
476 22–33. doi:10.1016/S0076-6879(05)07003-5.
- 477 Salzer, J. L. (2015). Schwann cell myelination. *Cold Spring Harb. Perspect. Biol.* 7, 1–26.
478 doi:10.1101/cshperspect.a020529.
- 479 Schmidt, M., Huber, L., Majdazari, A., Schütz, G., Williams, T., and Rohrer, H. (2011). The transcription
480 factors AP-2 β and AP-2 α are required for survival of sympathetic progenitors and differentiated
481 sympathetic neurons. *Dev. Biol.* 355, 89–100. doi:10.1016/j.ydbio.2011.04.011.
- 482 Schmittgen, T. D., and Livak, K. J. (2008). Analyzing real-time PCR data by the comparative C(T)
483 method. *Nat. Protoc.* 3, 1101–8.
- 484 Sharghi-Namini, S., Turmaine, M., Meier, C., Sahni, V., Umehara, F., Jessen, K. R., et al. (2006). The
485 structural and functional integrity of peripheral nerves depends on the glial-derived signal desert
486 hedgehog. *J. Neurosci.* 26, 6364–76. doi:10.1523/JNEUROSCI.0157-06.2006.
- 487 Stewart, H. J. S., Brennan, A., Rahman, M., Zoidl, G., Mitchell, P. J., Jessen, K. R., et al. (2001).
488 Developmental regulation and overexpression of the transcription factor AP-2, a potential regulator
489 of the timing of Schwann cell generation. *Eur. J. Neurosci.* 14, 363–372. doi:10.1046/j.0953-
490 816X.2001.01650.x.
- 491 Sundaram, V. K., Sampathkumar, N. K., Massaad, C., and Grenier, J. (2019). Optimal use of statistical
492 methods to validate reference gene stability in longitudinal studies. *PLoS One* 14, e0219440.
493 doi:10.1371/journal.pone.0219440.
- 494 Svaren, J., and Meijer, D. (2008). The molecular machinery of myelin gene transcription in schwann
495 cells. *Glia* 56, 1541–1551. doi:10.1002/glia.20767.
- 496 Takahashi, M., and Osumi, N. (2005). Identification of a novel type II classical cadherin: Rat cadherin19
497 is expressed in the cranial ganglia and Schwann cell precursors during development. *Dev. Dyn.*
498 232, 200–208. doi:10.1002/dvdy.20209.
- 499 Taveggia, C., and Bolino, A. (2018). “DRG neuron/schwann cells myelinating cocultures,” in *Methods in*
500 *Molecular Biology* (Humana Press Inc.), 115–129. doi:10.1007/978-1-4939-7862-5_9.
- 501 Timsit, S. G., Bally-Cuif, L., Colman, D. R., and Zalc, B. (1992). DM-20 mRNA Is Expressed During the

- 502 Embryonic Development of the Nervous System of the Mouse. *J. Neurochem.* 58, 1172–1175.
503 doi:10.1111/j.1471-4159.1992.tb09378.x.
- 504 Topilko, P., Schneider-Maunoury, S., Levi, G., Baron-Van Evercooren, A., Chennoufi, A. B. Y.,
505 Seitanidou, T., et al. (1994). Krox-20 controls myelination in the peripheral nervous system. *Nature*
506 371, 796–799. doi:10.1038/371796a0.
- 507 Voiculescu, O., Charnay, P., and Schneider-Maunoury, S. (2000). Expression pattern of a Krox-20/Cre
508 knock-in allele in the developing hindbrain, bones, and peripheral nervous system. *genesis* 26,
509 123–126. doi:10.1002/(SICI)1526-968X(200002)26:2<123::AID-GENE7>3.0.CO;2-O.
- 510 Woodhoo, A., Alonso, M. B. D., Droggiti, A., Turmaine, M., D'Antonio, M., Parkinson, D. B., et al.
511 (2009). Notch controls embryonic Schwann cell differentiation, postnatal myelination and adult
512 plasticity. *Nat. Neurosci.* 12, 839–847. doi:10.1038/nn.2323.
- 513 Woodhoo, A., and Sommer, L. (2008). Development of the Schwann cell lineage: From the neural crest
514 to the myelinated nerve. *Glia* 56, 1481–1490. doi:10.1002/glia.20723.

3.2.9 Schwann cells in LXR β ScKO mice die between DIV5 and DIV8 in culture

Using the framework established in the previous study, we compared dissociated DRG cultures established from E13.5 Control and LXR β ScKO mice (**Figure 8**). At DIV5, no palpable differences existed between Control and mutant cultures (**Figure 8A**). However, at DIV7, the Schwann cells in mutant cultures exhibited a rounded shape whereas the cells in control cultures retained their spindle shaped morphology (**Figure 8A**). At DIV8, these cells detached and started floating in the cell culture media. We also mechanically removed the neurite network at DIV8 and digested it enzymatically in order to count the total number of cells (Neurons + Schwann cells) obtained from each culture at DIV8. In Control cultures, we obtained around 1 million cells whereas in mutant cultures the total number of cells was reduced to 0.5 million (**Figure 8B**). These preliminary results suggested that Schwann cells in LXR β ScKO cultures detached from neurites between DIV5 and DIV8.

When we compare this data to the results obtained in the previous study, we are able to cautiously glean into the exact time-period where mutant Schwann cells were likely to disappear in embryonic peripheral nerves. From our results *in vitro*, we speculated that LXR β ScKO Schwann cells either did not successfully make the transition from SCP to iSC or they died prematurely once they have transitioned into iSC. Further experiments are underway to provide to concrete evidence of probable Schwann cell death in culture. Moreover, we are also performing IHC on mutant embryonic spinal nerves to demonstrate the reduction of Schwann cell numbers either during the SCP/iSC transition or right afterwards. Additionally, we are also performing apoptosis assays using Cleaved Caspase 3 IHC in mutant and control embryos at E13.5 (SCP stage) and E16.5 (iSC stage).

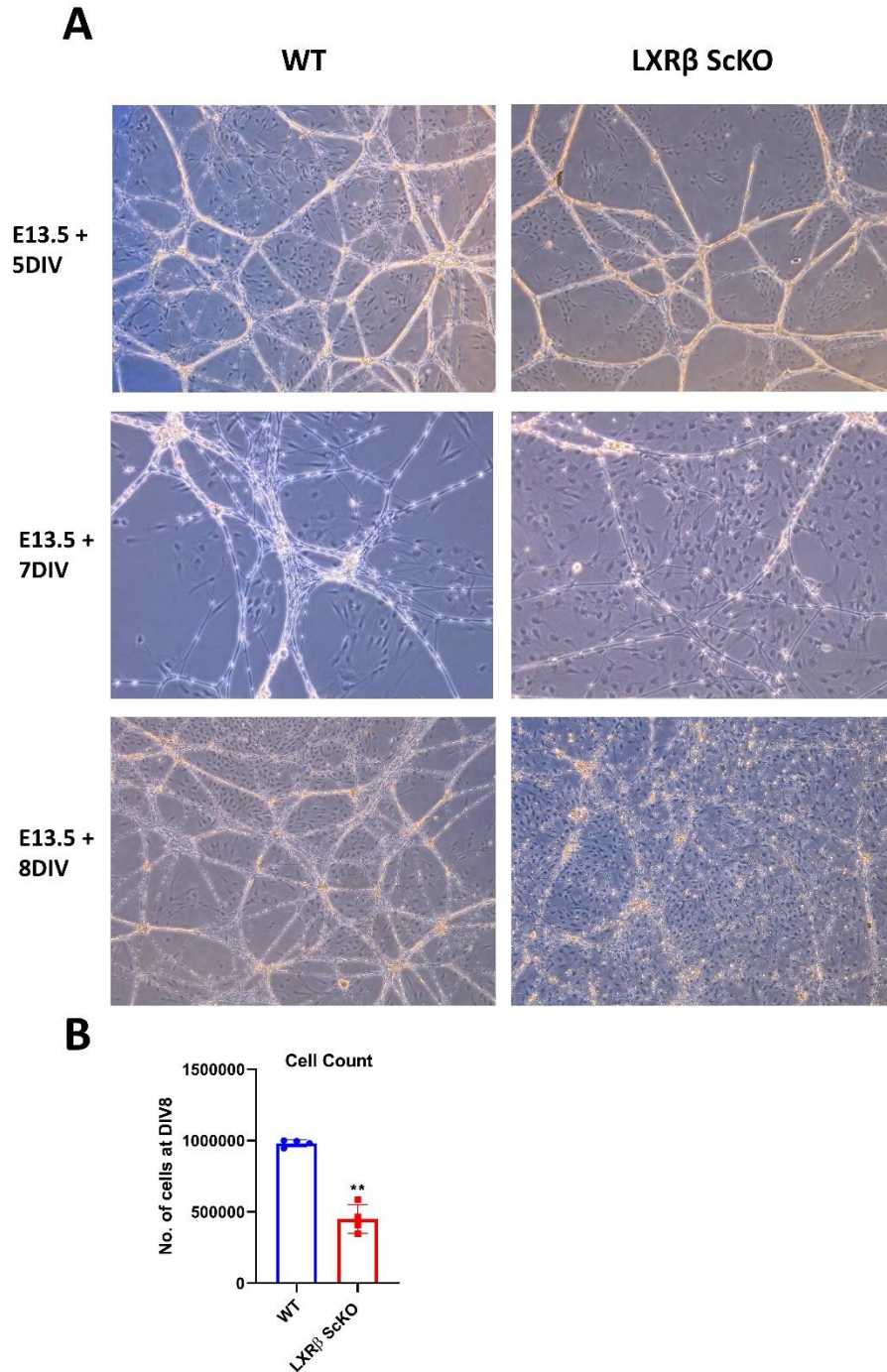


Figure 8: DRG-SC co-cultures established from WT and mutant embryonic DRGs at E13.5. (A) Phase contrast microscopy images of cultures after 5 days in vitro (E13.5 + 5DIV), 7 days in vitro (E13.5 + 7DIV) and 8 days in vitro (E13.5+8DIV). (B) Number of cells obtained after mechanical removal and enzymatic digestion of the neurite-Schwann cell network at DIV8. Non-parametric Mann-Whitney test was performed to analyze statistical differences between the groups and P values are represented as follows: $P < 0.05$: *, $P < 0.01$: **, $P < 0.001$: ***.

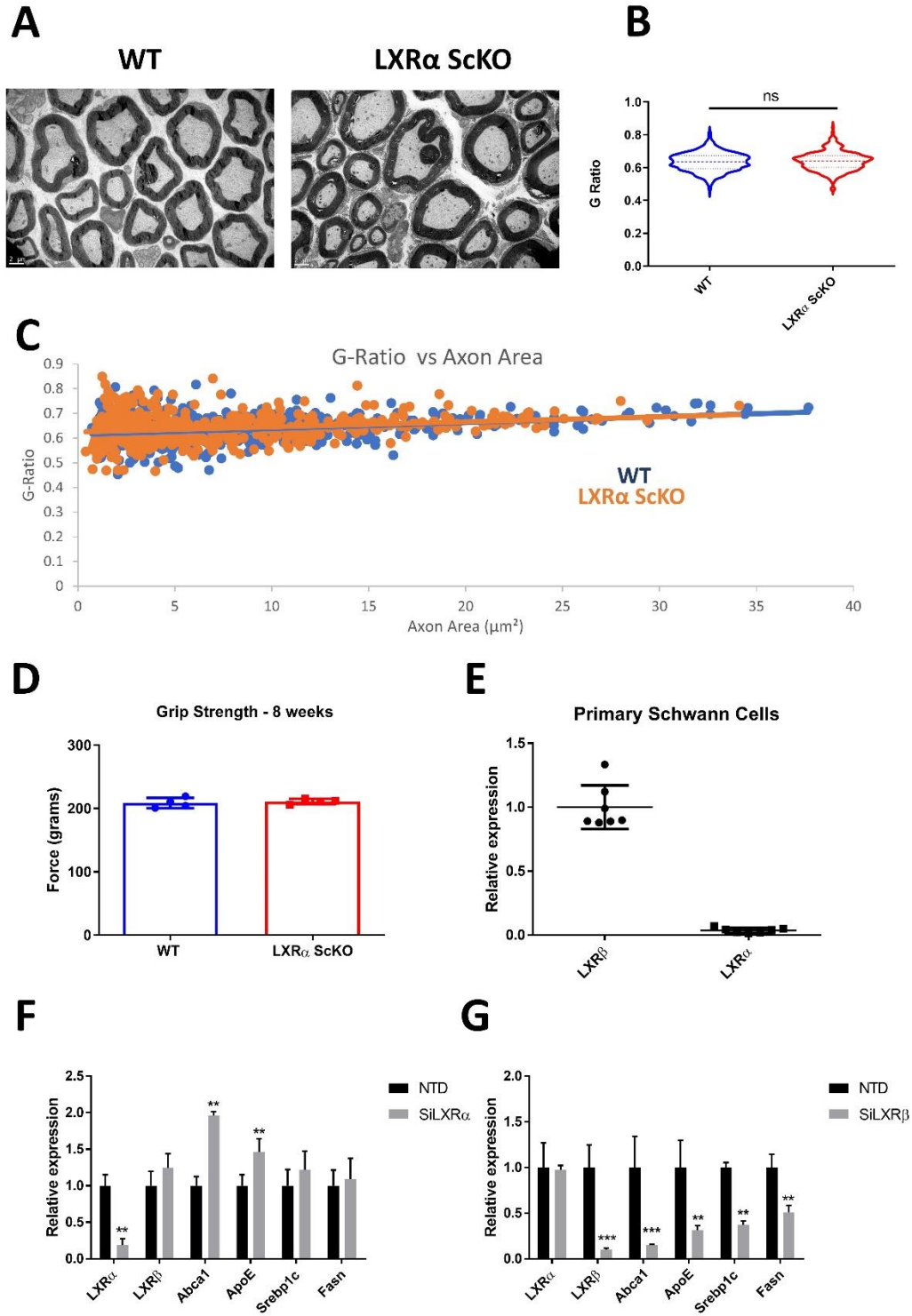
Chapter 4: SUPPLEMENTARY RESULTS

4.1 LXR β is the functional isoform in Schwann cells

As discussed earlier, during the course of my doctoral studies, we generated both LXR α^{ff} :DhhCre (LXR α ScKO) and LXR β^{ff} :DhhCre (LXR β ScKO) mice along with LXR α/β^{ff} :DhhCre (LXR α/β ScKO mice). Only LXR α/β ScKO mice and LXR β ScKO mice exhibit the phenotype described herein. LXR α ScKO mice, on the contrary, do not exhibit any behavioral or ultrastructural deficits and the results were comparable to their respective Controls (**Supplementary Figure 1**). We first assayed the mRNA expression levels of LXR α and LXR β in primary WT Schwann cells using qPCR. We observed that LXR β was expressed about 70-folds more than LXR α (LXR α Mean Cq: 29.6 cycles and LXR β Mean Cq: 23.2 cycles) (**Supplementary Figure 1E**). Our results suggest that LXR β might be the predominant functional isoform in Schwann cells.

We then transfected primary WT Schwann cells with either SiLXR α or SiLXR β to determine which among the two would lead to a concomitant decrease in the LXR target genes implicated in lipogenesis (Srebp1c, Fasn) and cholesterol homeostasis (Abca1, ApoE) (**Supplementary Figure 1F & 1G**). We observed that silencing LXR β elicited the decrease in expression of all LXR targets (**Supplementary Figure 1G**). However, interestingly, silencing LXR α increased Abca1 and ApoE expression but had no effect on Srebp1c and Fasn (**Supplementary Figure 1F**). These results taken together suggest that LXR β is the functional isoform in Schwann cells and this isoform could possibly play a compensatory role in the absence of LXR α in the context of cholesterol homeostasis. These results taken together possible explain why LXR α ScKO animals did not exhibit any phenotype.

However, in order to rule-out any mild phenotypes, we performed the G-Ratio analysis on 8-week-old LXR α ScKO mice (**Supplementary Figure 1B**). WT and mutants exhibited comparable G-Ratios (mean G-Ratio WT: 0.6345, mean G ratio LXR α ScKO : 0.6399). We next plotted the G-ratios as a function of the axonal area to verify if there are any differences in the G-Ratios of smaller and larger axons across both groups (**Supplementary Figure 1C**). Regression analysis of all data points revealed that both the populations were identical (**Supplementary Figure 1C**). Furthermore, LXR α ScKO mutants did not exhibit any behavioral phenotype in grip tests (**Supplementary Figure 1D**) suggesting that they did not suffer from any muscular deficits. Furthermore, absence of LXR α in Schwann cells had no effect on Schwann cell physiology or myelination when compared to LXR β .



Supplementary Figure 1: **LXR β is the functional isoform in Schwann cells.** (A) Representative TEM images of adult 8-week old sciatic nerves of WT and LXR α ScKO animals. (B) Violin plots of G-ratios of all axons from both the WT and mutant group from 8-week old sciatic nerve sections. Violin plots show a gaussian distribution of data points in both groups. The dotted lines inside the

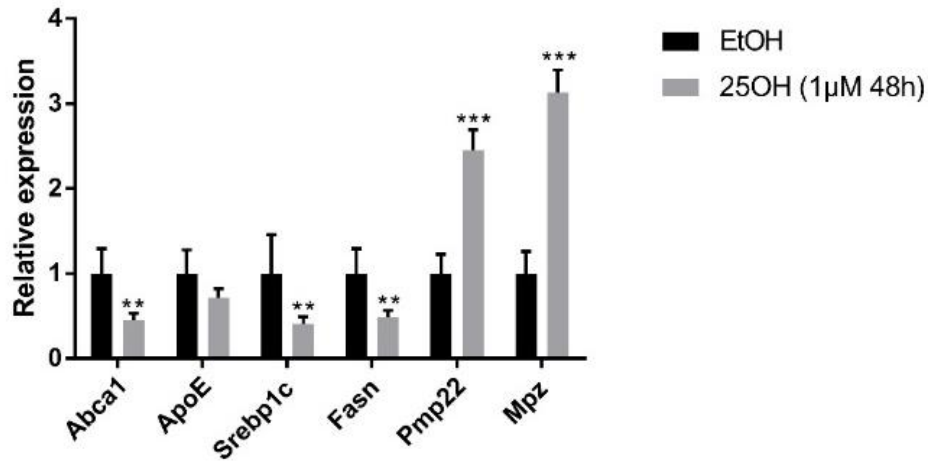
violin plots represent the median in the center, quartile 3 above and quartile 1 below the median. T-test was performed to determine statistically significant differences between the groups and none were found. (C) Regression analysis of G-Ratios plotted as a function of axonal area (size). WT data points are represented in **blue** and mutant data points are represented in **orange**. (D) Grip strength test of 8-week old WT and LXR α ScKO animals. Both Groups exhibit similar and comparable grip strengths. (E) mRNA expression of LXR α and LXR β in primary Schwann cells assessed through RTqPCR. The difference in expression is represented as a fold difference of LXR α expression with respect to LXR β . (F) mRNA expression of LXRs and their target genes assessed through RTqPCR after RNA silencing of LXR α in primary Schwann cells. (G) mRNA expression of LXRs and their target genes assessed through RTqPCR after RNA silencing of LXR β in primary Schwann cells. Non-parametric Mann-Whitney test was performed to analyze statistical differences between the groups and P values are represented as follows: P<0.05: *, P<0.01: **, P<0.001: ***.

4.2 The putative role of 25HC in myelin gene regulation during Schwann cell development

We next assessed the LXR ligands that could potentiate the role of the nuclear receptor in Schwann cells. In previous studies 3 potential ligands were identified in adult sciatic nerves (Makoukji et al., 2011). Among the three ligands, we chose to treat primary immature Schwann cells with 25HC. Our choice of the ligand was based on previous microarray data on developing Schwann cells from embryonic nerves (Buchstaller et al., 2004). We reanalyzed the dataset and found that Cholesterol 25-Hydroxylase (Ch25h), the enzyme that catalyzes the conversion of cholesterol to 25HC, was upregulated in the developing embryonic nerves during the SCP/iSC transition (**Supplementary Figure 2B**). The upregulation of Ch25h (leading to a possible increase in endogenous 25HC) is also correlated with the increase in myelin gene expression and the decrease in Abca1 (LXR target) mRNA levels at the SCP/iSC transition (**Supplementary Figure 2B**). We therefore hypothesized that 25HC could play a crucial role with respect to myelin gene regulation and cholesterol homeostasis during the SCP/iSC transition.

Thus, we treated primary Schwann cells with 1 μ M 25HC for 48 hours (**Supplementary Figure 2A**). This treatment resulted in a 3-fold increase in Mpz and Pmp22 RNA levels. Interestingly, 25HC also exhibited antagonistic properties with respect to LXR function. 25HC reduced the expression of ABCA1, Srebp1c and Fasn in primary Schwann cells. A tendency towards reduction was observed in ApoE mRNA levels. Our *in vitro* data partially recapitulates what happens *in vivo* during the embryonic development of Schwann cells (**Supplementary Figure 2B**).

These results taken together suggest that 25HC regulates myelin gene expression at the mRNA level either in an LXR dependant or an independant manner. Furthermore, treatment with 25HC exerts an antagonistic effect on LXR target genes such as Abca1, Srebp1c and Fasn. However, interestingly, the antagonistic effects of 25HC on ABCA1 and Srebp1c expression is unconventional.

A**B**

Gene	Mean expression level at developmental stages					
	NCC	SCP	SCP/iSC	SCP/iSC	iSC	iSC/mSC
	E9.5	E12	E14	E16	E18	P0
cholesterol 25-hydroxylase	71	64	83	152	71	182
ABCA1 (LXR Target)	122	928	1668	818	341	370
myelin basic protein	148	217	987	2713	3994	4160
myelin protein zero	11	114	378	390	644	1407
early growth response 2/Krox20	434	835	2183	3403	4347	3117
proteolipid protein (myelin)	252	701	876	1078	1536	1467

Supplementary Figure 2: *Putative role of 25HC in Schwann cell development.* (A) mRNA expression of myelin genes and LXR target genes following treatment of Primary Schwann cells with 1µM 25 Hydroxycholesterol (25OH) for 48 hours. Expression differences are expressed as fold changes with respect to the Vehicle (Ethanol – EtOH) group. Non-parametric Mann-Whitney test was performed to analyze statistical differences between the groups and P values are represented as follows: P<0.05: *, P<0.01: **, P<0.001: ***. (B) Microarray data generated from neural crest cells and their derivatives at different developmental stages (Buchstaller et al., 2004). The column names are titled based on developmental time points and the corresponding stage in Neural Crest differentiation. NCC-Neural Crest Cell, SCP-Schwann cell Precursor, iSC-immature Schwann cell, mSC-myelinating Schwann cell. The rows are titled based on the gene names. The data points of the table represent mean mRNA expression levels assessed through microarrays. The number are also used to generate a heat map where shades of red indicate lower mRNA levels, shades of yellow indicate moderate expression and shades of green indicate higher expression. The heat maps were generated relative to the expression levels of each gene in question.

Chapter 5: DISCUSSION

5.1 Embryonic disappearance of Schwann cells and changes in the cellular anatomy of the nerve

LXR β ScKO displayed an adverse phenotype postnatally that involves an astonishing lack of myelin sheath around axons that results from the absence of Neural Crest Derivatives (and therefore Schwann cells) in the sciatic nerve as early as Post Natal Day 0 (P0). This was accompanied by a drastic alteration of the nerve ultrastructure both perinatally and postnatally, culminating in the invasion of Perineurial cells into the endoneurial space. The dialogue between Schwann cells and Perineurial cells during embryonic development is crucial for proper anatomical arrangement of the nerve. Seminal work from Jessen and Mirsky lab has previously demonstrated that the DHH protein secreted by Schwann cells during embryonic development permits the perineurial cells to establish proper fasciculations of spinal nerves and thus maintain the structural integrity of nerves (Sharghi-Namini et al., 2006). Indeed, using *Dhh*^{-/-} total mutants, they demonstrated that the lack of Dhh signaling leads to the invasion of the perineurial cell into the endoneurial space and these cells form mini-fascicles around myelinated axons. In LXR β ScKO mice, this phenomenon is exactly recapitulated, although not due to a faulty dialogue between Schwann cells and Perineurial cells. We have sufficient data to show that the untimely disappearance of Schwann cells leads to an environment where no Dhh signaling is possible. Hence, in post-natal timepoints, perineurial cells invade into the endoneurial space and strangely ensheath axonal bundles. Furthermore, electron microscopy images from E18.5 mutant sciatic nerves (**Figure 7, Results Section**) also suggests that this invasion takes place even before birth. This is further corroborated by the fact that Dhh mRNA is produced by Schwann cell precursors from E12.5 and therefore the protein might play a role during embryonic nerve development. Thus, collectively, these observations suggest that the drastic alteration in the nerve ultrastructure might have its underpinnings during embryonic development.

Our mouse model also phenocopies Sox10 Schwann cell mutants (*Sox10*^{fl/fl}:DhhCre) (Finzsch et al., 2010; Küspert et al., 2012). As stated earlier, Sox10 is one of the most important transcription factors of Neural Crest Cells and it is crucial for the survival and differentiation of their peripheral nerve derivatives (Svaren and Meijer, 2008). In Sox10 mutants, Schwann cells die embryonically, and the nerve is devoid of

Schwann cells before birth thus resulting in a similar phenotype as LXR β ScKO animals. Yet again, perineurial cells invade into the endoneurial space and form mini fascicles around naked axonal bundles. These observations can further be confirmed by comparing our mice to the *Krox20GFP(DT)^{+/+}HtPA:Cre* mice where peripheral nerves are depleted of Schwann cells due their death at embryonic stages following Diphtheria Toxin mediated cytotoxicity (Coulpier et al., 2010). Our model, yet again, phenocopies *Krox20GFP(DT)^{+/+}HtPA:Cre* suggesting that Schwann cells disappear or die during embryonic development. However, it is equally possible that the embryonic Schwann cells in our mouse model cease to proliferate and thus present a phenotype with highly reduced Schwann cell numbers after birth.

5.2 Do Schwann cells die due to endogenous causes? Do they stop proliferating? Or do they detach from axons and thus die?

To determine the exact embryonic timepoint when Schwann cells disappear or halt proliferation, we retraced the embryonic development of Schwann cells using Dorsal Root Ganglia (DRG)/Schwann Cell cocultures established from E13.5 LXR β ScKO mutants and their respective controls. We first performed a preliminary study using WT C57Bl6 mice to correlate *in vitro* Schwann cell development in DRG/SC cocultures to *in vivo* development in spinal nerves (Sundaram et al., 2020). Briefly, our study revealed that Schwann Cell Precursors (SCP) appear in culture at DIV3. They proliferate between DIV3 and DIV5 on neurites. At DIV5 they begin their transition to immature Schwann Cells (iSC) and at DIV7 most of the Schwann cells transition to the immature stage. However, in cultures established from LXR β ScKO mutants, iSC at DIV7 detach from axons and start floating in culture suggesting that they probably die in this time window. Furthermore, at DIV8, we found that the mutant cultures are full of floating cells as observed under phase contrast microscopy. This was further corroborated by the sparse number of cells that we could recuperate from the neurite-Schwann cell network in mutants. However, apoptosis assays are required to provide conclusive evidence of Schwann cell death in cultures. We are currently performing Annexin V / PI apoptosis assay at different time points.

Nevertheless, assuming that the cells die (as they are not present *in vivo* at birth) these floating cells at DIV8 give rise to two hypotheses. Either Schwann cells detach first due to a loss of communication

with neurons or they die first and then detach from neurons due to natural circumstances arising from cell death.

Of note, at DIV5, there were no palpable differences between mutant and WT cultures suggesting that the mutant Schwann cells seem to have a problem with survival or remaining attached to neurons only during the SCP/iSC transition or thence. Nevertheless, these *in vitro* observations provide key insights to look for *in vivo* evidence for Schwann cell death in mutants. IHC analysis of mutant spinal nerves is thus warranted at two stages – one at around E14.5 when SCP actively proliferate in developing axons and the other at around E17.5 when SCP have successfully transitioned in iSC.

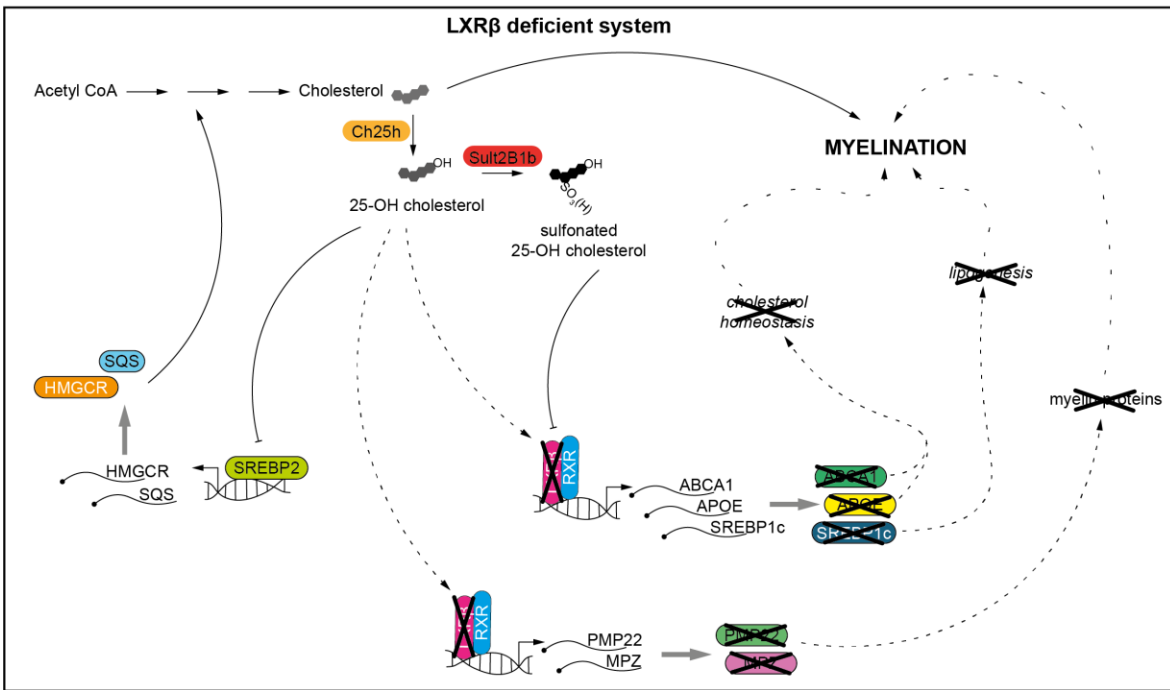
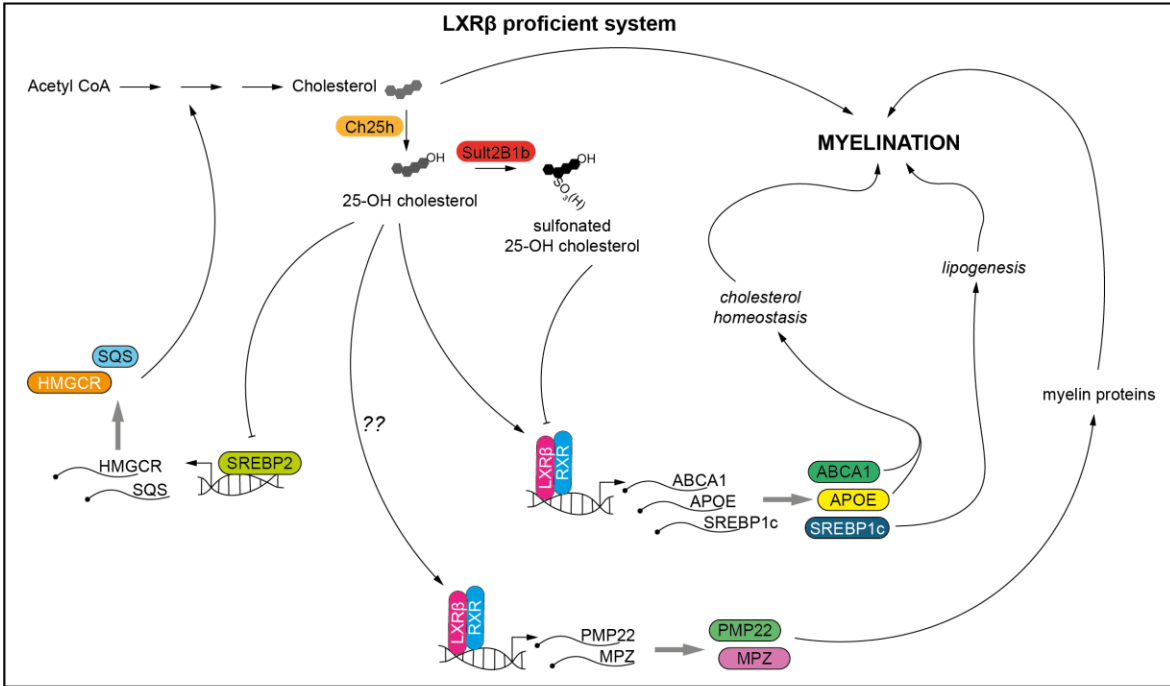
5.3 The plausible causes for Schwann cell death during the SCP/iSC transition or afterwards

A lot of important structural and functional changes occur when SCP transition to iSC in embryonic nerves (Jessen and Mirsky, 2019a). A striking characteristic change that occurs during this transition is the switch from a paracrine survival mechanism (assured majorly by Neuregulin during the SCP stage) to an autocrine survival mode at the iSC stage (Jessen and Mirsky, 2005; Woodhoo and Sommer, 2008). In our mutant model, it is still unclear whether the Schwann cells die during the transition or just after. However, there are a few important observations regarding LXR signaling and oxysterols that must be taken into consideration in order to holistically understand why Schwann cells disappear from embryonic nerves in LXR β ScKO mice.

Previous microarray data suggests that Ch25h mRNA levels robustly rise during the SCP/iSC transition (**Supplementary Figure 2B**) (Buchstaller et al., 2004). Thus, we can speculate that this would translate to Schwann cells producing endogenous 25HC during this transition. To understand the rationale behind this phenomenon, we treated primary Schwann cells with 25HC (**Supplementary Figure 2A**). Our results indicate that 25HC increase *Mpz* and *Pmp22* mRNA levels in culture and we also observed a correlation between Ch25h expression and the concomitant increase in myelin genes *in vivo*. However, we do not know if this happens through LXR. 25HC treatment also reduces the mRNA expression of genes implicated in Cholesterol efflux such as *Abca1* and *ApoE* that are LXR targets (**Supplementary Figure 2A**).

This might probably be because 25HC is known to reduce cholesterol biosynthesis in different systems by inhibiting the maturation and nuclear translocation of SREBP2 protein (Radhakrishnan et al., 2007; Waltl et al., 2013). This serves as a feedback loop to inhibit cholesterol synthesis when sufficient amounts of Cholesterol are present in the cell. Since we have disturbed this homeostasis by treatment with 25HC, the Schwann cells might try to counteract this change by reducing the efflux of Cholesterol (**Supplementary Figure 2A**). This hypothesis can also be applied to *in vivo* settings where we observed in the microarray data that increase in Ch25h during the SCP/iSC transition also correlates with a concomitant decrease in Abca1. Furthermore, myelin gene expression also increases following Ch25h upregulation in Schwann cells thus corroborating our *in vitro* data. We also have sufficient evidence to suggest that LXR β is the functional isoform in Schwann cells as it controls both cholesterol efflux and lipogenesis (**Supplementary Figure 2G**). Thus, we hypothesize that in an LXR β deficient system, the increase in 25HC during the SCP/iSC transition does not culminate in an increase in myelin gene expression assuming that the process is mediate by LXR β . Furthermore, increase in 25HC would concomitantly decrease cholesterol biosynthesis and in the absence of LXR β , the Schwann cell would lose its capacity to retain existing levels of cholesterol through ABCA1 and APOE.

An intriguing phenomenon is the reduction in the mRNA levels of Srebp1 and its downstream target Fasn after 25HC treatment (**Supplementary Figure 2A**). A reduction in cholesterol biosynthesis can be speculated based on the canonical action of 25HC on SREBP2 protein. However, it does not explain why lipogenesis is affected. There is some literature indicating that sulfation of 25HC by Hydroxysterol Sulfotransferase 2B1b (SULT2B1b) can inhibit both lipogenesis and Cholesterol efflux through the LXR/SREBP1 axis in different types of cells (Ren et al., 2007; Ma et al., 2008; Ren and Ning, 2014). Thus, expression of SULT2B1b in Schwann cells needs to be assayed during 25HC treatment and during the SCP/iSC transition. Given these observations we propose the following schematic model to the explain the phenotype that arises in LXR β ScKO animals (**recapitulated from the Graphical abstract**).



Graphical Representation: The role of LXR β in Schwann cell development. In an LXR β proficient system, the synthesis cholesterol gives rise to 25-Hydroxycholesterol (25OH) by the enzyme Cholesterol 25 Hydroxylase (Ch25h). This oxysterol binds LXR β to induce the expression of cholesterol efflux genes ABCA1 and ApoE as well as the master regulator of lipogenesis Srebp1c. However, our data also suggests that 25OH can induce myelin gene expression possibly through LXR β . Cholesterol homeostasis, lipogenesis and myelin protein expression together can positively Schwann cell differentiation and myelination. Furthermore, prolonged treatment of primary Schwann cells with 25OH results in a reduction in LXR β target genes, which is possibly mediated by the Sulfonated form

of the oxysterol. In an LXR β deficient system, cholesterol homeostasis, lipogenesis and myelin protein expression might be directly compromised due to the absence of the receptor. Moreover, the intracellular oxysterol and cholesterol levels would be dysregulated and eventually lead to a failure in Schwann cell differentiation and possibly death.

5.4 The difference between total and specific LXR ablation

Another important concern that needs to be addressed is the huge difference in phenotype that we observe between the total LXRdKO animals and LXR β ScKO animals. Our observations demonstrate that LXRdKO animals have a very mild phenotype where Schwann cell are still present in post-natal timepoints and myelinate, although, not as effectively as their respective controls. However, in LXR β ScKO animals, Schwann cells die embryonically and therefore the mice are born with a drastic reduction in Schwann cell numbers. The difference between the two models is that total mutants were generated by the insertion of Neo Cassette in the coding strand of LXR isoforms whereas Schwann cell mutants are generated at the SCP (E12.5) using the Cre LOX system.

Thus, our hypothesis is that in total mutants are, neural crest cells and their derivatives had the time to adopt compensatory mechanisms arising from the lack of LXRs. However, in Schwann cell mutants the sudden ablation of LXR at the SCP stage when its role is seemingly important, does not permit the cells to adapt to the changes and hence they die embryonically. However, we cannot rule out the possibility that the total mutants in fact elicit a dominant negative phenotype that confers partial activity to LXRs. We are currently generating total mutants by breeding the LXR β f/f animals to CMV Cre mice to delete the nuclear receptor in all tissues (*refer to section 6.4 in Perspective and Future Directions*)

Chapter 6: PERSPECTIVES AND FUTURE DIRECTIONS

In this section, I summarize the different scientific questions that have emanated from my work and put forth hypotheses and experiments that can be performed to verify them. In doing so, I hope to detail a path forward towards further scientific enquiry into this theme of research. The section also culminates with a brief discussion on how the information gained from this fundamental research can be used to formulate investigations in a clinical setting.

6.1 Question 1: Why is the phenotype in LXR β ScKO animals not completely homogenous?

Hypothesis 1: Some Schwann cells escape Cre-recombinase mediated gene ablation, as Dhh is not expressed in all Schwann cells during embryonic development

Hypothesis 2: All SC recombine but not all of them die.

Empirical Observation: It is well known in the Schwann cell research community that Dhh-Cre is not 100% efficient (Wu et al., 2008). Thus, it is probable that not all Schwann cells recombine.

Experiment: Using Fluorescence In-Situ Hybridization (FISH) on sciatic nerve sections presenting with the moderate phenotype, we can categorically assess if the Schwann cells that remain and myelinate have been subjected to LXR β deletion. Thus, we would perform FISH using 2 RNA probes, one directed towards s100 β (Schwann cell marker) and the other directed towards LXR β . A co-localization would imply that these cells have escaped recombination.

Alternatively, we breed the LXR β f/f: DhhCre mice to a reporter line such as TdTomato and look the TdTomato fluorescence in the surviving cells.

6.2 Question 2: What are the complete set of transcriptomic modifications that arise as NCC transition into SCP and then iSC?

This is an exploratory question and we do not have a specific hypothesis to highlight. Previously, high throughput studies were conducted using microarrays with a limited set of probes (Buchstaller et al., 2004; D'Antonio et al., 2006b). However, we believe that the study has to be repeated using RNA-seq to achieve better depth and also gain a holistic picture of the transcriptomic landscape during these developmental transitions. Our personal interest in this study is to obtain gene expression data pertaining to lipid and cholesterol metabolism.

Experiment 1: The *in vivo* approach would entail the use of *PfpGFP* mice to isolate GFP positive cells at different stages of embryonic spinal nerve development by FACS followed by single cell RNA-seq. This is the same approach adopted by Buchstaller and colleagues, but we plan on using Single cell RNA-seq to identify a greater number of targets, obtain a resolution higher than that of microarrays and finally classify the different sub-populations of Schwann cells during development, if any.

Experiment 2: The *in vitro* approach would employ the same mouse line to generate dissociated DRG cultures to isolate GFP positive cells by FACS at DIV3, DIV5 and DIV7. RNA-seq can then be performed to assess the transcriptomic changes that arise as SCP transition into iSC between DIV5 and DIV7.

6.3 Question 3: What is the role of oxysterols (that are LXR ligands) in Schwann cell development and myelination?

Hypothesis: Different LXR ligands potentiate cholesterol homeostasis, lipogenesis and myelin gene expression

Preliminary data: 25HC increases myelin gene expression but decreases cholesterol efflux in primary Schwann cells.

Experiment 1: Treatment of primary Schwann cells with different LXR ligands that have previously been identified in the PNS – 24(S)HC, 25HC and 27HC (Makoukji et al., 2011). Primary output analysis by RTqPCR for genes implicated in cholesterol homeostasis, lipogenesis and myelination.

Experiment 2: Treatment of primary Schwann cells with different LXR ligands in the absence of LXR β (either by using SiLXR β on WT primary cells or by using TAT-Cre on primary cells from LXR $\beta^{f/f}$ mice). This would give us an idea whether the effects of the oxysterol treatment are mediated through LXR β .

Experiment 3: Oxysterol assays using GC-MS on primary Schwann cells under proliferation and differentiation (induced by the addition of cAMP). This experiment would give us an idea of Schwann cell endogenous oxysterols that regulate gene expression in an autocrine manner.

6.4 Question 4: Why do LXRdKO mice not display such drastic phenotypes when compared to LXR β ScKO mice?

Hypothesis: In total LXR mutants (LXRdKO), compensatory mechanisms are set into place as the genetic ablation is achieved much earlier during embryonic development

Experiment 1: Breed LXR $\beta^{f/f}$ mice with a Cre line that results in total ablation of the nuclear receptor (Eg: CMVCre). This would be to establish a proof of concept that total ablation at an earlier embryonic time point would confer some compensatory benefits with respect to LXR mediated cellular processes as NCC transition into SCP and then iSC.

Experiment 2: RNA seq analysis and comparison of WT vs LXR β ScKO vs LXRdKO dissociated DRG-SC cocultures at DIV5 (right before Schwann cells detach from neurons in LXR β ScKO cultures). This would give us a clear picture of the transcriptomic landscape of Schwann cells and the potential compensatory mechanisms at the RNA expression level exhibited by LXRdKO cells. This data would also permit us to establish rescue experiments for LXR β ScKO cells based on the mechanisms adopted by the total mutants.

6.5 Benefit of this research in a clinical setting:

The data generated on LXR β ScKO mice can be used to interpret certain pathological conditions at the molecular level. During the course of my PhD research, we have gained significant insights on how fatty acid metabolism is regulated in Schwann cells through LXR β and its downstream target Srebp1c.

Malignant Peripheral Nerve Sheath Tumor (MPNST), a malignant form of neurofibromas in Neurofibromatosis Type 1 (NF1) resulting from a combined loss of function mutation in the Neurofibromin 1 gene and various tumor suppressor genes has been characterized with an altered lipid metabolism resulting from increased fatty acid synthesis and fatty acid oxidation. Hence, it was previously suggested that Fatty acid synthase (FASN – regulated by the LXR β /Srebp1c axis) is a potent and targetable metabolic oncogene (Patel et al., 2015). Therefore, pharmacological or genetic inhibition of LXR β can be a plausible therapeutic strategy in combatting the proliferation of neoplastic Schwann cells in these tumors.

Another approach that has rendered positive results in combatting the hyper-proliferative tumor is the inhibition of the mTORC pathway (Johansson et al., 2008; Varin et al., 2016). From a reductionist perspective, these two strategies seem like two sides of the same coin as mTORC1 is classically known to activate Srebp1c in Schwann cells through RXR γ (Norrmén et al., 2014). Thus, it is quite probable that Srebp1c mediated lipogenesis in Schwann cells is regulated by LXR β :RXR γ heterodimer at the transcriptional level both in physiological and pathological conditions. Furthermore, bulk RNA-seq data (unpublished) from our collaborator Dr. Eric Pasmant also shows an upregulation of LXR β in patient MPNST biopsies. Taken together, these observations support the therapeutic strategy of combatting MPNST by genetic or pharmacological inhibition of LXR β .

Moreover, the intricate association between LXRs, lipids, and cholesterol offer unexplored possibilities of using the LXR pathway therapeutically in the treatment of Charcot-Marie-Tooth 1A (CMT1A). CMT1A in humans is characterized by a duplication of Chromosome 17p12 (c17p12), which is a large segment of DNA that encodes the PMP22 protein (Valentijn et al., 1992). This results in higher expression levels of PMP22 and compromises the structural and functional integrity of the myelin sheath around peripheral axons. Recently, Fledrich and colleagues have shown that in rodent models of CMT1A, there is a systematic downregulation of lipogenic genes in the nerves (Fledrich et al., 2018). In the CMT1A model, administration of phospholipids improved myelin ultrastructure, electrophysiology, and muscle strength of affected animals. Thus, LXR activation using GW3965 or other ligands can be envisaged as a therapeutic approach to increase the expression of lipogenic enzymes through Srebp1c.

REFERENCES:

- Annicotte, J. S., Schoonjans, K., and Auwerx, J. (2004). Expression of the Liver X Receptor α and β in Embryonic and Adult Mice. *Anat. Rec. - Part A Discov. Mol. Cell. Evol. Biol.* 277, 312–316. doi:10.1002/ar.a.20015.
- Arthur-Farraj, P., Wanek, K., Hantke, J., Davis, C. M., Jayakar, A., Parkinson, D. B., et al. (2011). Mouse schwann cells need both NRG1 and cyclic AMP to myelinate. *Glia* 59, 720–733. doi:10.1002/glia.21144.
- Bae, C.-J., and Saint-Jeannet, J.-P. (2014). Induction and Specification of Neural Crest Cells: Extracellular Signals and Transcriptional Switches. *Neural Crest Cells*, 27–49. doi:10.1016/B978-0-12-401730-6.00002-8.
- Bala, U., Tan, K.-L., Ling, K.-H., and Cheah, P.-S. (2014). Harvesting the maximum length of sciatic nerve from adult mice: a step-by-step approach. *BMC Res. Notes* 7, 714. doi:10.1186/1756-0500-7-714.
- Beirowski, B., Babetto, E., Golden, J. P., Chen, Y.-J., Yang, K., Gross, R. W., et al. (2014). Metabolic regulator LKB1 is crucial for Schwann cell-mediated axon maintenance. *Nat. Neurosci.* 17, 1351–61. doi:10.1038/nn.3809.
- Bermingham, J. R., Shearin, H., Pennington, J., O'Moore, J., Jaegle, M., Driegen, S., et al. (2006). The claw paw mutation reveals a role for Lgi4 in peripheral nerve development. *Nat. Neurosci.* 9, 76–84. doi:10.1038/nn1598.
- Birchmeier, C., and Nave, K. A. (2008). Neuregulin-1, a key axonal signal that drives schwann cell growth and differentiation. *Glia* 56, 1491–1497. doi:10.1002/glia.20753.
- Boissaud-Cooke, M., Pidgeon, T. E., and Tunstall, R. (2015). “The Microcirculation of Peripheral Nerves: The Vasa Nervorum. The Vasa Nervorum,” in *Nerves and Nerve Injuries* (Elsevier Ltd), 507–523. doi:10.1016/B978-0-12-410390-0.00039-1.
- Brennan, A., Dean, C. H., Zhang, A. L., Cass, D. T., Mirsky, R., and Jessen, K. R. (2000). Endothelins control the timing of Schwann cell generation in vitro and in vivo. *Dev. Biol.* 227, 545–557. doi:10.1006/dbio.2000.9887.
- Brinkmann, B. G., Agarwal, A., Sereda, M. W., Garratt, A. N., Müller, T., Wende, H., et al. (2008). Neuregulin-1/ErbB Signaling Serves Distinct Functions in Myelination of the Peripheral and Central Nervous System. *Neuron* 59, 581–595. doi:10.1016/j.neuron.2008.06.028.
- Britsch, S., Goerich, D. E., Riethmacher, D., Peirano, R. I., Rossner, M., Nave, K. A., et al. (2001). The transcription factor Sox10 is a key regulator of peripheral glial development. *Genes Dev.* 15, 66–78. doi:10.1101/gad.186601.
- Buchstaller, J., Sommer, L., Bodmer, M., Hoffmann, R., Suter, U., and Mantei, N. (2004). Efficient Isolation and Gene Expression Profiling of Small Numbers of Neural Crest Stem Cells and Developing Schwann Cells. *J. Neurosci.* 24, 2357–2365. doi:10.1523/JNEUROSCI.4083-03.2004.
- Bustin, S. A., Benes, V., Garson, J. A., Hellemans, J., Huggett, J., Kubista, M., et al. (2009). The MIQE Guidelines: Minimum Information for Publication of Quantitative Real-Time PCR Experiments. doi:10.1373/clinchem.2008.112797.

- Camargo, N., Smit, A. B., and Verheijen, M. H. G. (2009). SREBPs: SREBP function in glia-neuron interactions. *FEBS J.* 276, 628–636. doi:10.1111/j.1742-4658.2008.06808.x.
- Carr, M. J., Toma, J. S., Johnston, A. P. W., Steadman, P. E., Yuzwa, S. A., Mahmud, N., et al. (2019). Mesenchymal Precursor Cells in Adult Nerves Contribute to Mammalian Tissue Repair and Regeneration. *Cell Stem Cell* 24, 240–256.e9. doi:10.1016/j.stem.2018.10.024.
- Catala, M., and Kubis, N. (2013). “Gross anatomy and development of the peripheral nervous system,” in *Handbook of clinical neurology*, 29–41. doi:10.1016/B978-0-444-52902-2.00003-5.
- Cermenati, G., Abbiati, F., Cermenati, S., Brioschi, E., Volonterio, A., Cavaletti, G., et al. (2012). Diabetes-induced myelin abnormalities are associated with an altered lipid pattern: protective effects of LXR activation. *J. Lipid Res.* 53, 300–310. doi:10.1194/jlr.m021188.
- Cermenati, G., Brioschi, E., Abbiati, F., Melcangi, R. C., Caruso, D., and Mitro, N. (2013). Liver X receptors, nervous system, and lipid metabolism. *J. Endocrinol. Invest.* 36, 435–43. doi:10.3275/8941.
- Cermenati, G., Giatti, S., Cavaletti, G., Bianchi, R., Maschi, O., Pesaresi, M., et al. (2010). Activation of the liver X receptor increases neuroactive steroid levels and protects from diabetes-induced peripheral neuropathy. *J. Neurosci.* 30, 11896–901. doi:10.1523/JNEUROSCI.1898-10.2010.
- Chan, J. R., Watkins, T. A., Cosgaya, J. M., Zhang, C., Chen, L., Reichardt, L. F., et al. (2004). NGF controls axonal receptivity to myelination by Schwann cells or oligodendrocytes. *Neuron* 43, 183–191. doi:10.1016/j.neuron.2004.06.024.
- Chen, Y., Wang, H., Yoon, S. O., Xu, X., Hottiger, M. O., Svaren, J., et al. (2011). HDAC-mediated deacetylation of NF- κ B is critical for Schwann cell myelination. *Nat. Neurosci.* 14, 437–441. doi:10.1038/nn.2780.
- Chomczynski, P., and Sacchi, N. (1987). Single-step method of RNA isolation by acid guanidinium thiocyanate-phenol-chloroform extraction. *Anal. Biochem.* 162, 156–159. doi:10.1016/0003-2697(87)90021-2.
- Clark, J. K., O’keefe, A., Mastracci, T. L., Sussel, L., Matise, M. P., and Kucenas, S. (2014). Mammalian Nkx2.2+ perineurial glia are essential for motor nerve development. *Dev. Dyn.* 243, 1116–1129. doi:10.1002/dvdy.24158.
- Cosgaya, J. M., Chan, J. R., and Shooter, E. M. (2002). The neurotrophin receptor p75NTR as a positive modulator of myelination. *Science (80-)*. 298, 1245–1248. doi:10.1126/science.1076595.
- Coulpier, F., Decker, L., Funalot, B., Vallat, J. M., Garcia-Bragado, F., Charnay, P., et al. (2010). CNS/PNS boundary transgression by central glia in the absence of schwann cells or Krox20/Egr2 function. *J. Neurosci.* 30, 5958–5967. doi:10.1523/JNEUROSCI.0017-10.2010.
- Courtois, A., Gac-Breton, S., Berthou, C., Guézennec, J., Bordron, A., and Boisset, C. (2012). Complement dependent cytotoxicity activity of therapeutic antibody fragments is acquired by immunogenic glycan coupling. *Electron. J. Biotechnol.* 15, 5. doi:10.2225/vol15-issue5-fulltext-3.

- D'Antonio, M., Droggiti, A., Feltri, M. L., Roes, J., Wrabetz, L., Mirsky, R., et al. (2006a). TGF β type II receptor signaling controls schwann cell death and proliferation in developing nerves. *J. Neurosci.* 26, 8417–8427. doi:10.1523/JNEUROSCI.1578-06.2006.
- D'Antonio, M., Michalovich, D., Paterson, M., Droggiti, A., Woodhoo, A., Mirsky, R., et al. (2006b). Gene profiling and bioinformatic analysis of Schwann cell embryonic development and myelination. *Glia* 53, 501–515. doi:10.1002/glia.20309.
- Da Silva, T. F., Eira, J., Lopes, A. T., Malheiro, A. R., Sousa, V., Luoma, A., et al. (2014). Peripheral nervous system plasmalogens regulate Schwann cell differentiation and myelination. *J. Clin. Invest.* 124, 2560–2570. doi:10.1172/JCI72063.
- de Preux, A. S., Goosen, K., Zhang, W., Sima, A. A. F., Shimano, H., Ouwens, D. M., et al. (2007). SREBP-1c expression in Schwann cells is affected by diabetes and nutritional status. *Mol. Cell. Neurosci.* 35, 525–534. doi:10.1016/j.mcn.2007.04.010.
- Domènech-Estévez, E., Baloui, H., Meng, X., Zhang, Y., Deinhardt, K., Dupree, J. L., et al. (2016). Akt Regulates Axon Wrapping and Myelin Sheath Thickness in the PNS. *J. Neurosci.* 36, 4506–21. doi:10.1523/JNEUROSCI.3521-15.2016.
- Dong, Z., Brennan, A., Liu, N., Yarden, Y., Lefkowitz, G., Mirsky, R., et al. (1995). Neu differentiation factor is a neuron-glia signal and regulates survival, proliferation, and maturation of rat schwann cell precursors. *Neuron* 15, 585–596. doi:10.1016/0896-6273(95)90147-7.
- Dykes, I. M., Tempest, L., Lee, S. I., and Turner, E. E. (2011). Brn3a and Islet1 act epistatically to regulate the gene expression program of sensory differentiation. *J. Neurosci.* 31, 9789–9799. doi:10.1523/JNEUROSCI.0901-11.2011.
- Endo-Umeda, K., Yasuda, K., Sugita, K., Honda, A., Ohta, M., Ishikawa, M., et al. (2014). 7-Dehydrocholesterol metabolites produced by sterol 27-hydroxylase (CYP27A1) modulate liver X receptor activity. *J. Steroid Biochem. Mol. Biol.* 140, 7–16. doi:10.1016/j.jsbmb.2013.11.010.
- Faroni, A., Castelnovo, L. F., Procacci, P., Caffino, L., Fumagalli, F., Melfi, S., et al. (2014). Deletion of GABA-B receptor in schwann cells regulates remak bundles and small nociceptive C-fibers. *Glia* 62, 548–565. doi:10.1002/glia.22625.
- Farrell, R. E. (2010). *RNA Methodologies: Laboratory Guide for Isolation and Characterization*. doi:10.1016/B978-0-12-374727-3.00025-5.
- Felten, D. L., and Shetty, A. N. (2014). *Netter 's Atlas of Neuroscience , Second Edition*.
- Feltri, M. L., Poitelon, Y., and Previtali, S. C. (2016). How Schwann Cells Sort Axons. *Neurosci.* 22, 252–265. doi:10.1177/1073858415572361.
- Finzsch, M., Schreiner, S., Kichko, T., Reeh, P., Tamm, E. R., Bösl, M. R., et al. (2010). Sox10 is required for Schwann cell identity and progression beyond the immature Schwann cell stage. *J. Cell Biol.* 189, 701–712. doi:10.1083/jcb.200912142.
- Fledrich, R., Abdelaal, T., Rasch, L., Bansal, V., Schütza, V., Brügger, B., et al. (2018). Targeting myelin lipid metabolism as a

- potential therapeutic strategy in a model of CMT1A neuropathy. *Nat. Commun.* 9, 3025. doi:10.1038/s41467-018-05420-0.
- Fledrich, R., Kungl, T., Nave, K. A., and Stassart, R. M. (2019). Axo-glia interdependence in peripheral nerve development. *Development* 146. doi:10.1242/dev.151704.
- Fontenas, L., and Kucenas, S. (2017). Livin' On The Edge: glia shape nervous system transition zones. *Curr. Opin. Neurobiol.* 47, 44–51. doi:10.1016/j.conb.2017.09.008.
- Fontenas, L., and Kucenas, S. (2018). Motor Exit Point (MEP) Glia: Novel Myelinating Glia That Bridge CNS and PNS Myelin. *Front. Cell. Neurosci.* 12, 333. doi:10.3389/fncel.2018.00333.
- Freese, C., Garratt, A. N., Fahrenholz, F., and Endres, K. (2009). The effects of α -secretase ADAM10 on the proteolysis of neuregulin-1. *FEBS J.* 276, 1568–1580. doi:10.1111/j.1742-4658.2009.06889.x.
- Fricker, F. R., Antunes-Martins, A., Galino, J., Paramsothy, R., La Russa, F., Perkins, J., et al. (2013). Axonal neuregulin 1 is a rate limiting but not essential factor for nerve remyelination. *Brain* 136, 2279–97. doi:10.1093/brain/awt148.
- Fricker, F. R., Zhu, N., Tsantoulas, C., Abrahamsen, B., Nassar, M. A., Thakur, M., et al. (2009). Sensory axon-derived neuregulin-1 is required for axoglial signaling and normal sensory function but not for long-term axon maintenance. *J. Neurosci.* 29, 7667–7678. doi:10.1523/JNEUROSCI.6053-08.2009.
- Furlan, A., and Adameyko, I. (2018). Schwann cell precursor: a neural crest cell in disguise? *Dev. Biol.* 444, S25–S35. doi:10.1016/j.ydbio.2018.02.008.
- Gabbi, C., Warner, M., and Gustafsson, J.-Å. (2009). Minireview: Liver X Receptor β : Emerging Roles in Physiology and Diseases. *Mol. Endocrinol.* 23, 129–136. doi:10.1210/me.2008-0398.
- Gabbi, C., Warner, M., and Gustafsson, J. Å. (2014). Action mechanisms of Liver X Receptors. *Biochem. Biophys. Res. Commun.* 446, 647–650. doi:10.1016/j.bbrc.2013.11.077.
- Garratt, A. N., Britsch, S., and Birchmeier, C. (2000). Neuregulin, a factor with many functions in the life of a Schwann cell. *BioEssays* 22, 987–996. doi:10.1002/1521-1878(200011)22:11<987::AID-BIES5>3.0.CO;2-5.
- Ghislain, J., and Charnay, P. (2006). Control of myelination in Schwann cells: A Krox20 cis-regulatory element integrates Oct6, Brn2 and Sox10 activities. *EMBO Rep.* 7, 52–58. doi:10.1038/sj.embor.7400573.
- Goebbels, S., Oltrogge, J. H., Kemper, R., Heilmann, I., Bormuth, I., Wolfer, S., et al. (2010). Elevated phosphatidylinositol 3,4,5-trisphosphate in glia triggers cell-autonomous membrane wrapping and myelination. *J. Neurosci.* 30, 8953–8964. doi:10.1523/JNEUROSCI.0219-10.2010.
- Goebbels, S., Oltrogge, J. H., Wolfer, S., Wieser, G. L., Nientiedt, T., Pieper, A., et al. (2012). Genetic disruption of Pten in a novel mouse model of tomaculous neuropathy. *EMBO Mol. Med.* 4, 486–499. doi:10.1002/emmm.201200227.

- Gokey, N. G., Srinivasan, R., Lopez-Anido, C., Krueger, C., and Svaren, J. (2012). Developmental Regulation of MicroRNA Expression in Schwann Cells. *Mol. Cell. Biol.* 32, 558–568. doi:10.1128/mcb.06270-11.
- Golan, N., Kartvelishvili, E., Spiegel, I., Salomon, D., Sabanay, H., Rechav, K., et al. (2013). Genetic deletion of *Cadm4* results in myelin abnormalities resembling Charcot-Marie-Tooth neuropathy. *J. Neurosci.* 33, 10950–10961. doi:10.1523/JNEUROSCI.0571-13.2013.
- Grigoryan, T., Stein, S., Qi, J., Wende, H., Garratt, A. N., Nave, K. A., et al. (2013). Wnt/Rspondin/ β -catenin signals control axonal sorting and lineage progression in Schwann cell development. *Proc. Natl. Acad. Sci. U. S. A.* 110, 18174–18179. doi:10.1073/pnas.1310490110.
- Grossmann, K. S., Wende, H., Paul, F. E., Cheret, C., Garratt, A. N., Zurborg, S., et al. (2009). The tyrosine phosphatase Shp2 (PTPN11) directs neuregulin-1/ErbB signaling throughout Schwann cell development. *Proc. Natl. Acad. Sci. U. S. A.* 106, 16704–16709. doi:10.1073/pnas.0904336106.
- Grove, M., and Brophy, P. J. (2014). FAK is required for schwann cell spreading on immature basal lamina to coordinate the radial sorting of peripheral axons with myelination. *J. Neurosci.* 34, 13422–13434. doi:10.1523/JNEUROSCI.1764-14.2014.
- Grove, M., Kim, H., Santerre, M., Krupka, A. J., Han, S. B., Zhai, J., et al. (2017). YAP/TAZ initiate and maintain Schwann cell myelination. *Elife* 6. doi:10.7554/eLife.20982.
- Guo, L., Lee, A. A., Rizvi, T. A., Ratner, N., and Kirschner, L. S. (2013). The protein kinase a regulatory subunit R1A (Prkar1a) plays critical roles in peripheral nerve development. *J. Neurosci.* 33, 17967–17975. doi:10.1523/JNEUROSCI.0766-13.2013.
- Guo, L., Moon, C., Niehaus, K., Zheng, Y., and Ratner, N. (2012). Rac1 controls schwann cell myelination through cAMP and NF2/merlin. *J. Neurosci.* 32, 17251–17261. doi:10.1523/JNEUROSCI.2461-12.2012.
- Harty, B. L., and Monk, K. R. (2017). Unwrapping the unappreciated: recent progress in Remak Schwann cell biology. *Curr. Opin. Neurobiol.* 47, 131–137. doi:10.1016/j.conb.2017.10.003.
- He, Y., Kim, J. Y., Dupree, J., Tewari, A., Melendez-Vasquez, C., Svaren, J., et al. (2010). Yy1 as a molecular link between neuregulin and transcriptional modulation of peripheral myelination. *Nat. Neurosci.* 13, 1472–1482. doi:10.1038/nn.2686.
- Hichor, M., Sundaram, V. K., Eid, S. A., Abdel-Rassoul, R., Petit, P. X., Borderie, D., et al. (2018). Liver X Receptor exerts a protective effect against the oxidative stress in the peripheral nerve. *Sci. Rep.* 8, 2524. doi:10.1038/s41598-018-20980-3.
- Höke, A., Ho, T., Crawford, T. O., LeBel, C., Hilt, D., and Griffin, J. W. (2003). Glial cell line-derived neurotrophic factor alters axon Schwann cell units and promotes myelination in unmyelinated nerve fibers. *J. Neurosci.* 23, 561–567. doi:10.1523/jneurosci.23-02-00561.2003.
- Horton, J. D., Goldstein, J. L., and Brown, M. S. (2002). SREBPs: activators of the complete program of cholesterol and fatty acid synthesis in the liver. *J. Clin. Invest.* 109, 1125–1131. doi:10.1172/jci15593.

- Irigoyen, M. P., Caro, M. T., Andrés, E. P., Manrique, A. B., Rey, M. V., and Woodhoo, A. (2018). Myelin. *1791*, 81–93. doi:10.1007/978-1-4939-7862-5.
- Jacob, C. (2015). Transcriptional control of neural crest specification into peripheral glia. *Glia* *63*, 1883–1896. doi:10.1002/glia.22816.
- Jacob, C., Christen, C. N., Pereira, J. A., Somandin, C., Baggiolini, A., Lötscher, P., et al. (2011). HDAC1 and HDAC2 control the transcriptional program of myelination and the survival of Schwann cells. *Nat. Neurosci.* *14*, 429–436. doi:10.1038/nn.2762.
- Jacob, C., Lötscher, P., Engler, S., Baggiolini, A., Varum Tavares, S., Brügger, V., et al. (2014). HDAC1 and HDAC2 control the specification of neural crest cells into peripheral glia. *J. Neurosci.* *34*, 6112–22. doi:10.1523/JNEUROSCI.5212-13.2014.
- Jaegle, M., Ghazvini, M., Mandemakers, W., Piirsoo, M., Driegen, S., Levavasseur, F., et al. (2003). The POU proteins Brn-2 and Oct-6 share important functions in Schwann cell development. *Genes Dev.* *17*, 1380–1391. doi:10.1101/gad.258203.
- Jagalur, N. B., Ghazvini, M., Mandemakers, W., Driegen, S., Maas, A., Jones, E. A., et al. (2011). Functional dissection of the Oct6 schwann cell enhancer reveals an essential role for dimeric sox10 binding. *J. Neurosci.* *31*, 8585–8594. doi:10.1523/JNEUROSCI.0659-11.2011.
- Jessen, K. R., Brennan, A., Morgan, L., Mirsky, R., Kent, A., Hashimoto, Y., et al. (1994). The Schwann cell precursor and its fate: A study of cell death and differentiation during gliogenesis in rat embryonic nerves. *Neuron* *12*, 509–527. doi:10.1016/0896-6273(94)90209-7.
- Jessen, K. R., and Mirsky, R. (2005). The origin and development of glial cells in peripheral nerves. *Nat Rev Neurosci* *6*, 671–682. doi:nrn1746 [pii]\n10.1038/nrn1746.
- Jessen, K. R., and Mirsky, R. (2016). The repair Schwann cell and its function in regenerating nerves. *J. Physiol.* *594*, 3521–3531. doi:10.1113/JP270874.
- Jessen, K. R., and Mirsky, R. (2019a). Schwann cell precursors; multipotent glial cells in embryonic nerves. *Front. Mol. Neurosci.* *12*, 69. doi:10.3389/fnmol.2019.00069.
- Jessen, K. R., and Mirsky, R. (2019b). The success and failure of the schwann cell response to nerve injury. *Front. Cell. Neurosci.* *13*, 1–14. doi:10.3389/fncel.2019.00033.
- Ji, X.-M., Wang, S.-S., Cai, X.-D., Wang, X.-H., Liu, Q.-Y., Wang, P., et al. (2019). Novel miRNA, miR-sc14, promotes Schwann cell proliferation and migration. *Neural Regen. Res.* *14*, 1651. doi:10.4103/1673-5374.255996.
- Jin, F., Dong, B., Georgiou, J., Jiang, Q., Zhang, J., Bharioke, A., et al. (2011). N-WASp is required for Schwann cell cytoskeletal dynamics, normal myelin gene expression and peripheral nerve myelination. *Development* *138*, 1329–1337. doi:10.1242/dev.058677.

- Johansson, G., Mahller, Y. Y., Collins, M. H., Kim, M.-O., Nobukuni, T., Perentesis, J., et al. (2008). Effective in vivo targeting of the mammalian target of rapamycin pathway in malignant peripheral nerve sheath tumors. *Mol. Cancer Ther.* 7, 1237–45. doi:10.1158/1535-7163.MCT-07-2335.
- Johnson, B., and Weldon, D. (2016). The Mind's Machine: Foundations of Brain and Behavior. *J. Undergrad. Neurosci. Educ.* 14, R32. Available at: <https://global.oup.com/ushe/product/the-minds-machine-9781605357300?cc=fr&lang=en> [Accessed November 26, 2019].
- Joseph, N. M., Mukoyama, Y.-S., Mosher, J. T., Jaegle, M., Crone, S. A., Dormand, E.-L., et al. (2004). Neural crest stem cells undergo multilineage differentiation in developing peripheral nerves to generate endoneurial fibroblasts in addition to Schwann cells. *Development* 131, 5599–612. doi:10.1242/dev.01429.
- Kainu, T., Kononen, J., Enmark, E., Gustafsson, J.-Å., and Peltö-Huikko, M. (1996). Localization and ontogeny of the orphan receptor OR-1 in the rat brain. *J. Mol. Neurosci.* 7, 29–39. doi:10.1007/BF02736846.
- Kandel, E. R., Schwartz, J. H. (James H., and Jessell, T. M. (2000). *Principles of neural science*. McGraw-Hill, Health Professions Division.
- Kao, S. C., Wu, H., Xie, J., Chang, C. P., Ranish, J. A., Graef, I. A., et al. (2009). Calcineurin/NFAT signaling is required for neuregulin-regulated Schwann cell differentiation. *Science (80-)*. 323, 651–654. doi:10.1126/science.1166562.
- Katarzyna, K. J., and Topilko, P. (2017). Boundary cap cells in development and disease. *Curr. Opin. Neurobiol.* 47, 209–215. doi:10.1016/j.conb.2017.11.003.
- Kim, H. A., and Maurel, P. (2009). “Primary Schwann Cell Cultures,” in (Humana Press), 253–268. doi:10.1007/978-1-60761-292-6_15.
- Kim, J., and Kim, H. A. (2018). “Isolation and expansion of Schwann cells from transgenic mouse models,” in *Methods in Molecular Biology* (Humana Press Inc.), 39–48. doi:10.1007/978-1-4939-7649-2_3.
- Komati, R., Spadoni, D., Zheng, S., Sridhar, J., Riley, K. E., and Wang, G. (2017). Ligands of Therapeutic Utility for the Liver X Receptors. *Molecules* 22. doi:10.3390/molecules22010088.
- Kucenas, S. (2015). Perineurial glia. *Cold Spring Harb. Perspect. Biol.* 7. doi:10.1101/cshperspect.a020511.
- Kucenas, S., Takada, N., Park, H. C., Woodruff, E., Broadie, K., and Appel, B. (2008). CNS-derived glia ensheath peripheral nerves and mediate motor root development. *Nat. Neurosci.* 11, 143–151. doi:10.1038/nn2025.
- Küspert, M., Weider, M., Müller, J., Hermans-Borgmeyer, I., Meijer, D., and Wegner, M. (2012). Desert hedgehog links transcription factor sox10 to perineurial development. *J. Neurosci.* 32, 5472–5480. doi:10.1523/jneurosci.5759-11.2012.
- La Marca, R., Cerri, F., Horiuchi, K., Bachi, A., Feltri, M. L., Wrabetz, L., et al. (2011). TACE (ADAM17) inhibits Schwann cell myelination. *Nat. Neurosci.* 14, 857–865. doi:10.1038/nn.2849.

- Laura Feltri, M., Suter, U., and Relvas, J. B. (2008). The function of rhogtpases in axon ensheathment and myelination. *Glia* 56, 1508–1517. doi:10.1002/glia.20752.
- Le Douarin, N. M., and Dupin, E. (2014). The Neural Crest, a Fourth Germ Layer of the Vertebrate Embryo: Significance in Chordate Evolution. *Neural Crest Cells*, 3–26. doi:10.1016/B978-0-12-401730-6.00001-6.
- LeBlanc, S. E., Srinivasan, R., Ferri, C., Mager, G. M., Gillian-Daniel, A. L., Wrabetz, L., et al. (2005). Regulation of cholesterol/lipid biosynthetic genes by Egr2/Krox20 during peripheral nerve myelination. *J. Neurochem.* 93, 737–748. doi:10.1111/j.1471-4159.2005.03056.x.
- Lehmann, J. M., Kliewer, S. A., Moore, L. B., Smith-Oliver, T. A., Oliver, B. B., Su, J.-L., et al. (1997). Activation of the Nuclear Receptor LXR by Oxysterols Defines a New Hormone Response Pathway. *J. Biol. Chem.* 272, 3137–3140. doi:10.1074/jbc.272.6.3137.
- Lewis, G. M., and Kucenas, S. (2014). Perineurial glia are essential for motor axon regrowth following nerve injury. *J. Neurosci.* 34, 12762–12777. doi:10.1523/JNEUROSCI.1906-14.2014.
- Lin, H. P., Oksuz, I., Svaren, J., and Awatramani, R. (2018). Egr2-dependent microRNA-138 is dispensable for peripheral nerve myelination. *Sci. Rep.* 8, 1–11. doi:10.1038/s41598-018-22010-8.
- Liu, G., Jiang, R., and Jin, Y. (2014). Sciatic nerve injury repair: a visualized analysis of research fronts and development trends. *Neural Regen. Res.* 9, 1716–22. doi:10.4103/1673-5374.141810.
- Livak, K. J., and Schmittgen, T. D. (2001). Analysis of relative gene expression data using real-time quantitative PCR and the $2^{-\Delta\Delta CT}$ Method. *Methods* 25, 402–408. doi:10.1006/meth.2001.1262.
- Luo, X., Prior, M., He, W., Hu, X., Tang, X., Shen, W., et al. (2011). Cleavage of neuregulin-1 by BACE1 or ADAM10 protein produces differential effects on myelination. *J. Biol. Chem.* 286, 23967–23974. doi:10.1074/jbc.M111.251538.
- Lutz, A. B. (2014). Purification of Schwann Cells from the Neonatal and Injured Adult Mouse Peripheral Nerve. *Cold Spring Harb. Protoc.* 2014, pdb.prot074989. doi:10.1101/pdb.prot074989.
- Ma, Q., Fode, C., Guillemot, F., and Anderson, D. J. (1999). NEUROGENIN1 and NEUROGENIN2 control two distinct waves of neurogenesis in developing dorsal root ganglia. *Genes Dev.* 13, 1717–1728. doi:10.1101/gad.13.13.1717.
- Ma, Y., Xu, L., Rodriguez-Agudo, D., Li, X., Heuman, D. M., Hylemon, P. B., et al. (2008). 25-Hydroxycholesterol-3-sulfate regulates macrophage lipid metabolism via the LXR/SREBP-1 signaling pathway. *Am. J. Physiol. - Endocrinol. Metab.* 295, E1369. doi:10.1152/ajpendo.90555.2008.
- Magida, J. A., and Evans, R. M. (2018). Rational application of macrophage-specific LXR agonists avoids the pitfalls of SREBP-induced lipogenesis. *Proc. Natl. Acad. Sci. U. S. A.* 115, 5051–5053. doi:10.1073/pnas.1805128115.
- Makoukji, J., Belle, M., Meffre, D., Stassart, R., Grenier, J., Shackelford, G., et al. (2012). Lithium enhances remyelination of

- peripheral nerves. *Proc. Natl. Acad. Sci.* 109, 3973–3978. doi:10.1073/pnas.1121367109.
- Makoukji, J., Shackelford, G., Meffre, D., Grenier, J., Liere, P., Lobaccaro, J.-M. a, et al. (2011). Interplay between LXR and Wnt/ β -catenin signaling in the negative regulation of peripheral myelin genes by oxysterols. *J. Neurosci.* 31, 9620–9629. doi:10.1523/JNEUROSCI.0761-11.2011.
- Malong, L., Napoli, I., White, I., Steirli, S., Bossio, A., and Lloyd, A. (2019). Macrophages enforce the blood nerve barrier. *bioRxiv*, 493494. doi:10.1101/493494.
- Mansuy-Aubert, V., Gautron, L., Lee, S., Bookout, A. L., Kusminski, C. M., Sun, K., et al. (2015). Loss of the liver X receptor LXR α/β in peripheral sensory neurons modifies energy expenditure. *Elife* 4. doi:10.7554/eLife.06667.
- Marmigère, F., and Ernfors, P. (2007). Specification and connectivity of neuronal subtypes in the sensory lineage. *Nat. Rev. Neurosci.* 8, 114–127. doi:10.1038/nrn2057.
- Marol, G. S., Vermeren, M., Voiculescu, O., Melton, L., Cohen, J., Charnay, P., et al. (2004). Neural crest boundary cap cells constitute a source of neuronal and glial cells of the PNS. *Nat. Neurosci.* 7, 930–938. doi:10.1038/nn1299.
- Maurel, P., Einheber, S., Galinska, J., Thaker, P., Lam, I., Rubin, M. B., et al. (2007). Nectin-like proteins mediate axon-Schwann cell interactions along the internode and are essential for myelination. *J. Cell Biol.* 178, 861–874. doi:10.1083/jcb.200705132.
- Mayor, R., and Theveneau, E. (2012). The neural crest. *Dev.* 140, 2247–2251. doi:10.1242/dev.091751.
- McFerrin, J., Patton, B. L., Sunderhaus, E. R., and Kretzschmar, D. (2017). NTE/PNPLA6 is expressed in mature Schwann cells and is required for glial ensheathment of Remak fibers. *Glia* 65, 804–816. doi:10.1002/glia.23127.
- Meffre, D., Shackelford, G., Hichor, M., Gorgievski, V., Tzavara, E. T., Trousson, A., et al. (2015). Liver X receptors alpha and beta promote myelination and remyelination in the cerebellum. *Proc. Natl. Acad. Sci. U. S. A.* 112, 7587–92. doi:10.1073/pnas.1424951112.
- Mei, L., and Nave, K. A. (2014). Neuregulin-ERBB signaling in the nervous system and neuropsychiatric diseases. *Neuron* 83, 27–49. doi:10.1016/j.neuron.2014.06.007.
- Michailov, G. V., Sereda, M. W., Brinkmann, B. G., Fischer, T. M., Haug, B., Birchmeier, C., et al. (2004). Axonal Neuregulin-1 Regulates Myelin Sheath Thickness. *Science (80-.)*. 304, 700–703. doi:10.1126/science.1095862.
- Mogha, A., Benesh, A. E., Patra, C., Engel, F. B., Schöneberg, T., Liebscher, I., et al. (2013). Gpr126 functions in schwann cells to control differentiation and myelination via G-protein activation. *J. Neurosci.* 33, 17976–17985. doi:10.1523/JNEUROSCI.1809-13.2013.
- Mollet, I. G., Ben-Dov, C., Felício-Silva, D., Grosso, A. R., Eleutério, P., Alves, R., et al. (2010). Unconstrained mining of transcript data reveals increased alternative splicing complexity in the human transcriptome. *Nucleic Acids Res.* 38, 4740–4754.

doi:10.1093/nar/gkq197.

Monje, P. V. (2015). To myelinate or not to myelinate: Fine tuning camp signaling in schwann cells to balance cell proliferation and differentiation. *Neural Regen. Res.* 10, 1936–1937. doi:10.4103/1673-5374.169622.

Monk, K. R., Feltri, M. L., and Taveggia, C. (2015). New insights on schwann cell development. *Glia* 63, 1376–1393. doi:10.1002/glia.22852.

Morrison, S. J., Perez, S. E., Qiao, Z., Verdi, J. M., Hicks, C., Weinmaster, G., et al. (2000). Transient notch activation initiates an irreversible switch from neurogenesis to gliogenesis by neural crest stem cells. *Cell* 101, 499–510. doi:10.1016/S0092-8674(00)80860-0.

Muse, E. D., Yu, S., Edillor, C. R., Tao, J., Spann, N. J., Troutman, T. D., et al. (2018). Cell-specific discrimination of desmosterol and desmosterol mimetics confers selective regulation of LXR and SREBP in macrophages. *Proc. Natl. Acad. Sci. U. S. A.* 115, E4680–E4689. doi:10.1073/pnas.1714518115.

Nave, K. A. (2010). Myelination and support of axonal integrity by glia. *Nature* 468, 244–252. doi:10.1038/nature09614.

Newbern, J., and Birchmeier, C. (2010). Nrg1/ErbB signaling networks in Schwann cell development and myelination. *Semin. Cell Dev. Biol.* 21, 922–928. doi:10.1016/j.semcdb.2010.08.008.

Newbern, J. M., Li, X., Shoemaker, S. E., Zhou, J., Zhong, J., Wu, Y., et al. (2011). Specific Functions for ERK/MAPK Signaling during PNS Development. *Neuron* 69, 91–105. doi:10.1016/j.neuron.2010.12.003.

Norrmén, C., Figlia, G., Lebrun-Julien, F., Pereira, J. A., Trötz Müller, M., Köfeler, H. C., et al. (2014). mTORC1 Controls PNS Myelination along the mTORC1-RXR γ -SREBP-Lipid Biosynthesis Axis in Schwann Cells. *Cell Rep.* 9, 646–660. doi:10.1016/j.celrep.2014.09.001.

Novak, N., Bar, V., Sabanay, H., Frechter, S., Jaegle, M., Snapper, S. B., et al. (2011). N-WASP is required for membrane wrapping and myelination by Schwann cells. *J. Cell Biol.* 192, 243–250. doi:10.1083/jcb.201010013.

Orita, S., Henry, K., Mantuano, E., Yamauchi, K., De Corato, A., Ishikawa, T., et al. (2013). Schwann cell LRP1 regulates Remak bundle ultrastructure and axonal interactions to prevent neuropathic pain. *J. Neurosci.* 33, 5590–5602. doi:10.1523/JNEUROSCI.3342-12.2013.

Özkaynak, E., Abello, G., Jaegle, M., Van Berge, L., Hamer, D., Kegel, L., et al. (2010). Adam22 is a major neuronal receptor for Lgi4-mediated Schwann cell signaling. *J. Neurosci.* 30, 3857–3864. doi:10.1523/JNEUROSCI.6287-09.2010.

Paavola, K. J., Sidik, H., Zuchero, J. B., Eckart, M., and Talbot, W. S. (2014). Type IV collagen is an activating ligand for the adhesion G protein-coupled receptor GPR126. *Sci. Signal.* 7, ra76. doi:10.1126/scisignal.2005347.

Parmantier, E., Lynn, B., Lawson, D., Turmaine, M., Namini, S. S., Chakrabarti, L., et al. (1999). Schwann cell-derived Desert hedgehog controls the development of peripheral nerve sheaths. *Neuron* 23, 713–24. Available at:

<http://www.ncbi.nlm.nih.gov/pubmed/10482238> [Accessed July 18, 2019].

- Patel, A. V., Johansson, G., Colbert, M. C., Dasgupta, B., and Ratner, N. (2015). Fatty acid synthase is a metabolic oncogene targetable in malignant peripheral nerve sheath tumors. *Neuro. Oncol.* 17, 1599–608. doi:10.1093/neuonc/nov076.
- Patton, K. T., and Thibodeau, G. A. (2018). *Anthony's Textbook of Anatomy and Physiology - E-Book*. Mosby.
- Pereira, J. A., Baumann, R., Norrmén, C., Somandin, C., Miehe, M., Jacob, C., et al. (2010). Dicer in Schwann cells is required for myelination and axonal integrity. *J. Neurosci.* 30, 6763–6775. doi:10.1523/JNEUROSCI.0801-10.2010.
- Petersen, S. C., Luo, R., Liebscher, I., Giera, S., Jeong, S. J., Mogha, A., et al. (2015). The Adhesion GPCR GPR126 Has Distinct, Domain-Dependent Functions in Schwann Cell Development Mediated by Interaction with Laminin-211. *Neuron* 85, 755–769. doi:10.1016/j.neuron.2014.12.057.
- Pooya, S., Liu, X., Kumar, V. B. S., Anderson, J., Imai, F., Zhang, W., et al. (2014). The tumour suppressor LKB1 regulates myelination through mitochondrial metabolism. *Nat. Commun.* 5, 4993. doi:10.1038/ncomms5993.
- Porrello, E., Rivellini, C., Dina, G., Triolo, D., Del Carro, U., Ungaro, D., et al. (2014). Jab1 regulates Schwann cell proliferation and axonal sorting through p27. *J. Exp. Med.* 211, 29–43. doi:10.1084/jem.20130720.
- Prendergast, A., and Raible, D. W. (2014). Neural Crest Cells and Peripheral Nervous System Development. *Neural Crest Cells*, 255–286. doi:10.1016/B978-0-12-401730-6.00014-4.
- Procacci, P., Ballabio, M., Castelnovo, L. F., Mantovani, C., and Magnaghi, V. (2013). GABA-B receptors in the PNS have a role in Schwann cells differentiation? *Front. Cell. Neurosci.* 6, 68. doi:10.3389/fncel.2012.00068.
- Radhakrishnan, A., Ikeda, Y., Kwon, H. J., Brown, M. S., and Goldstein, J. L. (2007). Sterol-regulated transport of SREBPs from endoplasmic reticulum to Golgi: Oxysterols block transport by binding to Insig. *Proc. Natl. Acad. Sci.* 104, 6511–6518. doi:10.1073/pnas.0700899104.
- Rasband, M. N. (2016). Glial Contributions to Neural Function and Disease. *Mol. Cell. Proteomics* 15, 355–61. doi:10.1074/mcp.R115.053744.
- Ratner, N., Williams, J. P., Kordich, J. J., and Kim, H. A. (2005). Schwann Cell Preparation from Single Mouse Embryos: Analyses of Neurofibromin Function in Schwann Cells. *Methods Enzymol.* 407, 22–33. doi:10.1016/S0076-6879(05)07003-5.
- Reiprich, S., Kriesch, J., Schreiner, S., and Wegner, M. (2010). Activation of Krox20 gene expression by Sox10 in myelinating Schwann cells. *J. Neurochem.* 112, 744–754. doi:10.1111/j.1471-4159.2009.06498.x.
- Ren, S., Li, X., Rodriguez-Agudo, D., Gil, G., Hylemon, P., and Pandak, W. M. (2007). Sulfated oxysterol, 25HC3S, is a potent regulator of lipid metabolism in human hepatocytes. *Biochem. Biophys. Res. Commun.* 360, 802–808. doi:10.1016/j.bbrc.2007.06.143.

- Ren, S., and Ning, Y. (2014). Sulfation of 25-hydroxycholesterol regulates lipid metabolism, inflammatory responses, and cell proliferation. *Am. J. Physiol. - Endocrinol. Metab.* 306, E123. doi:10.1152/ajpendo.00552.2013.
- Repa, J. J., Liang, G., Ou, J., Bashmakov, Y., Lobaccaro, J. M., Shimomura, I., et al. (2000). Regulation of mouse sterol regulatory element-binding protein-1c gene (SREBP-1c) by oxysterol receptors, LXRalpha and LXRbeta. *Genes Dev.* 14, 2819–2830. doi:10.1101/gad.844900.
- Richard, L., Topilko, P., Magy, L., Decouvelaere, A.-V., Charnay, P., Funalot, B., et al. (2012). Endoneurial Fibroblast-Like Cells. *J. Neuropathol. Exp. Neurol.* 71, 938–947. doi:10.1097/NEN.0b013e318270a941.
- Richard, L., Védrenne, N., Vallat, J.-M., and Funalot, B. (2014). Characterization of Endoneurial Fibroblast-like Cells from Human and Rat Peripheral Nerves. *J. Histochem. Cytochem.* 62, 424–435. doi:10.1369/0022155414530994.
- Richner, M., Ferreira, N., Dudele, A., Jensen, T. S., Vaegter, C. B., and Gonçalves, N. P. (2019). Functional and Structural Changes of the Blood-Nerve-Barrier in Diabetic Neuropathy. *Front. Neurosci.* 12, 1038. doi:10.3389/fnins.2018.01038.
- Rigaud, M., Gemes, G., Barabas, M.-E., Chernoff, D. I., Abram, S. E., Stucky, C. L., et al. (2008). Species and strain differences in rodent sciatic nerve anatomy: Implications for studies of neuropathic pain. *Pain* 136, 188–201. doi:10.1016/j.pain.2008.01.016.
- Rong, S., Cortés, V. A., Rashid, S., Anderson, N. N., McDonald, J. G., Liang, G., et al. (2017). Expression of SREBP-1c Requires SREBP-2-mediated Generation of a Sterol Ligand for LXR in Livers of Mice. *Elife* 6. doi:10.7554/eLife.25015.
- Salzer, J. L. (2015). Schwann cell myelination. *Cold Spring Harb. Perspect. Biol.* 7, 1–26. doi:10.1101/cshperspect.a020529.
- Schmittgen, T. D., and Livak, K. J. (2008). Analyzing real-time PCR data by the comparative C(T) method. *Nat. Protoc.* 3, 1101–8.
- Shackelford, G., Makoukji, J., Grenier, J., Liere, P., Meffre, D., and Massaad, C. (2013). Differential regulation of Wnt/beta-catenin signaling by Liver X Receptors in Schwann cells and oligodendrocytes. *Biochem. Pharmacol.* 86, 106–114. doi:10.1016/j.bcp.2013.02.036.
- Sharghi-Namini, S., Turmaine, M., Meier, C., Sahni, V., Umehara, F., Jessen, K. R., et al. (2006). The structural and functional integrity of peripheral nerves depends on the glial-derived signal desert hedgehog. *J. Neurosci.* 26, 6364–76. doi:10.1523/JNEUROSCI.0157-06.2006.
- Sheean, M. E., McShane, E., Cheret, C., Walcher, J., Müller, T., Wulf-Goldenberg, A., et al. (2014). Activation of MAPK overrides the termination of myelin growth and replaces Nrg1/ErbB3 signals during Schwann cell development and myelination. *Genes Dev.* 28, 290–303. doi:10.1101/gad.230045.113.
- Shen, Y.-A. a, Chen, Y., Dao, D. Q., Mayoral, S. R., Wu, L., Meijer, D., et al. (2014). Phosphorylation of LKB1/Par-4 establishes Schwann cell polarity to initiate and control myelin extent. *Nat. Commun.* 5, 4991. doi:10.1038/ncomms5991.
- Sherman, D. L., Krols, M., Wu, L. M. N., Grove, M., Nave, K. A., Gangloff, Y. G., et al. (2012). Arrest of myelination and reduced

- axon growth when Schwann cells lack mTOR. *J. Neurosci.* 32, 1817–1825. doi:10.1523/JNEUROSCI.4814-11.2012.
- Shimizu, F., Sano, Y., Abe, M. aki, Maeda, T., Ohtsuki, S., Terasaki, T., et al. (2011). Peripheral nerve pericytes modify the blood-nerve barrier function and tight junctional molecules through the secretion of various soluble factors. *J. Cell. Physiol.* 226, 255–266. doi:10.1002/jcp.22337.
- Shimomura, I., Goldstein, J. L., and Brown, M. S. (1997). Differential expression of exons 1a and 1c in mRNAs for sterol regulatory element binding protein-1 in human and mouse organs and cultured cells. *J Clin Invest* 99. doi:10.1172/JCI119247.
- Shin, Y. K., Jang, S. Y., Park, S. Y., Park, J. Y., Kim, J. K., Kim, J. P., et al. (2014). Grb2-associated binder-1 is required for neuregulin-1- induced peripheral nerve myelination. *J. Neurosci.* 34, 7657–7662. doi:10.1523/JNEUROSCI.4947-13.2014.
- Snyder, J. M., Hagan, C. E., Bolon, B., and Keene, C. D. (2018). Nervous System. *Comp. Anat. Histol.*, 403–444. doi:10.1016/B978-0-12-802900-8.00020-8.
- Spiegel, I., Adamsky, K., Eshed, Y., Milo, R., Sabanay, H., Sarig-Nadir, O., et al. (2007). A central role for Necl4 (SynCAM4) in Schwann cell-axon interaction and myelination. *Nat. Neurosci.* 10, 861–869. doi:10.1038/nn1915.
- Stewart, H. J., Brennan, A., Rahman, M., Zoidl, G., Mitchell, P. J., Jessen, K. R., et al. (2001). Developmental regulation and overexpression of the transcription factor AP-2, a potential regulator of the timing of Schwann cell generation. *Eur. J. Neurosci.* 14, 363–72. doi:10.1046/j.0953-816x.2001.01650.x.
- Su-chun Ho, M., Navarro, X., Andrews, M. R., Zoidl, G., Lehmann, H., Franzen, R., et al. (2017). Molecular Mechanisms Involved in Schwann Cell Plasticity. *Front. Mol. Neurosci. / www.frontiersin.org* 10, 38. doi:10.3389/fnmol.2017.00038.
- Sundaram, V. K., Barakat, R., Massaad, C., Grenier, J., and Sundaram, V. K. (2020). Retracing Schwann cell developmental transitions in embryonic dissociated DRG cultures 2. *bioRxiv*, 2020.07.31.231258. doi:10.1101/2020.07.31.231258.
- Sundaram, V. K., Massaad, C., and Grenier, J. (2019a). Liver X Receptors and Their Implications in the Physiology and Pathology of the Peripheral Nervous System. *Int. J. Mol. Sci.* 20, 4192. doi:10.3390/ijms20174192.
- Sundaram, V. K., Sampathkumar, N. K., Massaad, C., and Grenier, J. (2019b). Optimal use of statistical methods to validate reference gene stability in longitudinal studies. *PLoS One* 14, e0219440. doi:10.1371/journal.pone.0219440.
- Svaren, J., and Meijer, D. (2008). The molecular machinery of myelin gene transcription in schwann cells. *Glia* 56, 1541–1551. doi:10.1002/glia.20767.
- Taneyhill, L. A., and Padmanabhan, R. (2014). “The Cell Biology of Neural Crest Cell Delamination and EMT,” in *Neural Crest Cells* (Elsevier), 51–72. doi:10.1016/B978-0-12-401730-6.00003-X.
- Taveggia, C., Zanazzi, G., Petrylak, A., Yano, H., Rosenbluth, J., Einheber, S., et al. (2005). Neuregulin-1 type III determines the ensheathment fate of axons. *Neuron* 47, 681–694. doi:10.1016/j.neuron.2005.08.017.

- Topilko, P., Schneider-Maunoury, S., Levi, G., Baron-Van Evercooren, A., Chennoufi, A. B. Y., Seitanidou, T., et al. (1994). Krox-20 controls myelination in the peripheral nervous system. *Nature* 371, 796–799. doi:10.1038/371796a0.
- Torii, T., Miyamoto, Y., Takada, S., Tsumura, H., Arai, M., Nakamura, K., et al. (2014). In vivo knockdown of ErbB3 in mice inhibits Schwann cell precursor migration. *Biochem. Biophys. Res. Commun.* 452, 782–788. doi:10.1016/j.bbrc.2014.08.156.
- Trimarco, A., Forese, M. G., Alfieri, V., Lucente, A., Brambilla, P., Dina, G., et al. (2014). Prostaglandin D2 synthase/GPR44: A signaling axis in PNS myelination. *Nat. Neurosci.* 17, 1682–1692. doi:10.1038/nn.3857.
- Ungos, J. M., Karlstrom, R. O., and Raible, D. W. (2003). Hedgehog signaling is directly required for the development of zebrafish dorsal root ganglia neurons. *Development* 130, 5351–5362. doi:10.1242/dev.00722.
- Valentijn, L. J., Bolhuis, P. A., Zorn, I., Hoogendijk, J. E., van den Bosch, N., Hensels, G. W., et al. (1992). The peripheral myelin gene PMP-22/GAS-3 is duplicated in Charcot–Marie–Tooth disease type 1A. *Nat. Genet.* 1, 166–170. doi:10.1038/ng0692-166.
- Varin, J., Poulain, L., Hivelin, M., Nusbaum, P., Hubas, A., Laurendeau, I., et al. (2016). Dual mTORC1/2 inhibition induces anti-proliferative effect in NF1-associated plexiform neurofibroma and malignant peripheral nerve sheath tumor cells. *Oncotarget* 7, 35753–35767. doi:10.18632/oncotarget.7099.
- Verheijen, M. H. G., Camargo, N., Verdier, V., Nadra, K., de Preux Charles, A.-S., Médard, J.-J., et al. (2009). SCAP is required for timely and proper myelin membrane synthesis. *Proc. Natl. Acad. Sci. U. S. A.* 106, 21383–8. doi:10.1073/pnas.0905633106.
- Viader, A., Golden, J. P., Baloh, R. H., Schmidt, R. E., Hunter, D. A., and Milbrandt, J. (2011). Schwann cell mitochondrial metabolism supports long-term axonal survival and peripheral nerve function. *J Neurosci* 31, 10128–10140. doi:10.1523/JNEUROSCI.0884-11.2011.
- Waltl, S., Patankar, J. V., Fauler, G., Nussold, C., Üllen, A., Eibinger, G., et al. (2013). 25-Hydroxycholesterol regulates cholesterol homeostasis in the murine CATH.a neuronal cell line. *Neurosci. Lett.* 539, 16–21. doi:10.1016/j.neulet.2013.01.014.
- Wanner, I. B., Mahoney, J., Jessen, K. R., Wood, P. M., Bates, M., and Bunge, M. B. (2006). Invariant mantling of growth cones by Schwann cell precursors characterize growing peripheral nerve fronts. *Glia* 54, 424–438. doi:10.1002/glia.20389.
- Woldeyesus, M. T., Britsch, S., Riethmacher, D., Xu, L., Sonnenberg-Riethmacher, E., Abou-Rebyeh, F., et al. (1999). Peripheral nervous system defects in erbB2 mutants following genetic rescue of heart development. *Genes Dev.* 13, 2538–2548. doi:10.1101/gad.13.19.2538.
- Wolpowitz, D., Mason, T. B., Dietrich, P., Mendelsohn, M., Talmage, D. A., and Role, L. W. (2000). Cysteine-rich domain isoforms of the neuregulin-1 gene are required for maintenance of peripheral synapses. *Neuron* 25, 79–91. doi:10.1016/s0896-6273(00)80873-9.

- Woodhoo, A., Alonso, M. B. D., Droggiti, A., Turmaine, M., D'Antonio, M., Parkinson, D. B., et al. (2009). Notch controls embryonic Schwann cell differentiation, postnatal myelination and adult plasticity. *Nat. Neurosci.* 12, 839–847. doi:10.1038/nn.2323.
- Woodhoo, A., and Sommer, L. (2008). Development of the schwann cell lineage: From the neural crest to the myelinated nerve. *Glia* 56, 1481–1490. doi:10.1002/glia.20723.
- Woolley, A. G., Tait, K. J., Hurren, B. J., Fisher, L., Sheard, P. W., and Duxson, M. J. (2008). Developmental loss of NT-3 in vivo results in reduced levels of myelin-specific proteins, a reduced extent of myelination and increased apoptosis of Schwann cells. *Glia* 56, 306–317. doi:10.1002/glia.20614.
- Wu, J., Williams, J. P., Rizvi, T. A., Kordich, J. J., Witte, D., Meijer, D., et al. (2008). Plexiform and Dermal Neurofibromas and Pigmentation Are Caused by Nf1 Loss in Desert Hedgehog-Expressing Cells. *Cancer Cell* 13, 105–116. doi:10.1016/j.ccr.2007.12.027.
- Yamamoto, M., Okui, N., Tatebe, M., Shinohara, T., and Hirata, H. (2011). Regeneration of the perineurium after microsurgical resection examined with immunolabeling for tenascin-C and alpha smooth muscle actin. *J. Anat.* 218, 413–425. doi:10.1111/j.1469-7580.2011.01341.x.
- Yamauchi, J., Chan, J. R., and Shooter, E. M. (2003). Neurotrophin 3 activation of TrkC induces Schwann cell migration through the c-Jun N-terminal kinase pathway. *Proc. Natl. Acad. Sci. U. S. A.* 100, 14421–14426. doi:10.1073/pnas.2336152100.
- Yang, C., McDonald, J. G., Patel, A., Zhang, Y., Umetani, M., Xu, F., et al. (2006). Sterol intermediates from cholesterol biosynthetic pathway as liver X receptor ligands. *J. Biol. Chem.* 281, 27816–27826. doi:10.1074/jbc.M603781200.
- Yu, W.-M. (2005). Schwann Cell-Specific Ablation of Laminin 1 Causes Apoptosis and Prevents Proliferation. *J. Neurosci.* 25, 4463–4472. doi:10.1523/JNEUROSCI.5032-04.2005.
- Zhou, Y., Miles, J. R., Tavori, H., Lin, M., Khoshbouei, H., Borchelt, D., et al. (2019). PMP22 regulates cholesterol trafficking and ABCA1-mediated cholesterol efflux. *J. Neurosci.* 39, 2942–18. doi:10.1523/jneurosci.2942-18.2019.